

**POLITECNICO DI TORINO**

Ph. D. in Mechanics  
(S.D. ING-IND/14)

XXVII Ph. D. Course

**Ph. D. Thesis**

**HIGH STRAIN-RATE AND TEMPERATURE BEHAVIOUR OF  
METALS: ADVANCED TESTING AND MODELLING**



Claudio Fichera

Tutor

Prof. Massimiliano Avalle

Coordinator

Prof. Luigi Garibaldi

March 2015



# Index

Index .....	i
Introduction.....	1
2. Dynamic response of metals .....	5
2.1 Strain-rate and temperature sensitivity of metals.....	6
2.2 Experimental equipment at various strain-rate .....	9
2.2.1 Electro-mechanical facilities .....	12
2.2.2 Servo-hydraulic equipments.....	13
2.2.3 Drop and pneumatic machines .....	14
2.2.4 Hopkinson Bar.....	16
2.2.5 Ultra-high strain-rate facilities .....	17
2.3 Heating systems .....	22
2.3.1 Furnace .....	23
2.3.2 Induction coil system.....	24
2.3.3 Infra-Red spot heater .....	25
2.4 Material strength models.....	26
2.5 Failure models .....	29
2.6 Finite Element Method simulations .....	30
3. Advanced high strain-rate and heating equipments.....	33
3.1 Experimental equipments at low strain-rate.....	34
3.2 Experimental equipments at high strain-rate.....	36

3.2.1 SHPB setup for compression test .....	36
3.2.2 Direct Split Hopkinson Tensile Bar .....	43
3.2.3 Miniaturized Split Hopkinson Tensile Bar .....	48
3.3 Digital image acquisition .....	54
3.3.1 High resolution camera for low strain-rate tests.....	55
3.3.2 High speed camera for high strain-rate tests .....	57
3.4 Combined experimental equipments.....	63
3.4.1 Setup for low strain-rate tests varying temperature.....	64
3.4.2 Setup for high strain-rate tests varying temperature.....	66
3.4.3 Advanced setup for high strain-rate tests with heating and image acquisition systems .....	69
4. Data analysis .....	73
4.1 Digital image processing.....	73
4.2 Calculation of uniaxial stress and strain.....	75
4.2.1 Experimental results for high chromium T91 steel .....	79
4.2.2 Experimental results for Glidcop Al-15 .....	82
4.2.3 Experimental results for heavy sintered molybdenum .....	86
4.2.4 Materials comparison .....	89
4.3 Material models.....	90
4.3.1 Johnson-Cook model .....	90
4.3.2 Zerilli-Armstrong model .....	94
4.4 Material strength model identification .....	98
4.4.1 Johnson-Cook model calibration.....	98
4.4.2 Zerilli-Armstrong model calibration .....	110
4.4.2 Modified Zerilli-Armstrong model calibration .....	117
5. Numerical analysis.....	125
5.1 Instability condition .....	125
5.2 Stress and strain distribution at the neck.....	127
5.2.1 Application of Bridgman equation .....	132
5.3 Numerical inverse optimization .....	137

5.3.1 Numerical Single-Objective Optimization .....	141
5.3.2 Numerical Multi-Objective Optimization .....	152
5.4 Advanced numerical inverse analysis .....	158
6. Conclusions.....	171
References.....	179



# Introduction

Nowadays the Finite Element Analysis is a valid support for the design and the understanding of complex phenomena such as machining processes, automotive crashworthiness, explosions, ballistic and high energy impacts, etc. In general, these phenomena are simultaneously affected by extended strain, high strain-rate, damage and pressure, as well as conspicuous temperature gradients. In order to correctly predict the real evolution of the investigated problem, a numerical model requires many data. Surely, the constitutive material model represents one of the most important.

In particular, in this thesis, the attention was mainly focused on the identification of a suitable strength model, depending on the material and the loading conditions. In this perspective, the experimental testing campaign and the definition of the methodology for the model calibration parameters could be essential.

In more detail, the main objective of this thesis was the prediction of the dynamic behaviour of metals. For this purpose, three different metals were considered: the high chromium ferritic/martensitic T91 steel, the copper-based composite Glidcop Al-15 and the heavy sintered molybdenum. In order to investigate the mechanical response of these metals in dynamic conditions, different experimental techniques were developed and used. The experimental data were analyzed through different procedures with the aim to provide consistent methodologies suited to extract sets of model parameters usable in the commercial FE codes.

In the chapter 2 the influence of dynamic solicitations on the behaviour of metals was described in detail, with particular reference to strain-rate and temperature effects, which are coupled in a high strain-rate regime. After that, a general overview on the experimental techniques used for the characterization of metals at different strain-rates and temperatures were presented. For each technique the operating principles were explained and the experimental difficulties in the test execution were highlighted. At the end of the chapter the criteria, on which the strength and failure models are based, were discussed, with particular attention to their implementation in the numerical codes. In this sense, the importance of the deviatoric and hydrostatic components, which define the stress and strain tensors, were put in evidence.

More exhaustive investigation and description of all the aspects related to the experimental techniques used in this work were concentrated in the chapter 3. For the complete characterization of the considered materials, it is necessary to conduct a testing campaign in which different loading conditions are investigated. In the thesis the tensile loading condition was analyzed at different strain-rates, temperatures and both of them. Several tensile testing equipments were used in order to investigate the mechanical response in the strain-rate range between  $10^{-3}$  up to  $10^4$  s<sup>-1</sup>. In addition, two digital acquisition systems were used. The investigation of the materials response varying the temperature was performed by using an induction coil system in both low and high strain-rates.

The experimental results were analyzed in the chapter 4. The critical aspects related to the correct evaluation of the material response in tensile tests were discussed at the beginning of the chapter. After that, the results in terms of true stress vs. true strain curves at different strain-rates and temperatures were reported for all the considered materials. In order to reproduce the experimental curves, two of the most commonly used strength models suitable to describe the dynamic behaviour of metals were presented: the Johnson-Cook (J-C) and the Zerilli-Armstrong (Z-A) models. The characteristics of both the models were analyzed in detail putting in evidence their strong points and limits. The analytical procedures for the identification of the J-C and Z-A model parameters were presented and applied in the

experimental results data fitting. Since some limits in the prediction of the materials response were come out, also a modified version of the Z-A model was considered.

In tensile tests the evaluation of the effective stress vs. strain relation up to fracture is particularly difficult to perform analytically, due to the strain localization and the non-uniform distribution of the quantities inside the specimen. In chapter 5, different solutions to solve these issues were shown. A first attempt to deal with the necking localization was presented at the beginning of the chapter, in which the problem of the instability in tension was analyzed. The model proposed by Bridgman, based on the actual specimen dimensions, was considered and applied to describe the mechanical response of the T91 steel up to fracture. Since this model does not consider the non-uniform distributions of the quantities during the specimen deformation, some numerical inverse methods were considered. By using Finite Element (FE) models, different numerical optimization procedures can be used in order to identify the strength model parameters which allow the correctly reproduce the experimental results. The great advantage of numerical inverse method is that no hypothesis about the internal specimen or component stress-strain, temperature, or strain-rate fields has to be made. In fact, usually, the optimization is made in terms of macroscopic quantities, such as force and displacement. In this perspective, both Single-Objective Optimization and Multi-Objective Optimization were applied. The first one was used when the aim of the iteration procedure was the determination of the model parameters based on the best fit with one specific experimental target; while the latter one was used if the final goal is the determination of the set of model parameters, which reproduces as best as possible the global behaviour of material in different loading conditions. In this work the numerical simulations were performed by using the FE code LSDYNA<sup>®</sup>, and the optimizations of the parameters were performed with a dedicated algorithm included in the software LS-OPT<sup>®</sup>. In order to increase the reliability of the numerical model, an advanced numerical optimization procedure, based on the control of the specimen shape, was finally proposed. The method was developed by using the necking information extracted from the digitally acquired images during the entire deformation process.



## 2. Dynamic response of metals

In many industrial applications to consider the dynamic response of materials is crucial. Indeed, for a careful safety design, in nuclear, ballistic or military fields, a deep knowledge of the mechanical behaviour at high strain-rates of considered materials is required. In general, impact or explosive phenomena are simultaneously affected by extended strain, high strain-rate, damage and pressure, as well as conspicuous temperature gradients. For these reasons the dynamic scenarios could be very complicated to investigate. In the past, in particular in the military field, the typical design approach was mainly based on the designers experience and validations through experimental tests. However, this methodology exhibits different disadvantages: a limited phenomena comprehension entails a rough estimation of the physical quantities that take part, the whole design process is hold in trust of the designer, to reproduce the case study experimentally could be very expensive and dangerous. Considering all these aspects and thanks to the modern calculators performance, nowadays, the industries are stressing to use the Finite Element Method in the design process. Indeed, the introduction of the FEM has drastically changed the design conception because the numerical models can be easily managed reducing the production cost and design time. At the same time, it represents a useful tool for the reproduction of dangerous phenomena (e.g. nuclear experiments or explosions) in a safety way.

Based on what mentioned before, at the beginning of this chapter the influence of dynamic solicitations on the behaviour of metals will be treated. After that, it will be

shown the main experimental devices used for the characterization of metals at high strain-rate and temperature. Successively, the criteria on which are based the strength and failure models will be discussed. Finally, some numerical simulation aspects will be discussed in order to better understand the importance of FEM simulations in the study of dynamic phenomena.

## 2.1 Strain-rate and temperature sensitivity of metals

It is proved that the mechanical behaviour of materials can be strongly influenced by the loading conditions. Considering dynamic solicitations, in general, the main effect on the metals response is an overall increment of the strength. From a microscopic point of view, this is primarily the result of dislocations moving through the crystal lattice [1]. Indeed, the flow stress of the material is determined by the material structure, at which are associated the short range barriers and the interaction of dislocations with the lattice and with the various obstacles encountered within the lattice (long range barriers). Because the motion of dislocations is closely tied to atomic level interactions, thermal vibrations of atoms within the lattice could have a profound effect on the macroscopic behaviour [2]. So, as it is well-known, the motion of a dislocation can occur only if the energy supplied by a combination of applied stress and thermal activation is enough to overcome the, so called, energy barrier. During the deformation process the dislocations interaction becomes gradually more intense and the necessary amount of energy rise up, generating the strain hardening effect in the mechanical response. Nevertheless, this combination of applied stress and thermal activation is dependent from loading condition. It is easy to imagine that varying the strain-rate the proportion of these quantities changes within the structure. The result is that the effective stress required to generate an overall plastic strain-rate is intimately tied to the temperature at which the deformation occurs (thermal activated regime). It is important to highlight that this discussion is limited to strain-rate regimes ( $<10^5 \text{ s}^{-1}$ ) which are below to those dominated by phonon drag and other viscous lattice interactions, where the whole

phenomenon is based on atomic vibrations [3,4]. Thus, it is important to point out that in thermal activated regime the metals behaviour is considered determined, at the microscopic level, by the mechanisms associated with dislocation motion and dislocation multiplication, by the statistics of mobile dislocation populations, by the nature of the obstacles and the statistics of obstacle distributions, and by the relationship between the externally imposed plastic strain-rate and the dislocation kinetics.

In dynamic tests the materials undergo impulsive loads, therefore the stress is applied in a very short time and the dislocation motion mechanism is quite different with respect to quasi-static case. Indeed, the dislocations encounter other dislocations or obstacles more rapidly which do not permit complete stress redistribution within lattice. Obviously, this mechanism requires more energy to allow dislocations to go on over. This effect is known as strain-rate hardening. However, all these considerations are true in an initial stage, because also the temperature has to be taken into account [5].

During the deformation process the plastic work is converted into heat. The temperature increase,  $dT$ , due to plastic deformation can be estimated by the well-known Taylor-Quinney relation:

$$dT = \frac{\beta}{\rho \cdot C_p} \cdot \int_0^{\varepsilon_p} \sigma \cdot d\varepsilon \quad (2.1)$$

where  $\sigma$  and  $\varepsilon$  are the stress and strain,  $\rho$  is the material density,  $C_p$  is its specific heat capacity at constant pressure, and  $\beta$  is the Taylor-Quinney coefficient which represents the fraction of energy transferred to heat. This last parameter depends on material properties, but, for metals, it is estimated varying within  $0.95 \div 1$  [6,7].

When the strain-rates are relatively low ( $< 10^1 \text{ s}^{-1}$ ), there is sufficient time to allow the heat transfer, so the whole deformation process could be considered isothermal. On the other side, if the strain-rate is high, the material could be subjected to a

conspicuous temperature increment and the process is assumed to be adiabatic. For materials which are bad heat conductors or have low densities and high strength (stainless steels, aluminium alloys, etc.) the phenomenon could be extremely important with temperature increase of around one hundred Celsius degree at plastic strain of 50%. Naturally, the material response is affected by the temperature increment: increasing the temperature the atoms vibration rises up. Consequently, the probability that an atom reaches a new equilibrium condition in another site increases, therefore the dislocations motion is facilitated (decrease of the required force) [8]. This phenomenon is known as thermal softening. However, this is not valid for long range barriers, which are correlated to defects such as solutes, vacancies, precipitates or other dislocations. In this case the obstacles can not be overcome by additional thermal energy, but supplying higher forces.

At this point, it is clear that in dynamic field to consider thermo-mechanical coupled problems is necessary. From a mechanical phenomenological point of view, increasing the strain-rate, the effects on the mechanical behaviour of metals can be summarized in this way:

- increase of the material strength due to strain-rate hardening. However, at high strains the thermal component becomes relevant and the material resistance undergoes a significant reduction. The thermal softening could be so much evident that the ultimate strength of a material solicited dynamically is lower than the quasi-static case. In the load vs. displacement diagrams this can be appreciate observing the dynamic curve response to across the quasi-static one;
- reduction of the ductility. In general, the ultimate strain for dynamic tests is smaller than quasi-static tests. The early collapse is firstly due to intense dislocations interaction at high strain-rate which accelerates the generation of cavities and, consequently, the rupture. Also in this case, the temperature increase can strongly affect this behaviour and, in contrast with the previous consideration, delay the collapse;

- modification of the relation between pressure, density and internal energy. At high strain-rate the hydrostatic component of stress increases and a linear dependence between pressure and density (constant bulk modulus) could be no longer valid and a more sophisticated Equation Of State (EOS) should be used [9]. Depending on the material, the pressure could significantly influence the mechanical response and the hydrostatic stress component becomes prevalent with respect to deviatoric one. Since the maximum strain-rates considered in this thesis are in the order of  $10^4 \text{ s}^{-1}$ , a linear EOS is used, neglecting phase changing of the material, which could take place in metals at high levels of pressure.

## 2.2 Experimental equipment at various strain-rate

During the last century the efforts of many researchers were focused to develop and improve various experimental devices in order to investigate the material behaviour varying the strain-rate ( $\dot{\epsilon}$ ). In many works the different experimental techniques were collected and explained in detail. It well known that it is not possible to completely characterize a material from low to high strain-rate with only one testing equipment because each one can operate in a limited range of velocity. Therefore, the mechanical tests are usually classified on the basis of strain-rate or testing setups used. The method of loading, the strain-rate regime and the important dynamic events needed to be considered for testing in the specific regime were analysed by Lindholm [10] and are summarized in the Fig. 2.1. Each of these methods can be used for obtaining particular information such as: dynamic strength and modulus, failure mechanisms, notch or temperature sensitivity, etc.

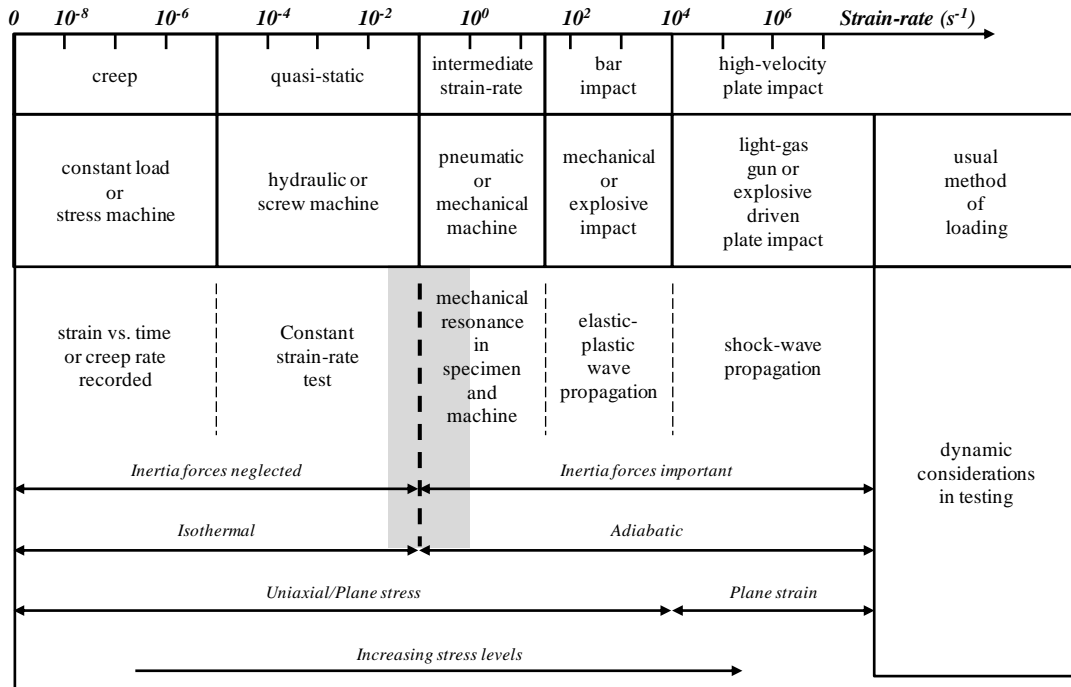


Fig. 2.1: Dynamic aspects of mechanical testing.

Considering each operating range of testing equipments in detail:

- the quasi-static tests ( $10^{-5} \leq \dot{\epsilon} \leq 10^{-1}$ ) represent the category wherein the thermal effects are neglected. Wave propagation and vibration phenomena are not considered and the mechanical tests are assumed isothermal. Generally, these tests are performed with standard electro-mechanic or servo-hydraulic machines using different types of specimens (beams, cylinders, dog-bone shapes, etc.). Furthermore, different loading conditions can be easily reproduced, such as: compression, tensile, bending, torsion, etc.;
- at intermediate strain-rate ( $10^{-1} \leq \dot{\epsilon} \leq 10^2$ ) the mechanical tests are considered a little more complicated respect the quasi-static tests. Increasing the loading rate the acquired signals start to be affected by noise, in particular the force data. This is primarily due to the combination of initial generation of dynamic effects in the material tested (vibrations, inertia forces) and the loading system. Usually, at medium strain-rate, conventional equipments

such as servo-hydraulic machines with high servo-valves capability are used or less conventional testing devices to perform punch, Charpy or drop weight tests. In this strain-rate range the mechanical transformations of the material could start to be assumed adiabatic;

- at high strain-rate ( $10^2 \leq \dot{\epsilon} \leq 10^4$ ), instead, the process must be considered adiabatic and the increase of temperature at high strains can not be neglected and. As it will be widely discussed in the next paragraphs, in high strain-rate tests the specimen is not uniformly loaded during the whole test execution time, so the data have to be accurately managed. In this range of velocity, surely, the Split Hopkinson Pressure Bar (SHPB) represents the test equipment widely used. It is based on the elastic waves propagation in elastic rods and several setups exist to perform compression, tensile, shear or bending tests;

- finally, the ultra-high strain-rate ( $10^4 \leq \dot{\epsilon} \leq 10^5$ ) tests involve the phenomena in which the mechanical transformations must be considered perfectly adiabatic. These velocities are typical of ballistic or explosion scenarios. Moreover, the material behaviour is regulated by waves propagation and it is possible to observe micro-structural changes such as phase transformations. At this category belongs the impact rod test, the Dynamic Tensile Extrusion (DTE) test and the flyer plate methodology. The main issue of these facilities is the way to get the information about the stress-strain field because not always the analytical formulations are able to describe it. For this reason, often it is necessary to use the numerical inverse method in order to extract the material strength parameters.

In the following, the main features of the equipments mentioned before will be briefly described in strain-rate ascending order. Probably, an accurate and complete material characterization from very low to extremely high strain-rates should be performed using all the testing equipments showed later. Nevertheless, the experimental facilities could be very expensive and, in particular for the

unconventional devices, the setup timing could be considerable. For this reason, a common solution is to perform experimental tests at specific strain-rates within of the strain-rate range of interest (usually at least the lower, middle and higher values of the range should be investigated). In this way, on the basis of the experimental results, the global material behaviour could be analyzed and extended to the other strain-rates.

### 2.2.1 Electro-mechanical facilities

Generally, almost all the mechanical laboratories are equipped with electro-mechanical machines. The motivation is that the largest part of the materials characterization is carried out in quasi-static conditions. On the basis of specimen and machine clamps geometries, it is possible to perform different solicitation conditions (compression, tensile, shear, etc.). Normally, the frame structure is composed by two columns which include the sliding guides and two ball-screws to transmit motion to a mobile crosshead (see Fig. 2.2). The tests are generally controlled in force or stroke and the motion is regulated by an asynchronous or a brushless electric motor connected to the ball-screws. Usually, the force signal is obtained by an extensimetric load cell placed between the crosshead and the clamp/anvil structure, while the machine stroke data is directly derived from the resolver transducer which equipped the electric engine. But, as it is known, the crosshead displacement is a rough quantity not very representative of the real specimen deformation (due to the tolerance between the specimen and the anvils as well as the machine deformation); therefore in the uniaxial tests the extesometers are commonly used to measure the specimen elongation, at least in the elastic field of mechanical response. The electro-mechanical equipments are distinguished for their high solidity and stiffness as well as high stroke capability. Generally, the control system is integrated and user-friendly. This kind of facilities is widely used for quasi-static tests thanks its simplicity and low, even null, signal noise. Instead, the principal

limit is the slowness, indeed the maximum velocity is in the order of one hundred of mm/min.

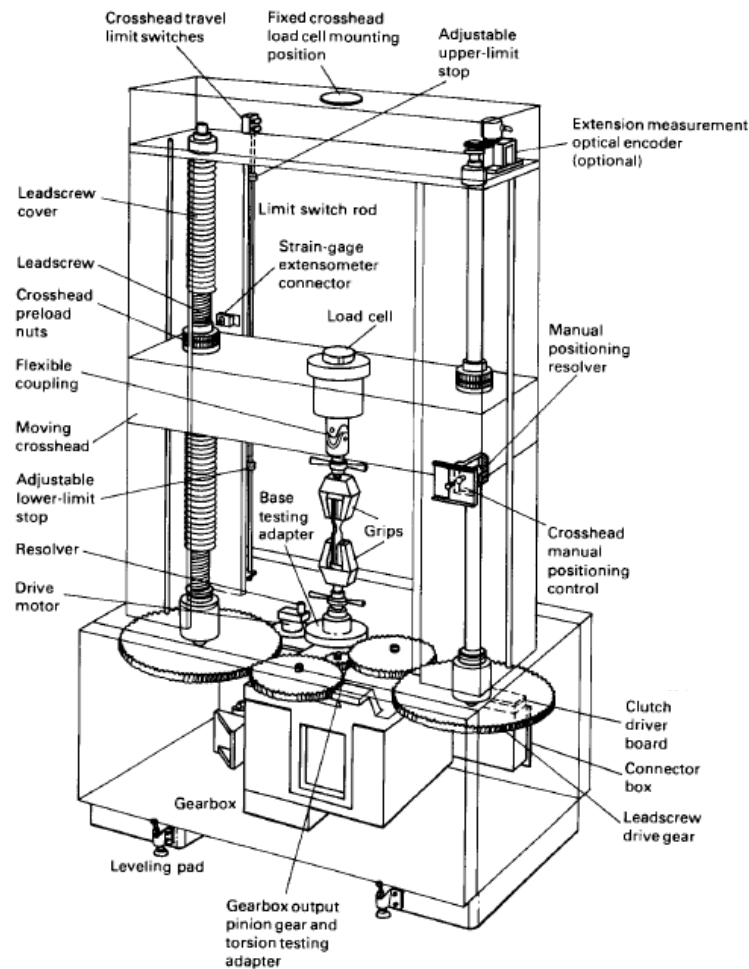


Fig. 2.2: Components of a screw-driven testing machine [11].

### 2.2.2 Servo-hydraulic equipments

With servo-hydraulic testing equipment it is possible to increase the strain-rate thanks to oleo-dynamic actuation. About one hundred of mm/s is the normal velocity limit of these machines, but advanced setups are able to reach deformation velocities around one m/s. A typical frame structure is very similar to electro-mechanic

machines; normally, the crosshead is fixed, while in the lower part there is a mobile actuator which is activated by two servo-valves.

The servo-hydraulic machine are more complex respect the electro-mechanic one because it has to be connected to an oil control unit for the motion of oleo-dynamic cylinder. Besides, the higher velocities allow a greater versatility than electro-mechanic machines, indeed the servo-hydraulic equipments are appropriated also for fatigue tests. For what concerns the signals extraction: the force is, generally, measured with extensimetric load cells, as before; while the cylinder stroke is measured with LVDT instrumentation (Linear Variable Differential Transducer) directly placed on the oleo-dynamic piston, or with laser transducer which has higher dynamic performance. The considerations about the accuracy of machine stroke are valid also in this case, therefore to use the extesometer is recommended. In conclusion, the servo-hydraulic facilities are recognised as universal mechanical testing machines for their versatility and the possibility to investigate the material behaviour in a wide strain-rate range ( $10^{-3} \leq \dot{\epsilon} \leq 10^2$ ).

### 2.2.3 Drop and pneumatic machines

The mechanical response of material at medium strain-rate can be studied using different testing equipments. The drop machines are typical and various versions exist. The operating principle of these facilities is quite simple: a weight is dropped down from a definite height and when it reaches the desired velocity impacts against the specimen or the specimen clamping system. Changing weight and height, the amount of energy, and consequently the strain-rate, can be easily modified. Obviously, the choice of these quantities depends also from the specimen or component strength, therefore it is possible to find drop weight machines with heights of few meters up to ten meters (drop tower) with weights growing until hundreds of kilograms. In order to reduce the vibrations and to better control the impact, generally, the dropped weight slides on guides or rails (see Fig. 2.3a).

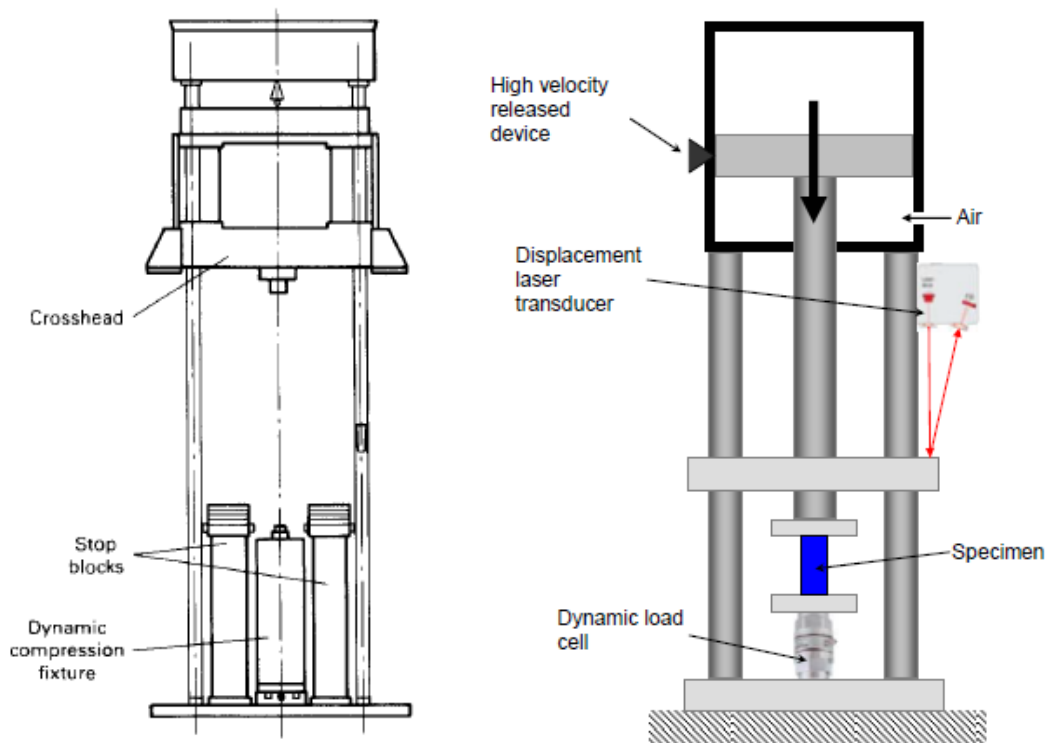


Fig. 2.3: Drop tower with compression fixture and stop blocks in place (left) [11] and pneumatic testing equipment (right) [12].

Similar to drop weight is the drop dart machine, in which the weight is substituted by a dart [13]. Normally, the drop darts are characterized by lower energy than drop towers and are equipped with dart mass smaller than ten kilograms and drop heights smaller than five meters. Respect to drop weight, which is the typical equipment for the evaluation of the energy absorption capabilities of materials, the drop dart is ideal for impact and penetration tests. The classic tests with the drop weight are performed on cylindrical, rectangular and filled beams or whole mechanical components, while for the drop dart the specimens are fundamentally metallic sheets or composite panels [14]. In the drop machines the acquisition system is usually composed by shock accelerometers, piezoelectric load cells and displacement/velocity transducers with high dynamic features. In the drop dart the dart itself is commonly a piezoelectric load cell.

In order to compact and to reduce the equipment dimensions, another suitable technique to store a great amount of energy is based on the use of pneumatic devices

charged with compressed air [12]. The operating principle is the same as before, but in this case, instead to accelerate a mass, a pneumatic cylinder is charged in pressure and released at high velocity. Setting the release pressure and the acceleration length before the impact, it is possible to estimate the amount of energy. Finally, it is important to highlight that independently from which type of facility is used, in this kind of test, problems in the acquisition of the force signals can rise due to transducer ringing phenomena. Therefore, the data have to be carefully managed to distinguish the material response from possible ringing phenomena of the equipment or transducer.

### 2.2.4 Hopkinson Bar

In the strain-rate range between  $10^2 \div 10^3 \text{ s}^{-1}$  the Hopkinson Bar represents the main testing device. As it will be discussed in the next chapter, using appropriate setup modifications it is possible to reach nominal strain-rate around  $10^4 \text{ s}^{-1}$ . However, although during the last decades several setups were proposed in order to perform compression, tensile, bending, torsion, Brazilian or multi-loading tests on different materials [15-18], the theory on which are based is common [19]. For the sake of simplicity, the compression setup (Split Hopkinson Pressure Bar) is taken into account to describe the operating principle, Fig. 2.4. This kind of equipment is founded on the theory of elastic waves propagation in elastic rods. The standard versions are composed by three coaxial rod bars called *striker* (or projectile), *input* and *output*. In order to guarantee a good alignment, the bars are supported by adjustable holders in which are free to slide. The specimen is placed between the input and the output bars. The test starts when the striker bar impacts against the input bar, generating a compression wave (incident wave) which propagates along the bar. The striker launch system, generally, is a light gas gun or a pre-loading apparatus [20,21]. At the interface between the input bar and the specimen, the wave is partially reflected back and partially transmitted through the specimen and the output bar. By measuring the reflected wave on the input bar and the transmitted

wave on the output bar, it is possible to reconstruct the dynamic stress vs. strain curve of the tested material. The wave signals are usually measured using strain-gages directly placed on the rods surface and sampled with high velocity acquisition systems, such as dynamic acquisition boards or oscilloscopes.

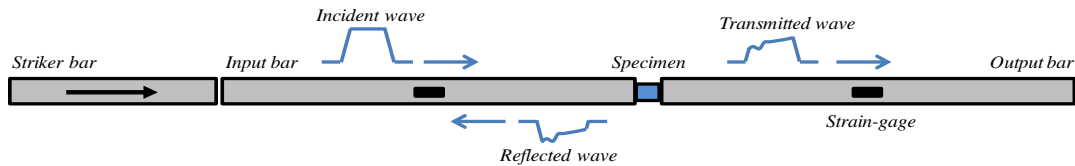


Fig. 2.4: Standard Split Hopkinson Pressure Bar for compression test.

The relations between strain bar histories and stress-strain field of the specimen are based on the mono-dimensional wave propagation theory which will be widely discussed in the next chapter.

### 2.2.5 Ultra-high strain-rate facilities

At ultra-high strain-rates the data acquisition systems start to experience serious measurement problems. In effect, at strain-rate higher than  $10^4 \text{ s}^{-1}$  only a few instrumentations are able to measure reliable values and usually they are very expensive. At this category belongs the high speed cameras, interferometer displacement transducers and some laser transducers. Generally, with these devices it is possible to extract the displacements, deformations and velocities, but not directly the stress evolution in the tested specimen.

For these reasons, in this strain-rate range it is necessary to simplify as much as possible the problem to study. Over the years different techniques were developed such as: the rod impact test (or Taylor test) [22- 24], the expanding ring test [25,26], the Dynamic Tensile Extrusion (DTE) [27] and the flyer plate impact test [28].

Over  $10^6 \text{ s}^{-1}$ , the plastic strain is significant, the stress-strain field is not uniform and no analytical expressions exist to describe it. Besides, the deviatoric stress component becomes irrelevant respect the hydrostatic one,  $\sigma_y \ll P$ , and the

phenomenon should be analyzed on the basis of the shock wave propagation theory in solids [3,29,30].

### ***Rod impact test***

The rod impact test, also known as Taylor test [22-24], consists to launch at velocity around one hundred m/s a small rod against a rigid wall or another rod of the same dimensions and material (see Fig. 2.5). The rod shot is generally realized with a light gas gun facility. Usually, it is favourable to reproduce the symmetric impact because when the rod impacts perfectly with another one it is possible to neglect the friction effect. This last consideration represents a conspicuous advantage in the study of this problem because a source of variability is eliminated from an event already characterized by high applied loads, relevant displacements and overheating. As mentioned before, at these velocities, generally, it is possible to measure the impact velocity, the rod shape and at most the impact force, but no information are available for the stress evolution and there are not analytical equations to describe the stress field. To overcome this problem, the common solution is to use the numerical inverse technique [31]. In practice a numerical model is realized in order to reproduce the experimental test with the same initial boundary conditions. After that, simulating the impact, it is possible to extract from the FE model the same data which were experimentally acquired. Probably, at the first attempt the numerical and experimental results will not be in a good agreement, but changing the material strength parameters it is possible to minimize the differences. Obviously, a good numerical-experimental correlation and the convergence are not guaranteed, which depend mainly from the optimization algorithm and material model employed. However, if the final result is satisfactory, the stress vs. strain curve of the material is known with a good level of accuracy. The numerical inverse method will be further analyzed in Chapter 5.

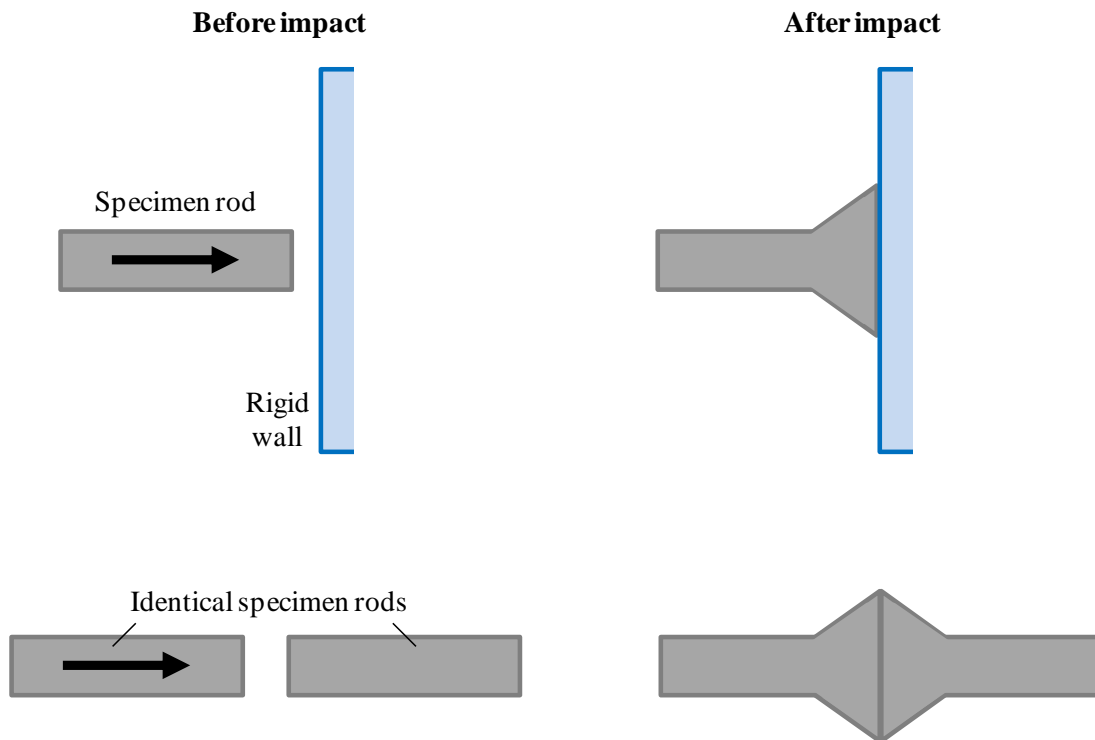


Fig. 2.5: Rod impact configurations: classical Taylor test (top) and symmetric rod impact test (bottom).

### ***Dynamic Tensile Extrusion***

The Dynamic Tensile Extrusion (DTE) technique was originally developed and applied to copper and tantalum spheres by Gray et al., [27,32] as a tensile corollary to compressive Taylor impact testing. Similar to Taylor testing, DTE is a strongly integrated test, probing a wide range of strain-rates, plastic strains, and stress states. Generally, a light gas gun is employed to drive spherical specimens at velocities on the order of hundreds of meters per second. However, unlike the case of the Taylor impact test where a rod is impacted against a semi-infinite rigid block or another rod, the DTE test drives the sample through an extrusion die. The resulting stress state is more dominantly tensile leading to dynamic tensile elongation followed by necking, particulation, and finally failure (see Fig. 2.6).

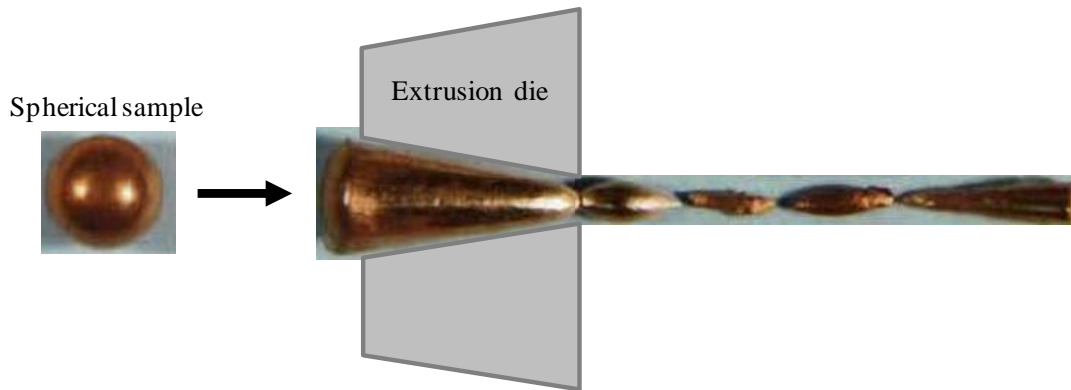


Fig. 2.6: 7.62-mm spherical Cu projectile accelerated at  $\sim 400$  m/s and extruded through a high-strength steel die [33].

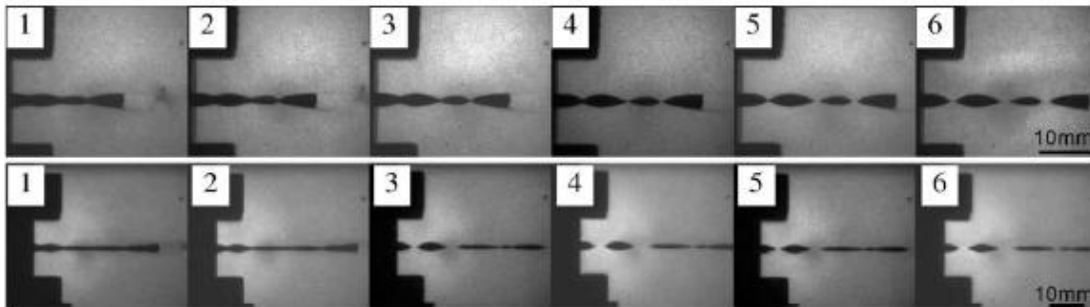


Fig. 2.7: High speed images of the DTE on tantalum launched at 384 m/s (top) and 553 m/s (bottom) [32].

Usually, the Helium-gas launcher or all-vacuumed air gun systems are used to accelerate the samples at very high velocities into a fixed conical high-strength steel extrusion die [34-38]. The post-extrusion macroscopic evolution of the samples can be captured using high-speed camera (see Fig. 2.7). Also for this experimental technique, the numerical simulations are commonly used to investigate in detail the material behaviour.

### ***Flyer plate impact test***

The flyer plate impact test is one of the experimental tests which allows to achieve the very high strain-rates ( $>10^5$  s $^{-1}$ ). As said before, at very high strain-rates, the material response should be analyzed taking into account the waves propagation in

solids. Thus, in this kind of test should be corrected to talk of investigation of the material behaviour to shock waves.

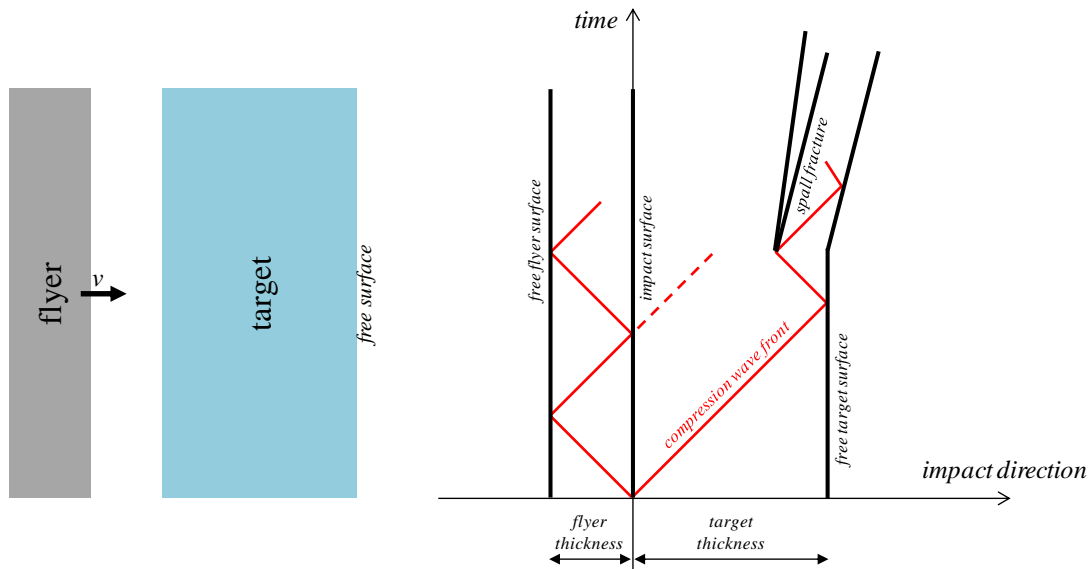


Fig. 2.8: Lagrangian diagram of waves propagation during flyer plate impact test.

The execution of the flyer plate impact remembers the Taylor test. In this case a flyer plate disk, generally supported by a plastic sabot, is accelerated using a gas gun and impacts against a target plate [39]. At the moment of the impact, since the plate diameters are much greater with respect to their thicknesses, along the impact direction a unidimensional strain field is generated inside the two plates and in this condition the shock waves travel in the materials [40]. With the support of the Lagrangian diagram, Fig. 2.8, it is quite simple to understand what happens. Under the hypothesis of elastic-plastic behaviour of the impacted materials, two compression waves propagate simultaneously in the plates starting from the impact surface towards the free surfaces. When the compression wave reaches the free boundary, it is reflected and changes sign becoming a tensile wave, which comes back towards the impact surface. Generally, the tensile strength of material is lower than in compression, therefore during the propagation of the tensile wave, the failure condition could be reached, generating the so called *spall fracture* (see Fig. 2.8). If this happens a crack is generated and new free surfaces are created, in which the

waves reflections go on. The maximum dynamic tensile stress is usually identified as  $\sigma_{spall}$ . In the literature is funded that it is possible to calculate this value, and also the other relevant quantities in shock phenomena, through direct correlations between stress and material particle velocity [41]. For these reasons, measuring the particles velocity on the free surface of the target plate, the stress-strain field in the material could be reconstructed.

## 2.3 Heating systems

As said at the beginning, the mechanical material response is influenced by the temperature. In order to investigate this aspect, several experimental techniques were developed until now [42]. Usually, the heating systems are distinguished on the basis of: the maximum temperature achievable, the heating rate and the heating area. In general, independently from the kind of test, the main problem is represented by the necessary time to reach the desired temperature, in particular for tests at high temperatures. From the material point of view, a long persistence at a certain temperature, especially if high, could give origin to annealing and microstructural changes such as grain growth and recrystallization. Obviously, if this happens, the test will be performed on a material with a structure strongly modified with respect to the initial one. Instead, considering the testing equipment, the characteristics of the measurement instrumentations (e.g. load cells, transducers, strain-gages) could be altered if maintained for long time at high temperature or influenced by electric and magnetic fields generated during the heating [43]. However, also the available heating zone is an important aspect because it represents a limitation for the specimen size and, consequently, determines the thermal distribution along the specimen.

To this day, substantially, three typologies of experimental heating systems exist: furnaces, induction coil systems and infra-red spot heaters. In the following, the main features of these heating systems will be discussed, focusing the attention on the

advantages and disadvantages of each one and considering their suitability to be used on dynamic testing equipments.

### 2.3.1 Furnace

The furnaces are widely used in the mechanical laboratories. Surely, this is due to the large diffusion of these systems on the market (therefore usually rather cheap with respect to other typologies) and the relative setting simplicity. Being the most commons, many developments were done upon them and, actually, it is possible to find different versions such as: vacuum furnace, tubular-shape furnace, small resistive tube furnace, electric combustion tube furnace, infra-red image furnace, electric-resistance-type oven, induction furnace [44-53]. Observing in particular the last ones, it is evident that some developments are going on different concepts of heating than the classic one. This is mainly the consequence of some disadvantages in the use of furnace systems. Indeed, for classic furnaces generally the difficulties are related to: remarkable structural frame dimensions, transfer to other testing equipments quite complex or impracticable, long heating time (tens of minutes), slow reaction time for the temperature control.

As previously said, the time necessary to reach the test temperature should be as little as possible, so in order to accelerate the heating process the developments are moving towards induction and infra-red systems, which have, furthermore, quick reaction times. For what concerns this work, in which a complete material behaviour investigation has to be performed using different machines, the possibility to transfer the heating system to other experimental equipments becomes a relevant aspect. Naturally, a bulky device, such as the classic furnaces, unlikely will be appropriate to be moved. In conclusion, it is possible to assert that the furnace heating system is not particular adapted to the purposes of this work, but it remains, anyway, the most common heating facility used also to perform dynamic tests.

### 2.3.2 Induction coil system

Especially for dynamic tests, the induction coil systems are also used as heating methodology. Observing the Fig. 2.9, the heating criteria should be easily understandable. Substantially, the sample to be heated is surrounded by an induction coil which carries a high-frequency current. The specimen is not in contact with the coil (composed by a small diameter copper tube), therefore it is not part of the closed electrical circuit and the generation of heat is solely by induction. The heating of metallic parts is the result of internal energy losses [54]. In ferrous materials, having magnetic properties, these losses are through both eddy currents and hysteresis, up to the Curie point. For higher temperatures and for nonmagnetic metals, the only losses present are due to eddy currents. Heating rates will be lower for nonmagnetic metals and for ferrous metals above their Curie points. Generally, the output power supplied to the coil is set to maximum in order to make the heating process as short as possible. Usually, the standard systems, with powers around 5÷10 kW, are able to heat ferrous materials at temperature greater than 1000 °C in few minutes. However, the magnetic field varies inversely with the square of the distance between the specimen and the coil, therefore as much the coil is closed to the sample as higher the heating rate. Summarizing, on the basis of what discussed just before, the temperature amplitude and heating rate in an induction coil system depends on: device power, tested material properties and the distance between the specimen and the coil.

In addition, this heating methodology is particularly appreciated because: the solenoid does not take up many space and the system is easily transportable; the implementation is quite simple with the possibility to set a feedback loop control and triggers; the heat rate is very quick and, finally, the heating area is extremely restricted and adjustable, therefore only the specimen gage-length could be directly heated (even if the conduction phenomena are inevitable). All these features make particularly appropriated this heating system to be utilized in dynamic test equipments [42,54-56].

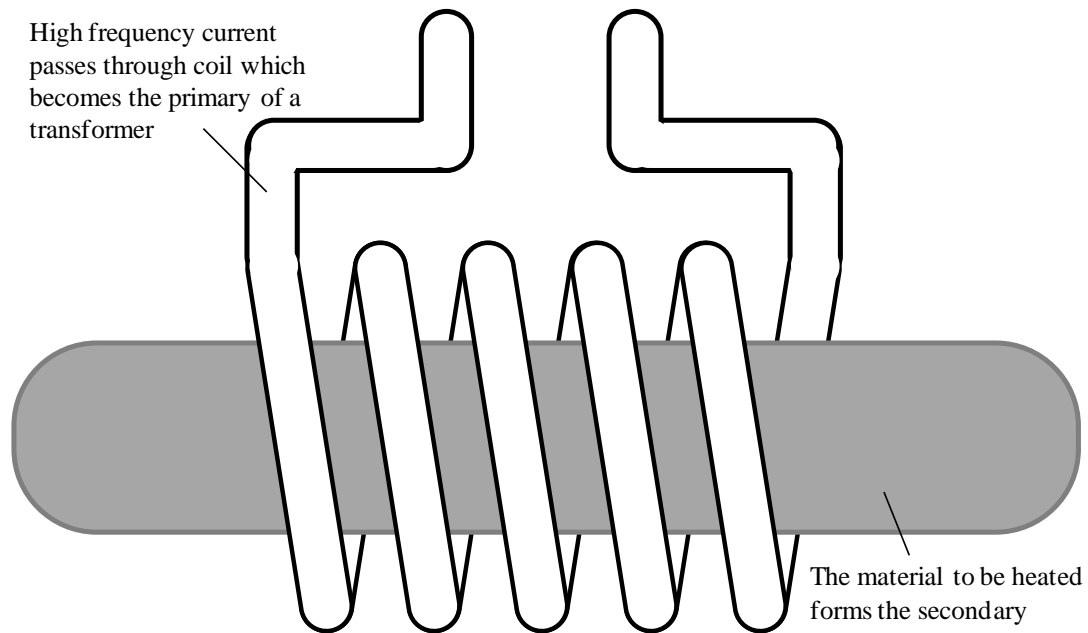


*Fig. 2.9: The induction-coil heater.*

### 2.3.3 Infra-Red spot heater

Another interesting heating methodology is based on the capability of the infra-red light to increase the temperature of a body through the electromagnetic radiation. Indeed, the red light has the highest degree of temperature change in the light spectrum, therefore, if correctly oriented, it can increase the temperature of a metal of several hundreds of degrees. Depending on the temperature of the emitting body, the wavelength of the peak of the infra-red radiation ranges from 780 nm to 1 mm [57]. The heat intensity is strictly related to the wavelength: the short-waves infra-red light, generally emitted through filaments at high temperatures (above 1800 °C), when concentrated in a target, can reach high power densities (of some hundreds of  $\text{kW/m}^2$ ), while increasing the wavelength the electromagnetic radiation is gradually lower.

On this base, the infra-red spot heaters were developed in order to improve the heating efficiency [2]. Usually, these heaters consist of a high temperature tungsten filament positioned at one focus of an elliptical reflector. The high-intensity infra-red radiation is concentrated onto an ellipsoidal spot. Power is supplied to the infra-red

emitter through a power controller. The heating rate depends essentially from the thermal mass and the surface reflectivity of the material heated, but usually few minutes are enough to reach temperatures greater than 500 °C.

In a similar way of induction coil systems, the infra-red spot heaters are generally characterized for: small device dimensions, high heating rate, high limit of temperature achievable, simple implementation with the possibility of a feedback control (in order to manage the reaction time of the system), restricted and adjustable heating area. Thinking to an embedded system composed by both high strain-rate and heating equipments, all the features mentioned previously could considerably facilitate the assembly and the systems interaction.

## 2.4 Material strength models

In order to better understand the importance of strength models, it could be useful to remember in which way the complete behaviour of materials is described in function of stress and strain tensors. The typical form is the following:

$$\sigma = \begin{bmatrix} \sigma_{xx} & \sigma_{xy} & \sigma_{xz} \\ \sigma_{yx} & \sigma_{yy} & \sigma_{yz} \\ \sigma_{zx} & \sigma_{zy} & \sigma_{zz} \end{bmatrix} \quad \varepsilon = \begin{bmatrix} \varepsilon_{xx} & \varepsilon_{xy} & \varepsilon_{xz} \\ \varepsilon_{yx} & \varepsilon_{yy} & \varepsilon_{yz} \\ \varepsilon_{zx} & \varepsilon_{zy} & \varepsilon_{zz} \end{bmatrix} \quad (2.2)$$

Since the pressure ( $p$ ) and the volumetric strain ( $\varepsilon_v$ ) are defined as:

$$p = -\frac{\sigma_{xx} + \sigma_{yy} + \sigma_{zz}}{3} \quad \varepsilon_v = \varepsilon_{xx} + \varepsilon_{yy} + \varepsilon_{zz} \quad (2.3)$$

it is possible to split the tensors into deviatoric and hydrostatic components.

$$\sigma = \begin{bmatrix} s_{xx} & s_{xy} & s_{xz} \\ s_{yx} & s_{yy} & s_{yz} \\ s_{zx} & s_{zy} & s_{zz} \end{bmatrix} - \begin{bmatrix} p & 0 & 0 \\ 0 & p & 0 \\ 0 & 0 & p \end{bmatrix} = s_{ij} - \begin{bmatrix} p & 0 & 0 \\ 0 & p & 0 \\ 0 & 0 & p \end{bmatrix} \quad (2.4)$$

$$\varepsilon = \begin{bmatrix} e_{xx} & e_{xy} & e_{xz} \\ e_{yx} & e_{yy} & e_{yz} \\ e_{zx} & e_{zy} & e_{zz} \end{bmatrix} + \frac{1}{3} \begin{bmatrix} \varepsilon_v & 0 & 0 \\ 0 & \varepsilon_v & 0 \\ 0 & 0 & \varepsilon_v \end{bmatrix} = e_{ij} + \frac{1}{3} \begin{bmatrix} \varepsilon_v & 0 & 0 \\ 0 & \varepsilon_v & 0 \\ 0 & 0 & \varepsilon_v \end{bmatrix} \quad (2.5)$$

The strength models define the relation between deviatoric stress ( $s_{ij}$ ) and strain ( $e_{ij}$ ) components, while the equations of state between the hydrostatic ones. For this reason, many times, the FE codes require both material model and equation of state simultaneously. Generally, the volumetric component begins to have relevant effects at very high strain-rate, while under  $10^4 \text{ s}^{-1}$  the relationship between the pressure and the density could be described through a simple linear law.

Since in this work the study of the mechanical behaviour of materials is considered in the strain-rate range between  $10^{-4} \div 10^4 \text{ s}^{-1}$  the attention will be focused only on the deviatoric behaviour. Remembering what said at the beginning of the chapter, in dynamic field the material behaviour is affected by high strain, strain-rate and temperature. Usually, a visco-thermo-plastic model can describe the flow stress as a combination of athermal and thermal components. The athermal part of the stress can be associated with strain, strain-rate, temperature and pressure, while the thermal one describes the temperature influence on the strain-rate effects on the flow stress. Accordingly to this, the flow stress ( $\sigma_y$ ) can be considered as the sum of two components:

$$\sigma_y = \sigma_{th} + \sigma_{ath} \quad (2.6)$$

in which  $\sigma_{th}$  is the thermal component correlated to the short range interaction and  $\sigma_{ath}$  is the athermal component correlated to the long range interaction [5].

During the last century several strength models were proposed in order to describe the thermo-structural coupled problems. Generally, the material models are distinguished in empirical, semi-empirical and physically-based models as described by Zhang, et. al. [58] and Wang, et. al. [59]. The empirical models have not any physical basis and are founded simply on the interpolation of the experimental data. On the contrary, the physically-based models are strictly related to the transformation in the material occurring during the deformation process. For these reasons, the calibration of an empirical or semi-empirical model needs a detailed test campaign, while for pure physically-based models the experimental tests should be only a simple verification. Nevertheless, the empirical models are widely diffuse than physical-based models because they are generally simpler and implemented in all commercial FE codes. Moreover, with the diffusion of the numerical codes, the experimental test planning is oriented to the extraction of model parameters. Indeed, many times, a strength model is preferred with respect of another one for the minor number of test to realize.

It is important to underline that some problems can arise when the material models are used. Surely, the greatest problem is related to the lack of model parameters for different materials. Indeed, the most part of these models were calibrated in the 80's and 90's only for few materials. Furthermore, the tested materials were usually pure metals or their typical alloys, often related to military or nuclear applications. However, even if the data are available, another problem is related to the comparison between the parameters obtained for different models, because they depend upon the micro-structural material properties or the chemical composition (for alloys) [46]. Therefore, the parameters of two different models can be comparable only if the material considered is exactly the same. In addition, in literature it is very simple to find for the same material and the same model many different set of parameters. This is due to the fact that the material models are strictly related to the data origin: the type of test performed (compression, tensile, etc.) and the investigated range of strain, strain-rate and temperature. As it will be discussed in the next chapters, also the methodology used to get the model parameters can be

source of considerable dissimilarity. Finally, a consideration on the implementation of the models in the FE codes has to be done. Many times, the formulation implemented in the codes is not exactly the same of the original one, in some cases, the parameters present different interpretation or range of applicability. For this reason, before to run the calculation, it is useful to accurately check the relative manual code.

## 2.5 Failure models

Through the strength models it is possible to reproduce only the evolution of the stress-strain field in the material, but no information are given about the failure. In order to consider this aspect, usually a strength material model is associated to a failure model.

As for the stress evolution, also the failure mechanism is influenced by many factors such as: the material properties and microstructure, the loading conditions (meaning the type of solicitation, strain-rate, temperature), the triaxiality. On the basis of their interaction, substantially two typologies of failure modes can be observed: ductile or brittle. The first case is typical for metals and polymers in which the nucleation, growth and coalescence of cavities in the microstructure generates extended plastic deformation, generally associated to necking phenomena, and the classical cup-and-cone shape of fractured surfaces. Instead, the brittle materials, e.g. ceramics and glasses, show very little plastic deformation at failure with rapid crack propagation perpendicular to applied load. Crack often propagates by cleavage, breaking atomic bonds along specific crystallographic planes (cleavage planes).

In the literature it is possible to find two categories of analytical expressions conceived to reproduce the failure [60]. In one case, the simplest one, the material failure happens when locally it overcomes one or more limit conditions. Generally, these limits correspond to maximum principal stress/strain to fracture or pressure levels. The second approach is based on the cumulative damage of the material in which the material starts to be damaged when determined conditions (similar to the

previous ones) are overcome. In this case the damage evolution is controlled by a damage parameter, which gradually increases up to the unity value determining the complete material failure [61,62]. Both the strategies are diffusely implemented in the FE codes and can be properly used for ductile or brittle behaviours. From a numerical point of view, when an element achieves the failure condition it is immediately kept out from the calculation and, if erosion algorithms are contemplated, it is removed from the model.

## 2.6 Finite Element Method simulations

Neglecting at this moment the numerical algorithms and the procedure features, in this paragraph the attention desires to be focused only on the importance of FEM simulations in the mechanical field and the related issues to perform them.

Thanks to the improvements of the calculators performance and the introduction of sophisticated algorithms, nowadays the Finite Element analysis are become an essential tool in the design field and in the study of complex phenomena. In the mechanical field, numerical simulations are widely used starting from simple structural calculations and validations up to the reproduction of manufactory processes or complex scenarios such as e.g. ballistic impacts, explosions or nuclear applications [63-65]. The great advantage to use numerical simulations consists in the possibility to create, modify and develop any interesting case, as many times is desired, with an incredible time and cost saving. Therefore, the amount of prototypes and experimental tests can be extremely reduced and limited for validations. In addition, this approach permits to analyze the whole study case in a total safety way (thinking about nuclear experiments or explosions) and to reproduce ethically susceptible events, such as human injuries, which are, naturally, many times not experimentally allowed [66].

Taking into account the dynamic phenomena, which are at the centre of attention in this thesis, it is important to underline that FEM simulation represents a useful computational tool. Indeed, the high strain-rate events represent thermo-mechanical

coupled problems where the plasticity and thermal softening should not be neglected. It is important to highlight that thermal softening phenomenon is quite complicated to reproduce analytically because, for example, it is not possible to establish the strain-rate threshold between the applicability of isothermal or adiabatic hypothesis. Besides, there are not analytical solutions able to exactly consider the non uniform distribution of the quantities such as: stress, strain, strain-rate, temperature, triaxiality inside the component during the deformation. For these reasons, the coupled thermo-mechanical FEM simulations are an optimal solution to correctly investigate the dynamic events and, nowadays, they are used by many researchers for the materials characterization.

Obviously, the main issue for numerical simulations is the great lack of data. Indeed, the simulation accuracy is strongly related to the algorithms and parameters used, but even if there is a notable amount of mathematical relations able to describe the various material behaviours, this is not true for the available data, in particular in dynamic field.



### 3. Advanced high strain-rate and heating equipments

In order to characterize the dynamic behaviour of materials it is necessary to conduct a test campaign in which different loading conditions are investigated. A complete study should take into account experimental tests varying strain-rate and temperature. Actually, there are not specifications about which experimental facilities have to be used for a dynamic material characterization and this represents a great source of discussion. With the diffusion of FE codes the material investigation is fundamentally dedicated to the extraction of model parameters. For this reason, the classical experimental approach is based on low-medium strain-rate tests using conventional test equipments (such as electro-mechanical and servo-hydraulic machines), while the Hopkinson Bar is the main facility exploits for dynamic tests up to  $10^4 \text{ s}^{-1}$ . Since also the temperature influences the mechanical behaviour, the experimental equipments mentioned before are generally integrated with heating systems.

In this chapter, some of the testing equipments available in the DYNLab Laboratory of the Politecnico di Torino will be shown. A detailed description of each machine will be furnished, focusing the attention on the critical aspects of experimental execution. Furthermore, some improvements specifically introduced in order to extent the range of strain-rate and temperature will be presented.

### 3.1 Experimental equipments at low strain-rate

In this work all data related to strain-rates up to  $10^1 \text{ s}^{-1}$  have been obtained with the traditional electro-mechanical testing machine Zwick-Roell Z100 (from  $10^{-3}$  up to  $10^1 \text{ s}^{-1}$ ) and the servo-hydraulic machine Dartec HA 100 (up to  $10^1 \text{ s}^{-1}$ ). In more detail, the first machine has a maximum load capacity of 100 kN at a maximum velocity of 5 mm/s and it is ideal for quasi-static tests. Instead, the servo-hydraulic machine is particularly appreciated for medium-low strain-rate because it is able to apply the same maximum load but with a maximum velocity of 100 mm/s. Both the machines use the same clamping devices.

These kinds of machines are widely used to perform uniaxial compression or tensile tests. Often, before to start the test, the specimen is pre-loaded in order to avoid sliding with the clamping apparatus. However, even if the strain-rates considered are relative low, the machines need a certain time to reach the constant test velocity. Therefore, it is evident that pre-loading the specimen the test is performed at not constant velocity, at least at the beginning. It was observed that about 5 mm of acceleration length are enough to reach a constant machine velocity. In order to overcome this problem, two specific components are been developed for compression and tensile tests, which are sketched in Fig. 3.1. These components were designed in order to allow the use of the extensometer and the acceleration of the machine. In both systems the specimen is simply clamped in a start position and loaded only when both sides of the clamping system take contact with the machine anvils.

The deformability of the machine and the clearance between the specimen and the clamp system are aspects to consider during the data elaboration in order to avoid incorrect evaluation of the strains. This problem could be simply overcome positioning an extensometer directly on the specimen or very close to it and in this way the measured signal corresponds exactly to the specimen displacement. Thus, using the extensometer, the specimen pre-loading is not so essential. For an accurate evaluation of the specimen elongation, it is crucial that the extensometer remains in a

stable position from the beginning until the end of its measurement field. Generally, in pre-loaded or very low strain-rate tests this is quite simple; on the contrary, when the loading happens with the machine in motion, the extensometer could slide out due to vibrations generated at the contact between the anvils and the specimen clamps. In this case, it is useful to insert a soft material, such as high density foam or rubber, in the contact area in order to damp the oscillations.

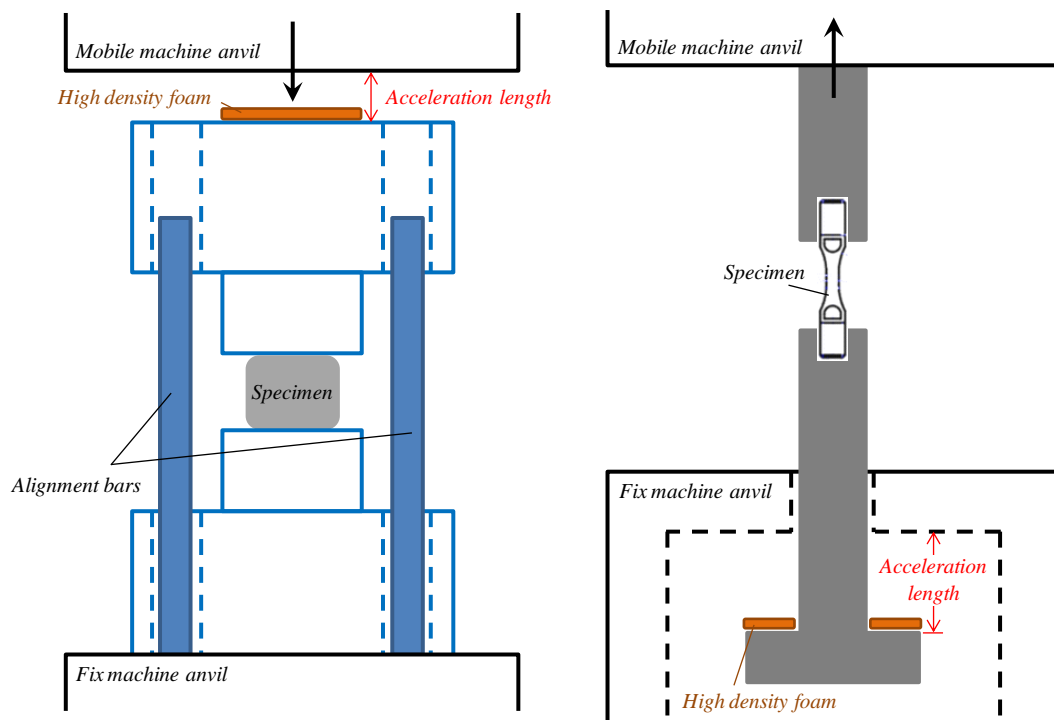


Fig. 3.1: Schematic representation of sliding clamps for test at constant velocity in (left) compression and (right) tension.

Finally, a consideration about the specimen dimensions has to be done. Since the strain-rate is defined as the ratio between the machine velocity and the initial gage length of the specimen ( $\dot{\epsilon} = v/l_0$ ), it is evident that, in order to perform tests until  $10^1 \text{ s}^{-1}$  with this kind of machines, the gage length of the specimen is limited by the maximum velocity of the machine. For this reason, specimens with a maximum initial gage length of 5 mm were used in this work.

## 3.2 Experimental equipments at high strain-rate

In this section only the Hopkinson Bar apparatus will be considered for test at high strain-rate. As discussed in the previous chapter, this testing equipment is widely recognized as the main mechanical facility for the investigation of material behaviour in strain-rate range  $10^2 \div 10^3 \text{ s}^{-1}$  and with particular modifications until  $10^4 \text{ s}^{-1}$ . In the following, the standard compression and tensile setups will be described as well as a miniaturized tensile setup for very high strain-rate tests.

### 3.2.1 SHPB setup for compression test

The compression setup is the typical configuration of the Hopkinson Bar which was invented by Kolsky in 1949 [67] on the basis of the pressure bar devised by Hopkinson in 1913 [68]. Usually, the standard configuration allows investigating the mechanical behaviour of materials at strain-rate from  $10^2$  up to  $10^3 \text{ s}^{-1}$ , typically on cylindrical specimens. This kind of equipment is based on the theory of elastic waves propagation in elastic rods. The operating principle was described in section 2.2.4. In Fig. 3.2 the simplified scheme of the compression Split Hopkinson Pressure Bar (SHPB) is shown with the Lagrangian diagram in order to explain the waves propagation during the test.

At the moment of the impact between the striker bar against the input bar, an incident wave of known length ( $l_I$ ) and amplitude ( $\sigma_I$ ) is generated and propagates along the input bar:

$$\sigma_I = \frac{1}{2} \cdot \rho_{input} \cdot C_{input} \cdot v_{imp} \quad (3.1)$$

$$l_I = 2 \cdot L_{striker} \quad (3.2)$$

where  $\rho_{input}$  is the input bar density,  $v_{imp}$  the impact velocity,  $L_{striker}$  the projectile length and  $C_{input}$  the mono-dimensional (longitudinal) elastic wave velocity in the input bar, which is related to Young's modulus ( $E_{input}$ ) and density:

$$C_{input} = \sqrt{\frac{E_{input}}{\rho_{input}}} \quad (3.3)$$

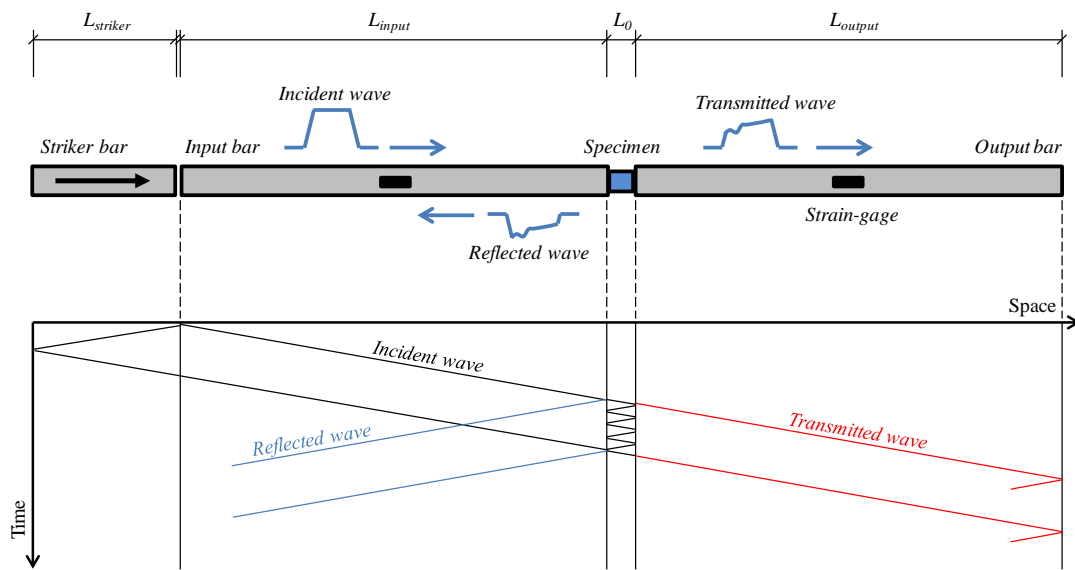


Fig. 3.2: Schematics of compression SHPB and space vs. time diagram of stress waves propagation.

When the incident wave reaches the specimen, it is partially reflected ( $\varepsilon_R$ ) in the input bar and partially transmitted ( $\varepsilon_T$ ) through the specimen and the output bar. Within the specimen the compressive loading wave propagates and arrives at the specimen output bar interface. By design, the specimen's impedance is smaller than the impedance of the bars surrounding the specimen on both sides. Since the output bar has higher impedance than the specimen itself, the wave that reflects from the specimen/output bar interface remains a loading wave, resulting in an even higher compressive stress. This wave now arrives at the specimen/input bar interface, again sees higher impedance and again reflects as a loading wave, resulting in a further

increase in the compressive stress. This process continues until the stress within the specimen reaches a value that is sufficiently high to generate inelastic strains, resulting in finite plastic flow of the specimen under the compressive loading. Once substantial plastic flow of the specimen material has commenced, further wave propagation within the specimen could be neglected, since the amplitude of the subsequent wave-fronts will be very small. Thus at these later times the stress within the specimen is essentially uniform; the stress is said to have equilibrated. If the boundary conditions are frictionless, the specimen stress is also uniaxial. Moreover, if the specimen dimensions are relatively smaller with respect the length of the compression pulse and the bars, the equilibrium condition is reached almost instantaneously [69,70].

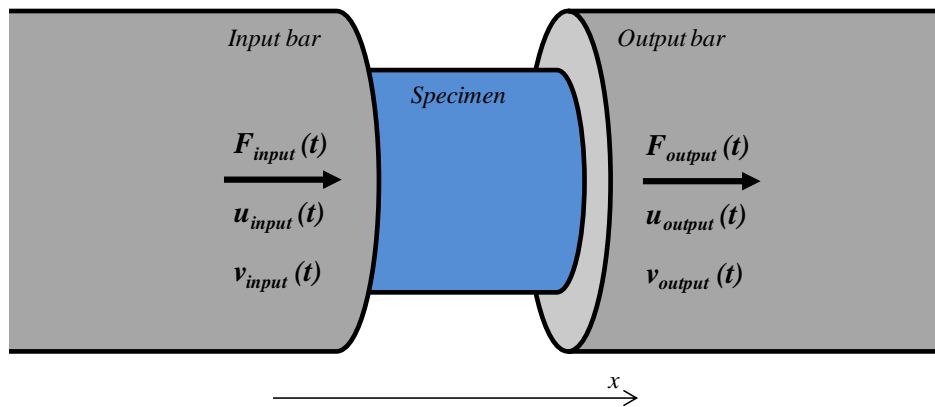


Fig. 3.3: Split Hopkinson Bar forces and displacements diagram.

At the equilibrium, the force in the input side ( $F_{input}$ ) balances the force on the output side ( $F_{output}$ ), as shown in Fig. 3.3. For what concern the displacements, the input stroke ( $u_{input}$ ) is the result of the sum of the incident strain wave ( $\varepsilon_I$ ) and the reflected strain wave ( $\varepsilon_R$ ), which has an opposite sign because the interface between the bar and specimen is like a free surface (the impedance of the input bar is higher with respect to that of the specimen). Introducing the relation between elastic strain waves and particle velocity,  $u = C \cdot \int \varepsilon(t)dt$ , the input bar stroke can be written as:

$$u_{input}(t) = C_{input} \int_0^t \varepsilon_I(t) dt - C_{input} \int_0^t \varepsilon_R(t) dt = C_{input} \int_0^t [\varepsilon_I(t) - \varepsilon_R(t)] dt \quad (3.4)$$

On the other specimen side, instead, only the transmitted strain wave ( $\varepsilon_T$ ) has to be considered:

$$u_{output}(t) = C_{output} \int_0^t \varepsilon_T(t) dt \quad (3.5)$$

with  $C_{output}$  the longitudinal elastic wave velocity of output bar. At this point, it is very simple to obtain the instantaneously specimen strain ( $\varepsilon_s$ ) considering that generally the input and output bars have the same properties ( $C_{input}=C_{output}=C$ ):

$$\varepsilon_s(t) = \frac{u_{input}(t) - u_{output}(t)}{L_0} = \frac{C}{L_0} \int_0^t [\varepsilon_I(t) - \varepsilon_R(t) - \varepsilon_T(t)] dt \quad (3.6)$$

where  $L_0$  is the initial specimen length.

The force equilibrium can be easily written using the Hooke's law:

$$\begin{aligned} F_{input}(t) &= F_{output}(t) \\ E_{input} \cdot A_{input} \cdot \varepsilon_{input}(t) &= E_{output} \cdot A_{output} \cdot \varepsilon_{output}(t) \\ E_{input} \cdot A_{input} \cdot [\varepsilon_I(t) + \varepsilon_R(t)] &= E_{output} \cdot A_{output} \cdot \varepsilon_T(t) \end{aligned} \quad (3.7)$$

with  $A_{input}$  and  $A_{output}$  the cross-section of input and output bars. As said before, normally the rods have the same properties and also the same diameter, therefore the (3.7) can be reduced in:

$$\varepsilon_I(t) + \varepsilon_R(t) = \varepsilon_T(t) \quad (3.8)$$

Once verified the equilibrium, the instantaneous axial stress of the specimen ( $\sigma_s$ ) can be calculated:

$$\begin{aligned} \sigma_s(t) &= \frac{F_{input}(t) + F_{output}(t)}{2 \cdot A_s} = \\ &= \frac{E_{input} \cdot A_{input} \cdot [\varepsilon_I(t) + \varepsilon_R(t)] + E_{output} \cdot A_{output} \cdot \varepsilon_T(t)}{2 \cdot A_s} \end{aligned} \quad (3.9)$$

with  $A_s$  the specimen cross-section. Using the same material properties ( $E_{input}=E_{output}=E$ ) and dimensions ( $A_{input}=A_{output}=A$ ) for the input and output bars:

$$\sigma_s(t) = \frac{E \cdot A \cdot [\varepsilon_I(t) + \varepsilon_R(t) + \varepsilon_T(t)]}{2 \cdot A_s} \quad (3.10)$$

If the equilibrium condition (Eq. 3.8) is verified during the whole test, Eq. 3.6 and 3.10 can be simplified:

$$\varepsilon_s(t) = \frac{C}{L_0} \int_0^t [\varepsilon_I(t) - \varepsilon_R(t) - \varepsilon_T(t)] dt = -\frac{2 \cdot C}{L_0} \int_0^t \varepsilon_R(t) dt \quad (3.6b)$$

$$\sigma_s(t) = \frac{E \cdot A \cdot [\varepsilon_I(t) + \varepsilon_R(t) + \varepsilon_T(t)]}{2 \cdot A_s} = E \frac{A}{A_s} \varepsilon_T(t) \quad (3.10b)$$

In the same way, it is possible to calculate the instantaneous axial strain-rate in the specimen ( $\dot{\varepsilon}_s$ ), which is also the first derivative of the strain (Eq. 3.6), therefore:

$$\dot{\varepsilon}_s(t) = \frac{v_{input}(t) - v_{output}(t)}{L_0} = -\frac{2 \cdot C}{L_0} \dot{\varepsilon}_R(t) \quad (3.11)$$

where  $v_{input}$  and  $v_{output}$  are the velocities of the input and output bars at the interface with the specimen, which are the first derivative of the displacements  $u_{input}$  and  $u_{output}$ , respectively.

From the Eq. 3.11, it could be perceived that with the SHPB equipment the tests are not performed exactly at constant strain-rate. Only in the ideal case of perfectly rectangular reflected wave, i.e. a perfectly plastic response of the specimen, the strain-rate is constant during the whole specimen deformation. In practice, this is almost impossible to observe and, generally, the nominal strain-rate, which is the average value of the effective strain-rate, is used to indicate the strain-rate of tests performed on the Hopkinson Bar apparatus.

Finally, it is important to remember that the equations (3.6b) and (3.10b) were obtained under the assumption of mono-dimensional elastic wave propagation. The rods are considered of relative small diameter and always in linear elastic condition neglecting the dispersion phenomena due to the lateral contraction. However, before to use the equations mentioned, it is recommended to use appropriate correction algorithms in order to reduce the signal oscillations and distortions, in particular when long, high cross-section and high dispersive (material with high Poisson's ratio) bars are used [19,12].

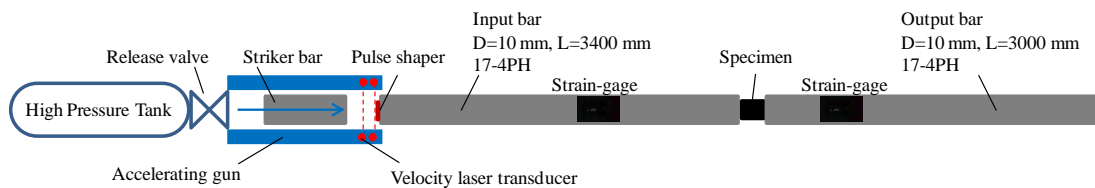


*Fig. 3.4: Scheme of SHPB setup for dynamic compression tests implemented in the DYNLab Laboratory of Politecnico di Torino (strain-rate up to  $10^3 \text{ s}^{-1}$ ).*

In the DYNLab Laboratory of the Politecnico di Torino two SHPB configurations were developed and implemented. Both the configurations have the same setup (see Fig. 3.4), but in one case bars with 10 mm of diameter are used and the striker accelerates in a barrel gun 2.5 m long, while in the other configuration the diameter of the bars is 12 mm and the gas-gun is 3 m long.

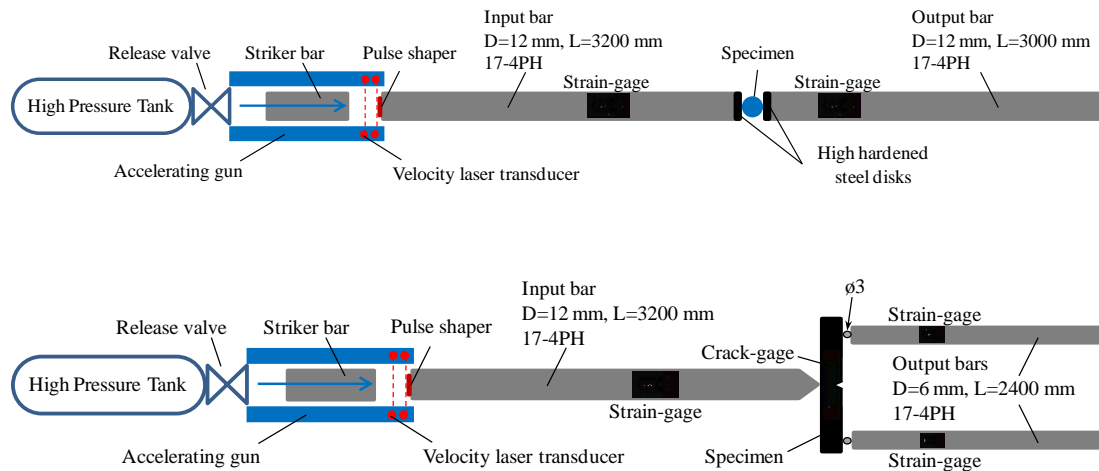


Fig. 3.5: Schemes of Hopkinson bar setups for dynamic Brazilian tests (top) and dynamic 3 points bending tests (bottom) implemented in the DYNLab Laboratory of Politecnico di Torino.

The configuration shown in Fig. 3.4 is designed to perform compression test on cylindrical specimens reaching a maximum level of 40 kN (usually 4 mm of length and diameter specimens are used [21]). In order to increase the maximum level of force, the setup with 12 mm-diameter bars was used. In both configurations the velocity of the projectile when impact against the input bar is measured by the laser transducer. These testing equipments are particularly versatile and could be used to perform different dynamic tests just changing the input and output bars configuration. In Fig. 3.5, the setups to perform dynamic Brazilian test and dynamic three points bending test are shown. The Brazilian test is a common experimental methodology used to investigate the tensile strength of brittle materials such as ceramics, rocks, glasses. The test consists in the diametrical compression of a cylindrical specimen in order to generate a tensile stress, along the specimen diameter, perpendicular to the direction of the load [71]. Since brittle materials are usually characterized by high hardness, thin high hardened steel disks are positioned between the specimen and the bars in order to prevent the damage of the bars.

The configuration reported in the bottom of Fig. 3.5 was designed to perform three points bending test. In order to reduce as much as possible the contact zone

between the bars and the specimen, a tip input bar is used, while 3 mm-diameter small rods are placed between the specimen and the two output bars. For all configurations, the strain-gages positioned on the bars are used to measure the forces and displacements.

In order to increase the rising time of the incident pulse, which allows to reduce the signals oscillation can be used the pulse shaping techniques. However, this aspect will be further analyzed in the next section.

Surely, the dynamic compression tests carried out with SHPB represent the most diffused experimental methodology used to study the mechanical behaviour of materials at high strain-rates. Nevertheless, two important aspects of compression tests have to be considered: from a point of view of the test execution and the data elaboration, the friction between the specimen and the bars remains always an uncertain variable [72], while for what concern the mechanical response, the information about the material failure can not be extracted from compression tests. This last consideration becomes particularly relevant when the final objective is a complete material characterization. For this reason, if the material to investigate it is not extremely brittle and it is machinable, a better solution is to perform tensile or shear tests in order to reach the fracture of the material. In this sense in this work the attention was mainly focused on the development of tensile configurations of Hopkinson Bar.

### 3.2.2 Direct Split Hopkinson Tensile Bar

In order to investigate the dynamic material behaviour up to failure the Split Hopkinson Tensile Bar setup can be considered as appropriate testing equipment. Generally, the greatest difficulty for this kind of configuration is the generation of the tensile elastic pulse in the incident bar. Using the classical dog-bone shape specimen with threaded ends to directly screw in the bars, substantially, two possible ways to perform dynamic tensile tests exist: the reflection and the direct systems. In the first one, a split ring is placed around the specimen and transmits the first

compression pulse (generated by the impact of striker bar) from the first to the second bar. The compressive stress pulse propagates until the end of the second bar. When the compression pulse reaches the free surface reflects by the shape of tensile stress pulse. The tensile stress pulse is recorded at the strain-gage placed on the second bar, which becomes the input bar. Part of the tensile stress pulse reached at the specimen propagates to the output bar (the first bar), and the rest of the wave reflects in the input bar. The tensile pulse is transmitted from one bar to the other only by the specimen, since the split ring is a unilateral constraint [73,74]. However, particular attention must be done in the strain-gage positioning because at the interface between the compression pulse and the split ring an unwanted reflection occurs, therefore it can interfere with the tensile pulse transmitted through the specimen. If the strain-gage is placed on the output bar in the area where the waves interacts, signals superposition can arise.

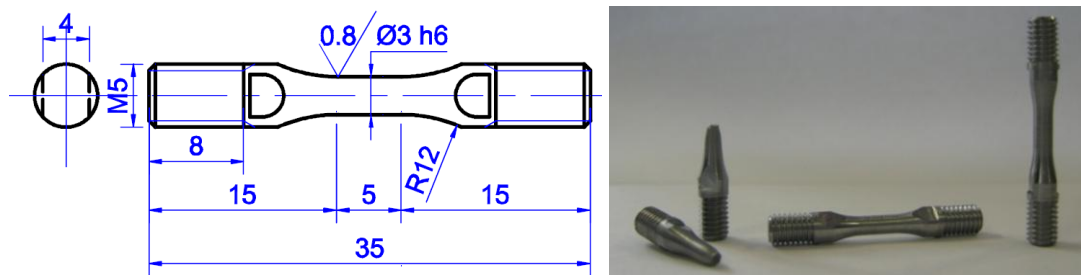


Fig. 3.6: Specimen geometry used for tests at different strain-rate up to  $10^3 \text{ s}^{-1}$ .

In the direct configuration the problem of unwanted reflection waves is not present because the tensile pulse stress is directly generated in the first bar [75]. One of the possible direct tensile configurations was developed and used in this work for the materials characterization. The reference geometry of dog-bone specimens adopted is shown in Fig. 3.6. In general, for Hopkinson Bar tests, there are no specific standards, as well as no specifications on the specimen dimension are available, but the chosen geometry has also been used by other researchers, e.g. [20,76,77]. Single specimen geometry was used, also for quasi-static tests, to avoid

the influence of geometry and dimension and to have the possibility to directly compare the results coming from different loading conditions [78].

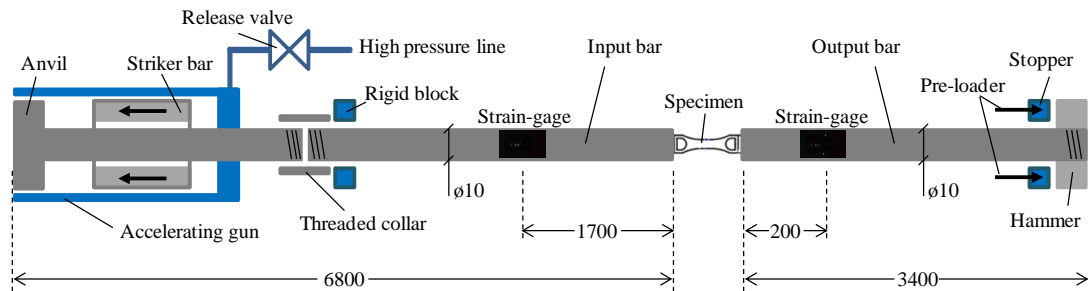


Fig. 3.7: Scheme of the Hopkinson bar setup used to perform dynamic tensile tests (direct tension up to  $10^3 \text{ s}^{-1}$ ).

The set up used in this work for tests at  $10^3 \text{ s}^{-1}$  consists of a gas-gun, an impactor and input and output bars (see Fig. 3.7). The striker bar is a 750 mm long tube made from glass reinforced nylon. The gas-gun is 1.5 m long and is driven with compressed air allowing a maximum velocity of the input bar of about 10 m/s. The input bar is made in martensitic high strength stainless steel (17-4PH); it is 10 mm in diameter and 6.8 m long, with an anvil at one end. The output bar has the same material properties of the input bar and has a length of 3.4 m. The anvil at the outer end of the input bar is hit by the striker which is pneumatically accelerated, in this way the initial compression pulse is immediately reflected as a tensile pulse. A tensile stress wave  $\sigma_I$  (incident wave) propagates along the input bar towards the specimen. Due to the difference of the sound velocity in the materials of the input and striker bars, the impact against the anvil produces a pulse which has a time duration of about  $600 \mu\text{s}$ , which corresponds to a length of about 3 m in the steel bars. When the wave reaches the specimen, the wave is partly reflected back into the input bar ( $\sigma_R$ , reflected wave) and partly transmitted to the output bar ( $\sigma_T$ , transmitted wave). The waves  $\sigma_I$ ,  $\sigma_R$  and  $\sigma_T$  are measured by means of semiconductor strain-gages. With respect to traditional resistance strain-gages, this type of gage provides signals with a very low noise level. Obviously, this aspect

becomes more relevant when small strains have to be measured. Besides, thanks to higher sensitivity (high gage factor), with respect to the standard resistance strain-gages (about 100 times), the semiconductor gages do not require dedicated amplifiers, but they can be directly connected to the data acquisition system (yielding a concomitant bandwidth increase).

The strain-gages are located at a distance of 1700 mm from the specimen on the input bar and 200 mm behind the specimen in the output bar. Two types of strain-gages were used (KYOWA KSP-1-350-E and MICRON INSTRUMENTS SS-060-033-1000PB). For each measurement point two strain-gages were used and a Wheatstone bridge circuit was completed with standard resistors. For the former strain-gages, standard resistors of  $309 \Omega \pm 0.1\%$  were used, while for the second type, standard resistors of  $1 \text{ k}\Omega \pm 0.1\%$  were used. The signals were acquired with a NATIONAL INSTRUMENTS PC-6133 acquisition board at a sampling rate of 2.5 MHz with a maximum resolution of  $150 \mu\text{V}$  (14 bits in the range  $\pm 1.25 \text{ V}$ ).

In order to achieve a better (more accurate and complete) acquisition of the material data some upgrades on the setup were performed.

The first problem to deal with is related to the presence of initial peaks in correspondence to the yield point of the material. These are recorded in the transmitted wave obtained during tensile tests performed at high strain-rates. The presence of this artificial peaks has to be carefully handled, especially if the ductility of the material is limited or similarly if the interest is focused on few percentages of deformation. As a matter of fact it should avoid that the time duration of the peaks overlaps the area of interest. As explained in [79] in case of one bar setup, “*the peaks are caused by micro-vibrations of the output bar at the interface with the specimen. They are possibly induced by the bending of the output bar by gravity and/or the misalignment of the impact block along the tensile direction*”. This was confirmed also by Kariem for a two bars setup [80].

In order to solve this problem, the alignment between input bar, specimen and rigid block “*should be strictly kept along the tensile direction*”. In this perspective an ad hoc system is developed in order to ensure the correct alignment between input

bar, specimen and output bar (see Fig. 3.8). To the same end, the specimen is properly clamped and then the system is statically pre-loaded: in this way the initial slacks of the system are eliminated as well as the misalignment due to the specimen threaded ends (the thread is needed for the mounting). The pre-loading system is realized through a threaded collar placed on the input bar which takes contact with a rigid block when the hammer positioned at the end of the output bar is pressed by a hydraulic ram, which also stops the output bar at the end of the specimen deformation (see Fig. 3.7). Following this approach, at the beginning of the test, the specimen is already well aligned avoiding to become aligned during the test. Another improvement for the data analysis regards the introduction of a block system which is able to stop the input bar after the end of the test in order to prevent the crash of the failure surfaces of the specimen. This allows to recover them as untouched and to use them for post-mortem analysis.

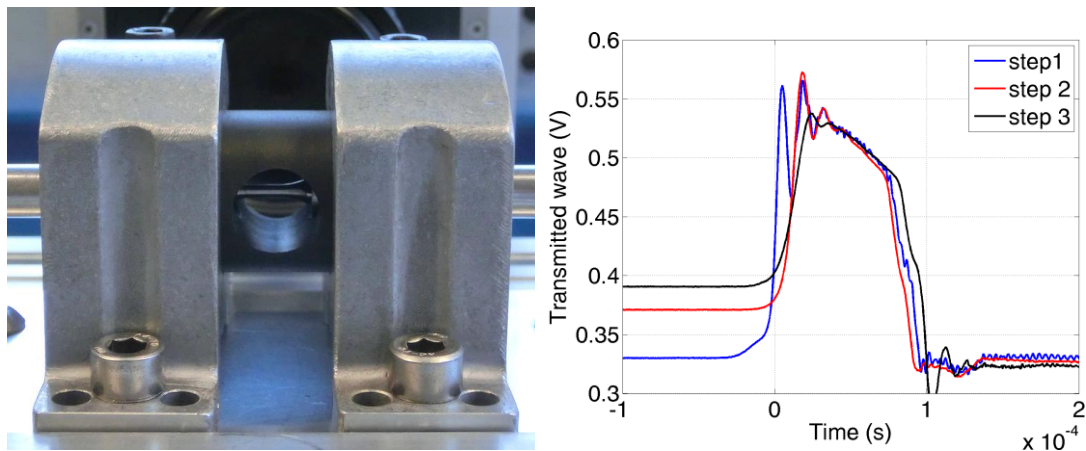


*Fig. 3.8: Alignment system for high strain-rate tensile tests (left) and recorded stress wave vs. time with and without the improvement in the alignment of the system and pre-loading (right).*

In Fig. 3.8, a picture of the system used for the alignment is reported as well as the comparison between the stress vs. time measurements of the improved configuration of the system in comparison with intermediate steps: step 1 is the starting configuration, step 2 is with the specimen only pre-loaded; step 3 is with the specimen pre-loaded and properly clamped. The data are compared in terms of

transmitted signal (V) vs. time and are obtained for standard specimen shown in Fig. 3.6 (triaxiality equal to 1/3). Observing the signals, it is evident that the modifications made on the standard direct tensile setup improve the accuracy of the measurements. With the enhanced configuration the force evolution is free from pseudo initial peaks and the residual oscillations are only attributable to the inevitable elastic response of the tested material due to a sudden loading.

The oscillations due to this last aspect can be reduced increasing the rise time of the load signal. The wave dispersion during the propagation along the bar modifies the pulse shape which reaches the specimen with a trapezoidal shape instead of the theoretical square one. However, the rising time can be further damped through the *pulse shaping* techniques which are based on the spread of the pulse in the incident bar [81,82]. During the years different methods were developed: the most common consists to introduce a thin disk of soft material, such as copper, or a thin layer of grease between the striker and the input bar, another strategy is to use projectile of a material with lower impedance than the material of the input bar, and more recently short bars of particular shape are positioned before the specimen in order to realize the desired loading pulse [83]. Nevertheless, the damping methods should be carefully used. Too much damping limits the strain-rate at the beginning of the deformation and this could change the apparent material behaviour. Thus, the information of strain-rate versus strain should be verified when pulse shaping techniques are used. In this work the anvil of the input bar was lubricated for each test.

### 3.2.3 Miniaturized Split Hopkinson Tensile Bar

A mechanical characterization up to  $10^3 \text{ s}^{-1}$  could result unsatisfactory for the description of the behaviour of materials involved in phenomena such as ballistic impacts or explosions. Indeed, in these scenarios the materials can be solicited at strain-rates much greater than  $10^3 \text{ s}^{-1}$ , therefore at least an order of magnitude more should be investigated.

In order to extend the range in strain-rate, different types of tests can be used (such as Hopkinson Bar, Taylor and Flyer Impact tests). Several researchers developed miniaturized Hopkinson setup to increase the strain-rate, keeping at the same time the test design simple and having the possibility to directly compare the results with those obtained at lower strain-rates. The benefits of developing miniaturized setup for compression tests have been reported in the work of Jia, et. al. [84]. In general, very high strain-rates using a Hopkinson bar setup can be achieved in two ways. One possibility is to increase the speed of the striker bar, but this also increases the stress level in the bar, which is limited by the yield strength of its material. Another possibility is the reduction of the specimen dimensions, but also here there are some restrictions. The reduction of the length of the sample can only be achieved by maintaining the length to diameter ratio of the specimen to ensure a uniaxial stress state. Decreasing the diameter of the specimen inevitably reduces the level of force on the output bar and concomitantly a low output signal to noise ratio is obtained. Furthermore, the specimen has to be large enough to be representative of the material under testing. A widely used technique requires the miniaturization of the setup (see e.g. [84-87]) followed by the removal of the input bar (see e.g. [88-90]), to give the so called Direct Impact Compression Tests. The removal of the input bar brings in turn two problems [84]. The measurement of strain (and strain-rate) has to be performed using external devices and a check for equilibrium in the specimen can not be performed.

Some of the more important design constraints, which should be taken into account for the arrangement of a miniaturized Hopkinson Bar setup, are provided here:

- ✓ the desired levels of strain-rate and strain and the expected yield stress of the material under testing;
- ✓ the admissible stress level in the bars (i.e. the yield strength of the bar material);

- ✓ the strain-gage base size and the maximum acceptable strain (3000  $\mu\epsilon$  for the semiconductor strain-gages used in this work);
- ✓ the impact velocity (to verify the gas-gun length with a fixed pressure level);
- ✓ the non-overlapping of the waves in the measuring point (especially in the incident one);
- ✓ the specimen dimensions (the ratio length/diameter should to be in the range 0.5÷2.0);
- ✓ the ratio between the reflected and transmitted waves.

Also when the configuration is the direct tension, the design constraints mentioned above are still valid, as they refer to incident, reflected and transmitted waves regardless of their sign. In this sense, in the scientific literature it is possible to find solutions in which miniaturized Kolsky Bar is used, as e.g. [91,92].

On these bases, the better solution to achieve very high strain-rates is the reduction of the entire setup dimensions (both specimen and bars). A tensile specimen with compact dimensions, 1.5 mm of diameter of the reduced section and 1.5 mm of gage length (instead of 3 mm of diameter and 5 mm of gage length of the standard sample) was adopted. With this dimensions the ratio length/diameter is almost the same of the standard specimen, therefore the results obtained from the two specimens geometry could be compared without particular size effects on the material response. The comparison between the standard and the miniaturized geometries is shown in Fig. 3.9. Using this kind of sample geometry, the strain-rates around  $10^4 \text{ s}^{-1}$  could be achieved only if the specimen motion occurs at velocity of 15÷20 m/s ( $\dot{\epsilon} = v/l_0$ ). Consequently, the stress and strain levels in the bars have to be carefully verified. The amplitude of the pulse stress must not overcome the elastic limit of the bar and the bar deformation have to be limited in the range of acceptable strain of strain-gages. Considering a rod of high strength stainless steel (as those of the standard setup) with a diameter of 10 mm, at impact velocity between 20÷30 m/s corresponds stresses around 400÷600 MPa and strains in the range of

2000÷3000  $\mu\epsilon$  which are admissible for the semiconductor strain-gages used in this work. As a consequence of specimen small dimensions, the output bar diameter has to be reduced in order to guarantee high output signal to noise ratio. For what concerns the impactor, the better solution is to use a material with lower impedance than the alloy of the input bar in order to guarantee a trapezoidal pulse shape for the reduction of elastic oscillations.

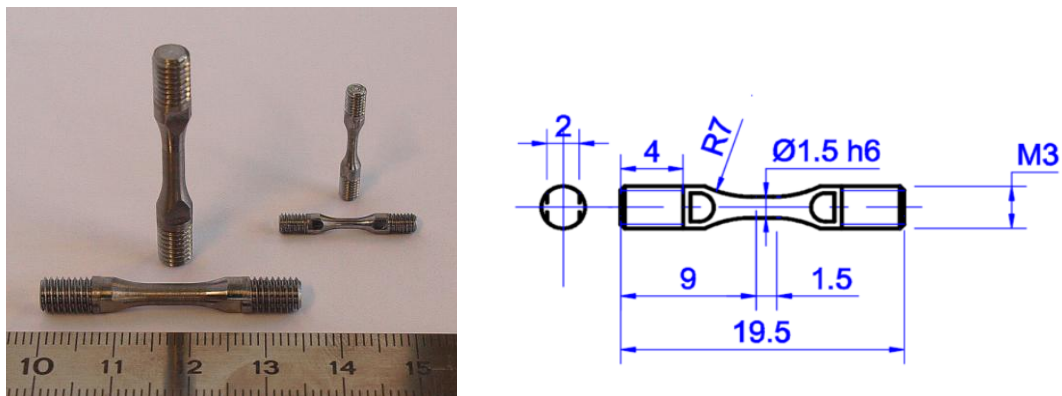


Fig. 3.9: Specimens used for tests at different strain-rate up to  $10^3 \text{ s}^{-1}$  and the miniaturized specimens used for high strain-rate tests at  $10^4 \text{ s}^{-1}$ .

The final design used for the  $10^4 \text{ s}^{-1}$  tests (with miniaturized samples) consists of a gas-gun 1 m long which uses compressed air. The impactor is a tube made from an aluminium alloy (Al7075T6) which is 150 mm long in order to generate a tensile pulse with a time duration of about 100  $\mu\text{s}$ . The input bar is made from martensitic high strength stainless steel (17-4PH) with a 10 mm of diameter and 2 m long, with an anvil at one end. The output bar has a diameter of 6 mm with a length of 500 mm. The strain-gages are located at 250 mm on the input bar and 50 mm on the output bar from the specimen, as shown in Fig. 3.10. The strain-gages and data acquisition device are the same of the standard setup previously described. The specimen pre-loading system is similar to that used in the standard configuration; in this case the threaded collar in the input bar takes contact with the rigid block when the hammer at the end of the output bar is screwed against the stopper block.

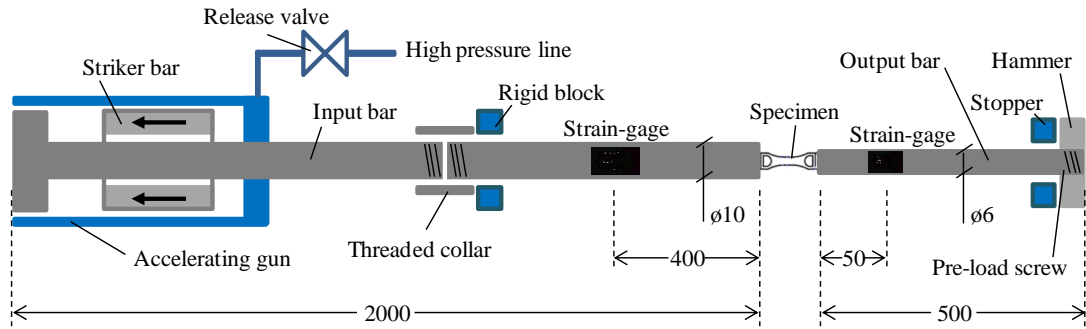


Fig. 3.10: Scheme of the miniaturized Hopkinson bar setup used to perform dynamic tensile tests (direct tension up to  $10^4 \text{ s}^{-1}$ ).

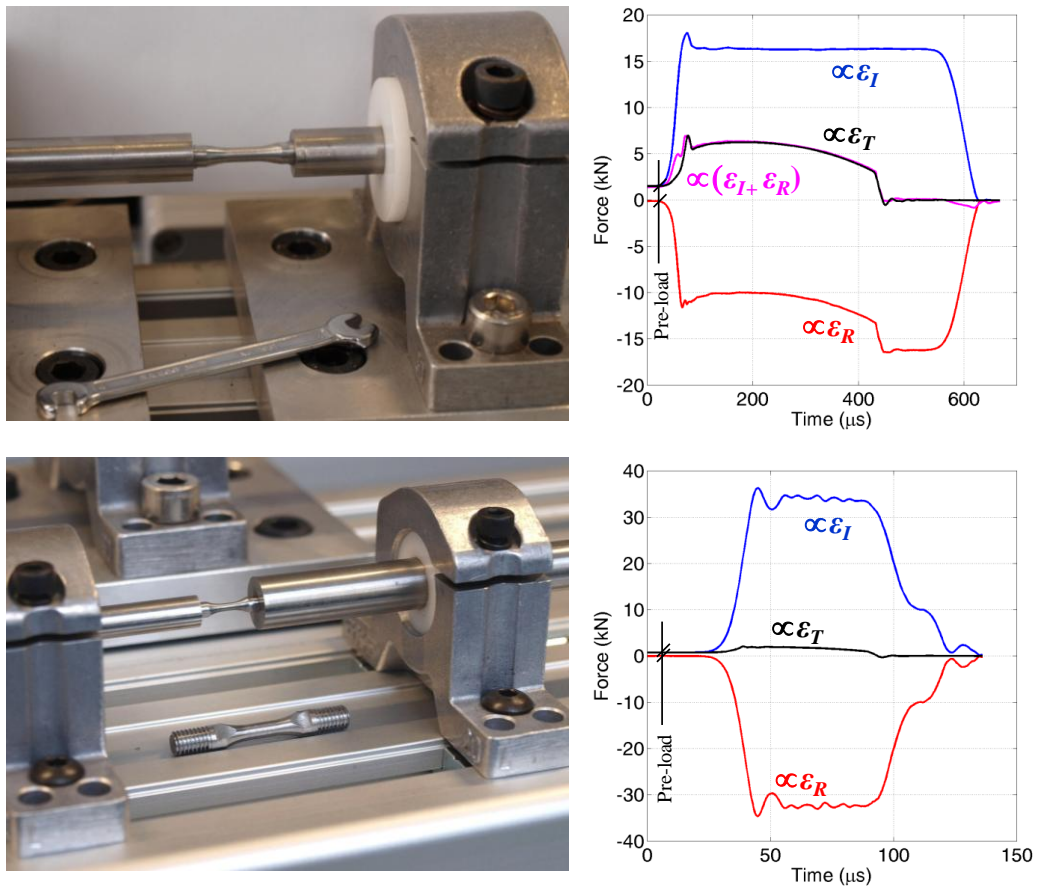


Fig. 3.11: Details of the specimens mounting for tests at  $10^3 \text{ s}^{-1}$  (top) and  $10^4 \text{ s}^{-1}$  (bottom) with diagrams of the waves recorded in terms of force vs. time.

In Fig. 3.11, the details of the specimens mounting on the two Hopkinson setups, the standard and the miniaturized ones, are shown along with the corresponding

waves (in terms of force vs. time) recorded during the tests for a high chromium ferritic/martensitic T91 steel. Since in both setups, the measuring points are located far from the specimen ends, the forces and displacements at the actual ends of the specimen necessitates shifting of the recorded signals forward or backward, towards the interface with the specimen. However, this time shifting is rather simple to perform because the signals are synchronized and both velocity of the wave inside the bars and the distance of the strain-gage from the specimen are known. Moreover, an algorithm for the wave dispersion correction was applied [19].

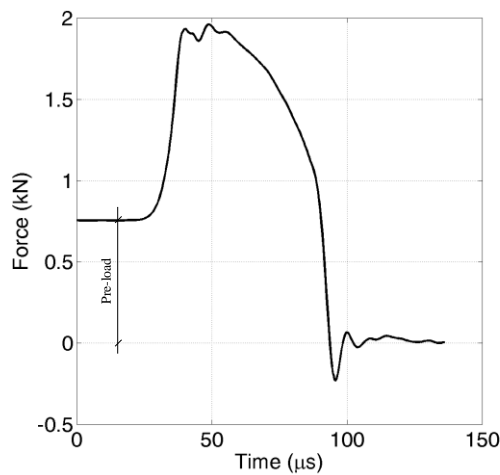


Fig. 3.12: Transmitted force measured on 6 mm-diameter output bar for a miniaturized sample of T91 steel tested at  $10^4 \text{ s}^{-1}$ .

Observing the diagrams, it is evident that the miniaturized sample generates a very low force level in the output bar due to the small specimen diameter and this explains the need to reduce the diameter of the output bar in order to measure an appreciable signal (see Fig. 3.12). Moreover, in the miniaturized setup, the force level measured on the output bar is much lower with respect to those recorded on input bar (incident and transmitted forces), thus the equilibrium is almost impossible to evaluate because small errors in the measurement of the incident and reflected forces could generate significant effects when their subtraction is compared with the transmitted force.

However, the evaluation of the mechanical response of the material tested is a critical aspect with this kind of configuration. Indeed, on the contrary of the standard Hopkinson Bar setup, in the miniaturized configuration the input bar can reach velocities higher of 25 m/s (twice over than standard setup), generating criticality on its signal acquisition system. In particular, this level of velocity is achieved in very short time, about 10  $\mu$ s, so the input bar is moved with very high acceleration, around  $10^6$  g. With these acceleration levels, all the components of the strain-gage apparatus are subjected to considerable inertia forces. For this reason, many times, it was observed the breakage of the wires in correspondence of the soldering zone with the strain-gage, as it was observed also by Bolduc [93]. It is important to underline that the signal recorded on the input bar is essential for the evaluation of the specimen strain, therefore an alternative and reliable measurement method has to be adopted. As it will be discussed later, a possible way is represented from the high speed video through a digital image analysis. The issue just described is characteristic only for the input bar because the output bar remains almost stationary and no problems arise in the extraction of the force signal (the force level is limited by the specimen).

### 3.3 Digital image acquisition

The digital image acquisition during the execution of the mechanical test can result useful for different reasons: for a better and detailed evaluation of the mechanisms which occur during the test, for measurements (displacements, strains, velocities), and numerical validations (e.g. through the comparison between the shape of the component experimentally tested and that reproduced with a numerical simulation) [94-98]. Obviously, the accuracy of the acquired images depends on the characteristics of the camera and the lens used. In particular, the digital image acquisition system has to be adequate to the phenomena to record. Generally, for scenarios at low strain-rate the image recording is carried out with high resolution camera, while high speed camera is indispensable at high strain-rate. The high speed

cameras can be used also at low strain-rate, but they are usually characterized by low high resolution which limits the accuracy of the data extracted.

The main problems related to the image acquisition techniques are: the distortion of the images due to the lens, the data analysis through the digital image correlation (DIC) methods, and their synchronization with the experimental testing equipment. The first problem can be reduced or completely solved using modern high quality lens, maintaining at the centre of the lens the object to film or using correction algorithms [99-101]. About the DIC analysis there are many studies in which the quality of speckle patterns and specific mathematical formulas are discussed in order to obtain the accurate measurements [102-104]. Finally, the synchronization of the camera and the testing machine could be performed using trigger signals.

### 3.3.1 High resolution camera for low strain-rate tests

The better solution to acquire digital images during the execution of test at low strain-rate is the use of a high resolution camera. In this way it is possible to record images of high definition with a frame-rate enough to well describe the scenario analyzed. It is important to highlight that the image quality depends also from the illumination. In order to obtain a good image elaboration the specimen has to result neither too much dark nor too much burned by the light. Moreover, during the image acquisition the illumination should be maintained as much as possible constant to avoid difficulties in the image analysis or introduce shadow effects.

In this work, for the mechanical tensile tests at very low strain-rate ( $10^{-3} \text{ s}^{-1}$ ) carried out with the Zwick-Roell machine, a PixeLINK<sup>®</sup> camera PL-B777 was used, Fig. 3.13. It is a high performance 5 mega pixel monochrome camera designed to fit a variety of applications: quality control, industrial inspection, security and surveillance, ITS/Traffic monitoring, etc.



*Fig. 3.13: High resolution camera PixeLINK® PL-B777.*

This camera is based on the Micron CMOS rolling shutter progressive scan sensor with a 1/2.5" optical format. Factory calibrated Digital Pixel Correction and on-board Flat Field Correction (FFC) provides image quality similar to high-end CCD cameras. External triggering and two general-purpose outputs provide users the flexibility to synchronize the camera with their processes and illumination [105]. The camera is supplied of dedicated software for the option setting and the image visualization. The main features are summarized in the following:

- ✓ Bit Depth: 8 & 12;
- ✓ Configuration: Right Angle, Board Level, Standard;
- ✓ Frame Rate: 7 fps;
- ✓ Interface: USB 2.0, Firewire A, GigE;
- ✓ Lens Mount: C-Mount;
- ✓ Resolution:  $2592 \times 1944$  (5.0MP);
- ✓ Sensor Size: 1/2.5";
- ✓ Sensor Type: CMOS;
- ✓ Shutter Type: Rolling;
- ✓ Triggering Options: Manual & Software.

A LED (Light Emitting Diode) spotlight was used as illumination source in order to guarantee a low heating of the specimen tested with respect of common

incandescent lamps. Moreover, a dedicated screw sled was designed for a precise camera positioning.

For each test the initial undeformed specimen shape is recorded to perform the image calibration. The camera was triggered when the pre-loading test condition was reached, i.e. a force level which depends from the material tested. The oscilloscope LeCroy® WaveStation 2012 was used to trigger and establish the sampling time of the camera [106].

### 3.3.2 High speed camera for high strain-rate tests

An improvement for the data analysis of high strain-rate tests is given using a high-speed camera (see Fig. 3.14 and 3.15). The high speed camera used in this work is the FASTCAM SA5 by Photron [107]. The main characteristics are summarized in the following:

- ✓ Maxima performances: full resolution 1024 x 1024 (7000 fps); maximum frame rate 1000000 f/s (64 x 16 pixels);
- ✓ Examples of performance:
  - 1024 x 1000 pixels @ 7500 fps (5588 frames; 0.745 s)
  - 512 x 512 pixels @ 25000 fps (21829 frames; 0.873 s)
  - 256 x 256 pixels @ 87500 fps (87317 frames; 0.998 s)
  - 128 x 128 pixels @ 262500 fps (349269 frames; 1.331 s)
  - 128 x 24 pixels @ 775000 fps (1862769 frames; 2.404 s)
- ✓ Shutter: global electronic shutter up to 1  $\mu$ s, independent from frame rate;
- ✓ Variable Region of Interest (ROI);
- ✓ Capture 12-bit uncompressed data;
- ✓ 20  $\mu$ m pixels ensure best light sensitivity for demanding high-speed or low light applications;

- ✓ 8 GB memory (standard: 5457 frames or 0.780 s @ maximum resolution);
- ✓ Gigabit Ethernet interface;
- ✓ Triggering and trigger delay options programmable and selectable;
- ✓ Phase lock to IRIG/GPS to precisely synchronize together with an external source.



*Fig. 3.14: High speed camera Photron Fastcam SA5.*

Correlated to the high speed imaging system there is the need of a high level of light, since the low sensitivity of the sensor and the short shutter time. Often to partially solve this problem, a backlight video is performed, but doing this only the specimen outline could be investigated. If there is the need to take front images (e.g. for DIC analysis), a powerful light source is necessary. Usually the best solution is represented by pulsed light devices like flashes. The direction of the light, the time for the activation of the system and the time of constant light are important parameters strictly correlated to the phenomenon to investigate. As a matter of fact,

first of all, it is necessary to accurately synchronize the duration of the test with the time in which the flash gives a light as constant as possible assuring, at same time, to take a sufficient number of frames during the deformation process.

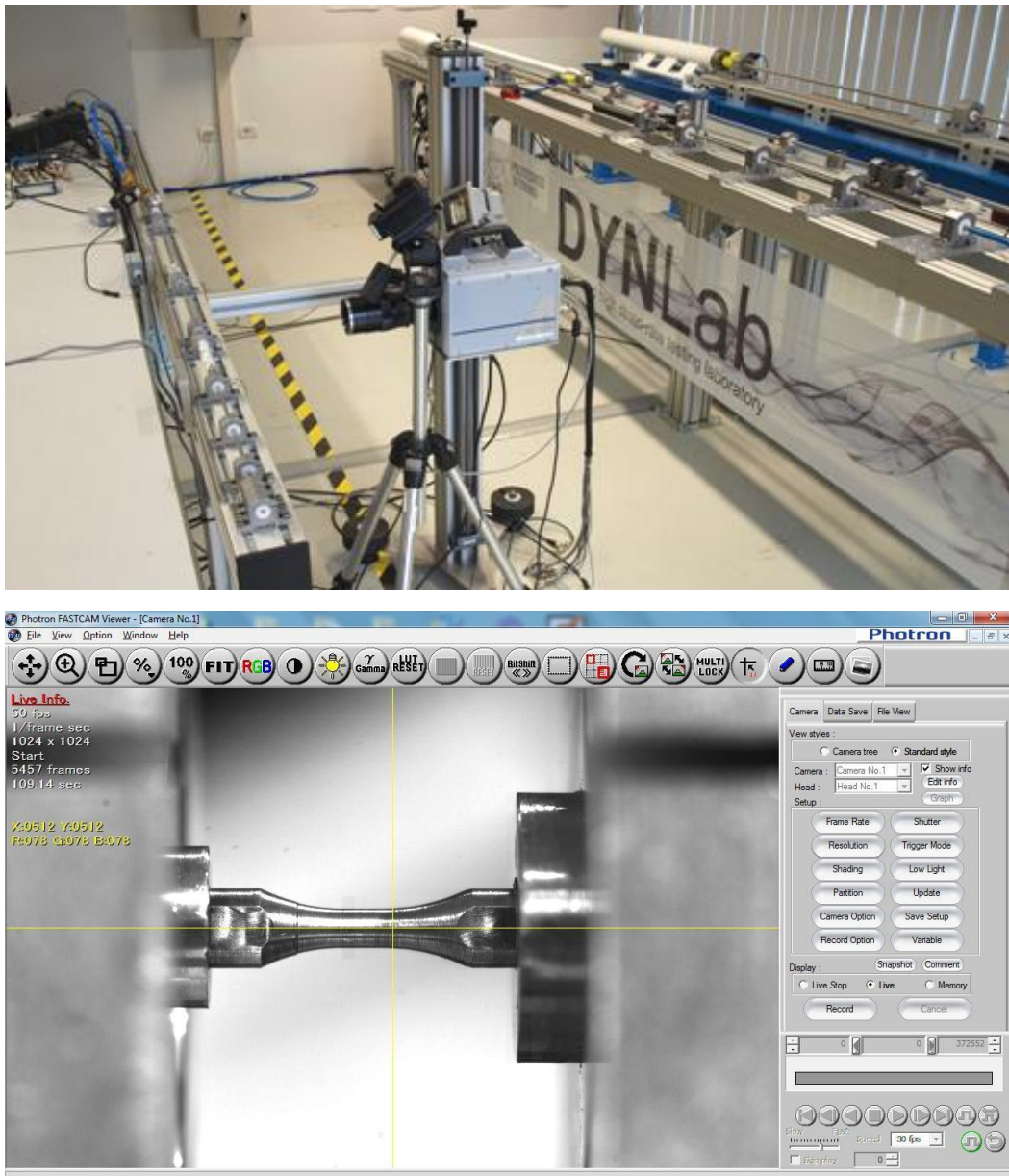


Fig. 3.15: Digital image acquisition system for miniaturized Hopkinson bar apparatus (top) and detail of the specimen for test at  $10^4 \text{ s}^{-1}$  view through the camera (bottom).

The Metz Mecablitz 30 B3 flash was used as illumination source. It was observed that the time required for the starting of the flash is about 10  $\mu\text{s}$  and the peak of light is reached in about 30  $\mu\text{s}$ , while the full light is given for about 200  $\mu\text{s}$ . This represents the limit in time for the acquisition: the trigger signal has to be generated at least in advance of this time. At the same time, it can not be generated too early due to the constraint of 200  $\mu\text{s}$  of full light. For these reasons, the strain-gage signal on the input bar is used to generate the trigger signals for flash and camera. For the standard setup the time in which the signal arrives to the strain-gage position is 350  $\mu\text{s}$  in advance with respect to the time in which the input wave reaches the specimen, while about 80  $\mu\text{s}$  for the miniaturized one. Thus, a delay of 250÷300  $\mu\text{s}$  is imposed to the starting of the flash in the standard setup, while no delay is used for the miniaturized version. Instead, for both setups no delay is used for the camera (this means that some frames are taken before the arrival of the light) since the record duration is much higher with respect to the sum of the time needed for the wave travelling and the duration of the test. For a precise camera positioning a bidirectional screw sled support was used (see Fig. 3.15).

With the aim to obtain the maximum number of images to describe the specimen deformation with a good level of accuracy, it is necessary to reduce as much as possible the dimension of the image recorded in order to increase the sampling rate of the camera. This last consideration needs a deeper analysis. In the miniaturized Hopkinson Bar the pulse duration is about 80  $\mu\text{s}$  which should need a sampling rate in the order of about ten MHz to obtain an adequate number of representative points. In this work, the wave signal is extracted through the strain-gage using a National Instruments board PCI 6132, 14 bit at 2.5 MHz (about 200 points describe the wave signals). A comparative study was conducted using a digital oscilloscope PicoScope 3425, 12 bit at 10 MHz (about 800 points describe the wave signals), but the definition level of the output signal was not increased (see Fig. 3.16a) because the dynamics of the measured signal is within the range of the mechanical response of the specimen-bars system, which has not relevant frequency components over 200 kHz (see Fig. 3.16b).

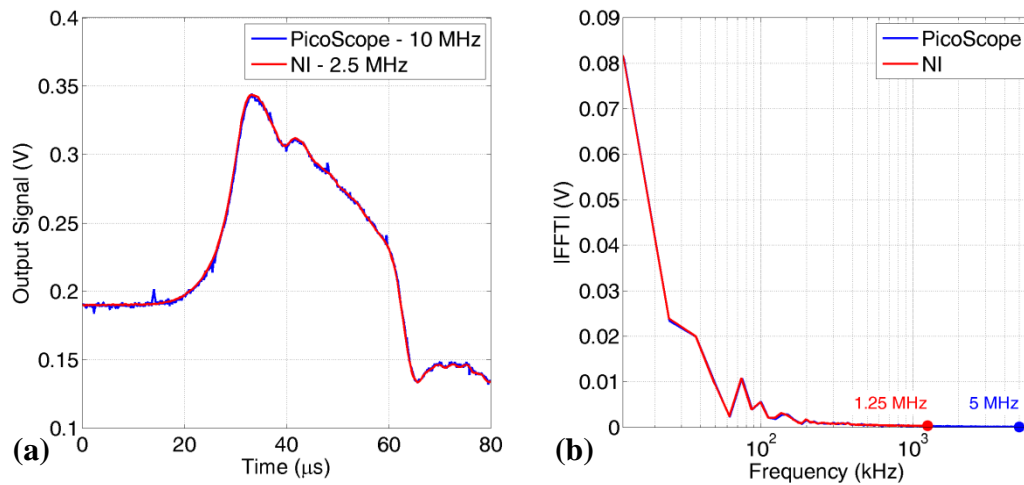


Fig. 3.16: a) Force signals measured on the output bar (miniaturized Hopkinson Bar) through two data acquisition systems: National Instruments board PCI 6132, 14 bit at 2.5 MHz and PicoScope 3425, 12 bit at 10 MHz. b) Signal frequency components calculated by performing the FFT for both force signals.

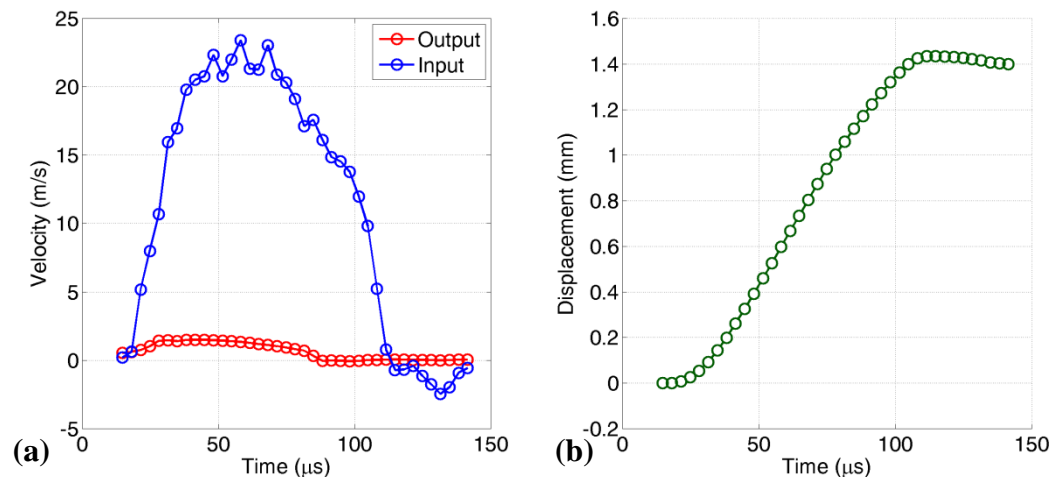
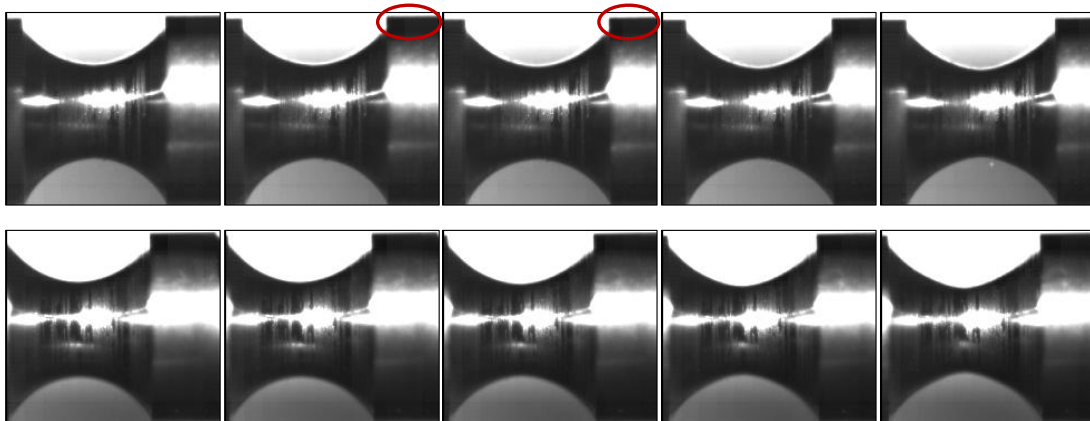


Fig. 3.17: a) Velocities of the input and output bars for the miniaturized Hopkinson Bar and b) displacement of a miniaturized specimen of T91 steel tested at nominal strain-rate of  $10^4 \text{ s}^{-1}$  extracted by analyzing images acquired at 300000 fps.

After several attempts, it was found that, with the miniaturized samples and with the Photron SA5 high-speed camera, it is possible to perform the digital image acquisition with a good level of resolution at 300 kHz. Even if this frame-rate is one

order of magnitude less than the sampling rate of wave signals, it is important to underline that the evolution of the kinematic quantities, such as the displacements, have a variation much softer than the forces, therefore they can be extracted also with not very high sampling rate levels, as shown in Fig. 3.17b. In Fig. 3.17a the velocity of the input bar is obtained by analyzing the images of the high-speed camera (300000 fps), while the velocity of the output bar is extracted by resampling the strain-gage signal, which is more accurate with respect to that measurable from the images elaboration.

Through the high speed video it is possible to observe which important advantage in the image elaboration is due to the introduction of the alignment and pre-loading systems described in the section 3.2.2. In Fig. 3.18, two sequences of the high speed recording of tests on notched specimens are reported and compared. In the first one it is possible to notice that the specimen alignment occurs during the test before the starting of the necking. In the second one, the specimen is already aligned at the beginning of the tests and no successive alignment is visible: this is due to the static pre-load applied to the specimen. Due to the vibrations induced in the first one, the differences between the two sequences are much more evident looking directly the video.



*Fig. 3.18: Sequence obtained with the high-speed camera (150000 fps) for a notched specimen: (top) alignment of the specimen during the test; (bottom) the specimen maintains its starting alignment.*

As mentioned in the section 3.2.3, the recording of high speed images becomes essential for tests carried out with the miniaturized Hopkinson Bar. Indeed, the strain-gage placed on the input bar, which gives the information about the strain of the specimen, is extremely solicited by the inertia forces threatening its integrity. This problem can be overcome measuring the specimen displacement through the image analysis. However, in the current configuration, the trigger signals start exactly when the stress pulse arrives in the strain-gage position, therefore at least at the beginning of the test the strain-gage must be operative. Obviously, also the instant of the striker shoot or the impact between the projectile and the input bar could be used for trigger, nevertheless these reference points have too variability to be considered as reliable. The time between the shoot and the impact changes for each test, even if only little, because the shoot pressure and the starting position of the projectile are not exactly the same, while the impact instant can be measured with velocity transducer, but also in this case the distance between the transducer and the input bar can change and the measurement can be influenced by the presence of the pulse shaper. In conclusion, the signal coming from the strain-gage, positioned on the input bar, is the only one accurate and must be used as start point for camera and flash trigger signal.

### 3.4 Combined experimental equipments

In order to completely characterize the material behaviour, it is important to perform tests at different temperatures, permitting the description of the thermal softening effects on the material strength. In the previous chapter the influence of the temperature on the mechanical response of metals was analyzed. Generally, mechanical tests at constant velocity and different temperatures are performed in order to evaluate the material behaviour and calibrate the part of the material model which takes into account the thermal effect. Nevertheless, in many works the dependency of the material response from the temperature was investigated also varying the strain-rate [47,49,76,78,108-113]. In some materials it was observed a

relevant difference of the temperature effect on the mechanical response at low or high strain-rate. These considerations explain the need to develop experimental techniques for the material characterization varying the temperature as well as the strain-rate.

In the perspective to perform tests in mixed loading conditions, in this work, a methodology for testing materials at high temperature and high strain-rate was adopted, using a standard Hopkinson Bar apparatus for direct tensile tests with a heating system. The same heating system was also used to perform quasi-static test at different temperatures.

### 3.4.1 Setup for low strain-rate tests varying temperature

The heating of the specimen in quasi-static condition was obtained with an induction coil system, designed to concentrate the heat flux in the gage length of the specimen (see Fig. 3.19). The temperature was controlled via a proportional-integral-derivative (PID) controller, commonly used in closed control loop, which adjusts the command signal to the heating system on the basis of the measurements obtained from thermocouples directly welded on the specimen surface far from the gage length. The choice to not weld the thermocouples in the middle of the specimens was to avoid of inducing any changes or altering the area of necking. Before to perform the tests, a calibration procedure was performed on the specimen, mounted in the machine to replicate the testing condition, in order to correlate the temperature in the middle of the gage length with the temperature where the thermocouples were welded and to monitor the uniformity of the heating. A schematic of the procedure is reported in Fig. 3.19: five thermocouples were used during the calibration procedure to obtain the temperature distribution along the gage length of the specimen. The calibration was performed for different materials, also up to 1000 °C, and the maximum difference in temperature between the middle of the specimen and the position of the control thermocouple T1 was in the range 5÷10 °C. This limited

variation of the temperature is mainly due to the small dimension of the specimen and the high power of the heating induction system.

In a real test, only the thermocouple welded in correspondence of the position 1 was used for the temperature control. Each specimen was kept about 5 min at the desired temperature before to perform the test in order to allow a uniform distribution of the temperature in the specimen. Obviously, since the quasi-static tests need quite long time to be performed, the material during the test persists for long time at high temperature, on the contrary of dynamic tests. This could cause some differences in the mechanical response of the material, especially with regard to the change of the microstructure during the deformation process, but this aspect can not be solved, since it is intrinsic in the test process itself.



*Fig. 3.19: Scheme of the location of the thermocouples ( $T_i$ ) for the temperature calibration (left); details of the testing system used in quasi-static strain-rate at high temperature (right).*

In order to maintain valid the profile of the temperature along the specimen, obtained from the calibration, the position of the coil was fixed and the threaded bars to clamp the specimen were taken back to the same start position for each test.

However, to guarantee the uniformity of the heating along the specimen during the test execution is the main problem for this kind of test. Indeed, during the

deformation the central part of the specimen, and in particular the gage length, gradually comes out from heated zone. Also moving the coil at the same velocity of the machine crosshead, this problem can not be solved. Nevertheless, performing the tests on different materials varying the temperature, also until 1000 °C, it was observed that up to 5 mm of machine stroke (which corresponds about 100% of engineering strain for standard specimen), the variation of temperature at the centre of the specimen is restricted at  $5 \div 10$  °C, which should not significantly influence the mechanical response of the material.

### 3.4.2 Setup for high strain-rate tests varying temperature

In the scientific literature, different solutions for testing materials at high strain-rate combined with high temperature are described [50,54,109,114,115]. Usually, the high strain-rate conditions are reached using the Hopkinson Bar system, while different heating systems are applied. The main problem related to this kind of equipment is that maintaining the specimen in contact with the bars during the heating implies an increase of the temperature along the rods. As widely discussed in the scientific literature, the increase of temperature changes the elastic constants, and thus the mechanical impedance of the bar material, leading to changes in stress wave propagation in the bars. This could generate significant errors in the evaluation of the response for the tested material [48,55]. Nevertheless, this problem can be overcome by using correction algorithms which take into account the variation of the elastic modulus [49,51,116], but this requires to know the temperature distribution along the bars.

In compression tests, the problem of the temperature increase in the bars can be completely solved using a synchronized SHPB apparatus, in which the bars are kept far from the heating zone and take contact with the specimen just before that the compression pulse reaches the specimen [45,48, 56,112].

The problem for tensile (and torsion) test is that the specimen has to be fixed a priori to the bars, which implies that the temperature at the grip section has to be kept

low. In this case, a common solution consists to use insensitive or low sensitive materials for the bars, such as stainless steels, which exhibit a significant reduction of the Young's modulus at temperature higher than 600 °C [54,55]. Often a cooling system is used in order to limit the temperature increase in the bars [117]. In the scientific literature few works about high temperature and strain-rate tests in tension can be found. Examples of them are the works reported in [54,55,76-78,113,118-120]. Different types of specimens can be used, such as sheet materials, which can be glued to the machine ends, or standard dog-bone specimens, with cylindrical section.

For the direct tensile Hopkinson Bar used in this work (described in the section 3.2.2, Fig. 3.7) the heating of the specimen was obtained with an induction coil system (see Fig. 3.20). The choice to use this heating system is based on the facility to move it also in other testing facilities and for the possibility to reach very high temperatures in a narrow area in a few time. As for the quasi-static test, a feedback loop, based on measurements from thermocouples directly welded on the specimen surface, was used to control the temperature of the specimen. The temperature calibration along the specimen was performed also in this case. Close to the gripping ends, the bearing bushes were made of insulating material. To solve the problem related to the heating of the gripping areas, a cooling system was predisposed. It was based on vortex tubes (see Fig. 3.20), which localize the cool air jet on the ends of the bars in contact with the specimen (minimum temperature -20 °C).

The strain signal measured on the input bar was used to generate an external trigger to turn off the heater (the same way used to start the high-speed camera and the lightening system). For both standard and miniaturized configurations, the time which needs the incident wave to travel from the strain-gage position to the specimen was sufficient to avoid the noise on the signal due to the disturbances induced by the electro-magnetic field and it was short enough to not produce a significant decrease of the temperature of the specimen. Also for the tests at high strain-rate the specimen was maintained about 5 min at the test temperature, before the test starting, in order to allow the temperature distribution in the specimen.

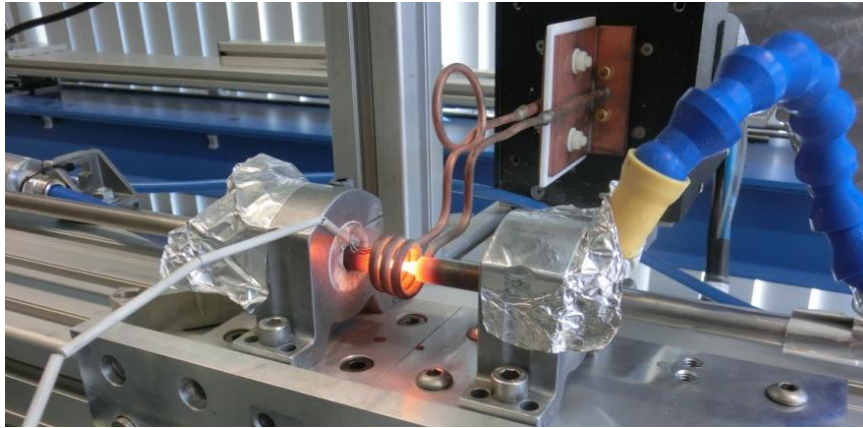


Fig. 3.20: Induction coil system used to heat the specimen for tensile tests at  $10^3 \text{ s}^{-1}$ .

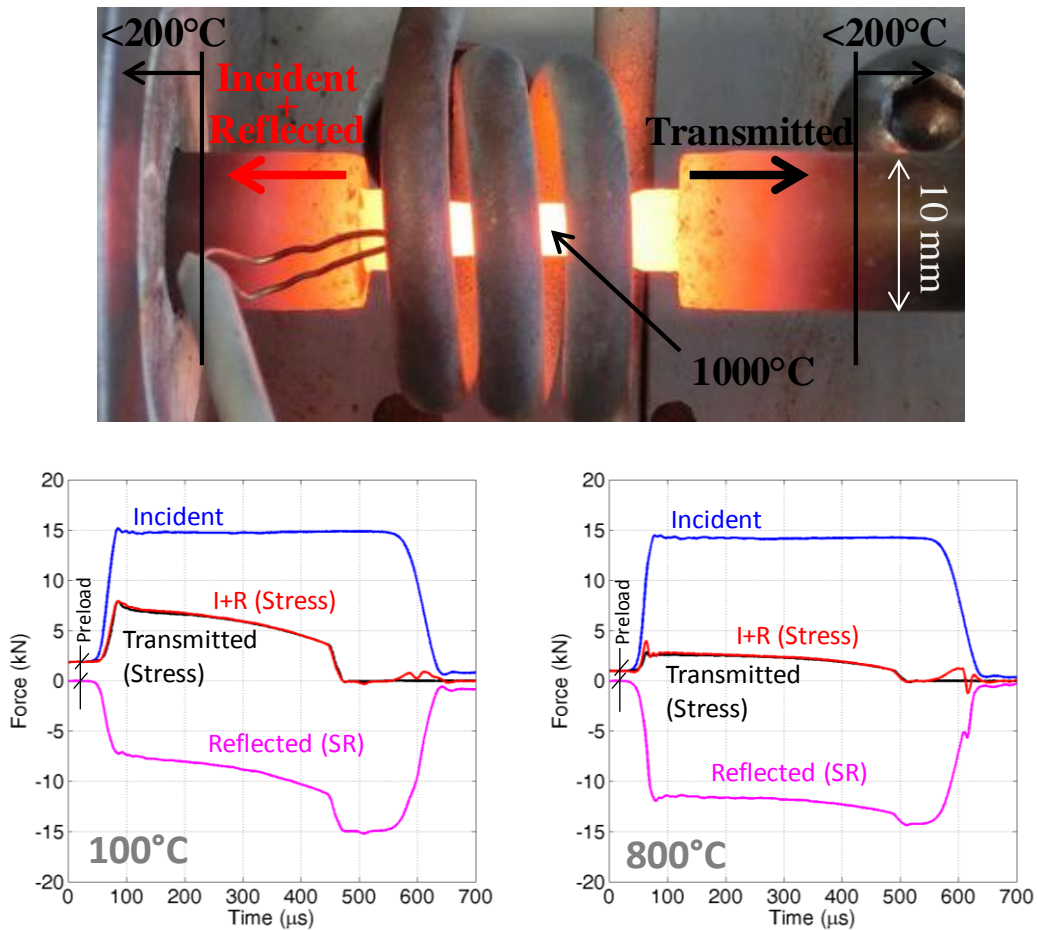
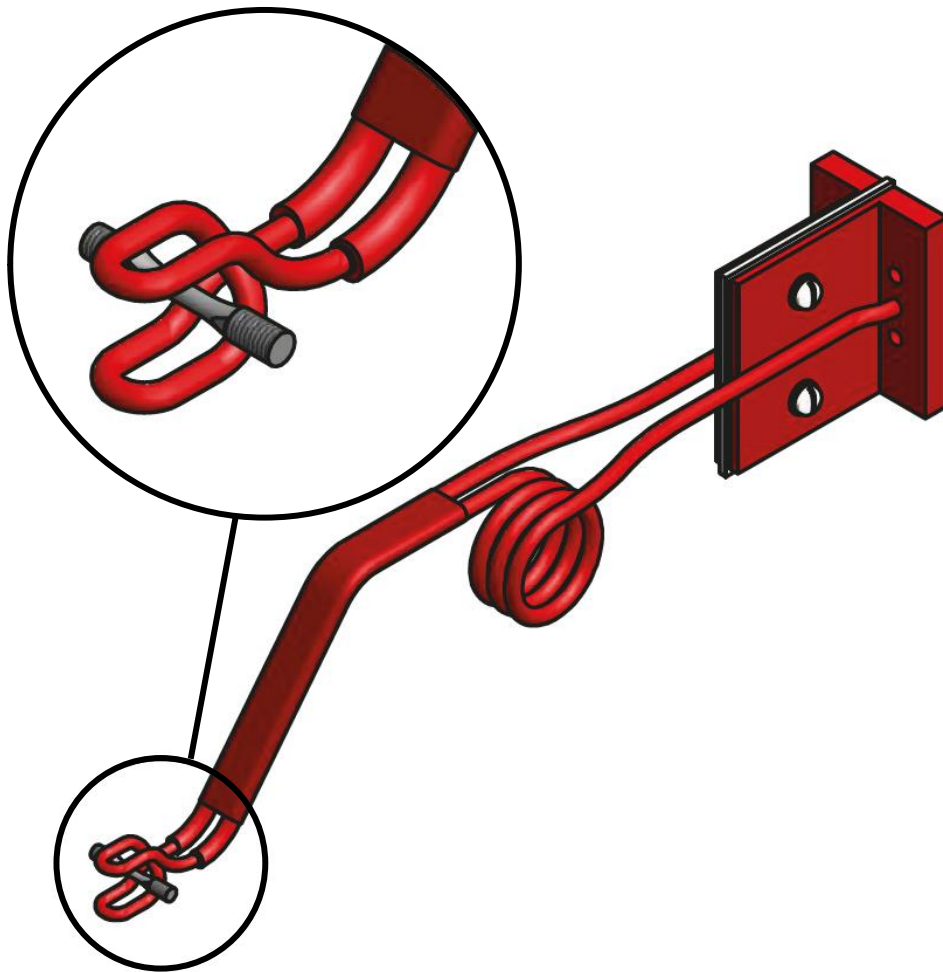


Fig. 3.21: Temperature distribution along the bars when a specimen of molybdenum is heated at 1000 °C (top); force equilibrium at 100 and 800 °C for molybdenum tested at  $10^3 \text{ s}^{-1}$  (bottom).

In Fig. 3.21, it is shown the temperature variation along the input and output bars when the specimen of heavy sintered molybdenum is heated at 1000 °C. Thanks the use of the 17-4 PH martensitic high strength stainless steel for the bars and the vortex tubes, the temperature increase is restricted in few millimetres. After about 10 mm the temperature is less than 200 °C. Considering that the pulse duration with this kind of setup is about 600  $\mu\text{s}$ , which corresponds to 3 m of length in the steel, it is evident that few millimetres, in which the elastic properties are modified, are not sufficient to considerably alter the wave propagation along the bars. Moreover, this consideration is supported by the good equilibria (see Fig. 3.21) obtained with this kind of direct tensile Hopkinson Bar setup at test temperature of 100 and 800 °C for molybdenum. Obviously, the same setup can be also used for the miniaturized Hopkinson Bar configuration.

### 3.4.3 Advanced setup for high strain-rate tests with heating and image acquisition systems

At this point it could be useful to combine the heating and the image acquisition systems for the execution of tests at high strain-rate. In particular, this becomes fundamental in the perspective to perform tensile tests varying the temperature with the miniaturized Hopkinson Bar. Indeed, as it was previously discussed, the digital image acquisition is necessary to reconstruct the specimen deformation for test at  $10^4 \text{ s}^{-1}$ . Obviously, positioning the induction coil heater between the specimen and the high speed camera, it is not possible to find any reference point on the specimen surface in order to carry out the elaboration of the images. Thus, it is clear that the unique way to perform the digital image acquisition is to modify the shape of the induction coil heater. In order to allow the optical access for the high speed camera a solenoid with a fork shape was designed (see Fig. 3.22), which is like that proposed by Davoodi [42].



*Fig. 3.22: Induction coil with fork shape.*

Obviously, with this kind of shape the efficiency of the induction heating is lower than the classical case, in which the coil heater is around the specimen. Nevertheless, increasing the power supplied by the high-frequency generator, it is possible to balance this efficiency loss. In Fig. 3.23, the details of the view through the high speed camera are shown for the standard and miniaturized specimens, while the standard Hopkinson Bar setup used to perform dynamic tensile test at different temperatures with an integrated digital image acquisition system is reported in Fig. 3.24.

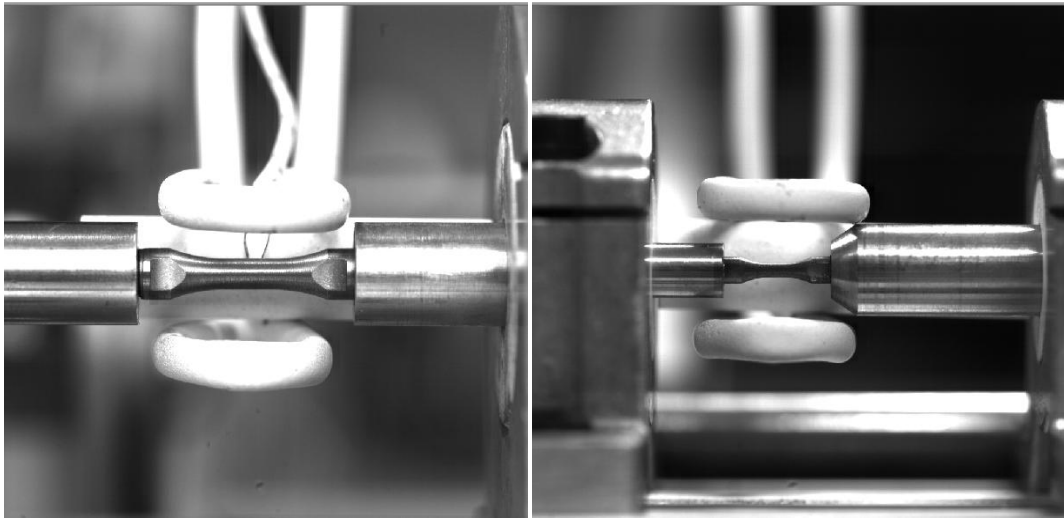


Fig. 3.23: Details of the specimen and the fork solenoid view through the camera for tensile test at  $10^3 \text{ s}^{-1}$  (left) and at  $10^4 \text{ s}^{-1}$  (right).

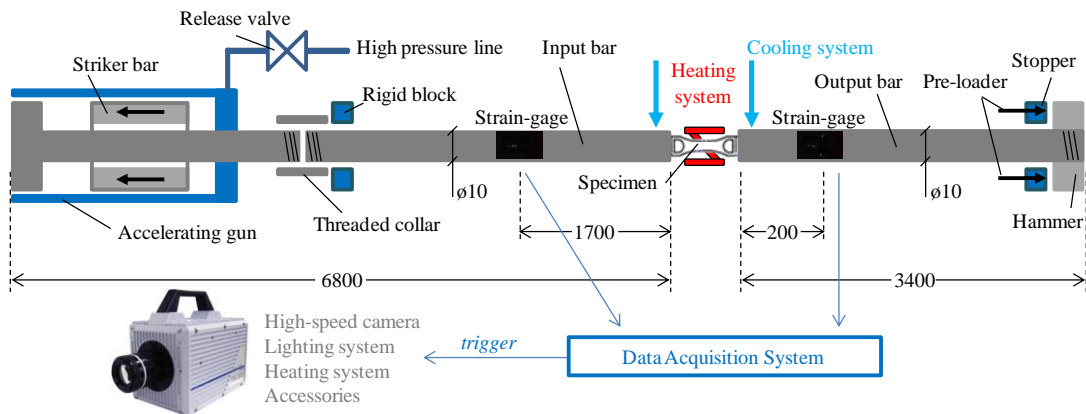


Fig. 3.24: Scheme of the Hopkinson bar setup used to perform dynamic tensile test at different temperatures with an integrated digital image acquisition system.



## 4. Data analysis

A testing campaign performed at different strain-rates and temperatures gives a copious number of information about the mechanical behaviour of the material which has to be managed with attention. The influence of the temperature and the strain-rate, or both simultaneously, on the mechanical response can be considered in different ways on the basis of which analysis approach is used.

An important aspect in the engineering field is to find the mathematical relations able to correctly describe what happens in the reality. With this aim, in this chapter, first of all the results of the experimental test campaigns performed on different materials will be shown in terms of stress-strain curves. Later, the most common strength models, implemented in the commercial FE codes and able to reproduce the dynamic behaviour of materials, will be presented. The Johnson-Cook [121] and Zerilli-Armstrong [122] material models will be considered. Particular attention will be focused on the influence of the model parameters in the reproduction of the material response. Moreover, the analytical approaches usable for the calibration of the models will be discussed and applied for the tested material.

### 4.1 Digital image processing

In the previous chapter the methods to obtain the force and displacement of the specimen were explained for the different testing equipments considered. However,

until now, the digital image analysis used to obtain the specimen elongation in high strain-rate tests was not explained.

The digital images acquired through the high-speed camera were elaborated with the software Tracker 4.8 [123]. In Fig. 4.1 an example of digital image processing performed for a test at  $10^4 \text{ s}^{-1}$  on a miniaturized sample is shown. Basically, the image was calibrated on the basis of the measurement of the diameter of the gage length and the distance between the fixing keys. The displacements of these two keys were tracked and considered to be equivalent to the displacement of the specimen heads.

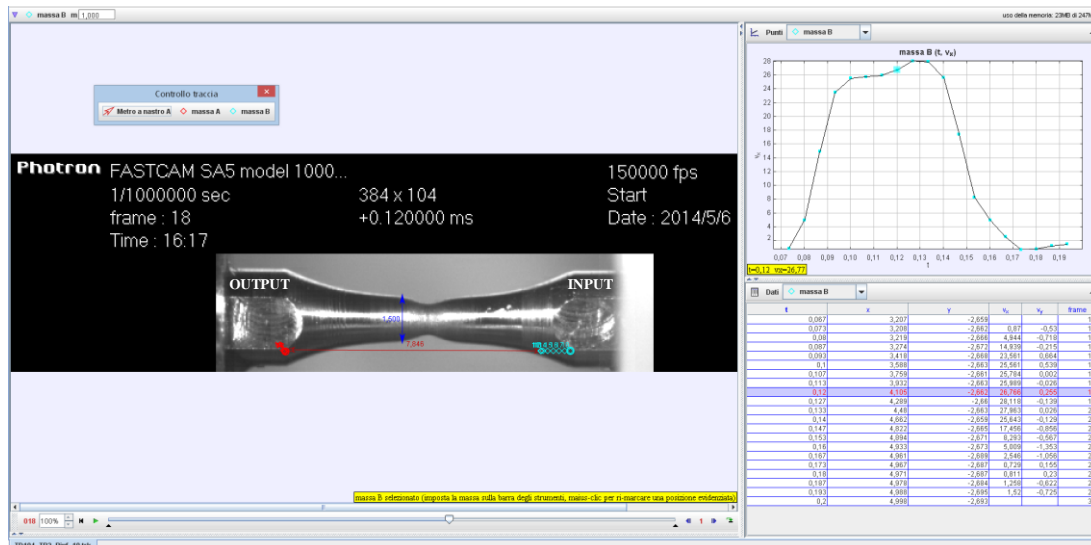


Fig. 4.1: Example of digital image processing to obtain the velocity profile.

Generally, the velocity profile (and consequently the displacement) obtained exhibits a low level of accuracy in the elastic phase due to the low level of the displacements (typical of this phase), which are complicated to appreciate with the available image resolution and time and the non-uniform illumination of the specimen. For this reason, one of the best solutions is to consider the load-displacement curve from a high value of initial load in order to eliminate the earlier part of the elastic curve. Obviously, the choice of the initial load depends from the material and the tested specimen dimension; however, it should be a fraction of the

yield force. Finally, the data extracted from the video analysis have to be resampled to obtain data with the same rate of the signals of the bars.

## 4.2 Calculation of uniaxial stress and strain

Considering uniaxial tensile test, the evaluation of the mechanical response in terms of stress and strain needs to be discussed in detail in order to avoid errors in the study of the material behaviour. On this aspect, an accurate analysis was done in [11].

In tensile test, performed in stroke control, the engineering stress-strain curve is constructed from the load-displacement measurements directly made on the specimen. The engineering stress,  $s$ , is the average longitudinal stress in the specimen, which is obtained by dividing the applied load,  $P$ , by the original area of the cross section of the specimen,  $A_s$ :

$$s = \frac{P}{A_s} \quad (4.1)$$

The engineering strain,  $e$ , is the average linear strain, which is obtained by dividing the elongation of the gage length of the specimen,  $\Delta L$ , by its original length,  $L_s$ :

$$e = \frac{\Delta L}{L_s} = \frac{L - L_s}{L_s} \quad (4.2)$$

Since both the stress and strain are obtained by dividing the load and the stroke by constant factors, the engineering stress-strain curve has the same shape as the load-displacement curve. The two curves frequently are used interchangeably.

The general shape of the engineering stress-strain curve for metals is characterized by an initial elastic region, in which the stress is linearly proportional to the strain, and a subsequent plastic region which starts when the stress exceeds a value corresponding to the yield strength. After the achievement of the yield point, the stress required to produce continued plastic deformation increases with increasing plastic strain, i.e. the metal strain hardens. The volume of the specimen remains constant during the plastic deformation:

$$A \cdot L = A_s \cdot L_s \quad (4.3)$$

and as the specimen deforms longitudinally, its cross-sectional area,  $A$ , decreases uniformly along the gage length.

Initially, despite the decrease of the specimen cross-section, the engineering stress continues to rise with increasing strain due to the strain hardening. However, at a certain instant, a point is reached where the decrease in specimen cross-sectional area becomes greater than the increase in deformation load arising from strain hardening. This condition will be reached first in the zone of the specimen that is slightly weaker than the rest. All further plastic deformation is concentrated in this region (the specimen necking). When the strain localization takes place and the cross-sectional area starts to decrease rapidly, the actual load required to deform the specimen falls off and the engineering stress, defined in the Eq. 4.1, continues to decrease until fracture occurs.

The engineering stress-strain curve does not give a true indication of the deformation characteristics of a metal, because it is based entirely on the original dimensions of the specimen, while these dimensions change continuously during the test. The engineering stress is an average stress based on the original cross-section area, therefore it does not take into account the diameter reduction, and this produces conservative stress estimation and the fall down in the engineering stress-strain curve over the point of maximum load. Instead, it is known that the material continues to strain harden to fracture, therefore the necessary stress to produce further

deformation should also increase. Considering the actual cross-sectional area of the specimen and the actual strain measurement, the curve that is obtained increases continuously and it is known as true stress-true strain curve. This is also known as a flow curve, because it represents the basic plastic-flow characteristics of the material.

Assuming that the material volume remains constant during the deformation, for tensile test the Eq. 4.3 can be rewrite in this way:

$$\frac{A_s}{A} = \frac{L}{L_s} = \frac{\Delta L + L_s}{L_s} = \frac{\Delta L}{L_s} + 1 = (1 + e) \quad (4.4)$$

Since the true stress,  $\sigma$ , is the stress determined by the instantaneous load,  $P$ , acting on the instantaneous cross-sectional area,  $A$ , it is related to engineering stress through this relation:

$$\sigma = \frac{P}{A} = \frac{P}{A} \cdot \frac{A_s}{A_s} = \frac{P}{A_s} \cdot \frac{A_s}{A} = \frac{P}{A_s} \cdot (1 + e) = s \cdot (1 + e) \quad (4.5)$$

The derivation of Eq. 4.5 assumes both constancy of volume and a homogeneous distribution of strain along the gage length of the tensile specimen. Thus, it should be used only until the onset of necking. Beyond the maximum load, the true stress should be determined from actual measurements cross-sectional area, which is not uniformly distributed.

Instead, the true strain,  $\varepsilon$ , is the instantaneous specimen elongation,  $dL$ , divided by the actual gage length of the specimen:

$$\varepsilon = \int \frac{dL}{L} = \ln\left(\frac{L}{L_s}\right) = \ln\left(\frac{\Delta L + L_s}{L_s}\right) = \ln\left(\frac{L_s}{L_s} + \frac{\Delta L}{L_s}\right) = \ln(1 + e) \quad (4.6)$$

Also in this case, this equation is applicable only to the onset of necking for the same reasons discussed previously.

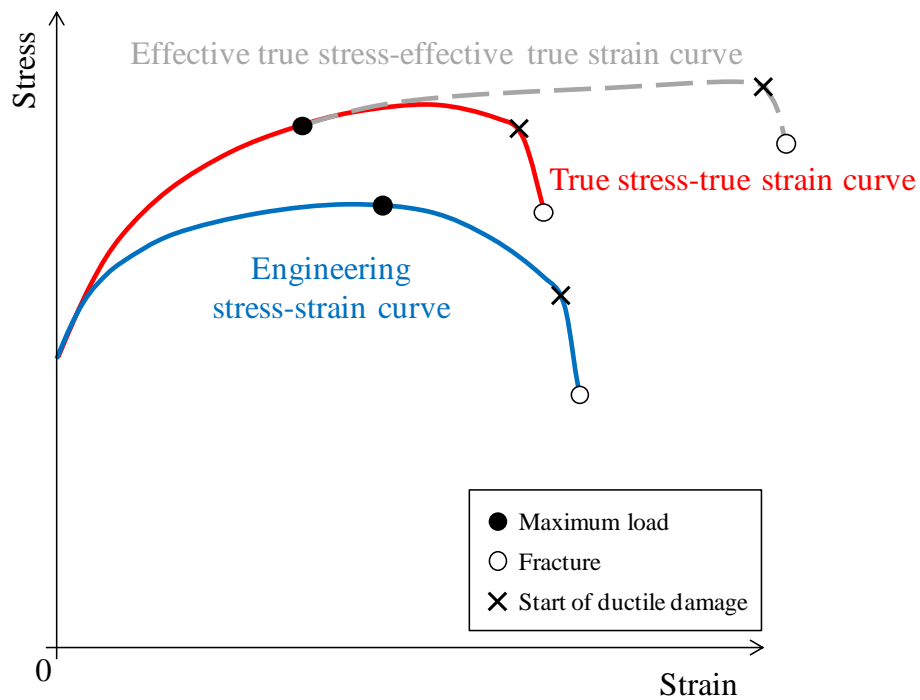


Fig. 4.2: Qualitative comparison between: engineering, true and effective stress vs. strain curves.

In Fig. 4.2 a qualitative comparison between the engineering, true and effective stress-strain curves is shown. First of all, it is important to underline that considering relatively large plastic strains, the elastic region is neglected. In accordance with Eqs. 4.5 and 4.6 the true stress-true strain curve is to the left of the engineering one. As said before, beyond the maximum load, the high localized strains in the necking region far exceed the strains calculated from Eqs. 4.2 and 4.6, and also the true stress-true strain curve is not more representative of the real material behaviour. The effective true stress vs. effective true strain curve could be obtained only considering the actual specimen length (or area) beyond the onset of the necking. However, the formation of a necking region or mild notch introduces triaxial stresses that make difficult to determine accurately the longitudinal tensile stress from the onset of necking until fracture occurs. All what happens beyond the maximum load represents the instability in tension of the material, which will be further discussed in the next

chapter. Instead, just before fracture, ductile materials are subjected to significant damage due to formation of small cavities and their coalescence. These mechanisms lead to rapid decreasing of the material strength which should be studied through appropriate relations.

On the basis of what said above, in the next sections the tensile true stress-true strain curves were calculated for some materials tested at different strain-rates and temperatures.

#### 4.2.1 Experimental results for high chromium T91 steel

An experimental testing campaign was performed for the high chromium ferritic/martensitic T91 steel (9% Cr, 1% Mo). This kind of material shows high radiation damage and swelling tolerance as well as good resistance to high temperature creep and corrosion [124]. For these reasons, it is widely used in the nuclear reactor sector. In this work, the interest to study the mechanical behaviour of T91 at high strain-rates and temperatures comes from to better understand the material resistance during cold welding, which is a technique used for cladding characterized by high velocity impacts [125-127].

The results of the tensile experimental tests are shown in Fig. 4.3. For each loading condition, at least two tests were performed in order to evaluate the repeatability of the results. The true stress vs. true strain curves are reported in function of temperature (from 25 °C up to 800 °C) and strain-rate (from  $10^{-3}$  up to  $10^4$  s<sup>-1</sup>). The levels of strain-rate shown in the figures mean the nominal values of the tests.

Observing the curves, the material is both strain-rate and temperature sensitive. By varying the strain-rate, the material strength increases due to the dynamic hardening. The initial oscillations observed in high strain-rate tests are not related to a material behaviour (yielding), but are typical signal aberrations in Hopkinson Bar tensile tests [79]. As discussed in the section 3.2.2, it is possible to control the source of error, such as misalignment, initial clearance, etc.; nevertheless, in miniaturized

setup  $10^4 \text{ s}^{-1}$ , the problem is amplified (higher level of acceleration) and more difficult to control. Two curves are labelled as  $10^{-3} \text{ s}^{-1}$ : one refers to the results obtained from the specimen with  $D=3 \text{ mm}$  and  $L=5 \text{ mm}$  (solid line), the other one refers to the results obtained from the specimen with  $D=1.5 \text{ mm}$  and  $L=1.5 \text{ mm}$  (dashed line). Comparing the quasi-static data obtained from the two geometries, it appeared evident that they produce the same results until necking starts. After this, the stress versus strain is strongly dependent on the geometry and the results differ. Moreover, the material strength gradually decreases with increasing the temperature and the shape of the stress-strain curve dramatically changes at  $800 \text{ }^\circ\text{C}$ , where the material behaves like a perfectly plastic material. The strain at failure increases with strain-rate and temperature.

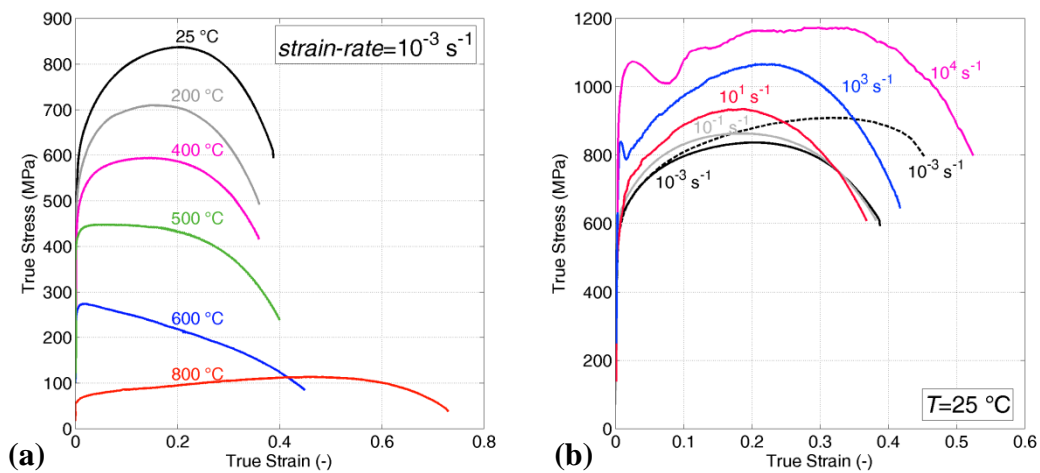


Fig. 4.3: Experimental results in terms of tensile true stress vs. true strain for high chromium ferritic/martensitic T91 steel: (a) varying the temperature at strain-rate  $10^{-3} \text{ s}^{-1}$ ; (b) varying the strain-rate at room temperature.

The high strain-rate tests were recorded using a high speed camera. The images show a long time in which the phase of necking occurs during the test. Moreover, also in high dynamic loading condition, the necking area was localized in the middle of the specimen, which reached an equilibrium status during the dynamic test and the deformed shape was comparable with that of a quasi-static test.

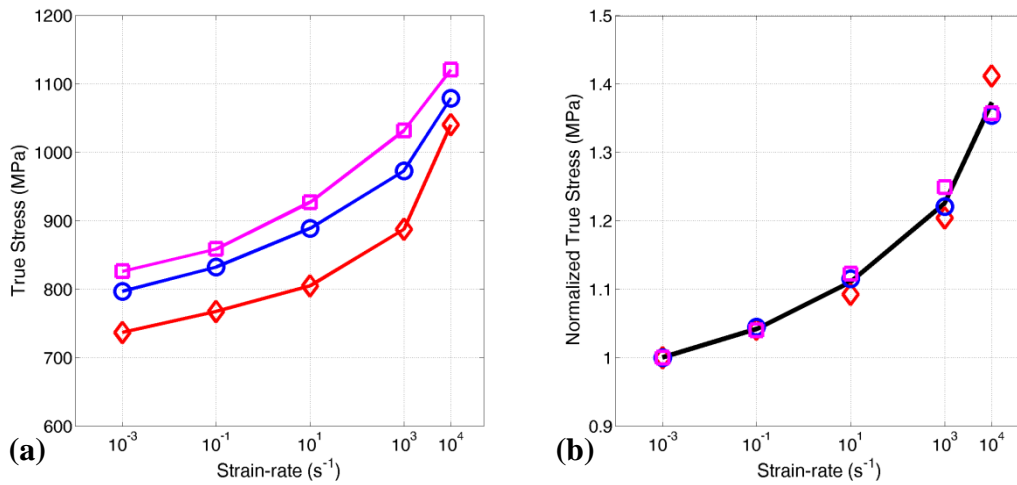


Fig. 4.4: Strain-rate sensitivity for high chromium ferritic/martensitic T91 steel at room temperature ( $T=25\text{ }^{\circ}\text{C}$ ) regime in terms of: (a) true stress vs. strain-rate and (b) normalized true stress vs. strain-rate ( $\diamond$ : 5%,  $\circ$ : 10% and  $\square$ : 15% of true strain; semi-logarithmic diagrams).

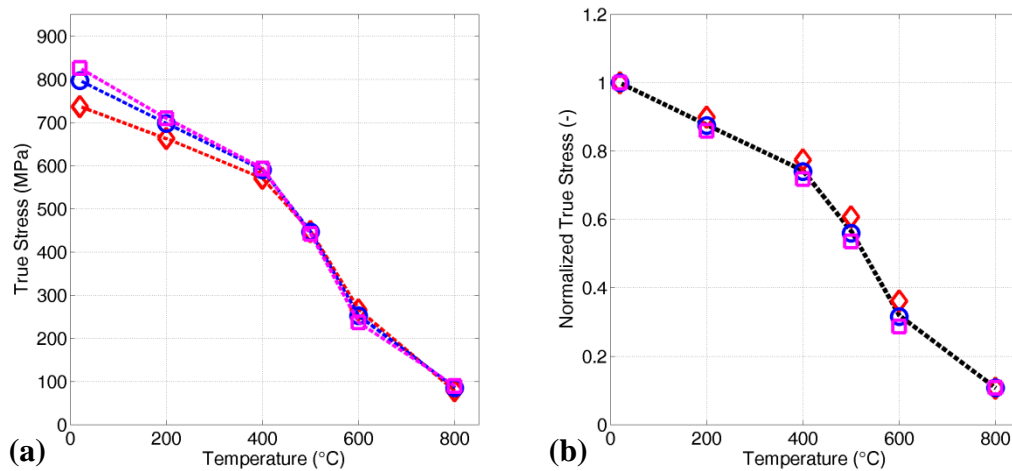


Fig. 4.5: Temperature sensitivity for high chromium ferritic/martensitic T91 steel in quasi-static ( $10^{-3}\text{ s}^{-1}$ ) regime in terms of: (a) true stress vs. temperature and (b) normalized true stress vs. temperature ( $\diamond$ : 5%,  $\circ$ : 10% and  $\square$ : 15% of true strain).

A more deep analysis on the strain-rate and temperature sensitivity of the material can be done showing the tendencies of true stresses as a function of strain-rate and temperature at fixed values of strain. These curves are reported in Fig. 4.4a and 4.5a at strains before the onset of the necking: 5, 10 and 15%. The same analysis was also

performed in terms of normalized true stress, as reported in Fig. 4.4b and 4.5b. The normalized stresses were obtained dividing each stress value at a fixed strain (5, 10 or 15%) by the correspondent value of stress at room temperature (25 °C) and in quasi-static condition ( $10^{-3} \text{ s}^{-1}$ ). This allows to directly compare the variation of the sensitivity at different values of strain starting from the same initial condition. For each strain-rate and temperature investigated, the average values of the normalized true stresses were calculated in order to appreciate the global strain-rate and temperature sensitivities of the material (black lines). These last figures confirm the strain-rate and temperature sensitivity of this material and, furthermore, it is essentially the same up to 15% of true strain.

## 4.2.2 Experimental results for Glidcop Al-15

Another testing campaign was performed for the mechanical characterization of Glidcop Al-15, a copper-based composite reinforced with alumina dispersion. In more detail, it is a composite material with metal matrix in copper strengthened with aluminium oxide particles. This composite is known by the trade name Glidcop<sup>®</sup>, which is available in several grades, depending on the weight percentage of alumina content: in this work, the Glidcop Al-15 (0.3 wt.%) was used. Thanks to the addition of ceramic particles, the good mechanical properties of the matrix are retained also at high temperatures and the resistance to the thermal softening is increased. In fact, the presence of the aluminium oxide particles in the copper matrix blocks the dislocation movement, preventing the grain growth [128]. Moreover, Glidcop<sup>®</sup> exhibits high resistance to radiation damage. Thanks to these properties, this material finds several applications in particle accelerator technologies, where problems of thermal management, combined with structural requirements, play a key role. Currently, for example, it is used for the construction of structural and functional parts of the collimation system of the Large Hadron Collider (LHC) at CERN (Geneva) [129]. Since the extreme condition in which the material could operate, it is interesting to investigate its response in a wide range both in strain-rate and temperature. As a

matter of fact, due to the interaction between the material and the high energy particle beam, the operating conditions could be characterized by high temperature, high strain-rate, or both of them [130].

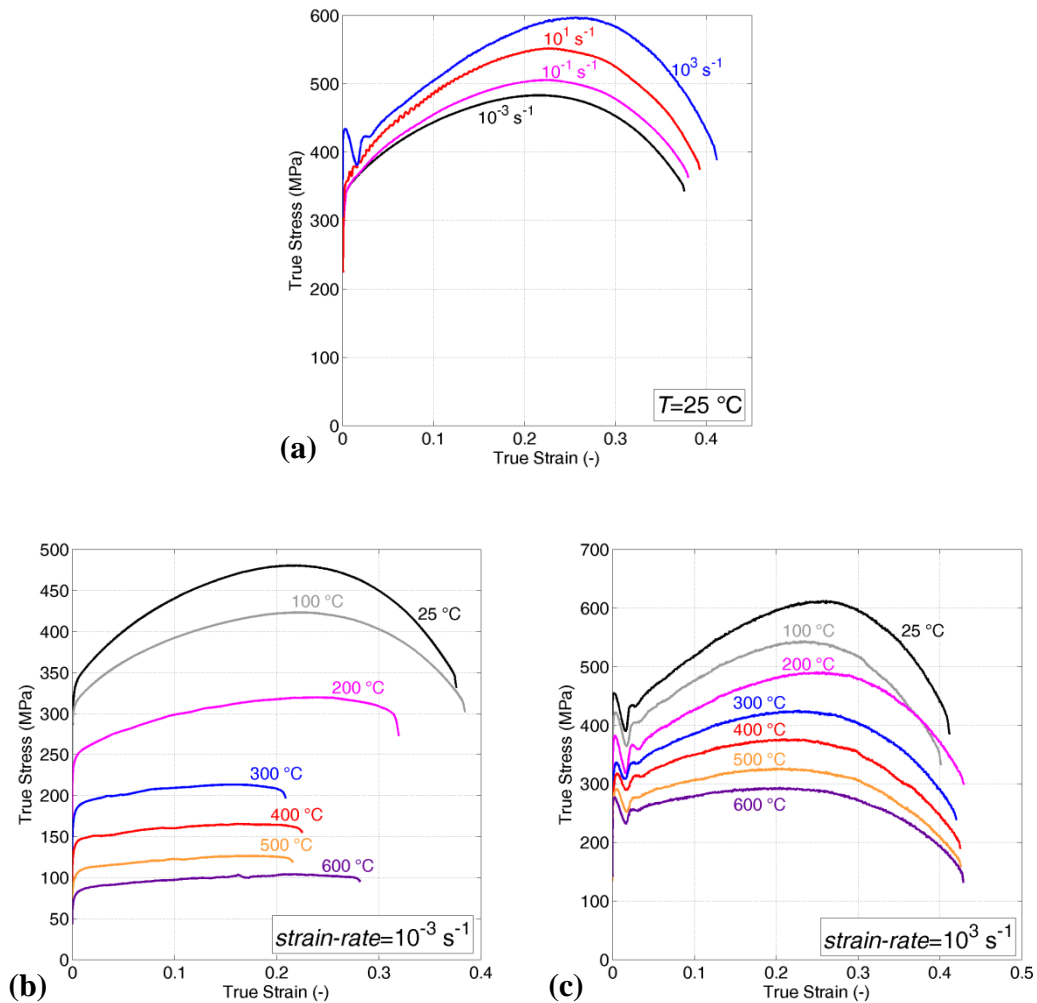


Fig. 4.6: Experimental results in terms of tensile true stress vs. true strain for Glidcop Al-15: (a) at room temperature varying the strain-rate, (b) at quasi-static loading conditions varying the temperature and (c) at high strain-rate loading conditions varying the temperature.

In Fig. 4.6 the experimental results are reported for tests at different strain-rates (a) and for tests at different temperatures in quasi-static (b) and dynamic (c) conditions, in terms of true stress versus true strain. For each testing condition at

least three repetitions were performed, but for sake of clarity, in the diagrams only the average results are shown (the maximum standard deviation is 3%). Also in this case, the small geometry of the specimen (low ratio between gage length and diameter) affects the results and their interpretation as the necking phase is a considerable part of the entire test duration.

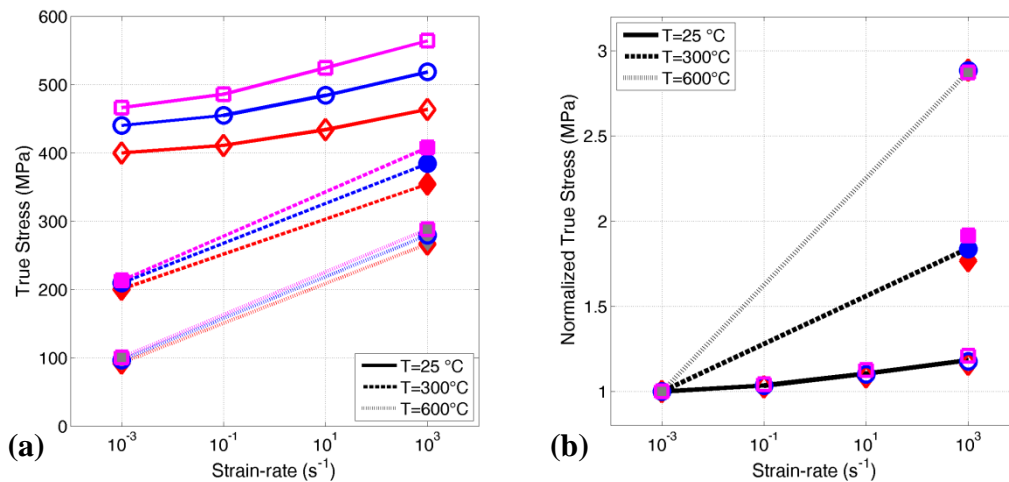


Fig. 4.7: Strain-rate sensitivity for Glidcop Al-15 at different temperatures (25, 300, 600 °C), in terms of: (a) true stress vs. strain-rate and (b) normalized true stress vs. strain-rate (◇: 5%, ○: 10% and □: 15% of true strain; semi-logarithmic diagrams).

The experimental results show that the material is strain-rate dependent, with an increment in the strength and also in the strain at failure with the strain-rate. This is also confirmed by the analysis of the strain-rate sensitivity performed at different values of temperature (25, 300 and 600 °C), Fig. 4.7a, and different levels of true strain before the onset of the necking: 5, 10 and 15%. The same diagram was obtained considering the normalized true stress, Fig. 4.7b, in which the normalized stresses were obtained dividing each stress value at a fixed strain (5, 10 or 15%) by the correspondent value of stress in quasi-static condition (10<sup>-3</sup> s<sup>-1</sup>) and at the same temperature (25, 300 or 600 °C). This allows to directly compare tests performed in different temperature conditions. Observing the Fig. 4.7b, the material show a good agreement of the strain-rate sensitivity at different strains (the values are very close

at equal strain-rate and temperature condition), but, at the same time, the dependency from the strain-rate is clearly influenced by the temperature. At room temperature the material exhibits lower strain-rate sensitivity than at 300 or 600 °C (at 600 °C the stress is almost three-times higher than 25 °C).

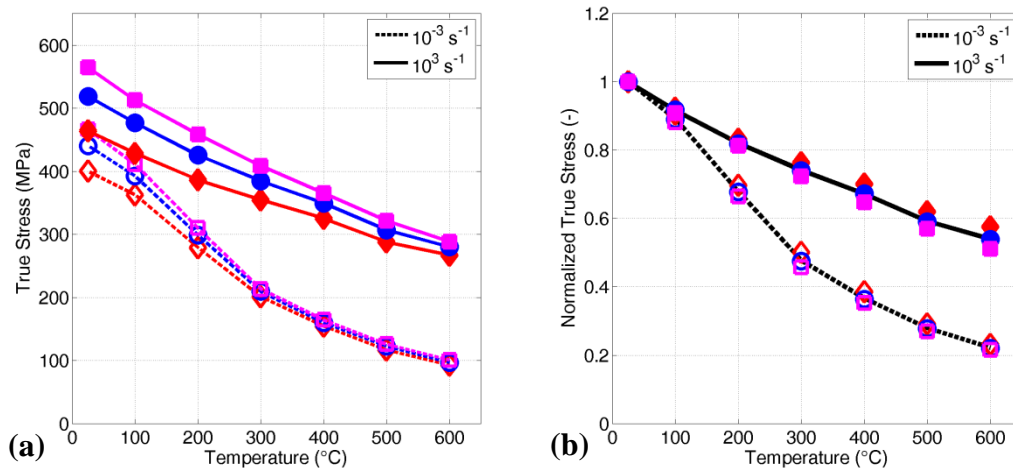


Fig. 4.8: Temperature sensitivity for Glidcop Al-15 in quasi-static ( $10^{-3} \text{ s}^{-1}$ ) and dynamic ( $10^3 \text{ s}^{-1}$ ) regimes in terms of: (a) true stress vs. temperature and (b) normalized true stress vs. temperature ( $\diamond$ : 5%,  $\circ$ : 10% and  $\square$ : 15% of true strain).

Similarly, the analysis of the temperature sensitivity was performed both at quasi-static and high strain-rates for the same levels of true strain considered before. In Fig. 4.8a, the results are reported for the two levels of strain-rate ( $10^{-3}$  and  $10^3 \text{ s}^{-1}$ ), from which it is possible to conclude that the decrement in strength is quite gradual increasing the temperature, both in static and dynamic regime.

The same analysis was also performed in terms of normalized true stress versus temperature, as reported in Fig. 4.8b. The normalized stresses were obtained dividing each stress value at a fixed strain (5, 10 or 15%) by the correspondent value of stress at room temperature (25 °C) and at the same strain-rate ( $10^{-3} \text{ s}^{-1}$  for the quasi-static data or  $10^3 \text{ s}^{-1}$  for the dynamic ones). This allows to directly compare tests performed in different loading conditions. Observing the normalized stresses, the material exhibits a different behaviour passing from static to dynamic condition: for high strain-rate tests, the growing in temperature produces a minor loss of the material

strength, i.e. the thermal softening effect is reduced. This material behaviour justifies the need to investigate the temperature influence also at different strain-rates in addition to the quasi-static case.

### 4.2.3 Experimental results for heavy sintered molybdenum

The introduction in recent years of new, extremely energetic, particle accelerators, such as the Large Hadron Collider (LHC), required the development of advanced methods to predict the behaviour of machine components which can directly interact with the high energy particle beam. These components have to be designed to operate in harsh radioactive environment highly solicited from thermo-structural point of view. This context gives impulse to the development and testing of refractory metals and alloys based on refractory materials such as molybdenum and tungsten. The molybdenum can fulfil the features need for application in the particle accelerators because it is characterized by: high melting point (about 2600 °C), high strength at elevated temperatures, low thermal expansion, high thermal conductivity, low heat capacity and high corrosion resistance [131]. Due to the great interest around this class of metals, the last material considered in this work is the heavy sintered molybdenum, produced by AT&M. AT&M produces this metal through a powder metallurgy process, in which fine-grained molybdenum powders of high purity are pressed, sintered, hot worked and annealed to obtain a regular grain structure. Also in this case, the tensile tests were carried out at different strain-rates and temperatures and the results in terms of true stress vs. true strain are shown in Fig. 4.9.

First of all, it is important to highlight that the investigated material exhibits a brittle behaviour at high strain-rates at room temperature. Tests with the Hopkinson Bar in these loading conditions were almost impossible to perform and many fractures occurred in the threaded ends of the specimen. In few tests the fracture taken place in the specimen gage length, but due to low elongation, the whole test occurs during the rise of the stress pulse with a low accuracy level in the data

analysis. This justifies the missing data at high strain-rates at room temperature. However, just starting from the temperature of 100 °C, it is possible to test this material also in dynamic conditions (see Fig. 4.9c). Observing the curves at room temperature varying the strain-rate, Fig. 4.9a, there is a dramatically changing of the material response at  $10\text{ s}^{-1}$ , probably due to thermal softening effect. The material shows strain-rate sensitivity as well as a temperature dependency both quasi-static and dynamic conditions.

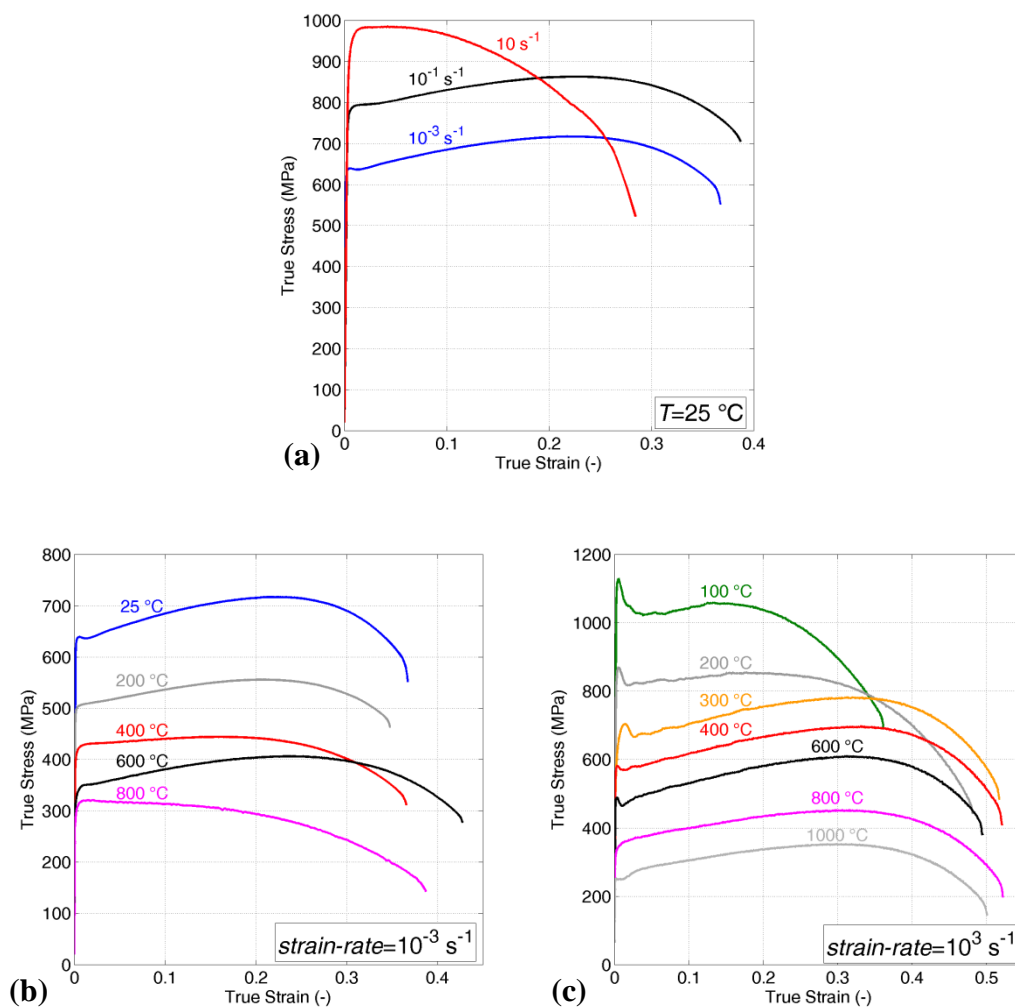


Fig. 4.9: Experimental results in terms of tensile true stress vs. true strain for heavy sintered molybdenum: (a) at room temperature varying the strain-rate, (b) at quasi-static loading conditions varying the temperature and (c) at high strain-rate loading conditions varying the temperature.

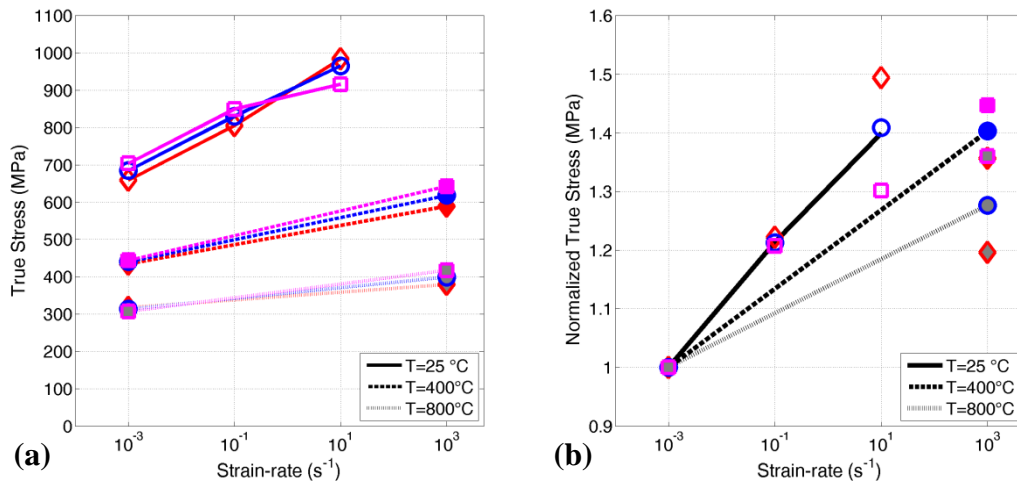


Fig. 4.10: Strain-rate sensitivity for heavy sintered molybdenum at different temperatures (25, 400, 800 °C), in terms of: (a) true stress vs. strain-rate and (b) normalized true stress vs. strain-rate ( $\diamond$ : 5%,  $\circ$ : 10% and  $\square$ : 15% of true strain; semi-logarithmic diagrams).

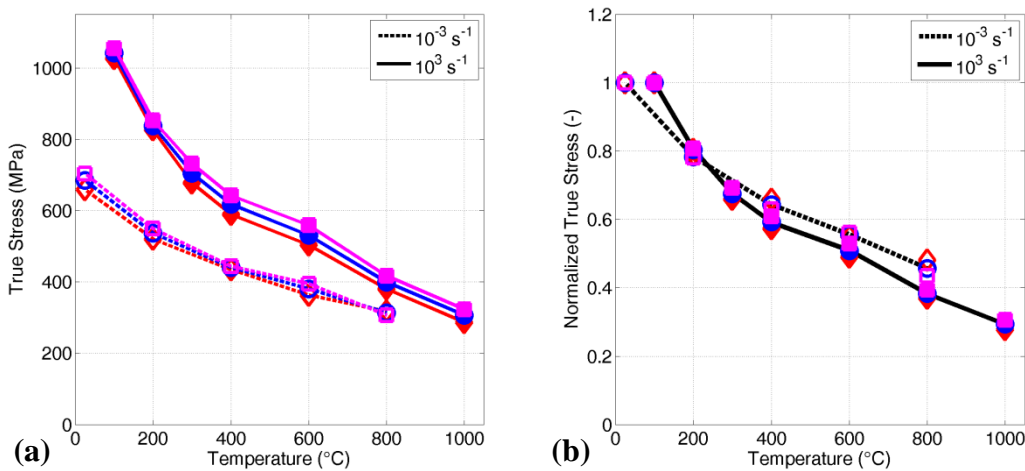


Fig. 4.11: Temperature sensitivity for heavy sintered molybdenum in quasi-static ( $10^{-3} s^{-1}$ ) and dynamic ( $10^3 s^{-1}$ ) regime in terms of: (a) true stress vs. temperature and (b) normalized true stress vs. temperature ( $\diamond$ : 5%,  $\circ$ : 10% and  $\square$ : 15% of true strain).

The influence of the temperature and the strain-rate on the material strength was analyzed in the same way of Glidcop Al-15, but in this case the reference true stress used to calculate the normalized values at  $10^3 s^{-1}$  was that which obtained at 100 °C

at the corresponding strains (Fig. 4.10b and 4.11b). Differently from Glidcop Al-15, for this material there are not significant differences in the strain-rate and temperature sensitivities passing from the quasi-static to dynamic conditions.

#### 4.2.4 Materials comparison

The different strain-rate and temperature sensitivities of the materials considered in this work are compared in Fig. 4.12. For the sake of clarity in the diagrams, only the average values of the normalized stresses at 5, 10 and 15% of true strain are reported for each loading condition.

The material with the BCC (Body-Centered Cubic) crystal lattice, i.e. the molybdenum, shows higher strain-rate sensitivity than Glidcop and T91 steel, which have FCC (Face-Centered Cubic) and BCT (Body-Centered Tetragonal) structures, respectively. This tendency, i.e. the higher strain-rate sensitivity of BCC materials with respect to the FCC materials, was observed also in the scientific literature [132-134]. For what concern the T91 steel, the BCT unit cell reveals that it has a close resemblance of a FCC diamond structure. Indeed, in addition to the one atom at the centre and eight atoms at the corners of the unit cell, there are four other atoms on four different faces. Therefore, a BCT unit cell contains four atoms with each atom having four nearest neighbours and it can be interpreted as a distorted diamond cubic structure. For this reason, the similarity between the strain-rate sensitivity in BCT and FCC metals is not unreasonable [135,136].

In order to directly compare the temperature sensitivities of three materials, it is necessary to show the normalized true stress values as function of the homologous temperature,  $T/T_m$ . In this way the different temperature dependencies are proportioned to the melting temperature of the materials. The molybdenum shows high temperature sensitivity, both in static and dynamic conditions. Instead, Glidcop is affected by the temperature likes molybdenum in static condition, while the temperature sensitivity is significantly reduced at high strain-rate, which represents a positive aspect in terms of material strength.

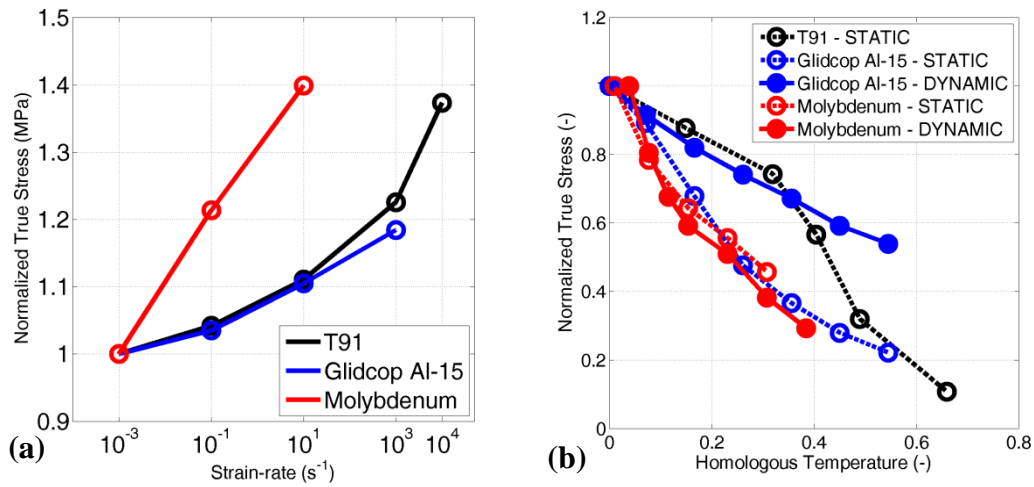


Fig. 4.12: Comparison of the strain-rate and temperature sensitivities for T91 steel, Glidcop Al-15 and heavy sintered molybdenum in terms of: (a) normalized true stress vs. strain-rate at room temperature (25 °C) and normalized true stress vs. homologous temperature in quasi-static ( $10^{-3} \text{ s}^{-1}$ ) and dynamic ( $10^3 \text{ s}^{-1}$ ) regimes.

### 4.3 Material models

During the last decades several material models were proposed with the aim to reproduce the mechanical response of the materials varying the strain-rate and the temperature [137,138]. In the following the two most common strength models implemented in the commercial FE codes will be described: Johnson-Cook and Zerilli-Armstrong models.

#### 4.3.1 Johnson-Cook model

The Johnson-Cook model (J-C) [121] is a purely empirical model and it is one of the most widely used. First of all, it is important to specify that the empirical models have not any physical basis. Thanks to the simple relation proposed by Johnson and Cook, this material model is implemented in many commercial FE codes and it is quite easy to find the parameters for different materials. Despite the many

simplifications of this model (discussed in the following), it is particularly appreciated for its simplicity to obtain the model parameters.

This model keeps into account strain-rate and temperature material sensitivities and for this reason it is used in problems such as machining processes, automotive crashworthiness, explosions, impacts. In the J-C model only the athermal stress component is considered and the flow stress,  $\sigma$ , is described by the following analytical relation:

$$\sigma = \left( A + B \cdot \varepsilon_{pl}^n \right) \cdot \left( 1 + C \cdot \ln \frac{\dot{\varepsilon}_{pl}}{\dot{\varepsilon}_0} \right) \cdot \left[ 1 - \left( \frac{T - T_r}{T_m - T_r} \right)^m \right] \quad (4.7)$$

where  $A$  represents the elastic limit,  $B$  and  $n$  are the work hardening parameters,  $C$  is the strain-rate sensitivity coefficient and  $\dot{\varepsilon}_0$  is the strain-rate threshold, that in the original formulation is set equal to 1. For what concerns the thermal effects:  $m$  is the thermal softening coefficient,  $T_r$  is the reference temperature at which no thermal effects are considered and  $T_m$  is the melting temperature at which the mechanical strength goes to zero. The actual plastic strain, strain-rate and temperature are respectively  $\varepsilon_{pl}$ ,  $\dot{\varepsilon}_{pl}$  and  $T$ . In more detail, the work hardening parameters influence the slope of the flow stress in the plastic domain. When  $n$  is equal to 0 means a perfect plastic model, instead if equal to 1, there is linear dependency in the plastic domain. The coefficient  $m$  determines the concavity of the temperature function ( $m < 1$  convex,  $m > 1$  concave,  $m = 1$  linear dependency). In the LS-DYNA FE code [139], although the implemented formulation is exactly the same of Eq. 4.7, there is a difference in the interpretation of the parameter  $\dot{\varepsilon}_0$ . Indeed, it is interpreted as the highest strain-rate for which the strain-rate effects on the flow stress are negligible. Consequently, for strain-rate lower of this value, there are not any strain-rate influences.

The J-C model is a multiplicative model, in which the effects of plastic strain, strain-rate and temperature are uncoupled. In Fig. 4.13, true stress vs. true plastic

strain curves at different strain-rates and temperatures are shown for the Armco Iron in according to J-C model [121]. It is possible to note that the work hardening rate grows up with the increasing of strain-rate despite this is in contradiction with most of metal experimental data that can be found in literature [140-142]. Normally, at high strain-rate it can be observed a decreasing of work hardening rate, defined as  $\vartheta = \partial\sigma/\partial\varepsilon$ , which represents the slope of the true stress vs. true plastic strain curve. The work hardening rate is a representative material property which is strongly related to the instability condition of material model in uniform tensile loading condition. On the other hand, for this model the work hardening rate decrease when the temperature grows up, which is in totally agreement with literature experimental data [143] and the experimental results previously shown.

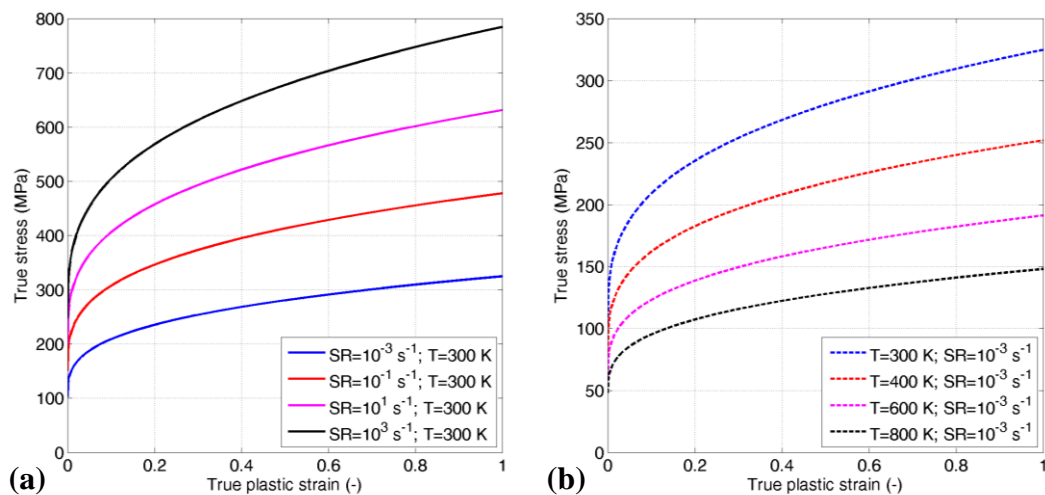


Fig. 4.13: (a) True stress vs. true plastic strain curves of J-C model for the Armco Iron [121] at different strain-rates and constant temperature,  $T=300\text{ K}$ , and (b) at different temperatures and constant strain-rate,  $\dot{\varepsilon} = 10^{-3}\text{ s}^{-1}$ .

It is clear that due to the multiplicative nature of the model, the strain-rate and temperature variation implies the scaling of the flow stress. Moreover, in the J-C model there are other simplifications such as: the influence of pressure and changes in volume are neglected, the melting temperature is kept constant, there are not considerations about the influence of the crystal lattice on the material strength and

the variation of the strain-rate and thermal sensitivities as function of the strain as well as the coupled effect of strain-rate and temperature on the material response are not considered. In order to put in evidence this last aspect, in Fig. 4.14, the comparison between the response under isothermal and adiabatic hypothesis for Armco Iron at  $10^3 \text{ s}^{-1}$  is reported.

With the J-C expression the isothermal case can be easily reproduced considering a constant material temperature ( $T$ ). Instead, in order to reproduce the adiabatic case, it is necessary to reconstruct the increase of the temperature using the Taylor-Quinney relation (Eq. 2.1,  $\beta=1$ ). Observing the Fig. 4.14a, the curve which corresponds to the adiabatic hypothesis is lower than isothermal one, representing correctly the effect of the thermal softening phenomena on the flow stress. For very bad conductor materials or at high strain-rate, the thermal softening could be so intense that the slope of the curve could become negative.

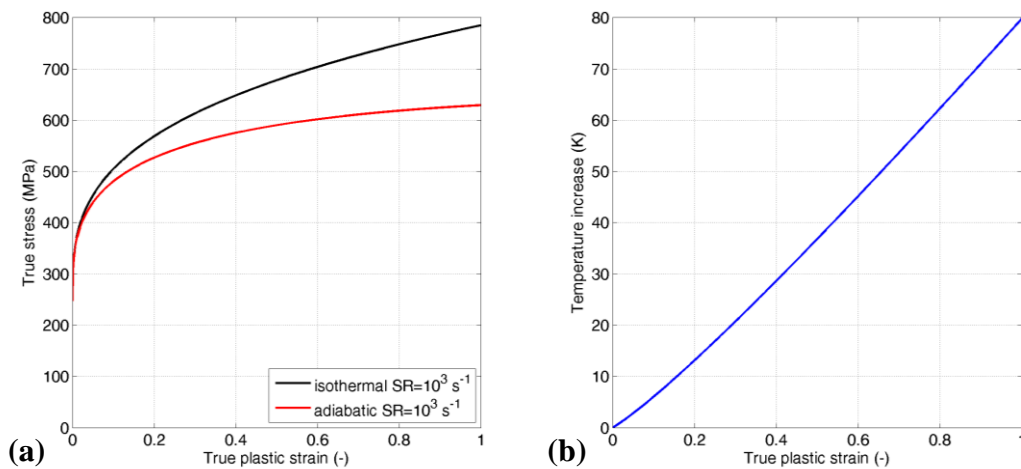


Fig. 4.14: (a) Comparison of true stress vs. true plastic strain curves of J-C model for the Armco Iron [121] with isothermal and adiabatic hypothesis; (b) the temperature increase, under adiabatic hypothesis, in according to Taylor-Quinney relation [6].

### 4.3.2 Zerilli-Armstrong model

The formulation proposed by Zerilli and Armstrong (Z-A) [132] is a typical example of semi-empirical model. Indeed, the Z-A model is obtained on the basis of the mechanical dislocation theory and defines different formulations for Body-Centred-Cubic (BCC) and Face-Centred-Cubic (FCC) materials. Even if this model takes into account the thermal activation, the Z-A relationship is very simplified with respect to dislocation theory equations and this characteristic allows to this model to be widely implemented in the commercial FE codes.

The constitutive equations are the following:

$$\sigma = \Delta\sigma_G + B \cdot e^{(-\beta_0 + \beta_1 \cdot \ln \dot{\varepsilon})T} + K_0 \cdot \varepsilon_{pl}^n + \frac{k_\varepsilon}{\sqrt{l}} \quad (\text{BCC}) \quad (4.8)$$

$$\sigma = \Delta\sigma_G + B \cdot \sqrt{\varepsilon_{pl}} \cdot e^{(-\beta_0 + \beta_1 \cdot \ln \dot{\varepsilon})T} + \frac{k_\varepsilon}{\sqrt{l}} \quad (\text{FCC}) \quad (4.9)$$

where  $l$  is the average grain size,  $\Delta\sigma_G$ ,  $k_\varepsilon$ ,  $B$ ,  $\beta_0$ ,  $\beta_1$ ,  $K_0$  and  $n$  are experimental constants related based on a dislocation mechanics analysis of the plastic deformation mechanisms and  $\varepsilon_{pl}$ ,  $\dot{\varepsilon}$  and  $T$  are the instantaneous plastic strain, strain-rate and absolute temperature, respectively [122]. Splitting the flow stress in the thermal and athermal components, it is possible to simplify as:

$$\sigma = \sigma_{ath} + B \cdot e^{(-\beta_0 + \beta_1 \cdot \ln \dot{\varepsilon})T} \quad (\text{BCC}) \quad (4.10)$$

$$\sigma = \sigma_{ath} + B \cdot \sqrt{\varepsilon_{pl}} \cdot e^{(-\beta_0 + \beta_1 \cdot \ln \dot{\varepsilon})T} \quad (\text{FCC}) \quad (4.11)$$

It is evident that in this model the effects of temperature and strain-rate on the flow stress are evaluated adding a certain quantity to the athermal component. This is greatly different respects to the J-C model, where all curves are scaled with respects of the reference static curve, simply multiplying for a parameter. In order to better understand this aspect, in Fig. 4.15 and 4.16, the true stress vs. true plastic strain

curves varying the strain-rates and temperatures are shown for the Armco Iron (BCC material) and for the pure copper (FCC materials) [132].

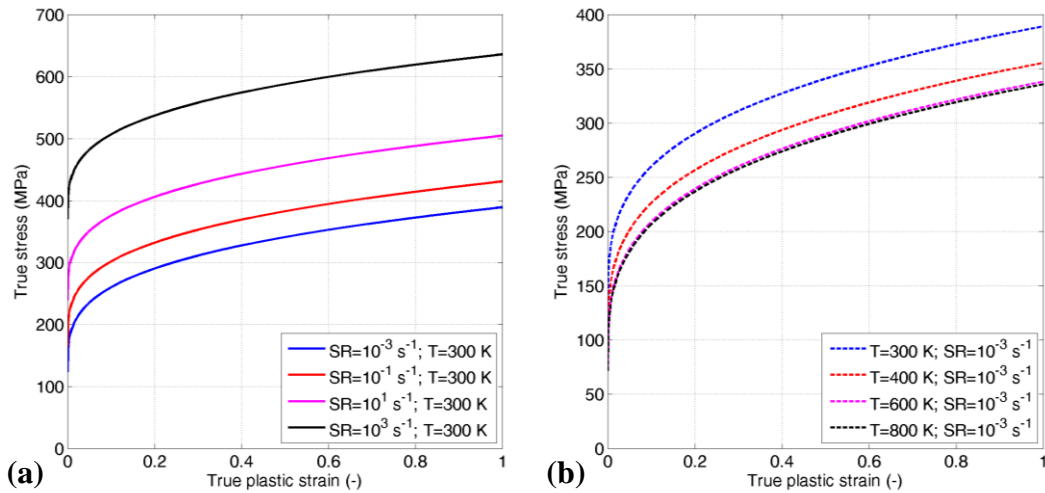


Fig. 4.15: True stress vs. true plastic strain curves of Z-A model for Armco Iron (BCC material) [132] at (a) different strain-rates and constant temperature,  $T=300\text{ K}$ , and (b) different temperatures and constant strain-rate,  $\dot{\epsilon}=10^{-3}\text{ s}^{-1}$ .

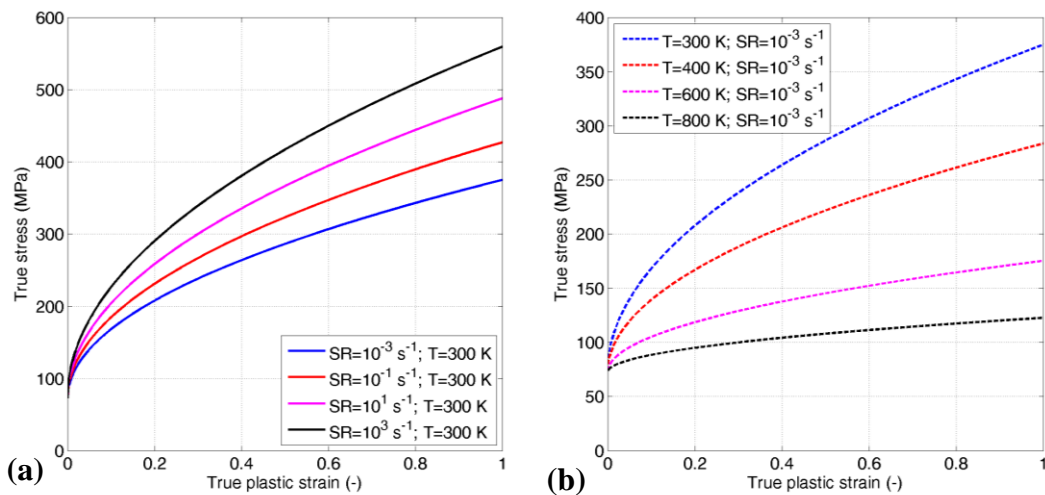


Fig. 4.16: True stress vs. true plastic strain curves of Z-A model for copper (FCC material) [132] at (a) different strain-rates and constant temperature,  $T=300\text{ K}$ , and (b) at different temperatures and constant strain-rate,  $\dot{\epsilon}=10^{-3}\text{ s}^{-1}$ .

Just observing the Eq. 4.8 and 4.9, it is possible to appreciate some differences between the two formulations. In the case of FCC equation, the thermal component directly depends by plastic strain, but this does not happen for the athermal part, while in the BCC formulation is exactly the opposite. The consequence is that for FCC materials all curves have a fixed yield stress ( $\varepsilon_{pl}=0$ ), for any temperature and strain-rate variations, while for the BCC materials the yield stress can change. Thanks to the distinction between BCC and FCC materials, the Z-A model can find a good correlation with many commonly used metals [144,145].

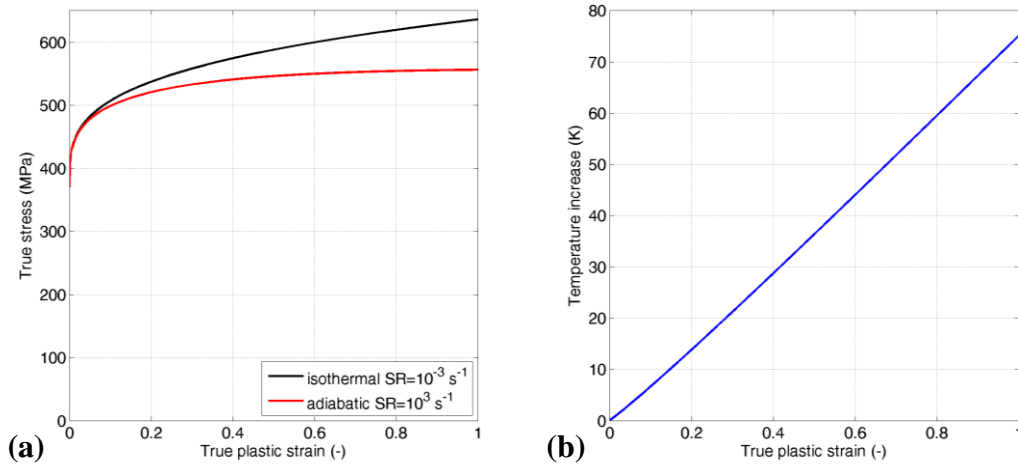


Fig. 4.17: (a) Comparison of true stress vs. true plastic strain curves of Z-A model for the Armco Iron [132] with isothermal and adiabatic hypothesis; (b) the temperature increase, under adiabatic hypothesis, in according to Taylor-Quinney relation [6].

The comparison between the isothermal and adiabatic curves is reported in Fig. 4.17. The way to reproduce the flow stress is similar as before. In the isothermal case the instantaneous temperature  $T$  is fixed to the reference one ( $T=300$  K), while using the Taylor-Quinney relation (Eq. 2.1,  $\beta=1$ ), the temperature profile is calculated in function of plastic work for the representation of the adiabatic behaviour. Although the material and the loading condition considered in Fig. 4.17 are the same of Fig. 4.14, in the Z-A model the strain hardening is lower than in the

J-C model and consequently also the temperature increase (at equal strain and in according to Eq. 2.1) is slightly reduced.

Another interesting aspect regards the comparison between the J-C and the Z-A models. In Fig. 4.18, the material response calculated with J-C and Z-A relations at different strain-rates and temperatures are reported for the same nominally material (Armco Iron). It is evident that results obtained with the two models strongly disagree. This is not only caused by the differences in the model expressions, but it is mainly originated by the experimental data used to calibrate the models and the used calibration methodology. For example, in Fig. 4.18 the parameters of the J-C model were obtained fitting the experimental data of torsion/tensile tests [121], while the Z-A parameters were extracted through a numerical inverse analysis of Taylor impact tests [132]. Obviously, these dissimilarities can introduce a great source of errors due to the interpretation of the data.

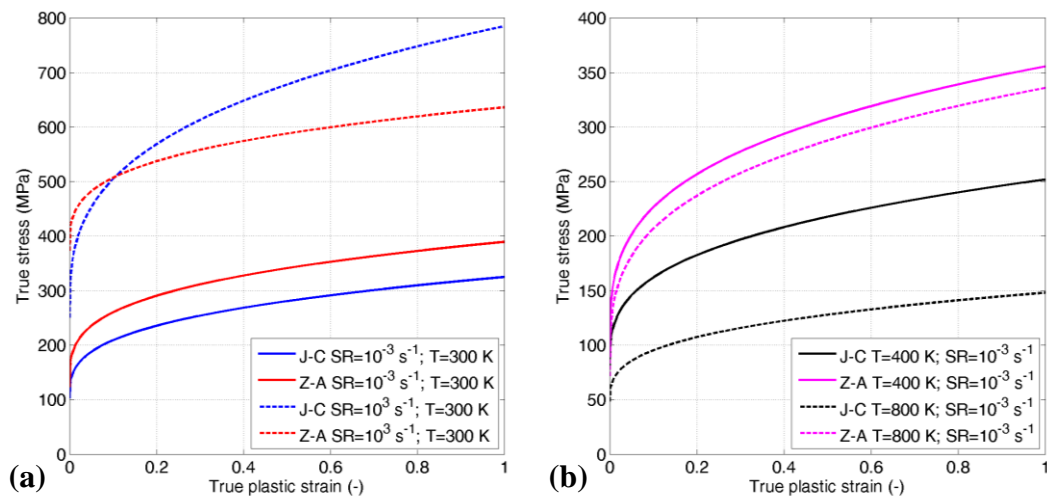


Fig. 4.18: True stress vs. true plastic strain curves calculated with J-C model and Z-A model for Armco Iron at (a) different strain-rates and constant temperature,  $T=300 \text{ K}$ , and (b) at different temperatures and constant strain-rate,  $\dot{\epsilon} = 10^{-3} \text{ s}^{-1}$ .

## 4.4 Material strength model identification

The present section aims to show some possible procedures adoptable for calibrating the parameters of the Johnson-Cook and Zerilli-Armstrong strength models. The procedures rely on input experimental data corresponding to a set of hardening functions obtained at different strain-rates and temperatures.

The experimental data of T91 steel, Glidcop Al-15 and heavy sintered molybdenum will be considered. The results will be presented in terms of plots showing the predicted material response against the experimental trends.

The consequences, determined by each calibration approach, will be compared and evaluated. The positive and negative aspects of each strategy will be discussed and some suggestions on how to choose the best calibration approach will be outlined, also considering the available experimental data. The proposed considerations should provide a useful guideline in the process of determining the best material models parameters in each specific situation in which the model is going to be adopted.

### 4.4.1 Johnson-Cook model calibration

In this paragraph the attention is focused on the procedure necessary to identify the material parameters of the Johnson-Cook model, Eq. 4.7. It is important to point out that the procedure used for the parameters identification has a crucial role for the correct prediction of the flow stress. The original paper that proposed the model, i.e. Johnson and Cook [121], did not provide a detailed description of the procedure necessary to calibrate the parameters of the model and did not establish the origin of the experimental data to use for the model identification (tension, compression, torsion, etc.). This fact has probably contributed to come out different interpretations and methods about the calibration procedure and many authors have treated this aspect [146-150] (just to cite a few).

The first aspect to consider about the calibration of the Johnson-Cook model is that it could depend on experimental data coming from tests of different kind.

Therefore it is important to underline that in the following the calibration strategies which rely on the experimental data consisting in a set of true stress vs. true plastic strain curves at different strain-rates and temperatures will be considered and described. The experimental data that will be used are those of the T91 steel obtained from tensile tests. The choice of this material is due to the propensity of its mechanical behaviour to be described with the J-C relation. Indeed the evolution of the flow stress for T91 is similar to the steel ones shown in the original work of Johnson and Cook [121]. Furthermore, in the original work of Johnson and Cook the problem of necking was taken into account and for this reason it was recommended to consider (when data obtained from tensile tests are used) the equivalent tensile flow stress and the related equivalent quantities during the parameter identification procedure: the equivalent plastic strain and the equivalent plastic strain-rate. These quantities represent the effective values of stress, strain and strain-rate also beyond the onset of the necking. For example, the equivalent flow stress could be determined by using the Bridgman correction factor [151,152]. These aspects are related to the instability in tension that will be deeply discussed in the next chapter; however, up to the onset of the necking the true stress and the true plastic strain are the same of the equivalent stress and equivalent strain [153]. Assuming low levels of true plastic strain for the next analysis, it is possible to presume that no significant errors on the evaluation of the effective tensile stress will be done.

The approaches that will be proposed appear to be the most simple and intuitive, but it is recognized that they are not the only possible ones and that other calibration strategies may be defined as well. Besides, even when the existence of more calibration strategies is recognized, it appears almost impossible to perform a direct comparison between the results provided by each of them because they are related to different materials or experimental test conditions.

All the strategies that will be shown are based on the experimental data fitting, as previously performed by many authors [44,46,56,59,109,137,145,154,155], and the differences from each of them consist in the way to interpret the model parameters. Indeed, it is important to underline that the J-C model is a purely empirical model

and it is necessary to decide which of its parameters should be considered as optimization variables without any physical interpretation.

For what concerns the strain-hardening effect, three parameters  $A$ ,  $B$ , and  $n$  are available to fit the data and different procedures can be used: all the strain-hardening coefficients can be optimized or one of them can be fixed a priori and the other two optimized. For what concerns the temperature sensitivity, usually, the only J-C temperature parameter that is considered as an optimization variable is  $m$ . This approach could lead to a poor fit, but an improvement can be achieved if also  $T_m$  is considered as an optimization variable. Regarding the reference temperature  $T_r$  a recommended option is that of taking it equal to the lowest temperature at which the material is tested. This choice is due to the fact that it is necessary to avoid the computation of negative homologous temperatures,  $T^* = (T - T_r)/(T_m - T_r)$ . This situation may lead to error terminations when the model is implemented in FE codes and therefore needs to be avoided. As a consequence, the model should then be considered for conditions which never involve temperatures lower than the chosen reference value.

Similarly, for the strain-rate sensitivity, only the parameter  $C$  is usually considered as an optimization variable, while the reference strain-rate  $\dot{\epsilon}_0$  is set equal to  $1 \text{ s}^{-1}$ , as in the original formulation. However, in some FE codes, such as LS-DYNA [139], this choice would mean that the strain-rate influence is neglected when the strain-rate is less than unity. Another possibility is to fix this parameter at the lowest value of strain-rate considered during the testing campaign. Nevertheless, if also  $\dot{\epsilon}_0$  is used as optimization variable, an improvement in the experimental data fit could be obtained.

On the basis of these considerations, only the value of the reference temperature,  $T_r$ , could be fixed a priori, while different strategies can be performed to obtain the other parameters.

Generally, the three strain hardening parameters  $A$ ,  $B$ , and  $n$  are the first ones to be determined. This is due to the fact that they depend only on the experimental curve

obtained from the test conducted at the reference temperature and at the reference plastic strain-rate ( $\dot{\varepsilon}_0$ ). This implies that in the J-C strength model the second and the third multiplicative terms become equal to 1, thus the Eq. 4.7 assumes the following form:

$$\sigma = (A + B \cdot \varepsilon_{pl}^n) \quad (4.12)$$

At this point, it is possible to determine all the parameters  $A$ ,  $B$  and  $n$ , or just some of them, by fitting the experimental points with the expression shown above. The parameters identification can be performed through an iterative procedure based on the minimization of the Root Mean Squared Error (RMSE), defined as:

$$RMSE = \sqrt{\frac{\sum_{i=1}^k (\sigma_i^{JC} - \sigma_i^{EXP})^2}{k}} \quad (4.13)$$

Where  $\sigma_i^{JC}$  and  $\sigma_i^{EXP}$  represent the  $i$ -th value of the computed flow stress and the corresponding  $i$ -th value of the experimental one, respectively, and  $k$  represents the number of samples, i.e. the number of experimental points.

A possible strategy is to fix the parameter  $A$  equal to the yield stress of the material, i.e. the true stress at  $\varepsilon_{pl} = 0$  (as in the original formulation), and then to determine the parameters  $B$  and  $n$ . Obviously, this implies that the yield stress has to be accurately evaluated. In other cases, depending from the material, the reference experimental curve could be better described by the basic relation  $\sigma = B \cdot \varepsilon_{pl}^n$ . Another possibility is to consider also  $A$  as an unknown parameter and to evaluate its value through the fitting, which is then responsible for determining the three parameters  $A$ ,  $B$  and  $n$  together. The last strategy, used by different authors, was chosen for the data analysis. The result of the fitting is reported in Fig. 4.19,

comparing the experimental curve with the reconstructed one accordingly to Eq. 4.12, while in Table 4.1 the corresponding parameters are shown.

*Table 4.1: J-C parameters to reproduce the flow stress in quasi-static condition at the reference temperature for T91 steel.*

<b>A</b>	<b>B</b>	<b>n</b>
MPa	MPa	-
397.3	657.6	0.215

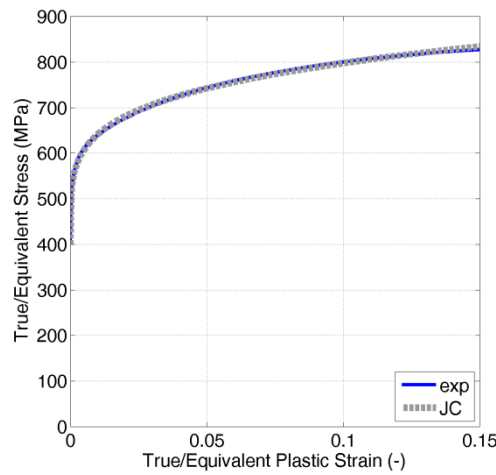


*Fig. 4.19: Result of the data fitting: comparison between the experimental curve of T91 steel obtained at  $10^{-3} \text{ s}^{-1}$  and room temperature ( $25 \text{ }^\circ\text{C}$ ) with the curve calculated through the first term of the J-C model.*

Before to illustrate the way to extract the parameters related to the strain-rate sensitivity, i.e.  $C$  and  $\dot{\epsilon}_0$ , it is important to highlight a consideration about the choice of the reference strain-rate ( $\dot{\epsilon}_0$ ). The reference strain-rate should be taken as the value at which the quasi-static parameters are evaluated, following the procedure just shown, although to choose any value is allowed. If the reference strain-rate considered to extract the parameters  $A$ ,  $B$  and  $n$  is not also maintained for the second term of the J-C relation, it is necessary to properly recalculate  $A$ ,  $B$  and  $n$  in accordance with the chosen value of  $\dot{\epsilon}_0$ .

Assuming at the moment the value of  $\dot{\varepsilon}_0$  equal to that considered for the extraction of the quasi-static parameters, the next step is relative to the determination of the strain-rate parameter  $C$ . This step involves experimental tests conducted at the reference temperature at different nominal strain-rates. In such conditions, the temperature term of the model becomes equal to 1. It is important to highlight that the self-heating of the material under adiabatic hypothesis is actually neglected because at low plastic strains the temperature increase is limited (see Fig. 4.14 and 4.18). Being the parameters  $A$ ,  $B$ ,  $n$  and  $\dot{\varepsilon}_0$  known, the only unknown remaining parameter is  $C$ , and it can be calculated through the flow stress by using the following equation:

$$C = \frac{\left( \frac{\sigma}{A + B \cdot \varepsilon_{pl}^n} \right) - 1}{\ln \left( \frac{\dot{\varepsilon}_{pl}}{\dot{\varepsilon}_0} \right)} \quad (4.14)$$

The parameter  $C$  can be the same for all the points of the curves considered only if the strain-rate hardening of the material grows linearly with the increase of the strain-rate and it is equal to each value of true plastic strain, as assumed by Johnson and Cook. Generally, the strain-rate sensitivity is easily observable using a semi-logarithmic diagram in which the true stresses at fixed values of true plastic strain are plotted as function of the corresponding strain-rate. In this kind of diagram the slope of the line that interpolates the points, corresponding to the same true plastic strain, represents the parameter  $C$ , i.e. the strain-rate sensitivity of the material.

Generally, the experimental points do not follow a perfect linear dependence, thus  $C$  assumes the mean of an average value. Moreover, often the strain-rate sensitivity of the material changes, i.e. the value of  $C$ , varying the true plastic strain considered, as shown in Fig. 4.20 for 5%, 10% and 15% of true plastic strain for the T91 steel. In this figure, the normalized true stress values, i.e. the true stress divided by the true stress corresponding to the quasi-static condition, were fitted in order to have a direct

comparison of the strain-rate sensitivity at different true plastic strains. It is clear that when the strain-rate dependency changes at different values of true plastic strain, a possible way to extend the accuracy of the model for all the true plastic strains considered is to calculate the average value of  $C$ . This assumption differs from which is at the basis of the J-C model. In this perspective, a  $\dot{\varepsilon} - \varepsilon$  coupled model should be used.

In some cases, an improvement in the data fitting could be obtained considering the parameter  $\dot{\varepsilon}_0$  as a further optimization variable, remembering that the second term of J-C model should saturate to 1 when the strain-rates considered are lower than the reference one, accordingly to the interpretation of the J-C model in LS-DYNA. Using this last interpretation for the parameter  $\dot{\varepsilon}_0$ , the estimation of the J-C parameters related to the strain-rate sensitivity was performed by fitting with a piecewise function.

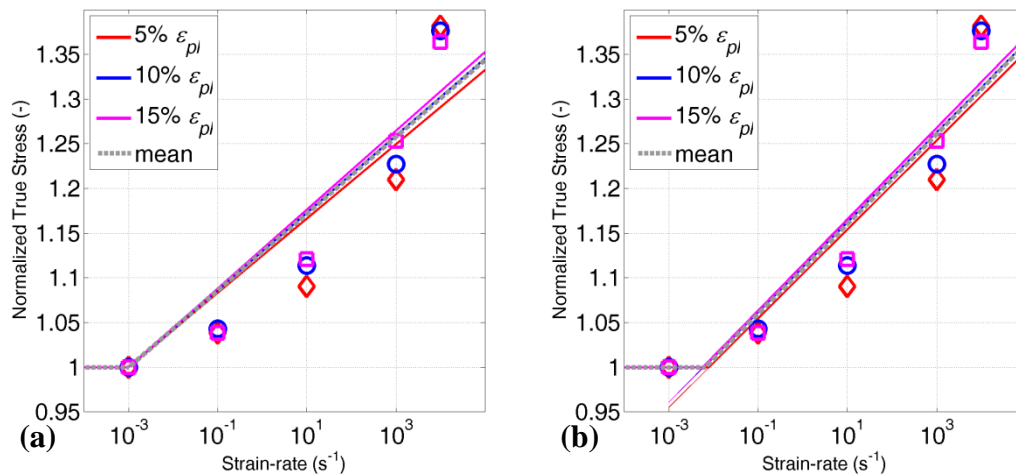


Fig. 4.20: Strain-rate sensitivity for T91 steel obtained with two approaches: a)  $C$  as optimization variable and  $\dot{\varepsilon}_0$  fixed at  $10^{-3} \text{ s}^{-1}$  and b) both  $C$  and  $\dot{\varepsilon}_0$  as optimization variables ( $\diamond$ : 5%,  $\circ$ : 10% and  $\square$ : 15% of true plastic strain; semi-logarithmic diagrams).

Table 4.2: J-C parameters  $C$  and  $\dot{\varepsilon}_0$  obtained at different true plastic strains with different approaches: Method A (with  $\dot{\varepsilon}_0$  fixed) and Method B (with  $\dot{\varepsilon}_0$  as optimization variable).

		$\varepsilon_{pl}=5\%$	$\varepsilon_{pl}=10\%$	$\varepsilon_{pl}=15\%$	average
<b>Method</b>	<b><math>C</math> (-)</b>	0.0180	0.0187	0.0191	0.0186
<b>A</b>	<b><math>\dot{\varepsilon}_0</math> (<math>s^{-1}</math>)</b>	$10^{-3}$			
<b>Method</b>	<b><math>C</math> (-)</b>	0.0216	0.0218	0.0222	0.0219
<b>B</b>	<b><math>\dot{\varepsilon}_0</math> (<math>s^{-1}</math>)</b>	$8.03 \cdot 10^{-3}$	$5.98 \cdot 10^{-3}$	$5.81 \cdot 10^{-3}$	$6.6 \cdot 10^{-3}$

In Fig. 4.20 the results of two different approaches are reported: in one case, Fig. 4.20a, which will be identified here as *Method A*, the value of  $\dot{\varepsilon}_0$  was fixed at  $10^{-3} s^{-1}$  and  $C$  was calculated at different levels of true plastic strain, while in the other approach, Fig. 4.20b, *Method B*, both  $C$  and  $\dot{\varepsilon}_0$  are considered as optimization variables. In Table 4.2 the parameters obtained with both methods are summarized.

From the Fig. 4.20, it is quite complicated to assert that considering the parameter  $\dot{\varepsilon}_0$  as an optimization variable gives some advantages in the data fitting. For this reason, the average values of  $C$  and  $\dot{\varepsilon}_0$ , obtained from both strategies, were used to reproduce the flow stress, in according to the J-C model, in order to appreciate if there are differences in the prediction of material behaviour.

The comparisons between the experimental and reproduced curves at different nominal strain-rates and at the reference temperature are shown in Fig. 4.21 in terms of true stress vs. true plastic strain. From a qualitative point of view, the analytical curves obtained by using the parameters extracted with the *Method B* are in better agreement with the experimental ones with respect to the analytical curves obtained with the parameters of the *Method A*. These comparisons were quantified by calculating the RMSE (Eq. 4.13) for each test condition. The results are summarized in Table 4.3. The sum of each RMSE gives information about the overall accuracy of the model to reproduce the experimental results. In this case, the sum of the RMSEs

obtained by using the parameters extracted with the *Method B* is lower than that of *Method A*, thus the *Method B* for identification of parameters  $C$  and  $\dot{\epsilon}_0$  is recommended to describe the behaviour of this material.

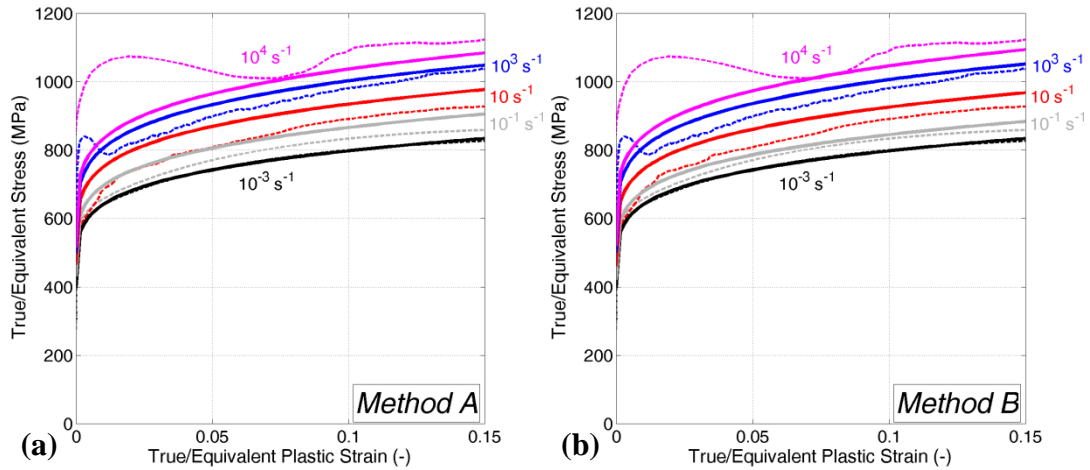


Fig. 4.21: Comparison between the experimental curves at different strain-rates at room temperature (dashed lines) of T91 and the curves obtained in according to J-C model (solid lines) using the parameters of the Method A (a) and the Method B (b).

Table 4.3: Root Mean Squared Error obtained with two different parameters identification approaches: Method A and Method B.

Test condition		<i>Method A</i>	<i>Method B</i>
$\dot{\epsilon}_0$ (s <sup>-1</sup> )	$T$ (°C)	RMSE (MPa)	RMSE (MPa)
$10^{-3}$	25	0.31	0.31
$10^{-1}$	25	3.67	1.74
$10^1$	25	5.52	4.74
$10^3$	25	3.66	3.86
$10^4$	25	10.86	10.26
		24.02	20.91

The last step of the calibration procedure concerns the determination of the temperature parameters, i.e. the parameters  $m$  and  $T_m$ . This step involves experimental tests conducted at the reference strain-rate and at different temperatures. Since the tests are carried out at the reference strain-rate, the strain-rate term of the Johnson-Cook strength model becomes equal to 1. Assuming that the melting temperature is known and being the parameters  $A$ ,  $B$ ,  $n$ , and  $T_r$  known, the unknown remaining parameters is  $m$ , and it can be calculated through the hardening function by using the following equation:

$$m = \frac{\ln \left[ 1 - \left( \frac{\sigma}{A + B \cdot \varepsilon_{pl}^n} \right) \right]}{\ln \left( \frac{T - T_r}{T_m - T_r} \right)} \quad (4.15)$$

At this point, the situation is similar to the one that arises for the calculation of the parameter  $C$  and the same considerations hold true, including the possibility of taking the value of the parameter  $m$  as an average value of all the calculated values at different true plastic strains. Another possibility is to consider both  $m$  and  $T_m$  as optimization variables in order to get a better level of accuracy in the data fitting. In the following, only this method is presented.

As was previously performed for the parameters  $C$  and  $\dot{\varepsilon}_0$ , the experimental normalized true stresses at different temperatures, but at the same strain-rate ( $10^{-3} \text{ s}^{-1}$ ), were considered at different values of true plastic strain (5%, 10% and 15%), in order to investigate if the temperature sensitivity changes increasing the strain. At this point the experimental points were analytically interpolated in according to the J-C expression for the thermal softening, as shown in Fig. 4.22a. Up to 15% of true plastic strain, the thermal sensitivity of this material is almost the same at different levels of true plastic strain. This means that the average values of  $m$  and  $T_m$  allow to the model to be more representative for all the true plastic strains considered. In the Table 4.4 the values of  $m$  and  $T_m$  for the different true plastic

strains investigated are reported as well as the average values. Finally, the predicted flow stresses of the J-C model at different temperatures and in quasi-static condition were calculated using the average value of  $m$  and  $T_m$  and compared with the experimental curves (see Fig. 4.22b).

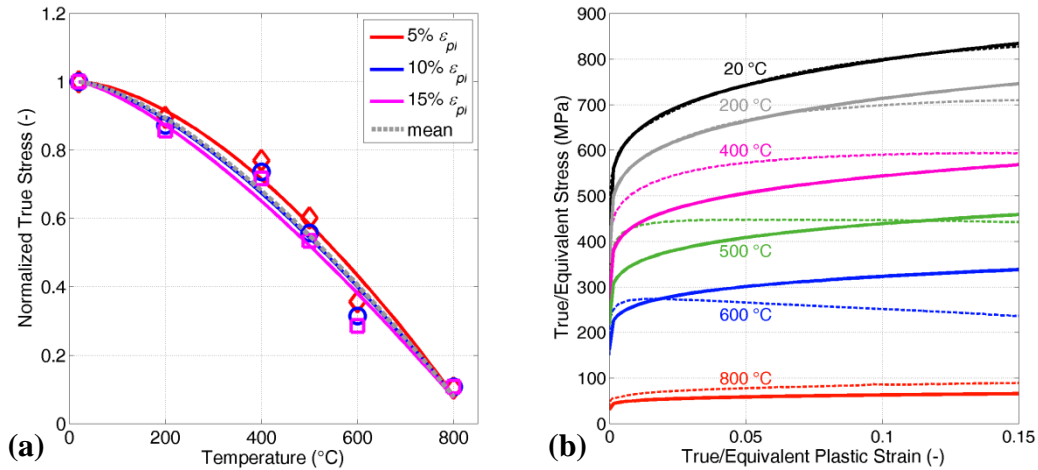


Fig. 4.22: a) Temperature sensitivity for T91 steel at: 5%, 10% and 15% of true plastic strain and b) comparison between the experimental curves at different temperatures in quasi-static condition (dashed lines) and the curves obtained in according to J-C model (solid lines).

Table 4.4: J-C parameters  $m$  and  $T_m$  at different true plastic strains.

	$\varepsilon_{pl}=5\%$	$\varepsilon_{pl}=10\%$	$\varepsilon_{pl}=15\%$	average
$m$ (-)	1.63	1.45	1.35	1.475
$T_m$ (K)	1114.6	1118.4	1119	1117.4

Also varying the temperature, the agreement between the experimental curves and the predicted ones is quite good. Also in this case, the RMSE for each test condition was calculated and reported in Table 4.5. Adding together the sum obtained in Table 4.5 with that one obtained in Table 4.3 for *Method B*, the total RMSE, which considers all test conditions, is 40.29 MPa. In Fig. 4.23, the correlation between the experimental and predicted stresses is shown. The resulting correlation coefficient ( $R$ ) is 0.986.

Table 4.5: Root Mean Squared Error obtained at different temperatures and quasi-static condition for T91 steel.

Test condition		RMSE
$\dot{\epsilon}_0$ (s <sup>-1</sup> )	$T$ (°C)	(MPa)
$10^{-3}$	200	1.58
$10^{-3}$	400	5.69
$10^{-3}$	500	3.99
$10^{-3}$	600	6.09
$10^{-3}$	800	2.03
		19.37

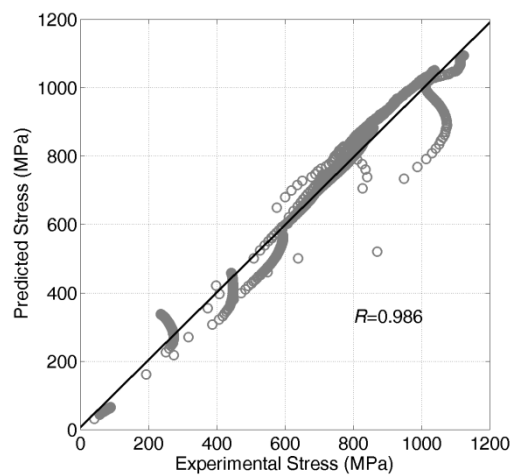


Fig. 4.23: Correlation between predicted and experimental stress over the entire range in temperature and strain-rate up to 15% of true plastic strain.

It is worthwhile to point out some considerations about the procedure stated above. Following this calibration strategy, the experimental data necessary for the determination of the Johnson-Cook parameters can be resumed in the following list:

- tests conducted at the reference temperature and at the reference strain-rate allow to determine the quasi-static parameters  $A$ ,  $B$  and  $n$ ;

- a series of tests conducted at the reference temperature and at strain-rates different from the reference one allow to determine the parameter  $C$  and, eventually, also  $\dot{\epsilon}_0$ ;
- a series of tests conducted at the reference strain-rate and varying the temperature allow to determine the parameters  $m$  and  $T_m$ .

Concerning the last two points, it is clear that increasing the number of tests also the accuracy of the model could be improved.

Finally, also the approximations of this parameter identification procedure have to be considered, in particular:

- the influence of the non-uniformity of strain-rate and temperature in the specimen is neglected. In this way, each experimental result is reproduced by a stress-strain relation and the obtained strength model could be considered representative of an average behaviour of the material at the nominal strain-rate and/or temperature conditions of the test (i.e., strain-rate and temperature are considered constant in the specimen);
- the self-heating of the material due to the adiabatic condition (conversion of mechanical work into heat) in high strain-rate tests is ignored.

However, if the interest in the study of the mechanical response of the material is limited at low levels of strain, the approximations mentioned above could be considered not so relevant.

#### 4.4.2 Zerilli-Armstrong model calibration

Starting from the experimental data shown in the section 4.2, for the Glidcop Al-15 and the heavy sintered molybdenum, the influence of the temperature at low and high strain-rates and the strain-rate sensitivity varying the temperature were studied. The variation of the temperature and strain-rate sensitivities at different

levels of strain-rate and temperature, respectively, can not be accurately described with the J-C model because it considers both temperature and strain-rate to act independently on the flow stress.

Instead, the Zerilli-Armstrong model considers the coupled effect of temperature and strain-rate on the mechanical response through the thermal stress component [132]. For this reason, the behaviour of the Glidcop Al-15 and heavy sintered molybdenum could be adequately described with the Z-A formulation. Commonly, the original formulation of the Z-A model for BCC and FCC materials (see Eq. 4.8 and 4.9) are simplified in more compacted versions as reported below [132]:

$$\sigma = c_0 + c_1 \cdot \varepsilon_{pl}^n + c_2 \cdot e^{(-c_3+c_4 \cdot \ln \dot{\varepsilon})T} \quad (\text{BCC}) \quad (4.16)$$

$$\sigma = c_0 + c_2 \cdot \sqrt{\varepsilon_{pl}} \cdot e^{(-c_3+c_4 \cdot \ln \dot{\varepsilon})T} \quad (\text{FCC}) \quad (4.17)$$

In practice, the athermal part is completely concentrated in the parameter  $c_0$  for FCC materials, while it is described through a hardening function, likes that the first term of the J-C model, using the constants  $c_0$ ,  $c_1$  and  $n$  for the BCC ones. Instead, the thermal component of the model is unchanged with respect to the original versions. In this way the Z-A model loses its physical-based concepts and should be considered an empirical expression.

Considering the materials tested in this work, in the following only the Z-A model for BCC materials will be taken into account because the Body-Centred Cubic crystal structure is the typical one for molybdenum, while for what concerns the Glidcop Al-15, although the matrix of the material is copper, due to the presence of particle dispersion, its mechanical behaviour in temperature and strain-rate is much more comparable to that of BCC pure metals, instead of FCC ones (the yield stress is a function of both temperature and strain-rate).

In the Eq. 4.16 the parameters can not be separately extracted, as it was done for the J-C model, because it is not a purely multiplicative model (unless to consider tests at the temperature of 0 K). Lin and Chen [145] were observed that for metals the value of  $c_0$  could tend at zero at elevated temperatures. One solution is to perform

a multi-objective optimization (MOO), in which the experimental true stress values, obtained at different temperatures and strain-rates within the range of true plastic strains desired, are simultaneously fitted by using the Z-A expression, where all six parameters, i.e.  $c_0$ ,  $c_1$ ,  $c_2$ ,  $c_3$ ,  $c_4$  and  $n$ , are considered as optimization variables. Obviously, the same approach could be also used for the identification of the J-C model parameters. The MOO procedure was used to obtain the parameters of the Z-A model for the heavy sintered molybdenum and Glidcop Al-15, in the range of true plastic strain between 0 and 15%. The parameters identification was performed by using an iterative procedure based on the minimization of the sum of RMSE (Eq. 4.13) of each test condition.

Table 4.6: Z-A model parameters obtained using a multi-objective optimization to fit all the experimental curves from 0 to 15% of true plastic strain.

	$c_0$	$c_1$	$c_2$	$c_3$	$c_4$	$n$
	MPa	MPa	MPa	K <sup>-1</sup>	K <sup>-1</sup>	-
<b>Molybdenum</b>	82	318	2348	$4.9 \cdot 10^{-3}$	$2.3 \cdot 10^{-4}$	0.058
<b>Glidcop Al-15</b>	0	500	698	$1.8 \cdot 10^{-3}$	$7.5 \cdot 10^{-5}$	0.969

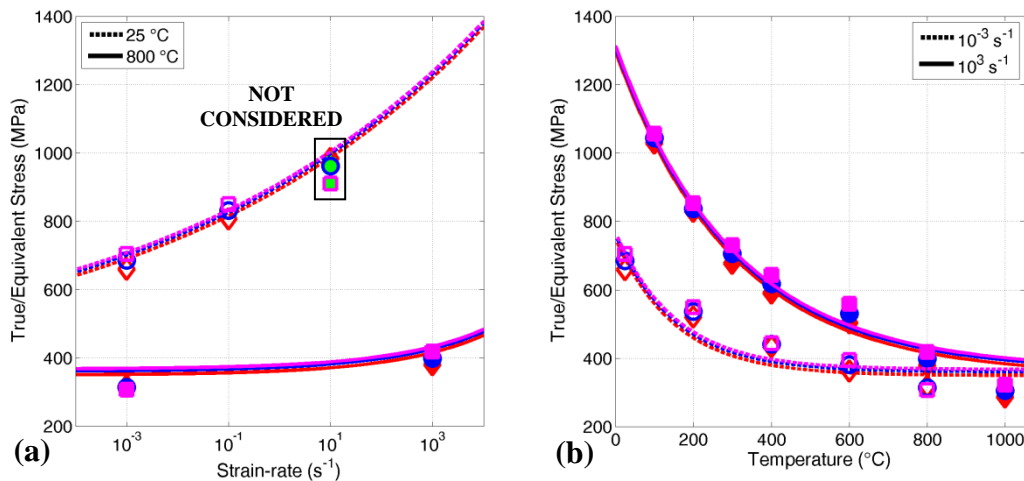


Fig. 4.24: a) Strain-rate and b) temperature sensitivities of the heavy sintered molybdenum using the Z-A model ( $\diamond$ : 5%,  $\circ$ : 10% and  $\square$ : 15% of true plastic strain).

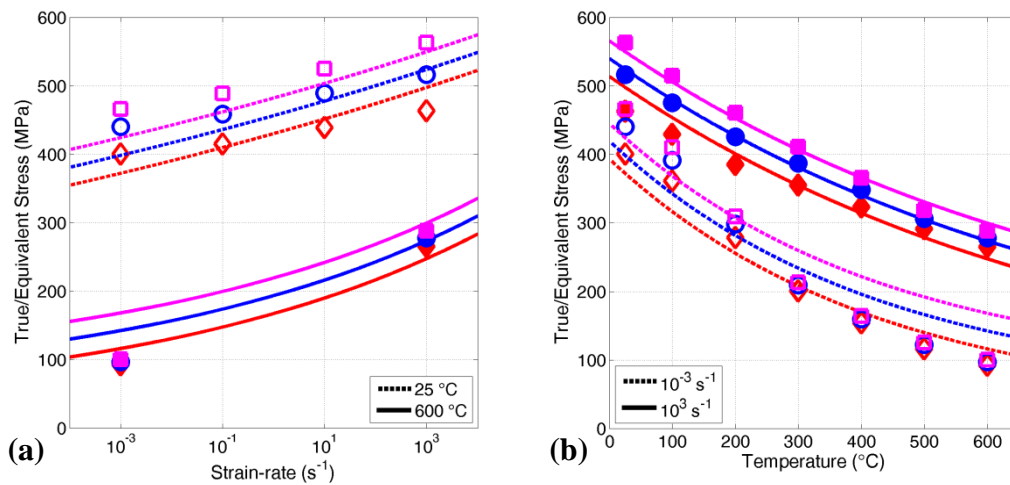


Fig. 4.25: a) Strain-rate and b) temperature sensitivities of Glidcop Al-15 using the Z-A model ( $\diamond$ : 5%,  $\circ$ : 10% and  $\square$ : 15% of true plastic strain).

In Fig. 4.24 and 4.25, it is possible to observe the accuracy of the model to match the experimental data in terms of true stress vs. strain-rate and in terms of true stress vs. temperature for both the materials. The sets of parameters obtained for each material is reported in Table 4.6. For the molybdenum, the experimental data at 10 s<sup>-1</sup> and room temperature were omitted from the optimization because the material, in this condition, shows significant thermal softening at low strains (<15%), which was not considered during the calculation of the true stress. Observing the Fig. 4.24 and 4.25, the calibrated Z-A models describe fairly well the temperature and strain-rate sensitivities of both materials in different loading conditions. Starting from the parameters of Table 4.6, this aspect could be better appreciated by reproducing the flow stress at different levels of strain-rate and temperature. The comparisons between the experimental and predicted curves are shown in Fig. 4.26 for the heavy sintered molybdenum and in Fig. 4.27 for the Glidcop Al-15.

The qualitative comparisons between the curves, shown in Fig. 4.26 and 4.27, confirm that the coupled effect of temperature and strain-rate on the flow stress, considered in the Z-A model, gives a great advantage in the correct description of the material behaviour with respect to the J-C model. Obviously, the J-C model requires few experiments to evaluate these constants, while an accurate calibration of the Z-A

model needs to perform experimental tests varying the temperature at least at two different strain-rate levels. The RMSE (Eq. 4.13) was calculated for each test condition for both materials in order to evaluate the accuracy of the models to reproduce the experimental curves. The results are summarized in Table 4.7. In Fig. 4.28, the correlations between the predicted and experimental stresses for both materials are shown. For both materials the correlation coefficient is equal to 0.983.

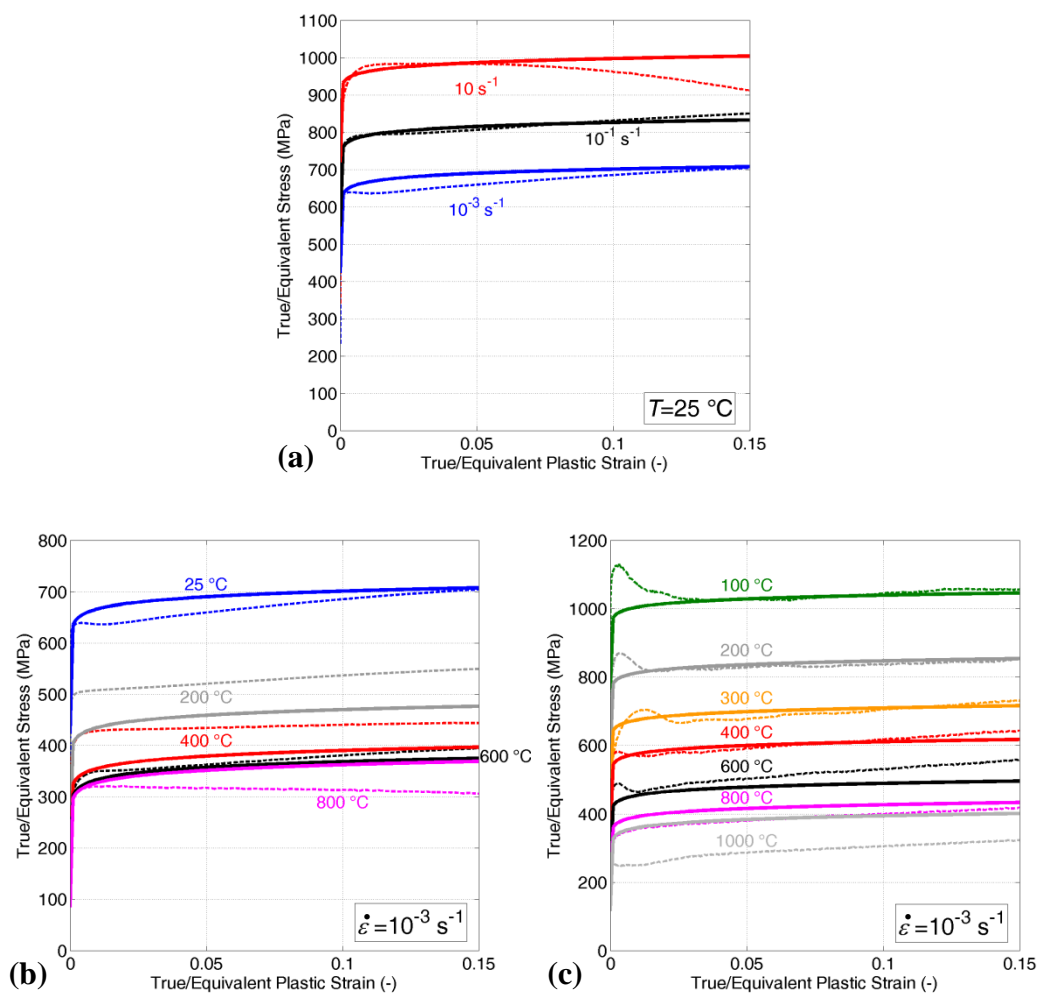


Fig. 4.26: Comparison between the experimental (dashed lines) and predicted curves (solid lines) using Z-A model for heavy sintered molybdenum at different loading conditions: a) varying the strain-rate at  $25\text{ }^{\circ}\text{C}$  and varying the temperature at b)  $10^{-3}\text{ s}^{-1}$  and c)  $10^3\text{ s}^{-1}$ .

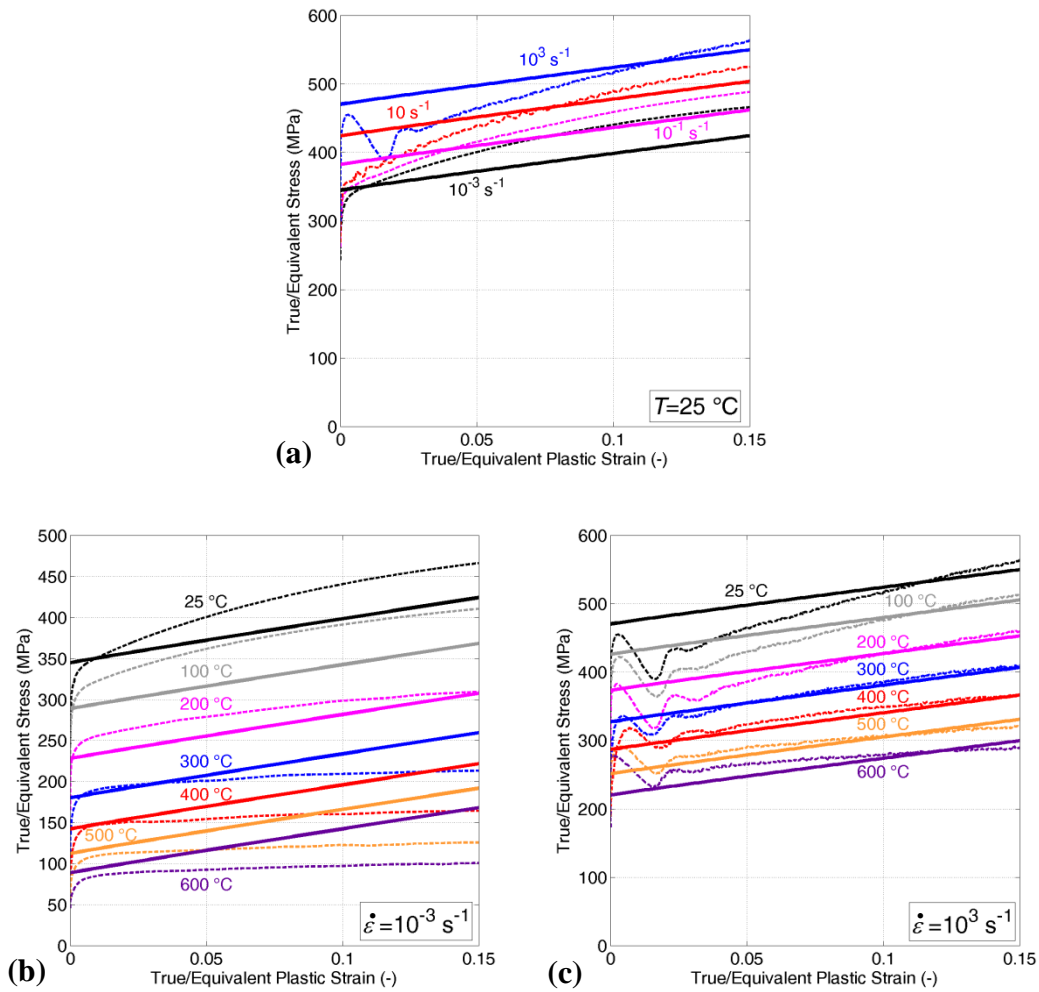


Fig. 4.27: Comparison between the experimental (dashed lines) and predicted curves (solid lines) using Z-A model for Glidcop Al-15 at different loading conditions: a) varying the strain-rate at 25 °C and varying the temperature at b)  $10^{-3}\text{ s}^{-1}$  and c)  $10^3\text{ s}^{-1}$ .

Finally, the strategy proposed in this section is characterized by the same approximations highlighted in the procedure used for the extraction of the J-C model parameters, i.e. the non-uniformity of the strain-rate and the temperature in the specimen is neglected and the self-heating of the material due to the conversion of the plastic work is not considered.

Table 4.7: Root Mean Squared Error obtained for each test condition for heavy sintered molybdenum and Glidcop Al-15.

<b>Molybdenum</b>			<b>Glidcop Al-15</b>		
Test condition		RMSE	Test condition		RMSE
$\dot{\epsilon}_0$ (s <sup>-1</sup> )	$T$ (°C)	(MPa)	$\dot{\epsilon}_0$ (s <sup>-1</sup> )	$T$ (°C)	(MPa)
10 <sup>-3</sup>	25	2.31	10 <sup>-3</sup>	25	2.87
10 <sup>-3</sup>	200	5.63	10 <sup>-3</sup>	100	3.60
10 <sup>-3</sup>	400	4.68	10 <sup>-3</sup>	200	1.56
10 <sup>-3</sup>	600	1.37	10 <sup>-3</sup>	300	1.92
10 <sup>-3</sup>	800	3.51	10 <sup>-3</sup>	400	2.59
10 <sup>-1</sup>	25	1.06	10 <sup>-3</sup>	500	3.16
10 <sup>1</sup>	25	4.13	10 <sup>-3</sup>	600	3.23
10 <sup>3</sup>	100	2.60	10 <sup>-1</sup>	25	1.87
10 <sup>1</sup>	200	1.49	10 <sup>1</sup>	25	2.25
10 <sup>3</sup>	300	1.37	10 <sup>3</sup>	25	2.91
10 <sup>3</sup>	400	1.10	10 <sup>3</sup>	100	2.35
10 <sup>3</sup>	600	3.32	10 <sup>3</sup>	200	1.72
10 <sup>3</sup>	800	2.51	10 <sup>3</sup>	300	1.12
10 <sup>3</sup>	1000	7.56	10 <sup>3</sup>	400	1.00
		<b>42.64</b>	10 <sup>3</sup>	500	0.94
			10 <sup>3</sup>	600	1.35
					<b>34.43</b>

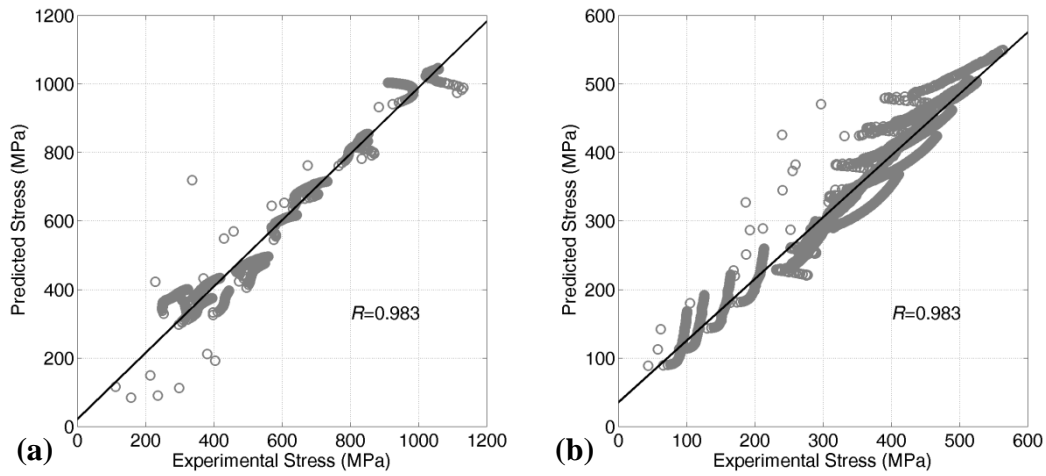


Fig. 4.28: Correlation between predicted and experimental stress over the entire range in temperature and strain-rate up to 15% of true plastic strain for a) heavy sintered molybdenum and b) Glidcop Al-15.

#### 4.4.2 Modified Zerilli-Armstrong model calibration

Many authors have to point out that the Zerilli-Armstrong model is particularly not suited to represent the flow behaviours of material at high temperatures and at low strain-rates [46,145]. For this reason, several modified Z-A models were developed, which substantially represent the combination of the Johnson-Cook and Zerilli-Armstrong models [46,145,156-158].

The modified version proposed by Samantaray, et. al. [158] considers isotropic hardening, temperature softening, strain-rate hardening, and the coupled effects of temperature and strain-rate and of strain and temperature on the flow stress through the following expression:

$$\sigma = (c_1 + c_2 \cdot \varepsilon_{pl}^n) \cdot e^{[-(c_3+c_4 \cdot \varepsilon_{pl})T^* + (c_5+c_6 \cdot T^*) \ln \dot{\varepsilon}^*]} \quad (4.18)$$

where  $T^* = (T - T_{ref})$  with  $T$  and  $T_{ref}$  equal to the current and reference temperatures, respectively,  $\dot{\varepsilon}^* = \dot{\varepsilon} / \dot{\varepsilon}_0$ , with  $\dot{\varepsilon}$  and  $\dot{\varepsilon}_0$  equal to the current and reference strain-rates, respectively, and  $c_1$ ,  $c_2$ ,  $c_3$ ,  $c_4$ ,  $c_5$ ,  $c_6$ , and  $n$  are material model

parameters. Although this version derives from the original Z-A model for FCC materials, there are not limitations to use it also for BCC materials. Thanks to the introduction of the reference temperature and strain-rate, it is possible to determine the model parameters in different steps, as described by Samantaray, et. al. [158] and Lin et. al. [157] for a similar model. Nevertheless, a similar approach to that previously used for the parameters identification of the original Z-A model was followed here, i.e. a multi-objective optimization in which all the experimental curves, from 0 to 15% of true plastic strain, were simultaneously fitted in accordance with Eq. 4.18. In [158] it was specified that the reference temperature and strain-rate should be fixed to the minimum temperature and strain-rate of the planned testing campaign, therefore they were fixed at 25 °C and  $10^{-3} \text{ s}^{-1}$ , respectively. All the other seven model constants were considered as optimization variables.

The model parameters were extracted for the heavy sintered molybdenum and for Glidcop Al-15 and they are reported in Table 4.8. In the Fig. 4.29 and 4.30, the strain-rate and temperature sensitivities for both the materials are reproduced using the modified Z-A model. These figures show that the modified version seems to describe better, with respect to the original Z-A model, the coupled effects of temperature and strain-rate on the flow stress, in particular for Glidcop. This improvement could be appreciate also observing the comparison between the experimental curves and the predicted ones by the modified Z-A model reported in Fig. 4.31 for the heavy sintered molybdenum and in Fig. 4.32 for the Glidcop Al-15. Observing these comparisons, the modified Z-A model (Eq. 4.18) seems to allow a light improvement in the description of the molybdenum behaviour with respect to the original version (Eq. 4.16), while it is particularly suited to reproduce the flow stress for Glidcop Al-15. In order to confirm these observations, the RMSE (Eq. 4.13) was calculated for each test condition for both materials. The results are summarized in Table 4.9. Comparing the final sums of Table 4.9 with those of Table 4.7, by using the modified Z-A model with respect to the original version, the total RMSE for molybdenum is slightly reduced from 42.64 to 41.28 MPa, while it is considerably reduced from 34.43 to 14.88 MPa for Glidcop. In Fig. 4.33, the

correlations between the predicted and experimental stresses for molybdenum and Glidcop are shown. For molybdenum the correlation coefficient is equal to 0.984 (while it was 0.983 by using the original Z-A model), while for Glidcop it is 0.995, which is much higher than that obtained previously with the original Z-A model ( $R=0.983$ ).

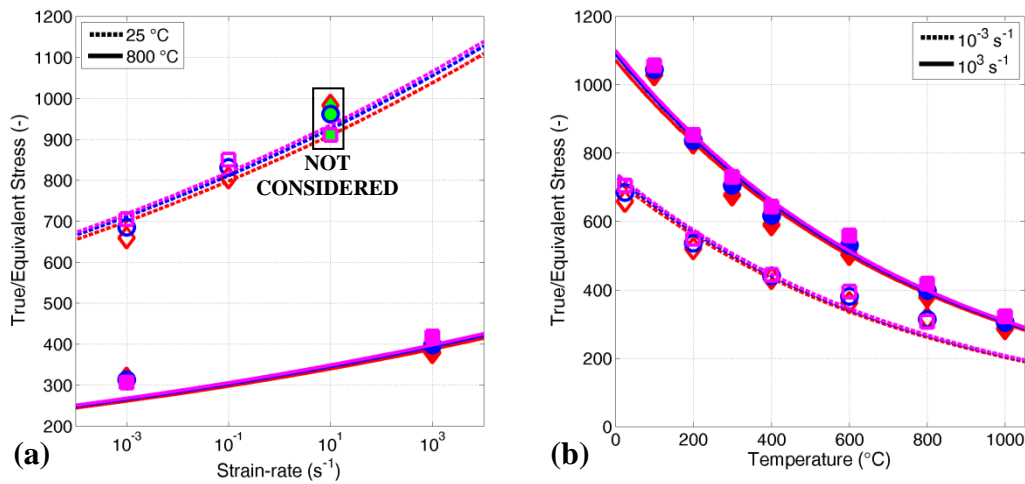


Fig. 4.29: a) Strain-rate and b) temperature sensitivities of the heavy sintered molybdenum using the modified Z-A model ( $\diamond$ : 5%,  $\circ$ : 10% and  $\square$ : 15% of true plastic strain).

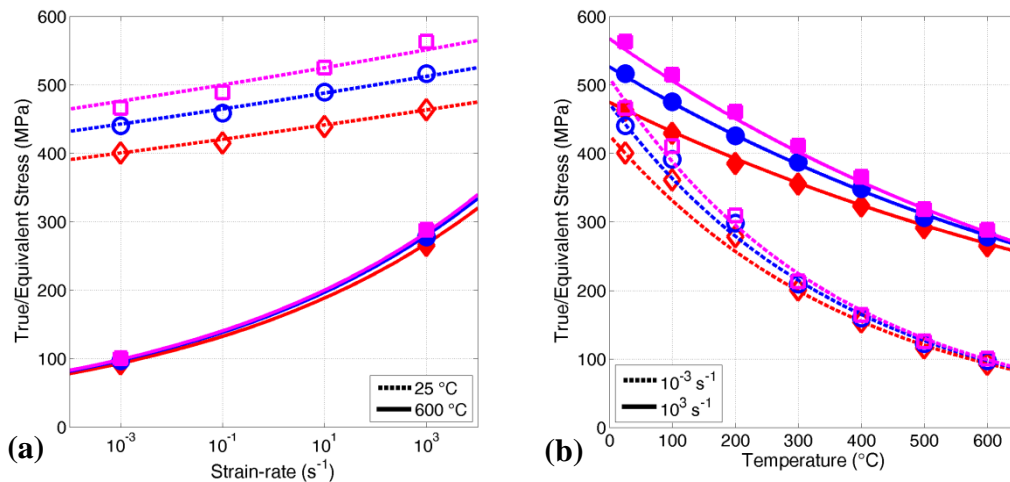


Fig. 4.30: a) Strain-rate and b) temperature sensitivities of Glidcop Al-15 using the modified Z-A model ( $\diamond$ : 5%,  $\circ$ : 10% and  $\square$ : 15% of true plastic strain).

Table 4.8: Modified Z-A model parameters obtained using a multi-objective optimization to fit all the experimental curves from 0 to 15% of true plastic strain.

	$c_1$	$c_2$	$c_3$	$c_4$	$c_5$	$c_6$	$n$
	MPa	MPa	K <sup>-1</sup>	K <sup>-1</sup>	-	K <sup>-1</sup>	-
<b>Molybdenum</b>	393	361	$1.3 \cdot 10^{-3}$	0	$2.9 \cdot 10^{-2}$	$2.5 \cdot 10^{-7}$	0.054
<b>Glidcop Al-15</b>	311	478	$2.4 \cdot 10^{-3}$	$2.0 \cdot 10^{-3}$	$1.1 \cdot 10^{-2}$	$1.1 \cdot 10^{-4}$	0.560

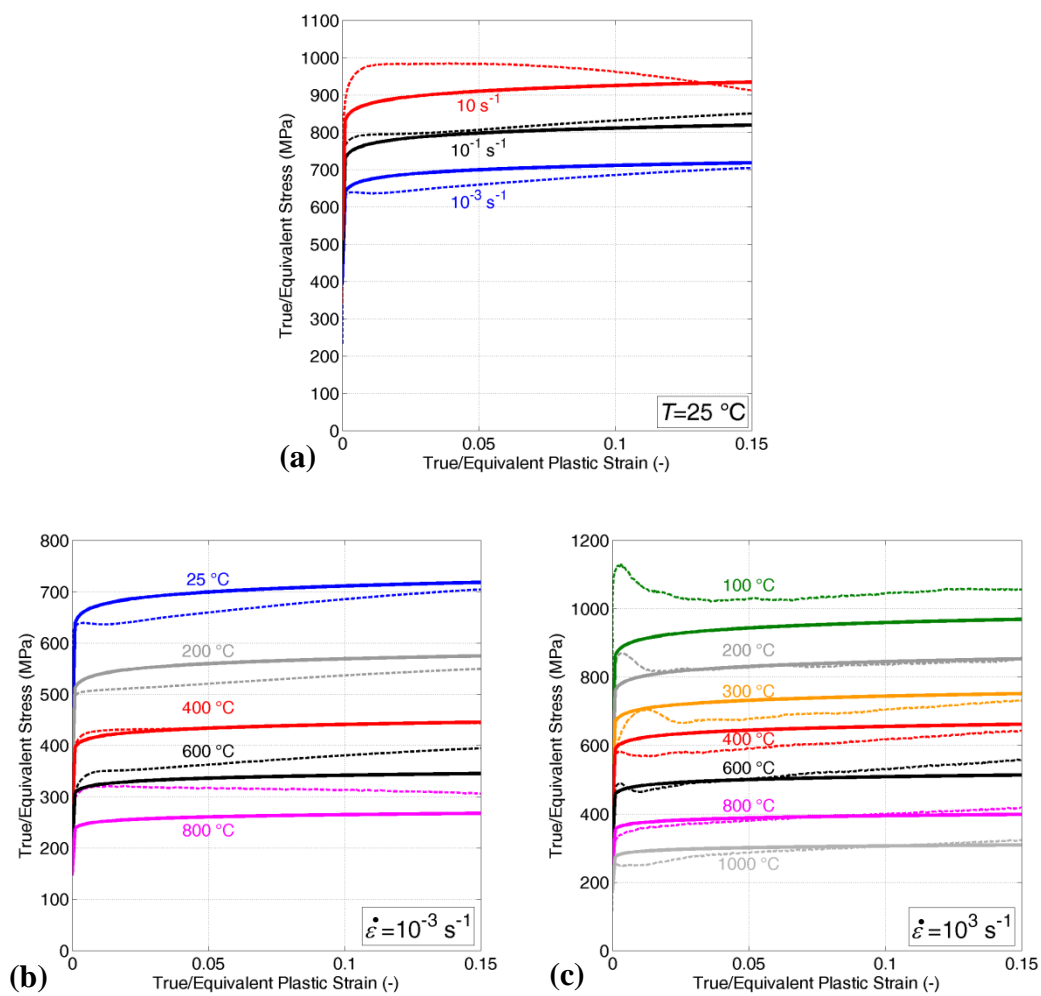


Fig. 4.31: Comparison between the experimental (dashed lines) and predicted curves (solid lines) using modified Z-A model for heavy sintered molybdenum at different loading conditions: a) varying the strain-rate at  $25\text{ °C}$  and varying the temperature at b)  $10^{-3}\text{ s}^{-1}$  and c)  $10^3\text{ s}^{-1}$ .

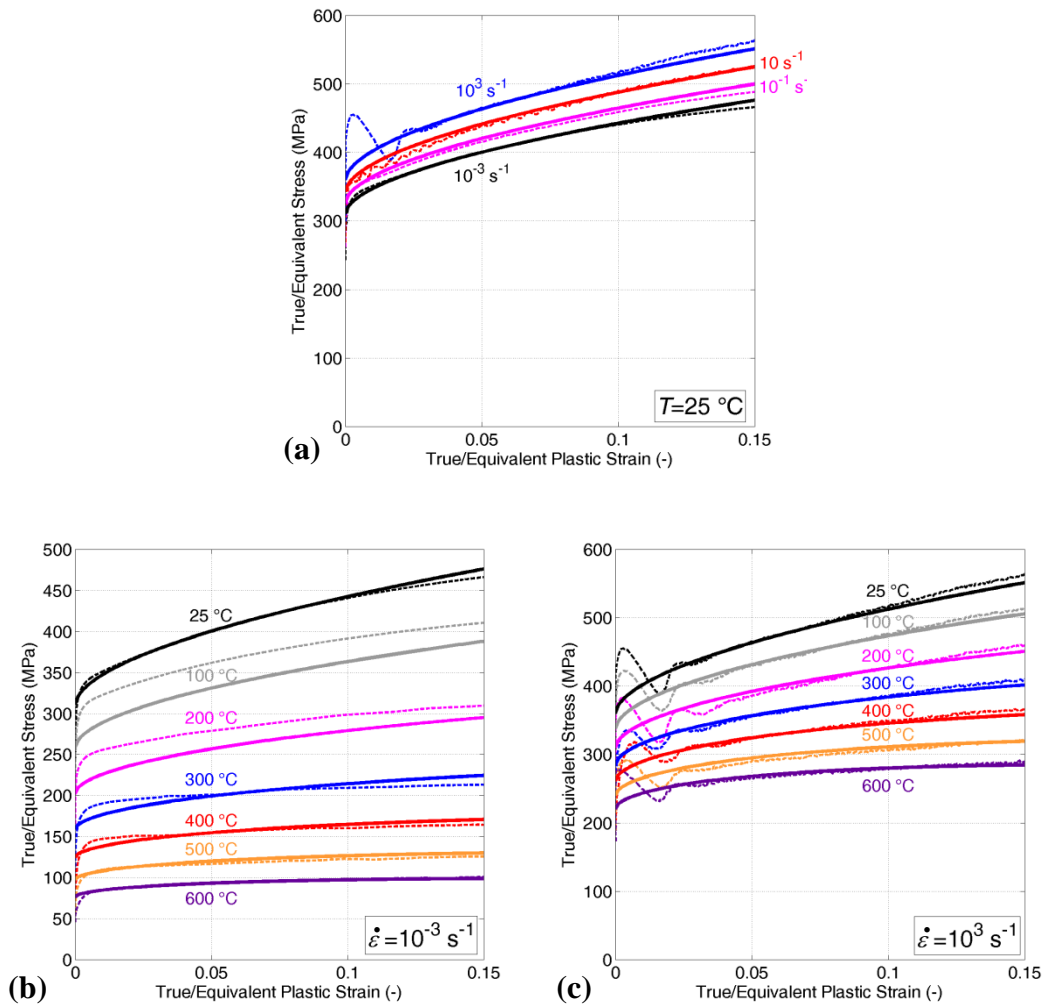


Fig. 4.32: Comparison between the experimental (dashed lines) and predicted curves (solid lines) using modified Z-A model for Glidcop Al-15 at different loading conditions: a) varying the strain-rate at 25 °C and varying the temperature at b)  $10^{-3} \text{ s}^{-1}$  and c)  $10^3 \text{ s}^{-1}$ .

It is important to note that the calibration of the modified Z-A model requires the same number of experimental tests needs for the calibration of the original version and only one parameter more to individuate. Thus, if the original Z-A model is not particularly suited to predict the behaviour of materials investigated, a valid alternative could be represented by this modified version. Nevertheless, this model is not actually implemented in the commercial FE codes, and this aspect represents a significant limitation.

Finally, it is necessary to remember that also in this parameters identification strategy the non-uniformity of the temperature and strain-rate inside the specimen and the self-heating due to the conversion of the plastic work are not considered.

Table 4.9: Root Mean Squared Error obtained for each test condition for heavy sintered molybdenum and Glidcop Al-15.

<i>Molybdenum</i>			<i>Glidcop Al-15</i>		
Test condition		RMSE	Test condition		RMSE
$\dot{\epsilon}_0$ (s <sup>-1</sup> )	$T$ (°C)	(MPa)	$\dot{\epsilon}_0$ (s <sup>-1</sup> )	$T$ (°C)	(MPa)
$10^{-3}$	25	2.82	$10^{-3}$	25	0.56
$10^{-3}$	200	2.80	$10^{-3}$	100	2.38
$10^{-3}$	400	0.48	$10^{-3}$	200	1.75
$10^{-3}$	600	2.83	$10^{-3}$	300	0.70
$10^{-3}$	800	4.32	$10^{-3}$	400	0.55
$10^{-1}$	25	1.65	$10^{-3}$	500	0.41
$10^1$	25	5.10	$10^{-3}$	600	0.25
$10^3$	100	8.42	$10^{-1}$	25	0.67
$10^1$	200	1.52	$10^1$	25	0.40
$10^3$	300	3.44	$10^3$	25	1.37
$10^3$	400	3.57	$10^3$	100	1.34
$10^3$	600	1.91	$10^3$	200	1.15
$10^3$	800	0.95	$10^3$	300	0.90
$10^3$	1000	1.47	$10^3$	400	0.81
		<b>41.28</b>	$10^3$	500	0.84
			$10^3$	600	0.80
					<b>14.88</b>

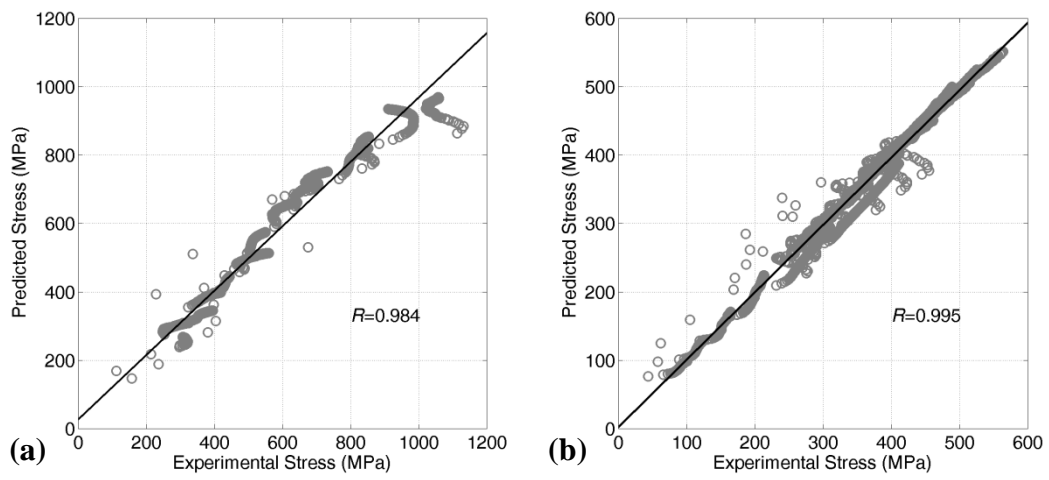


Fig. 4.33: Correlation between predicted and experimental stress over the entire range in temperature and strain-rate up to 15% of true plastic strain for a) heavy sintered molybdenum and b) Glidcop Al-15.



## 5. Numerical analysis

The plastic properties of the materials are exploited in many sectors such as machining processes, automotive crashworthiness or ballistic protections. Thus, the study of the material behaviour at high plastic strains holds a fundamental role. However, the mechanical response in plastic field is not simple to describe because the state of stress and strain could become extremely complex.

In this chapter the problems related to the evaluation of the stress and strain beyond the onset of the necking in tensile test using round test specimens will be discussed. The Bridgman equation and the numerical inverse analysis will be used to describe the material behaviour up to fracture. Moreover, an advanced numerical inverse analysis will be presented in order to improve the prediction of the mechanical response when localized deformation occurs.

### 5.1 Instability condition

For ductile metals, the strain hardening effect exhibited during the first phase of tensile test is opposed by the gradual decrease in the cross-sectional area of the round specimen as it elongates. Usually, necking or localized deformation begins at maximum load, where the increase in stress due to decrease in the cross-sectional area of the specimen becomes greater than the increase in the load-carrying ability of

the metal due to strain hardening. This condition of instability leading to localized deformation is defined by the condition  $dP = 0$ , thus:

$$P = \sigma \cdot A \quad (5.1)$$

$$dP = \sigma \cdot dA + A \cdot d\sigma = 0 \quad (5.2)$$

From the constancy of volume relation (Eq. 4.4):

$$\frac{dL}{L} = -\frac{dA}{A} = d\varepsilon \quad (5.3)$$

and since the instability condition (Eq. 5.2) can be written as:

$$-\frac{dA}{A} = \frac{d\sigma}{\sigma} \quad (5.4)$$

Then the tensile instability occurs when:

$$\frac{d\sigma}{d\varepsilon} = \sigma \quad (5.5)$$

The necking criterion can be expressed more explicitly if the engineering strain ( $e$ ) is used. Starting from Eq. 5.5:

$$\frac{d\sigma}{d\varepsilon} = \frac{d\sigma}{de} \cdot \frac{de}{d\varepsilon} = \frac{d\sigma}{de} \cdot \frac{L_s}{\frac{dL}{L}} = \frac{d\sigma}{de} \cdot \frac{L}{L_s} = \frac{d\sigma}{de} \cdot (1+e) = \sigma \quad (5.6)$$

$$\frac{d\sigma}{de} = \frac{\sigma}{1+e} \quad (5.7)$$

where  $L$  and  $L_s$  are the actual and the initial length of the specimen, respectively. The Eq. 5.7 permits an interesting geometrical construction for the determination of the point of maximum load. In Fig. 5.1, an indicative stress-strain curve is plotted in terms of true stress vs. engineering strain. The line drawn from the point A (negative strain of 1), which is tangent to the stress-strain curve, establishes the point of maximum load (point B), because according to Eq. 5.7, the slope at this point is  $\sigma/(1+e)$  [11]. The point B represents the instability condition, i.e. the end of the uniform distribution of stress and strain, in a tensile test. Beyond true uniform strain,  $e_u$ , the Eq. 4.5 and 4.6 are not valid to calculate the true stress and strain.

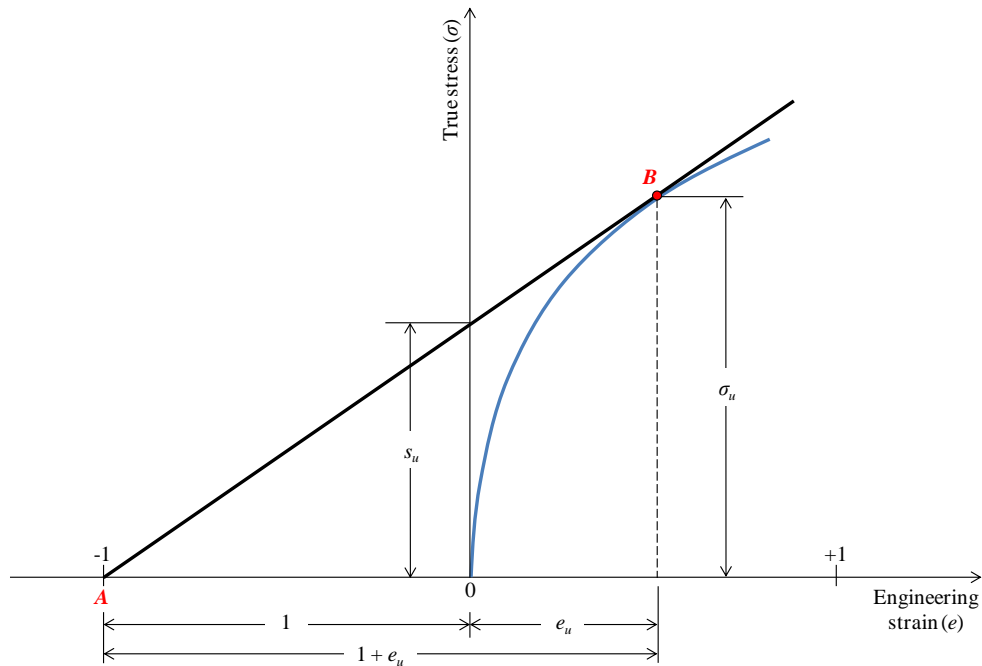


Fig. 5.1: Construction for the determination of the point of maximum load [11].

## 5.2 Stress and strain distribution at the neck

True stress ( $\sigma$ ) and true strain ( $\varepsilon$ ) are usually calculated by using the Eq. 4.5 and 4.6 in order to describe the material behaviour. Nevertheless, these equations are valid only as long as the deformation is uniform.

Generally, for ductile metals, beyond the maximum load the round specimen undergoes localized deformation and the true strain should be based on actual area or diameter measurements. Assuming the volume conservation hypothesis (Eq. 4.4), the correct way to evaluate the true strain is the following:

$$\varepsilon = \int \frac{dL}{L} = \ln\left(\frac{L}{L_s}\right) = \ln\left(\frac{A_s}{A}\right) = \ln\left(\frac{\frac{\pi}{4} \cdot D_s^2}{\frac{\pi}{4} \cdot D^2}\right) = 2 \cdot \ln\left(\frac{D_s}{D}\right) \quad (5.8)$$

where  $L$ ,  $A$  and  $D$  are the minimum length, area and diameter in the neck, respectively, and  $L_s$ ,  $A_s$  and  $D_s$  are the initial length, area and diameter of the specimen, respectively. The Eq. 5.8 remains valid also after the necking occurs, but the main problem is to obtain the values of the instantaneous diameter ( $D$ ) during the execution of the test. The possible solutions could be represented by: photography methods, performing stepwise tensile tests, i.e. straining a specimen a given amount beyond necking and unloading to directly measure the diameter [153], or using tapered ring-gage [11]. Really, also the Eq. 4.5, which is based on the minimum length in the neck, would be suitable to calculate the true strain beyond the onset of necking, nevertheless, it requires the measurement of the length of the necked region which is almost impossible to evaluate.

On the basis of what said above, the total extension of a tensile test specimen could be considered as a sum of two components: the uniform extension up to necking and localized extension once necking begins. The extension of uniform elongation depends on the metallurgical condition of the material, while the development of the neck is affected by the size and shape of the specimen. The extension of a specimen at fracture could be expressed by:

$$L_f - L_s = \alpha + e_u \cdot L_s \quad (5.9)$$

where  $\alpha$  is the local necking extension,  $L_f$  the final specimen length, and  $e_u \cdot L_s$  is the uniform extension. Thus, the tensile elongation ( $e_f$ ) results:

$$e_f = \frac{L_f - L_s}{L_s} = \frac{\alpha}{L_s} + e_u \quad (5.10)$$

This relation shows that the total specimen elongation depends directly by its gage length. The shorter the gage length, the greater the influence of localized deformation at the neck on the total elongation of the gage length [78,125].

The state of stress at the centre of the neck is not uniaxial tension, but a complex triaxial stress distribution across the neck appears. The necked region could be compared to a mild notch, which, under tension, produces radial and transverse stress that cause the raising of the longitudinal stress needed to produce plastic flow. Therefore, the average true stress at the neck is higher than the stress that would be required to cause flow in uniaxial stress condition.

In Fig. 5.2, a schematic illustration of the stress distribution in the neck of a round tensile test specimen is shown, where:  $R$  is the radius of curvature of the neck profile,  $a$  is the minimum radius of the neck cross-section, and  $\sigma_{xx}$ ,  $\sigma_{yy}$ ,  $\sigma_{zz}$  are the true principal stresses in the radial, tangential, and axial directions, respectively.

Bridgman formulated a mathematical analysis that provides a correction to the average axial stress to compensate for the introduction of transverse stresses [152,151]. This analysis was based on the following assumptions:

- the contour of the neck is approximated by the arc of a circle;
- the cross-section of the necked region remains circular during the whole test, i.e. rotational symmetry about the longitudinal axis, thus:

$$\sigma_{xx} = \sigma_{yy} \quad (5.11)$$

- the strains are constant over the cross-section of the neck;

- the von Mises plasticity condition is applied for yielding:

$$\sigma = \sqrt{\frac{1}{2}[(\sigma_{zz} - \sigma_{xx})^2 + (\sigma_{xx} - \sigma_{yy})^2 + (\sigma_{yy} - \sigma_{zz})^2]} \quad (5.12)$$

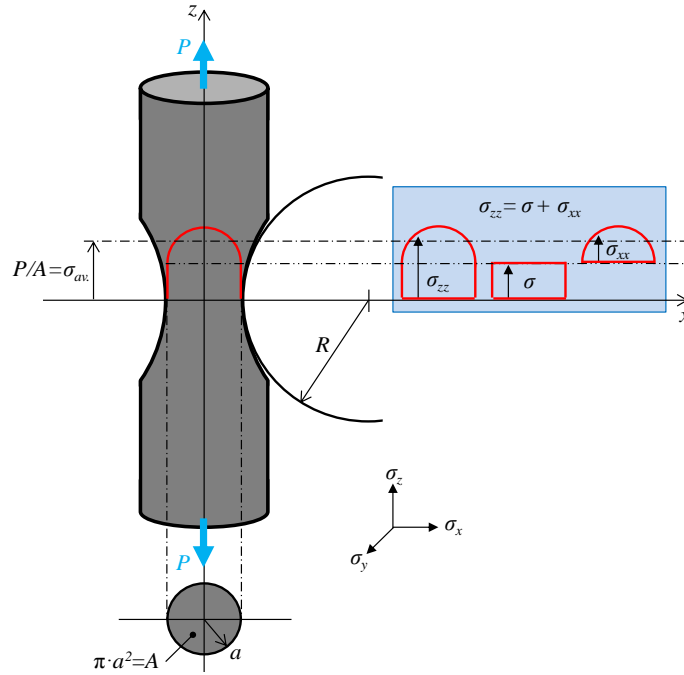


Fig. 5.2: Schematic illustration for stress distribution in the neck of a round tensile test specimen.

By using Eq. 5.11 and 5.12, the following equation is obtained for the axial stress:

$$\sigma_{zz} = \sigma + \sigma_{xx} \quad (5.13)$$

This indicates that the stress at any point can be considered to be composed of a uniform true stress ( $\sigma$ ) and a non-uniform hydrostatic tension ( $\sigma_{xx}$ ) as seen in Fig. 5.2. At the external surface,  $\sigma_{zz}$  is equivalent to  $\sigma$  because the stress component of  $\sigma_{xx}$  is zero at the neck. The variation law of the hydrostatic tension

$\sigma_{xx}$  along the radial distance in the minimum section of the neck ( $x$ ) was proposed by Bridgman through:

$$\frac{d\sigma_{xx}}{dx} \left( R + \frac{a^2 - x^2}{2 \cdot a} \right) + \frac{x}{a} \cdot \sigma = 0 \quad (5.14)$$

By solving this equation,  $\sigma_{xx}$  and  $\sigma_{zz}$  are given by the following equations:

$$\sigma_{xx} = \sigma \cdot \ln \left( \frac{a^2 + 2 \cdot a \cdot R - x^2}{2 \cdot a \cdot R} \right) \quad (5.15)$$

$$\sigma_{zz} = \sigma \cdot \left[ 1 + \ln \left( \frac{a^2 + 2 \cdot a \cdot R - x^2}{2 \cdot a \cdot R} \right) \right] \quad (5.16)$$

The average stress ( $\sigma_{av.}$ ) is obtained by:

$$\sigma_{av.} = \frac{P}{A} = \frac{P}{\pi \cdot a^2} \quad (5.17)$$

where  $P$  is the longitudinal load which is related to the Eq. 5.16 by the following equation:

$$P = 2 \cdot \pi \int_0^a x \cdot \sigma_{zz} dx = \pi \cdot \sigma \cdot (a^2 + 2 \cdot a \cdot R) \cdot \ln \left( 1 + \frac{a}{2 \cdot R} \right) \quad (5.18)$$

Therefore, the equivalent stress beyond the onset of the necking is:

$$\sigma = \frac{\sigma_{av.}}{\left(1 + \frac{2 \cdot R}{a}\right) \cdot \left[\ln\left(1 + \frac{a}{2 \cdot R}\right)\right]} = \frac{P}{\pi \cdot a^2 \cdot \left(1 + \frac{2 \cdot R}{a}\right) \cdot \left[\ln\left(1 + \frac{a}{2 \cdot R}\right)\right]} \quad (5.19)$$

The Bridgman equation means to describe the equivalent stress of the material during the non-uniform deformation phase and for this reason when  $R$  tends to infinite it has not sense to exist. In order to avoid the measurements of  $a$  and  $R$ , Bridgman tried to present an empirical relation between the ratio  $a/R$  and the true strain in the neck, but it resulted in close agreement only for steel specimens [159].

### 5.2.1 Application of Bridgman equation

In this work, the used specimen geometries are those shown in Fig. 3.6 and 3.9, i.e. 3 mm of diameter and 5 mm of gage length for the standard typology and 1.5 mm of gage length and diameter for the miniaturized one. Both geometries are characterized by low ratio between gage length and diameter, thus the necking phase is a considerable part of the entire test duration. To correctly compute this effect, the true stress versus true strain relationship of the material should be extracted by using the Bridgman equation (Eq. 5.19).

With this perspective, an optical procedure, similar to that used by Hopperstad [160], was used for the measurement of the radius of curvature of the neck profile ( $R$ ) and the minimum radius of the neck cross-section ( $a$ ). This analysis was carried out for the T91 steel in a tensile test performed on standard specimen in quasi-static condition ( $10^{-3} \text{ s}^{-1}$ ) at room temperature (25 °C). From the start of the test until the specimen fracture, every 2 seconds the image of the specimen was recorded by the high-resolution camera PixeLINK® PL-B777 [105].

For what concern the optical procedure, the first requirement is represented by having images with sharp edges, in order to precisely distinguish the background and the specimen. To this end, brightness and contrast corrections of the images could be need. The final result should be gray-scale images represented by a matrix of  $n \times m$

pixels. At this point, an algorithm for the identification of edges can be used. With this aim, in this work an automatic edge detection algorithm, implemented in MATLAB<sup>®</sup>, was used (see Fig. 5.3). The calibration of the images was performed setting the average distance between the upper and lower edges inside the gage length equal to 3 mm (on the unloaded specimen). In this way the scale factor between pixels and millimetres was obtained.

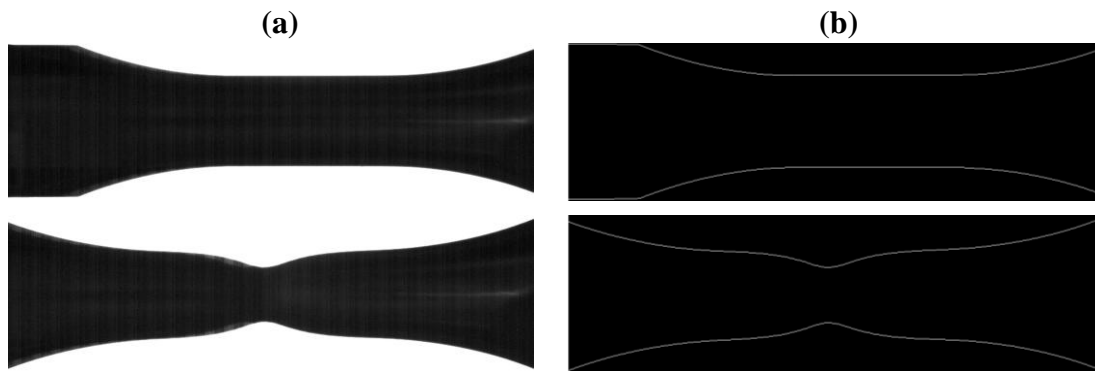


*Fig. 5.3: a) Corrected images recorded by the camera and b) the specimen edges obtained processing the images: first image (top) and last image before fracture (bottom).*

Once recognised the specimen edges, different approaches could be used to measure the minimum section and the curvature radius of the neck. First of all, assuming that the specimen deforms symmetrically, the average profile was calculated. Then, it was considered that in a specimen with low ratio between gage length and diameter, the necking should occur in the closeness of the centre of the gage length. Since the displacements of the specimen ends are known at each time, also the position of the centre of the gage length in the images can be easily identified at each time. Thus, starting from this reference point, a proper neighbourhood (the size has to be defined each time as a function of the specimen dimensions, materials properties, image resolution, etc) is defined (see Fig. 5.4). Inside it, the exact identification of the minimum section position and size (tagged as *a*) is performed. Moreover, the coordinate of all the points (pixels) included in the defined neighbourhood are fit with the expression of a circumference:

$$(x_i - x_c)^2 + (y_i - y_c)^2 = R^2 \quad (5.20)$$

where  $x_i$  and  $y_i$  are the coordinates of each point which defines the necking region, while  $x_c$ ,  $y_c$  are the coordinates of the centre of the osculating circle (see Fig. 5.4).  $x_c$ ,  $y_c$  and  $R$  have to be determined through the data fitting.

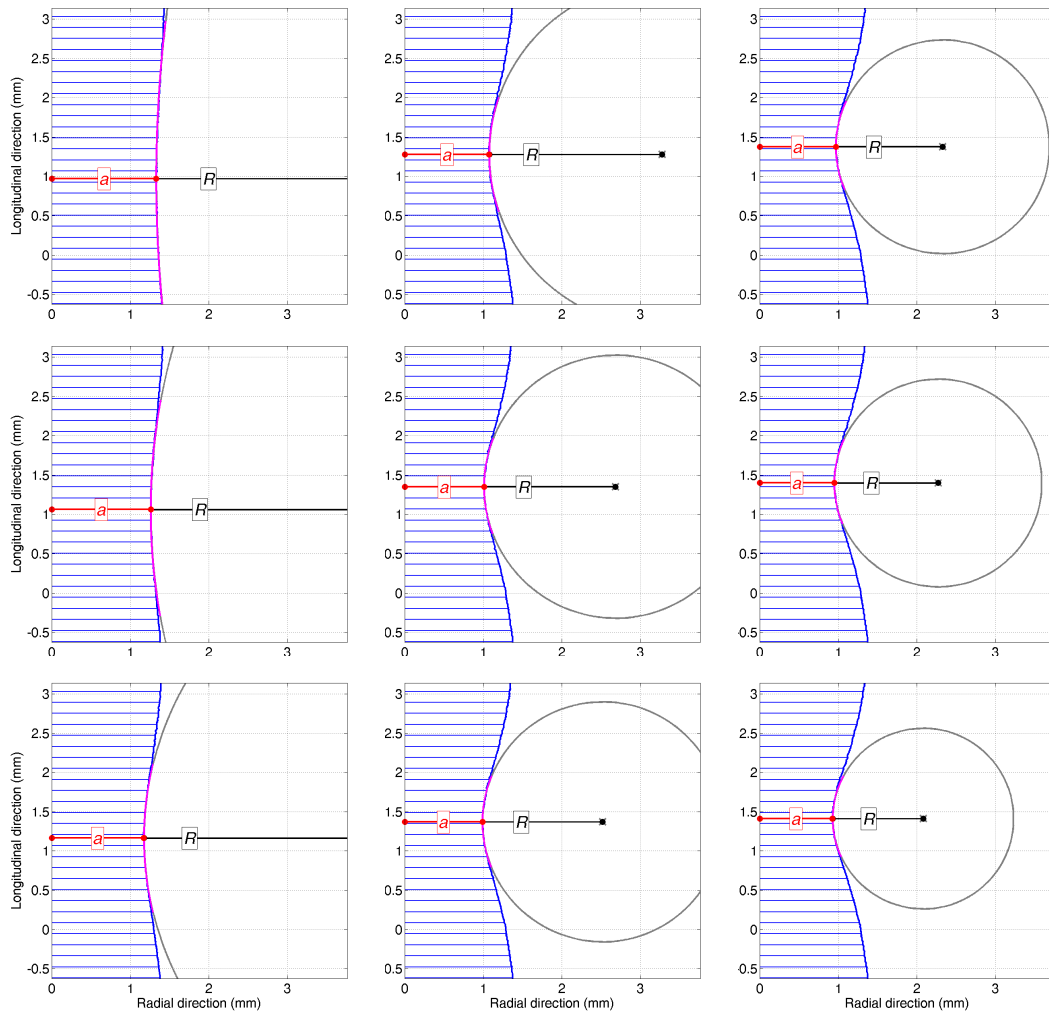


Fig. 5.4: Measurement of the minimum section of the specimen and the radius of the osculating circle during the localized necking phase (after instability starts).

In Fig. 5.4 the sequence of the obtained results for a test at  $10^{-3} \text{ s}^{-1}$  and  $25^\circ \text{C}$  performed on T91 steel is reported. The specimen is identified by the blue colour, the

neck is identified by the magenta colour, the minimum radius of the neck cross-section is indicated in red and labelled as  $a$ , and finally the osculating circle of the necking zone is plotted in gray and identified with its radius  $R$ . The first frame of the sequence corresponds to the time in which the localized necking is already present, since during uniform plastic deformation the radius of the osculating circle tends to infinity.

In Fig. 5.5 the time history profiles of  $a$  and  $R$  are shown. As it is expected,  $R$  asymptotically tends to infinity at the limit of the uniform deformation. In the diagrams the limit of the uniform deformation is reported: it is calculated as the time corresponding to the maximum of the engineering stress-strain curve. As it is possible to notice, a considerably portion of the tests occurs when the necking is localized.

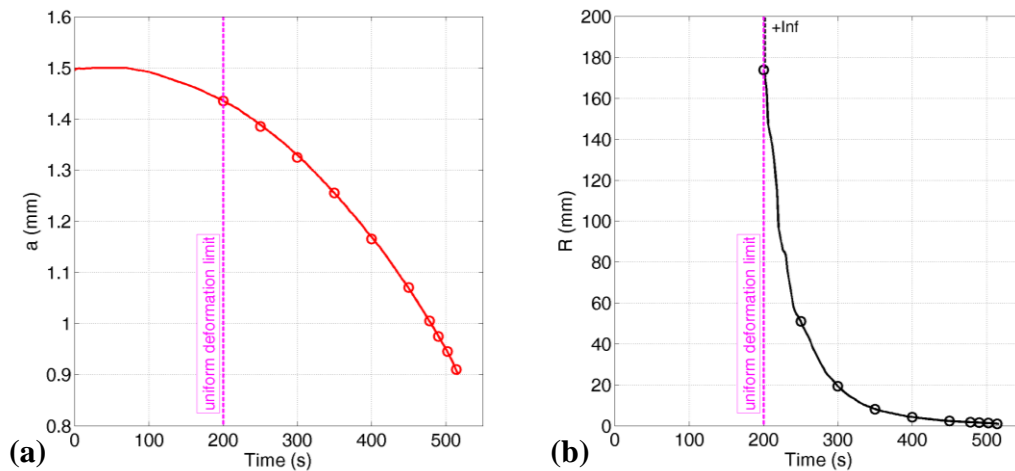


Fig. 5.5: a) Time history profiles of the minimum section and b) of the curvature radius of the neck during tensile test at  $10^{-3} \text{ s}^{-1}$  and  $25 \text{ }^\circ\text{C}$  on standard specimen of T91 steel.

In Fig. 5.6 the comparison between the engineering, true and equivalent (in according to Bridgman equation) curves is shown for the test considered until now. It is important to underline that the equivalent strain, which refers the curve identified by the blue colour, was obtained in according to the Eq. 5.8. Obviously, since the equivalent stress is based on the Bridgman equation (Eq. 5.19), the stress accuracy at

the connection point between the uniform and non-uniform deformation phases depends primarily by the precision of the measurements (stroke,  $R$  and  $a$ ). The Fig. 5.6 highlights that using specimen with low ratio between gage length and diameter the necking phase could represent a relevant part of the entire deformation process. Besides, as expected, the curve obtained using the Bridgman equation is a monotonically increasing curve. Thus, the study of the material behaviour at high strains should be done using the stress-strain relation proposed Bridgman. This last consideration is valid also for the identification of the material model parameters in order to extent the strength model validity at high strains.

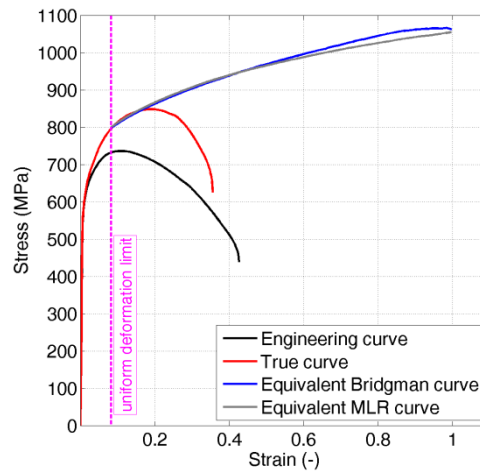


Fig. 5.6: Comparison between the engineering, true and equivalent (using the Bridgman and MLR models) curves for T91 steel at  $10^{-3} s^{-1}$  and  $25\text{ }^{\circ}C$ .

The procedure described above can be used in the same way also for test at high strain-rate. Generally, the main problem for dynamic tests is related to the characteristic low resolution (in space and time) of the high speed camera which can generate a poor quality in the extraction of the necking information.

Although the Bridgman equation represents the most known model to describe the stress and strain relationship in the post-necking phase of a round tensile test specimen, in some works large errors in the prediction of the stresses and strains on the minimum cross-section of the neck were found [161,162]. In particular, it was

noted that in the Bridgman model the assumption regarding the uniformity of both the strains and the flow stress all over the necking section and the adoption of a logarithmic plastic strain as governing variable for the evolution of the necking effect could be approximations far from the real stress and strain distribution in the necking region [163]. Besides, the difficulties and possible imprecision in the measurement of the necking profile could induce further errors in the material characterization. In order to overcome all these issues, recently Mirone [163] proposed the MLR model of necking effect which is based on the material-independency of the necking-induced modifications of the stress state, related to an opportunely reduced strain. With respect to the Bridgman model, the MLR model does not require the measurement of the necking curvature ( $R$ ), but only of the minimum section up to fracture ( $a$ ). The equivalent curve for T91 steel tested at quasi-static condition and room temperature calculated with the MLR model is reported in Fig. 5.6. For simplicity, only the expression proposed by Mirone [163] for the determination of the equivalent stress was used, while the equivalent strain refers to the Eq. 5.8.

Finally, in tensile tests also the non-uniformity of the other quantities, such as strain-rate, temperature and triaxiality, along the specimen should be taken into account [76,164-168]. In this case, also using very accurate mathematical expressions able to predict the effective stress-strain relation in the post-necking phase, this aspect is very difficult to consider through pure analytical approaches. In order to solve this issue, the most common solution is to use a numerical procedure [125].

### 5.3 Numerical inverse optimization

As explained before, the effective stress and strain in a round specimen tested in tension could be quite complicated to determine because the necking phase is a considerable part of the entire test duration (ductile materials). Moreover, non-uniform stress, strain, strain-rate, and temperature distributions could develop inside the specimen. To correctly compute these effects, a possible solution is to reproduce

numerically the test, i.e. to perform a numerical simulation with the same experimental test conditions. Indeed, the material behaviour in a Finite Element Method (FEM) simulation could be simultaneously affected by all the aspects mentioned above.

However, the numerical simulation could correctly describe the experimental test studied only if its results are in agreement to the experimental ones. In order to achieve this condition, the material model used in the FEM model should be representative of the material behaviour. Since at high strains an accurate identification of the strength model parameters is quite complicated to achieve in analytical way, as discussed until now, a numerical optimization procedure based on an inverse method should be performed to overcome this issue, as described in [146].

The main objective of such an inverse optimization method is the determination of a selected set of unknown parameters (of the chosen strength model) in a numerical model. Starting from a trial point, the unknown parameters are estimated iteratively by comparing experimentally measured with numerically computed quantities for the same material test conditions. The great advantage of this procedure is that no hypothesis about the internal specimen or component stress-strain, temperature, or strain-rate fields is made. In fact, the comparison is made in terms of macroscopic quantities that, in general, are force and displacement. The main disadvantage of inverse methods is the high computational times that these algorithms need in an iterative procedure using many FEM simulations. The number of iterations increases dramatically when the degrees of freedom of the problem grow or the trial parameters are far from optimum.

The first phase of a numerical optimization procedure concerns the creation of the model. In this work two specimen geometries were considered, the standard and the miniaturized ones (see Fig. 3.6 and 3.9) and the same approach in the realization of the models was used. The FE models consist of 2D-axial-symmetric elements (4 nodes) with 1 point of integration and hourglass control. The number of elements in the minimum radius is 21 as shown in Fig. 5.7. This choice is in accordance with the results shown in [169,167], in which for a specimen geometry similar to the standard

one used in this work, the mesh sensitivity on the results was performed. The loading is prescribed in terms of velocity profile,  $v(t)$ , applied to one end of the specimen, while the other one is fixed. In order to simulate the tests carried out with the Hopkinson Bar, in which both the specimen ends move, the assigned velocity profile consists in the difference between both the experimental velocities of the specimen ends ( $\Delta v$ ). The force is measured in correspondence of the specimen cross-section at the end of the gage length. When the stroke was experimentally measured by means of an extensometer, during the corresponding simulation, the elongation of the specimen was measured as the difference between the displacements of the two nodes positioned on the specimen edge in correspondence of the ends of the gage length (nodes A and B of Fig. 5.7). Instead, for the other loading conditions the displacement is measured on the specimen end (displacement of the node C of Fig. 5.7), which is directly related to the assigned velocity profile.

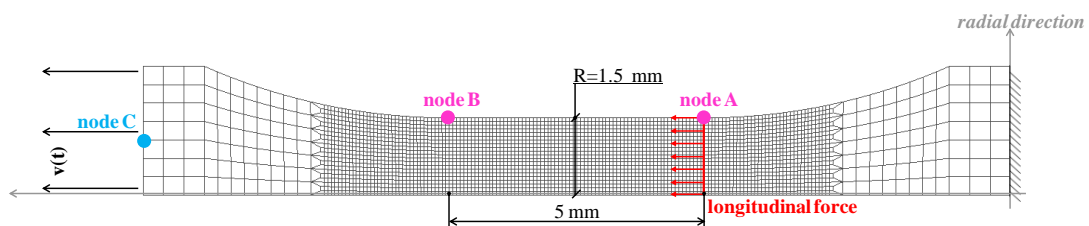


Fig. 5.7: Finite element model for standard smooth specimen.

The numerical inverse optimization could be a Single-Objective Optimization (SOO) or a Multi-Objective Optimization (MOO). In the first case, the iteration procedure for the determination of the model parameters has the aim to obtain the best fit with one specific experimental target, i.e. the force versus stroke curve of one loading condition.

On the other hand, if the final goal is the determination of the set of model parameters, which reproduces as best as possible the global behaviour of material in different loading conditions, a MOO should be performed. With this approach all the tests, at different strain-rates and temperatures have to be simultaneously simulated.

Once established the material model to optimize and the optimization strategy, the numerical inverse analysis can be run. In this work, the optimization of the parameters was performed with a dedicated algorithm included in the software LS-OPT [170] that manages the parameter variation strategy, runs the numerical simulation, performed in LS-DYNA [139], analyzes the results, and extracts the optimum set of parameters (see Fig. 5.8) [171,172]. The simulations were performed with an explicit integration method and in order to reduce the computational time for low strain-rate tests the deformation rate was increased with respect to the experimental conditions (this aspect will be further discussed).

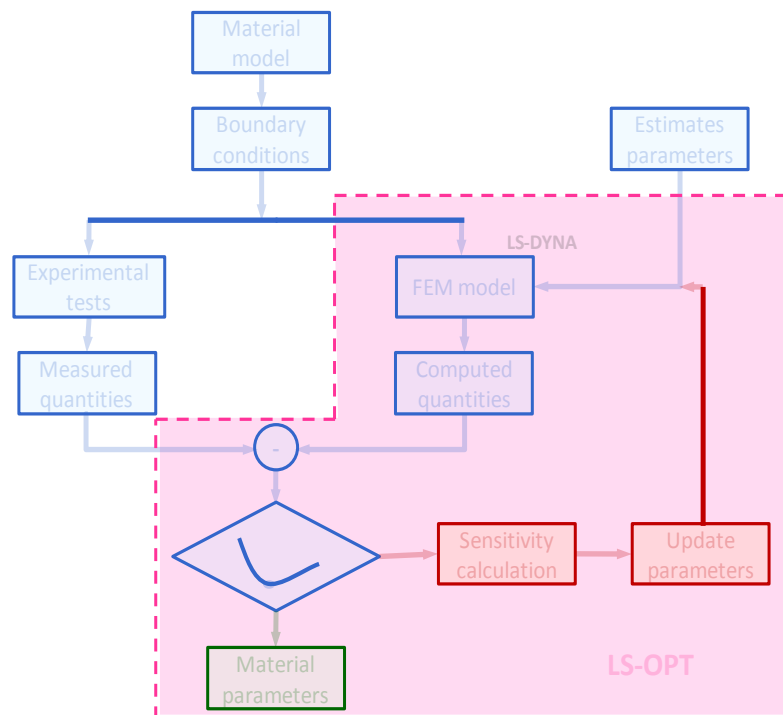


Fig. 5.8: Scheme of the numerical inverse method applied for the identification of the material model parameters.

It is important to underline that the numerical inverse optimization is a common procedure used to identify the material model parameters starting from different kinds of test, such as: compression/tension/shear tests, Taylor test, expanding ring test, Dynamic Tensile Extrusion, etc. [31,33,171,173-180].

### 5.3.1 Numerical Single-Objective Optimization

In this work, several single-objective optimizations were performed to determine the equivalent stress vs. equivalent strain relation at different loading conditions for the T91 steel and Glidcop Al-15. For the present study, the single objective function was the Mean Squared Error (MSE)  $\Phi_k$ , defined as [170]:

$$\Phi_k = \frac{1}{P} \sum_{p=1}^P W_p \cdot \left( \frac{f_p(x) - G_p}{s_p} \right)^2 \quad (5.21)$$

where  $P$  is the number of points in which the MSE is calculated,  $G_p$ , varying  $p$ , are the values on the target curve  $G$  and  $f_p(x)$  the corresponding components of the computed curve  $f$ .  $W_p$  and  $s_p$  are scale functions for each point  $p$  and finally  $x$  is the design vector. Several definitions of the MSE are possible by varying the value of the scale function  $s_p$ . In this analysis, the normalized MSE is considered with  $s_p$  constant and equal to the maximum of  $G$ .

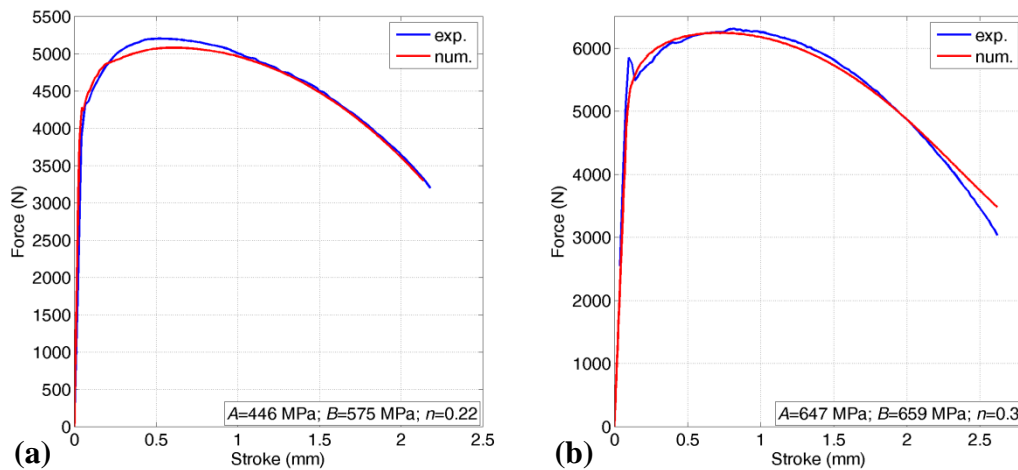


Fig. 5.9: Comparison between numerical and experimental force vs. displacement curve for a) quasi-static ( $\dot{\epsilon} = 10^{-3} \text{ s}^{-1}$ ;  $T = 25 \text{ }^\circ\text{C}$ ) and b) high strain-rate ( $\dot{\epsilon} = 10^3 \text{ s}^{-1}$ ;  $T = 25 \text{ }^\circ\text{C}$ ) tests on standard specimens ( $D = 3 \text{ mm}$ ;  $L = 5 \text{ mm}$ ) of T91 steel.

For what concern the T91 steel, the simulations were performed using the J-C model [121], which was widely discussed in the section 4.3.1. Since in the SOO the final goal is to obtain the best fit with the experimental force versus stroke curve of a specific loading condition, in this work only the strain hardening part of the model was optimized ( $\sigma = A + B \cdot \varepsilon_{pl}^n$ ), in which also the effects of temperature and strain-rate were included. For each experimental curve, the fitting of the experimental data was performed (see Fig. 5.9), which is basically equivalent to the calculation of true stress-true strain data starting from experimental force-stroke curve. By performing this calculation numerically (instead of a standard analytical approach), it is possible to account of the change in shape of the specimen during necking. The deformation mechanism of the specimen is supposed to be a function only of the stress-strain relation of the material and not of the test speed. After an analysis of the experimentally deformed shapes, this hypothesis could be considered as reasonable (i.e., inertia effects could be neglected). Generally, only the necking location is influenced by the inertia effects [168]. The failure condition of each curve was numerically obtained in correspondence to the stroke at which the specimen failure occurred: for each curve, the maximum strain is the equivalent plastic strain at failure (average value in the necking section).

The equivalent stress vs. equivalent plastic strain curve obtained for each testing condition is reported in Fig. 5.10 (solid line) and compared with the true stress vs. true plastic strain calculated analytically, Eq. 4.5 and 4.6 (dashed line). As expected, until the instability occurs, the two curves are closed, while after the instability the analytical calculation does not allow to correctly evaluate the stress-strain relation.

The goodness of the procedure was confirmed by the results obtained from the models of the two geometries (3 mm diameter specimens and 1.5 mm diameter specimens) in quasi-static tests: the same J-C model was obtained (see Fig. 5.11a), i.e. if the material properties are based on the same strength model, they must be geometry independent. Instead, in Fig. 5.11b, the curve obtained with the numerical optimization, simulating the test performed in quasi-static condition at room temperature, is compared with that one calculated through the Bridgman equation

(Eq. 5.19). Considering the inevitable approximations of both procedures, the two curves are relatively close.

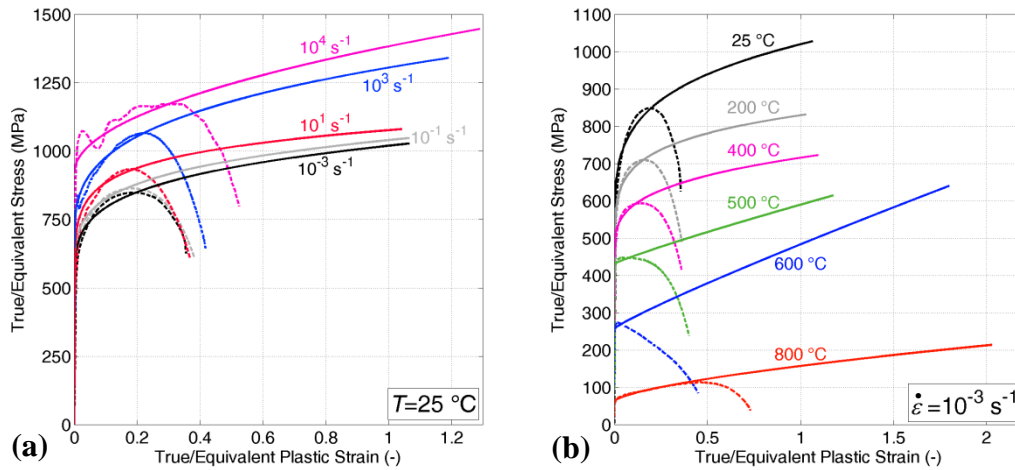


Fig. 5.10: True (dashed lines) and equivalent (solid lines) stress vs. plastic strain curves for T91 steel: a) at room temperature varying the strain-rate and b) at quasi-static conditions varying the temperature.

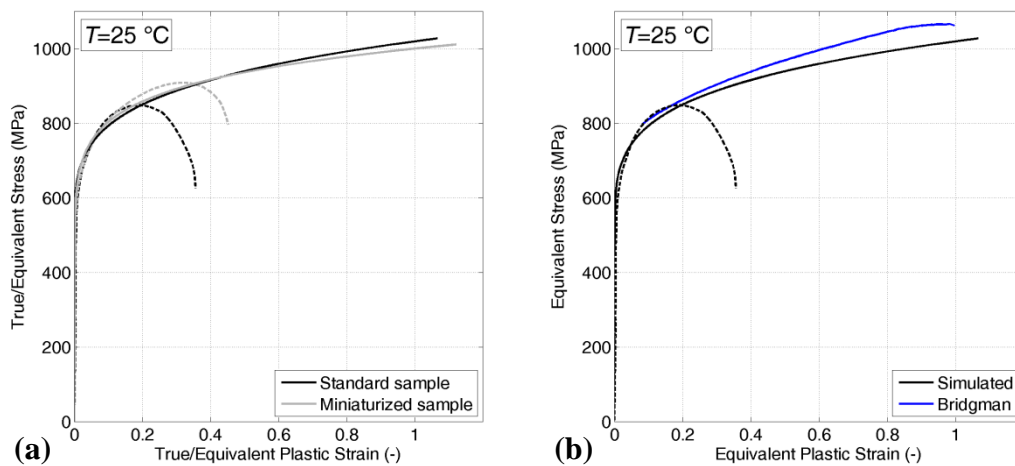


Fig. 5.11: a) Comparison between the true (dashed lines) and equivalent (solid lines) curves obtained for the standard and miniaturized specimens and b) comparison between the curves obtained through the numerical inverse optimization and by using the Bridgman equation for T91 steel at  $10^{-3} \text{ s}^{-1}$ .

Once the equivalent stress vs. equivalent plastic strain curves were obtained, the thermal softening and the strain-rate sensitivities of the material could be analyzed in order to identify the J-C parameters as described in section 4.4.1. With this prospective, the stress values (obtained at the fixed value of strain of 20%) were normalized with respect to the stress value obtained for quasi-static test at room temperature. The 20% data were considered as representative of the behaviour over a wider range in strain, also because, in accordance with the J-C formulation, the behaviour is the same at each strain (both in temperature and strain-rate). For the evaluation of the temperature sensitivity, the data were analytically fitted in according with the term of the J-C model which considers the thermal softening. In order to get the best level of accuracy, as explained in section 4.4.1, both  $m$  and  $T_m$  were considered as fitting variables. Similarly, it was possible to obtain the estimation of J-C model parameters  $C$  and  $\dot{\epsilon}_0$ , by performing a linear piecewise interpolation of the data. In Fig. 5.12, the stress data and their interpolation are compared with literature data [121] for two different types of steel. For the strain-rate sensitivity, the stress level is saturated at the quasi-static value for strain-rate less  $\dot{\epsilon}_0$ , accordingly to the implementation of the J-C model in LS-DYNA.

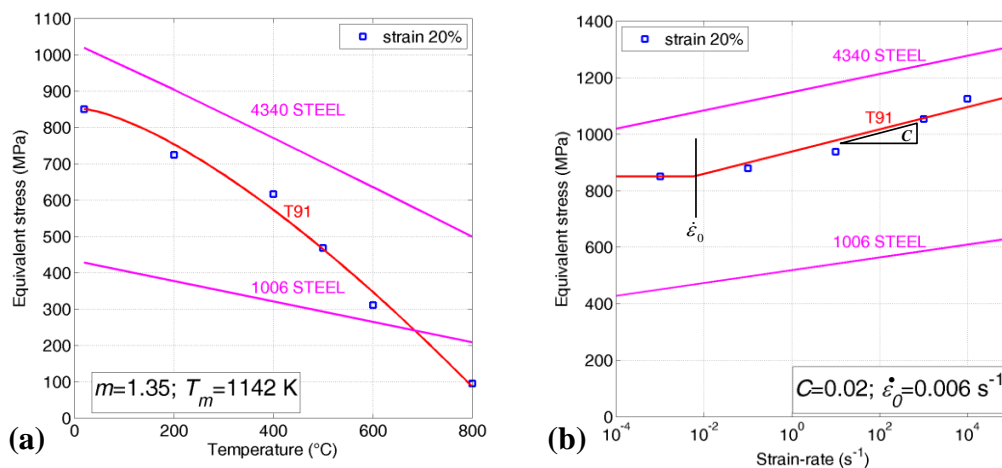


Fig. 5.12: a) Temperature and b) strain-rate sensitivity for T91 steel.

At this point, all the parameters of the J-C model are known:  $A$ ,  $B$  and  $n$  from the numerical optimization of the quasi-static test (see Fig. 5.9a), while  $C$ ,  $\dot{\epsilon}_0$ ,  $m$  and  $T_m$  from the analytical fitting of the experimental data. The set of parameters is reported in Table 5.1 and in Fig. 5.13 is shown the comparison between the curves obtained from each SOO and the curves predicted by the J-C model by using the set of parameters extracted. The curves are particularly in disagreement at 600 and 800 °C in quasi-static condition because the material exhibits a sharp changing of the mechanical behaviour which can not be correctly described with the J-C model.

Table 5.1: J-C model parameters for T91 steel obtained through a numerical-analytical procedure.

$A$	$B$	$n$	$C$	$\dot{\epsilon}_0$	$m$	$T_m$
MPa	MPa	-	-	$s^{-1}$	-	K
446	575	0.22	0.02	$6 \cdot 10^{-3}$	1.35	1142

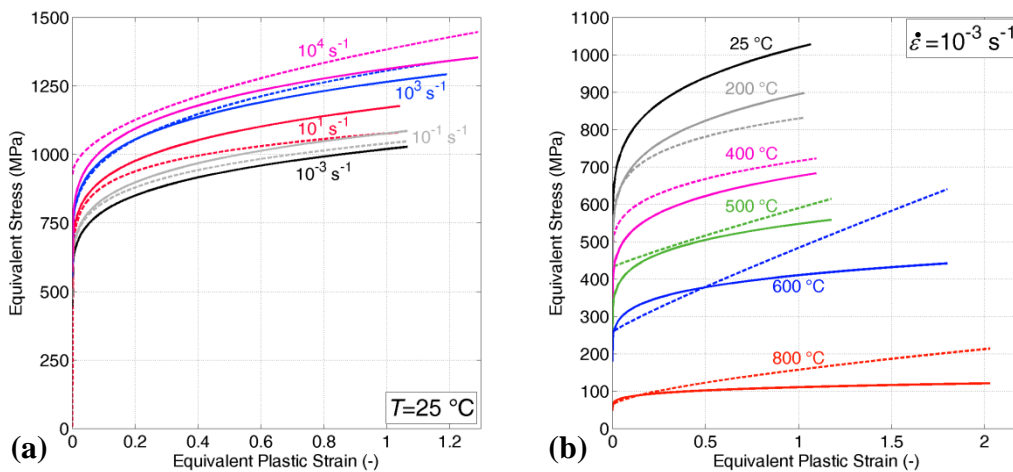


Fig. 5.13: Comparison between the equivalent stress vs. equivalent plastic strain curves obtained from each SOO (dashed lines) and by using the J-C model (Table 5.1) with a unique set of parameters (solid lines) for T91 steel: a) at room temperature varying the strain-rate and b) in quasi-static condition varying the temperature.

Table 5.2: Root Mean Squared Error at different temperatures and strain-rates.

Test condition		RMSE
$\dot{\epsilon}_0$ (s <sup>-1</sup> )	$T$ (°C)	(MPa)
$10^{-3}$	25	0.01
$10^{-3}$	200	4.44
$10^{-3}$	400	5.08
$10^{-3}$	500	3.58
$10^{-3}$	600	9.77
$10^{-3}$	800	5.44
$10^{-1}$	25	2.79
$10^1$	25	8.40
$10^3$	25	2.84
$10^4$	25	6.80
		<b>49.14</b>

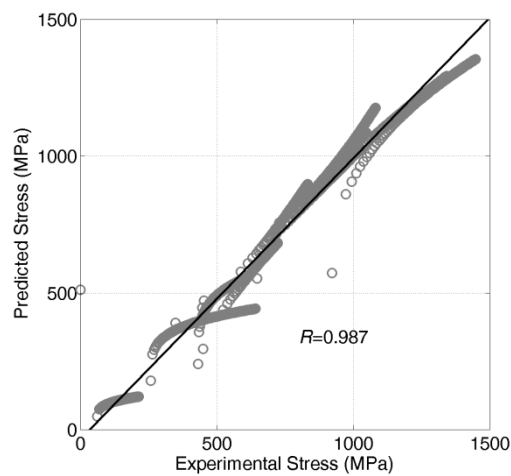


Fig. 5.14: Correlation between predicted and experimental stress over the entire range in temperature and strain-rate up to fracture.

The RMSE (Eq. 4.13) between the curves obtained from each SOO and the curves predicted by the J-C model was calculated for each test condition and the results are reported in Table 5.2. The correlation coefficient of these data is 0.987, which is

almost the same of that obtained calibrating the model up to 15% of true plastic strain ( $R=0.986$ ). The stress correlation diagram is shown in Fig. 5.14.

The same kind of analysis was performed for Glidcop Al-15. In Fig. 5.15, the results of each numerical optimization are compared with the analytical true stress vs. true strain curve. Also for this material, the analytical calculation describes correctly the stress-strain relationship until the instability condition is reached.

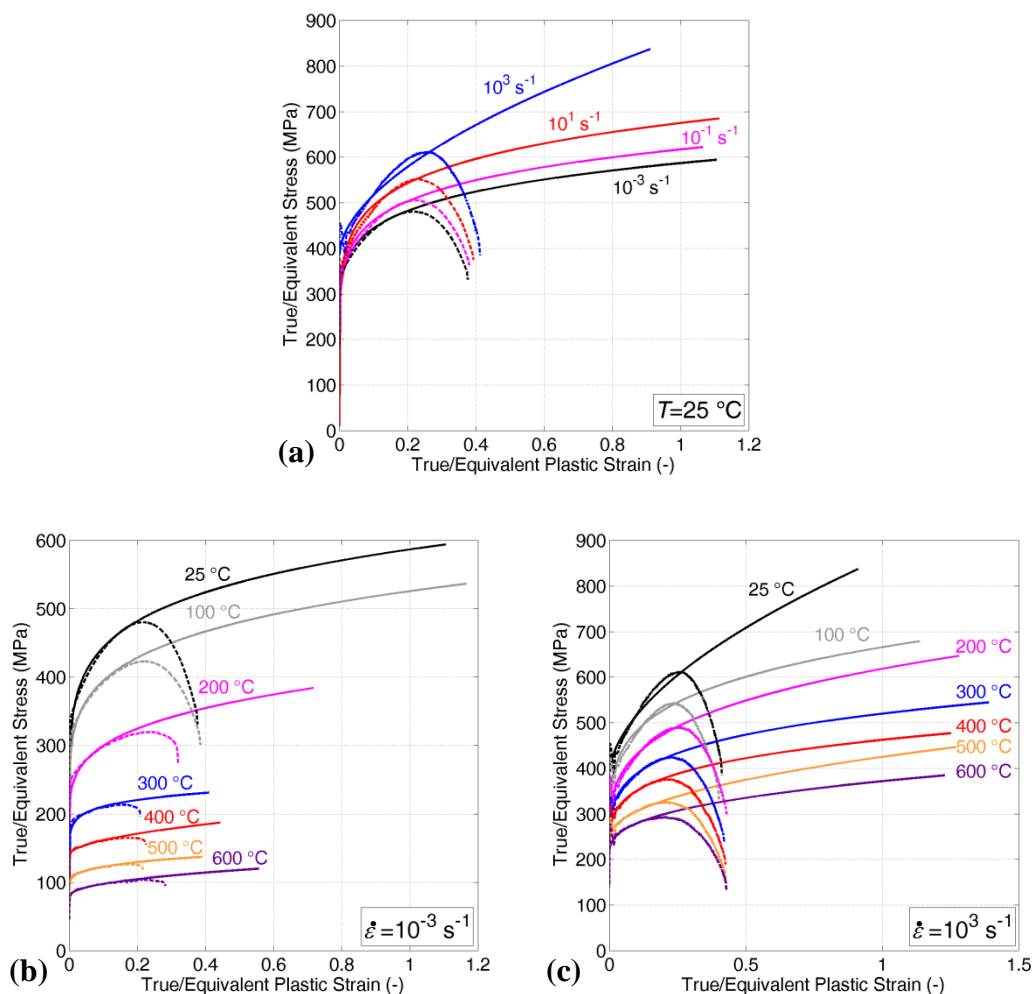


Fig. 5.15: True (dashed lines) and equivalent (solid lines) stress vs. plastic strain curves for Glidcop Al-15: a) at room temperature varying the strain-rate, b) at quasi-static conditions varying the temperature and c) at high strain-rate loading conditions varying the temperature.

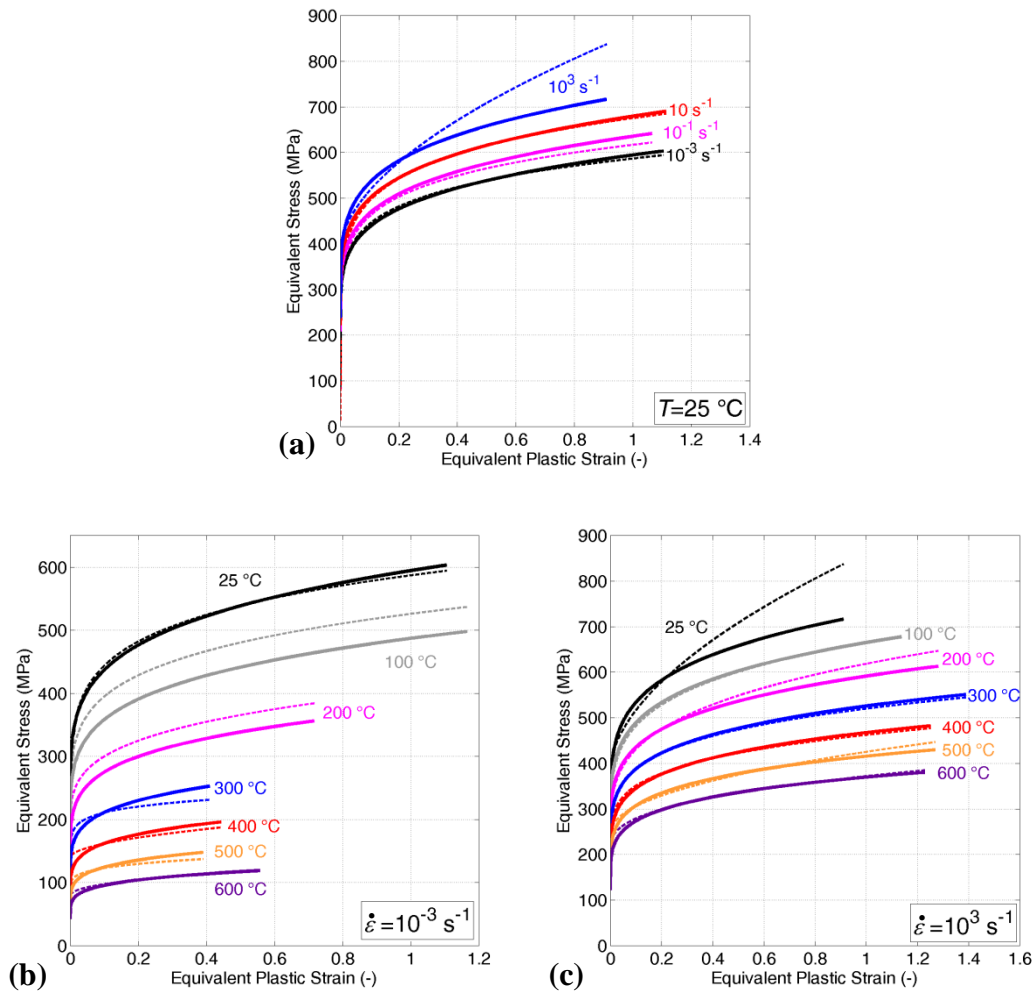


Fig. 5.16: Comparison between the equivalent stress vs. equivalent plastic strain curves obtained from each SOO (dashed lines) and by using the modified Z-A model (Table 5.3) with a unique set of parameters (solid lines) for Glidcop Al-15: a) at room temperature varying the strain-rate, b) in quasi-static condition varying the temperature and c) at high strain-rate loading conditions varying the temperature.

Table 5.3: Modified Z-A model parameters for Glidcop Al-15 obtained using the analytical multi-objective optimization of the equivalent stress vs. equivalent plastic strain curves up to fracture.

$c_1$	$c_2$	$c_3$	$c_4$	$c_5$	$c_6$	$n$
MPa	MPa	K <sup>-1</sup>	K <sup>-1</sup>	-	K <sup>-1</sup>	-
194.6	400	$2.6 \cdot 10^{-3}$	$1.3 \cdot 10^{-5}$	$1.4 \cdot 10^{-2}$	$1.1 \cdot 10^{-4}$	0.217

In section 4.4.2, the modified Zerilli-Armstrong model (Eq. 4.17) exhibited a particular suitability to describe the mechanical behaviour of Glidcop Al-15 up to 15% of true plastic strain. For this reason, the same procedure for the extraction of the model parameters was used again to investigate if the modified Z-A model is suited to predict the mechanical response of this material up to fracture. In this case, the analytical multi-objective optimization was based on the fitting of all the equivalent stress vs. equivalent plastic strain curves at different strain-rates and temperatures (see Fig. 5.16). The set of parameters obtained is reported in Table 5.3.

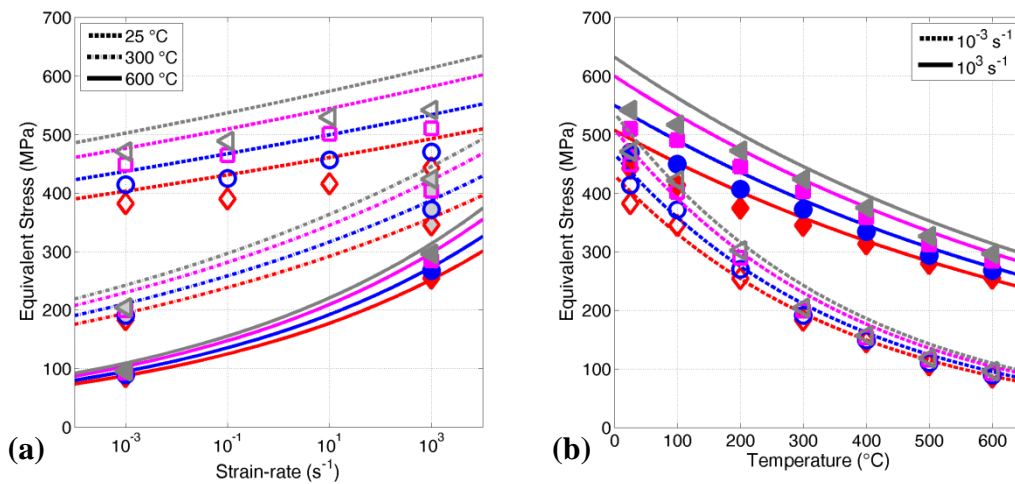


Fig. 5.17: a) Strain-rate and b) temperature sensitivities of Glidcop Al-15 using the modified Z-A model. ( $\diamond$ : 5%,  $\circ$ : 10%,  $\square$ : 20% and  $\triangleleft$  30% of equivalent plastic strain).

In Fig. 5.16, the equivalent stress vs. equivalent plastic strain curves obtained from each SOO (dashed lines) are compared with the curves reproduced by using the calibrated modified Z-A model (solid lines). These qualitative comparisons confirm that this strength model is appropriated to describe the mechanical behaviour of Glidcop Al-15 up to fracture at different strain-rates and temperatures. As said before, this result is mainly due to the suitability of this model to describe the coupled effect of temperature and strain-rate, and temperature and strain on the material response. This last aspect can be easily appreciated observing the Fig. 5.17,

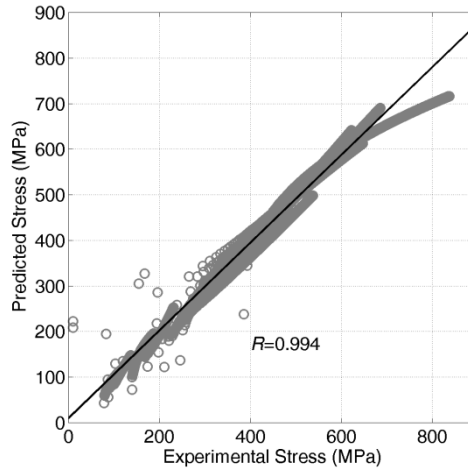
in which both the strain-rate and temperature sensitivities change as function of temperature and strain-rate, respectively, and also strain.

Table 5.4: Root Mean Squared Error at each loading condition for Glidcop Al-15.

Test condition		RMSE
$\dot{\epsilon}_0$ (s <sup>-1</sup> )	$T$ (°C)	(MPa)
10 <sup>-3</sup>	25	0.21
10 <sup>-3</sup>	100	1.21
10 <sup>-3</sup>	200	0.83
10 <sup>-3</sup>	300	0.42
10 <sup>-3</sup>	400	0.26
10 <sup>-3</sup>	500	0.22
10 <sup>-3</sup>	600	0.10
10 <sup>-1</sup>	25	0.48
10 <sup>1</sup>	25	0.32
10 <sup>3</sup>	25	1.96
10 <sup>3</sup>	100	0.14
10 <sup>3</sup>	200	0.62
10 <sup>3</sup>	300	0.14
10 <sup>3</sup>	400	0.15
10 <sup>3</sup>	500	0.29
10 <sup>3</sup>	600	0.18
		7.54

The RMSE (Eq. 4.13) between the curves obtained from each SOO and the curves predicted by the modified Z-A model was calculated for each test condition and the results are reported in Table 5.4. In this case the resulting correlation coefficient,  $R$ , is 0.994, at which corresponds the diagram of Fig. 5.18. The value of  $R$  is very similar to that obtained with the same model calibrated up to 15% of true plastic

strain, which was 0.995; thus also extending the validity of the model up to fracture, the model accuracy remains substantially the same.



*Fig. 5.18: Correlation between predicted and experimental stress over the entire range in temperature and strain-rate up to fracture for Glidcop Al-15.*

Although this combined numerical-analytical procedure for the identification of the strength model parameters allows to correctly consider the material response until fracture, the results are affected by two different types of approximation:

- the influence of the non-uniformity of strain-rate and temperature in the specimen is neglected. In this way, each experimental result is reproduced by a stress-strain relation and the obtained strength model could be considered representative of an average behaviour of the material at the nominal strain-rate and/or temperature condition of the test (i.e., strain-rate and temperature are considered constant in the specimen);
- the self heating of the material due to the adiabatic condition (conversion of mechanical work into heat) in high strain-rate tests is ignored.

To overcome these issues, a possible solution is to perform a numerical Multi-Objective Optimization.

### 5.3.2 Numerical Multi-Objective Optimization

In a numerical multi-objective optimization, all the tests at different strain-rates and temperatures can be simultaneously simulated. The final goal of this procedure is the determination of the global set of material model parameters, which reproduces as best as possible all the tests [150,125]. In this case, both the thermal softening and the strain-rate parameters should be estimated considering the variation of the corresponding properties on the basis of multiple data curves.

This procedure was used to optimize the J-C model for T91 steel. All the tests at strain-rate lower than  $10^2 \text{ s}^{-1}$  were assumed and simulated as isothermal, while the other tests were considered to be adiabatic. The dynamic tests were simulated imposing the real velocity profiles. Instead, in the low strain-rate tests the deformation rate was increased in order to reduce the computational time. This was done by performing the simulation at constant velocity of 10 m/s. In order to correctly consider the strain-rate hardening and to eliminate the self-heating of the specimen two expedients have to be used: the strain-rate parameter  $\dot{\epsilon}_0$  has to be scaled with respect to the used velocity profile and the specific heat capacity at constant pressure,  $C_p$ , has to be increased (to simulate the isothermal behaviour).

For what concerns the optimization procedure, if the different objectives conflict, no single solution can be considered optimum with respect to all the objectives [181]. The optimal solution is such that any further attempts to optimize on a single objective lead to worse results for the other(s) [182]. Mathematically, the MOO unconstrained problem is defined as follows:

$$\min F(\Phi_1, \Phi_2, \dots, \Phi_N) \quad (5.22)$$

where  $F$  represents the multi-objective function and  $\Phi_k = \Phi_k(x_1, x_2, \dots, x_n)$  ( $k = 1, \dots, N$ ) are the various objective functions with  $x_i$  ( $i = 1, \dots, n$ ) the  $n$  design variables. In particular, the MOO function is defined as:

$$F = \sum_{k=1}^N \omega_k \Phi_k \quad (5.23)$$

where  $\omega_k$  are the weights to assign to each single objective function. It is important to note that each objective function has a target. For the analysis performed in this work, all the weights  $\omega_k$  are set to unity, so all the objectives are equally important.

The different strategies to optimize the J-C model, as explained in section 4.4.1, could be adopted also with this procedure. In this case, three different procedures, called SET 1, 2 (2A and 2B), and 3, were used and the results are summarized in Table 5.5.

*Table 5.5: J-C model parameters for T91 steel obtained as results of the MOO procedure: the parameters fixed a priori for each case are reported in italic.*

	<b>A</b>	<b>B</b>	<b>n</b>	<b>C</b>	$\dot{\epsilon}_0$	<b>m</b>	<b>T<sub>m</sub></b>	<b>rRMSE</b>
	MPa	MPa	-	-	s <sup>-1</sup>	-	K	%
SET 1	<i>446</i>	601	0.186	0.039	10.5	<i>1.35</i>	<i>1142</i>	3.58
SET 2A	<i>446</i>	511	0.221	0.022	<i>1·10<sup>-3</sup></i>	<i>1.35</i>	<i>1142</i>	6.50
SET 2B	<i>475</i>	545	0.221	0.022	<i>1</i>	<i>1.35</i>	<i>1142</i>	6.50
SET 3	<i>446</i>	592	0.174	0.027	6.27	...	...	4.40

For SET 1, the optimization was performed on the strain-hardening and strain-rate parts of the model, while the thermal softening parameters were fixed to those analytically obtained on the basis of quasi-static curves varying the temperature ( $m=1.35$  and  $T_m=1142$  K, Table 5.1). The parameter  $A$  was fixed to that obtained for the quasi-static test at room temperature ( $A=446$  MPa). The variables for the optimization were  $B$ ,  $n$ ,  $C$ , and  $\dot{\epsilon}_0$ . The optimized set of parameters produced a medium percentage rRMSE (relative Root Means Square Error), i.e. the root of the average value of each MSE (Eq. 5.21), of 3.6%. This model could be applied in case

of dynamic loading conditions with self-heating (e.g. impacts) and for quasi-static loading conditions at different temperatures.

For SET 2A and SET 2B, the procedure was similar to that used for SET 1, but in this case the strain-rate threshold was fixed equal to the lowest strain-rate level of the tests ( $10^{-3} \text{ s}^{-1}$ ) in case 2A and equal to  $1 \text{ s}^{-1}$  in case 2B (as the original J-C formulation). The parameter  $A$  was fixed to that obtained for the quasi-static test at room temperature for case 2A ( $A=446 \text{ MPa}$ ) and properly scaled for case 2B, in accordance with the variation of the strain-rate threshold ( $A=475 \text{ MPa}$ ). The variables for the optimization were  $B$ ,  $n$ , and  $C$ . The optimized sets of parameters produce a medium percentage error of 6.5% and much more precise results with respect to the previous set were obtained for the low strain-rate loading condition. The set 2B could be suitable for numerical simulations performed in FE codes in which the J-C model is implemented in its original formulation ( $\dot{\epsilon}_0=1 \text{ s}^{-1}$  without threshold, i.e. different from LS-DYNA).

In case of SET 3, the effect of the self-heating was included in the strain-rate sensitivity, i.e. the thermal part of the J-C model was considered to be unity. The parameter  $A$  was fixed for the single optimization of the quasi-static test at room temperature ( $A=446 \text{ MPa}$ ). The variables for the optimization were  $B$ ,  $n$ ,  $C$ , and  $\dot{\epsilon}_0$ . The optimized set of parameters produced a medium percentage error of 4.4% and should be used in dynamic loading conditions.

By the evaluation of the rRMSE, it is possible to conclude that the best set of parameters is the SET 1, for which the comparison between experimental and numerical results in terms of force versus displacement is reported in Fig. 5.19. The greatest error lies in the quasi-static test, but for low and high strain-rate tests, the model is able to reproduce the material behaviour with a good level of accuracy.

Looking the results of the numerical simulations, it is interesting to analyze the stress and strain fields (and the related quantities) which develop inside the specimen during the deformation. In the following, the numerical simulation performed for the miniaturized sample at the nominal strain-rate  $10^4 \text{ s}^{-1}$  and room temperature by using the parameters of SET 1 will be considered. In Fig. 5.20, it is possible to observe the

results at two different simulation instants: in the *pre-necking* phase (at  $40 \mu\text{s}$  from the start of the test), where the different quantities are uniformly distributed along the gage length of the specimen, and in the *necking* phase (at  $80 \mu\text{s}$ ), in which they are concentrated around the minimum cross-section. These results allow to observe the distribution of strain-rate, temperature and triaxiality (i.e. the ratio between the von Mises stress and the pressure) that usually are very complicated to evaluate.

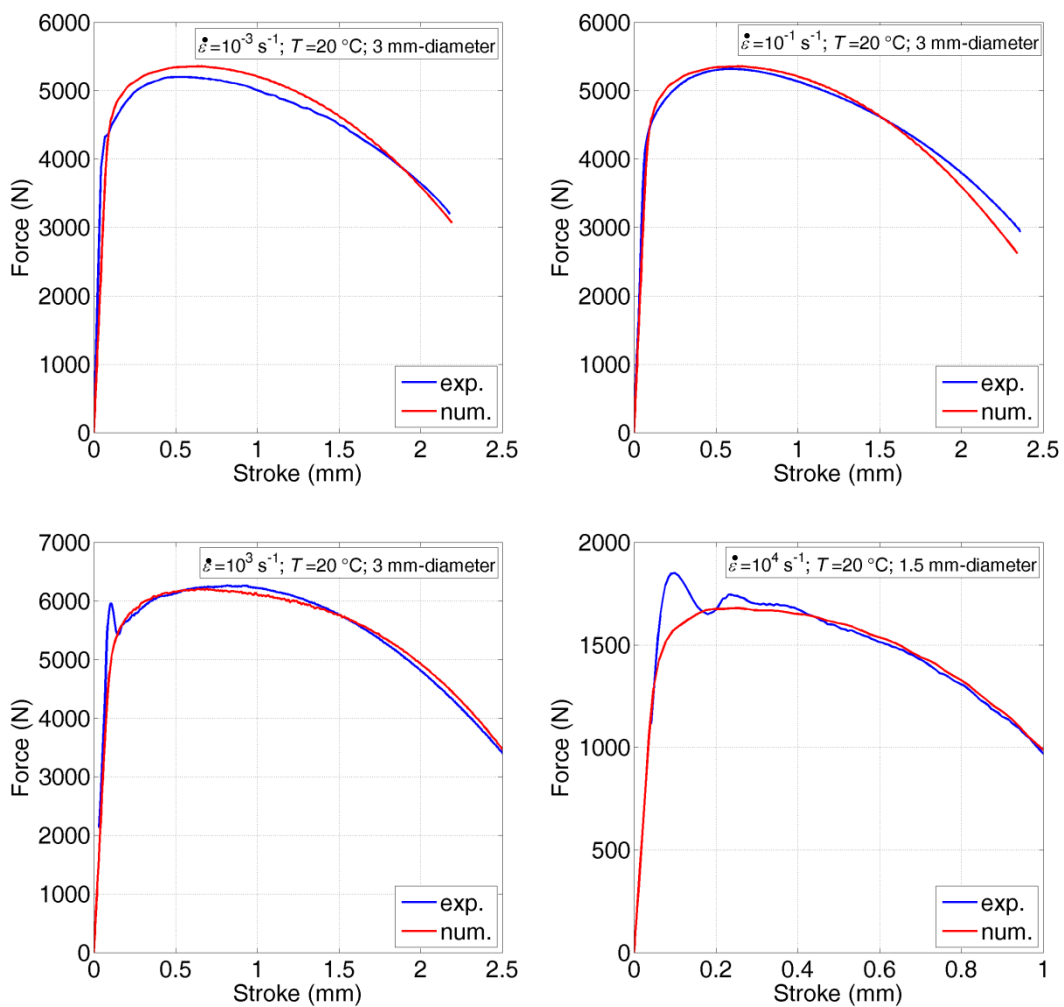


Fig. 5.19: Results of the optimization (SET 1): comparison between numerical and experimental force vs. displacement curves for quasi-static, low and high strain-rate tests performed on T91 steel.

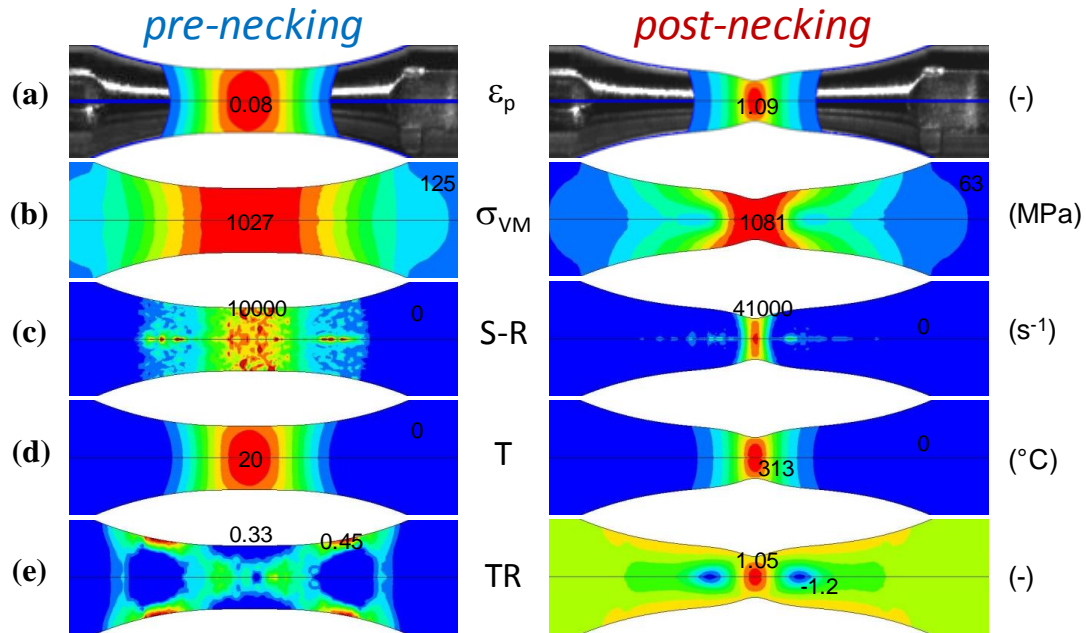


Fig. 5.20: Distributions of: a) equivalent plastic strain, b) equivalent stress, c) strain-rate, d) temperature and e) triaxiality factor inside a miniaturized specimen of T91 steel simulated at  $10^4 \text{ s}^{-1}$  and  $25 \text{ }^\circ\text{C}$  by using the parameters of SET 1 at  $40 \mu\text{s}$  (left) and  $80 \mu\text{s}$  (right) from the start of the test.

As expected, due to the concentration of the flow stress in the necking area, the strain-rate and temperature grow up considerably, reaching, at the end of the test, values greater than the nominal ones at the beginning of the test. Thus, it is evident that the specimen self-heating and the strain-rate localization should be strictly considered during the study of the material behaviour, in particular at high plastic strains. Also the triaxiality factor increases a lot in the necking region with respect to the value expected for a tensile tests.

Another interesting aspect of the non-uniform distribution of the mechanical quantities (plastic strain and Von Mises stress) inside the specimen can be observed in Fig. 5.21. Always referring to the same simulation, the equivalent stress vs. equivalent plastic strain curves in three different points of the specimen (solid lines) were extracted and compared with the model predictions (parameters of SET 1). Two curves are reported: one was obtained neglecting the thermal softening (dashed line)

and the other one neglecting both thermal softening and strain-rate hardening (dash-dotted line). The points P1 and P2 correspond to the centre and to the end of the gage length, respectively, while P3 is far from central part of the specimen.

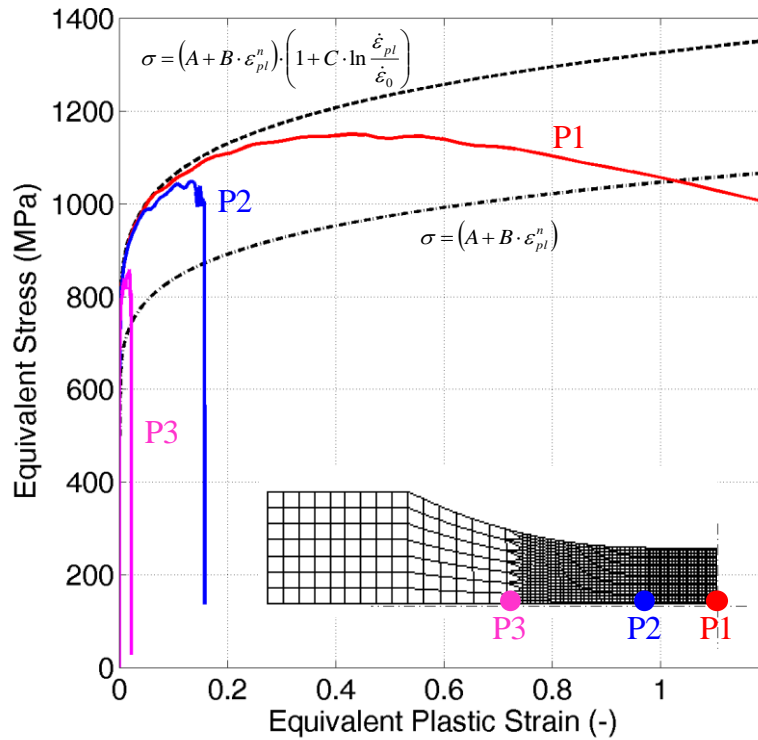


Fig. 5.21: Equivalent stress vs. equivalent plastic strain curves in three different points of the specimen P1, P2 and P3 (solid lines) compared with the model predictions obtained neglecting only the thermal softening (dashed line) and neglecting both strain-rate hardening and thermal softening (dash-dotted line) for T91 steel at nominal strain-rate  $10^4 \text{ s}^{-1}$  and  $25 \text{ }^\circ\text{C}$ .

At the beginning of the test, the strain is uniformly distributed along the entire sample and also in correspondence of the point P3 the specimen is slightly deformed. Generally, at low strains the temperature increase is restrained and the non-uniformity of the strain-rate inside the specimen is not significant; this explains why all the curves are in agreement with the dashed curve, in which no temperature effects and uniform strain-rate distribution are considered. Comparing the solid lines with the dash-dotted line (pure strain hardening curve), it is possible to observe the

hardening effect due to strain-rate. When the strain localization occurs, P1 continues to deform while in P2 and P3 the deformation stops. By further increasing the deformation of the specimen, the strain-rate hardening is gradually contrasted by the thermal softening: the slope of the curve of P1 starts to decrease with respect to the dashed curve due to the thermal softening because the specimen undergoes a gradually temperature increase up to about 300 °C before fracture (see Fig. 5.20). Although the equivalent stress vs. equivalent plastic strain curve should always show a positive slope, at most null, this could not happen when the thermal softening becomes relevant.

## 5.4 Advanced numerical inverse analysis

The numerical analysis discussed until now represents the classical and most common procedure for the identification of the model parameters. Nevertheless, with this numerical methodology, the material model parameters are determined only on the basis of the comparison between global quantities, i.e. forces and displacements. The variation of the specimen shape is taken into account, but this does not guarantee that the shape obtained from the simulation reproduces correctly the experimental one.

Generally, the specimen shape obtained from the simulation is simply compared with the experimental one at different test times in order to verify the accuracy of the simulation, but this is done once the model parameters are obtained [97]. In case of dissimilarities between the geometrical profiles, the problem could be solved performing again the numerical optimization changing, for example, the set of considered experimental targets or their relative weights, the set of material model parameters considered as optimization variables and the used strength model. Obviously, this procedure could require much time and many attempts, furthermore the achievement of a satisfactory result is not guarantee.

Another possible solution is to use information about the specimen shape during the numerical inverse optimization. In this sense, performing the analysis of the

images acquired during the test, as explained in section 5.2.1, many data about the actual shape of the specimen could be extracted, such as: the minimum cross-section radius, the curvature radius of the necking and, consequently, the triaxiality factor [151]. Nevertheless, it is difficult to use these information in a routine for the strength material model optimization, in which the parameters identification is usually based on the fitting of experimental and computed macroscopic quantities; unless a dedicated algorithm is implemented for this aim. Obviously, this aspect could represent a relevant complication in the optimization procedure.

In order to overcome this issue, the information about the correct specimen shape could be introduced creating another component (a sort of mould) in the FE model which deforms exactly as observed during the test (see Fig. 5.22). This could be done because performing the image analysis, the position of each point which defines the specimen profile is known at each time. The points which correspond to the undeformed specimen condition can be converted into nodes inside of the FE model. At this point, at each node can be assigned the corresponding experimental motion (both in radial and longitudinal directions).

Once realized the mould, a contact algorithm can be introduced between the components in order to force the specimen deformation. The contact force represents an appropriate quantity for the evaluation of the goodness of the deformation: it is null when the specimen deforms exactly as the mould and grows up when the mould penetrates the specimen. On the other hand, if the motion is correctly applied to the mould and under the hypothesis of volume conservation (which is obviously true for the numerical model), it is not possible that the two components are completely separate and consequently the contact force goes to zero. However, the magnitude of the contact force has to be considered. As a matter of fact, greater the contact force, more significant its influence on the longitudinal force inside the specimen. To limit the introduced modifications, the stiffness of the contact has to be kept as low as possible (this aspect has to be carefully handled since it strongly depends on the ratio between the longitudinal and the contact forces).

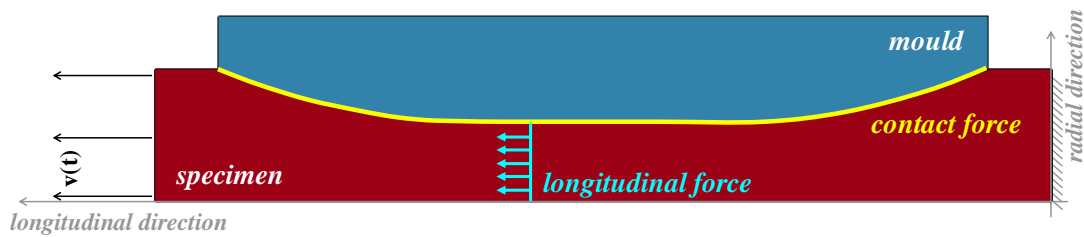


Fig. 5.22: Advanced FE model used in the numerical inverse optimization.

The FE model shown in Fig. 5.22 allows to perform the numerical inverse optimization with two objectives: one is the minimization of the error between the experimental and computed force vs. displacement curves and the second one is the minimization of the contact force between the specimen and the mould. The aim of this numerical optimization approach should be to guarantee that the set of parameters obtained is suited to correctly reproduce the flow stress of the material as well as the evolution of the specimen deformation. Naturally, this procedure is more complicated with respect to that described in the previous section because it requires an image acquisition system and the analysis of the images to create the mould.

This kind of optimization was performed for T91 steel for the test on standard specimen at quasi-static condition and room temperature. For simplicity, only the strain hardening part of the J-C model ( $\sigma = A + B \cdot \varepsilon_{pl}^n$ ) was optimized to describe the material behaviour. In Fig. 5.23a, the results in terms of force vs. displacement are compared. Three curves are reported: the experimental target and the computed curves obtained by performing the SOO with and without the control of the specimen shape. The parameters extracted are reported in Table 5.6 and the relative flow stress curves are compared in Fig. 5.23b. It is important to put in evidence that the experimental curve shown in Fig. 5.23a refers to a different test with respect to that shown in Fig. 5.9, in which the image acquisition was not performed. For this reason the SOO without the control of the deformed shape was performed again.

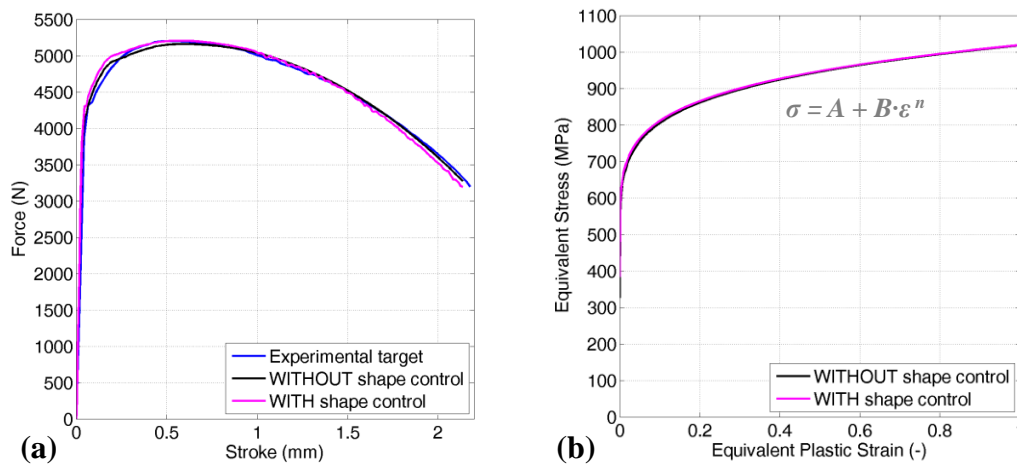
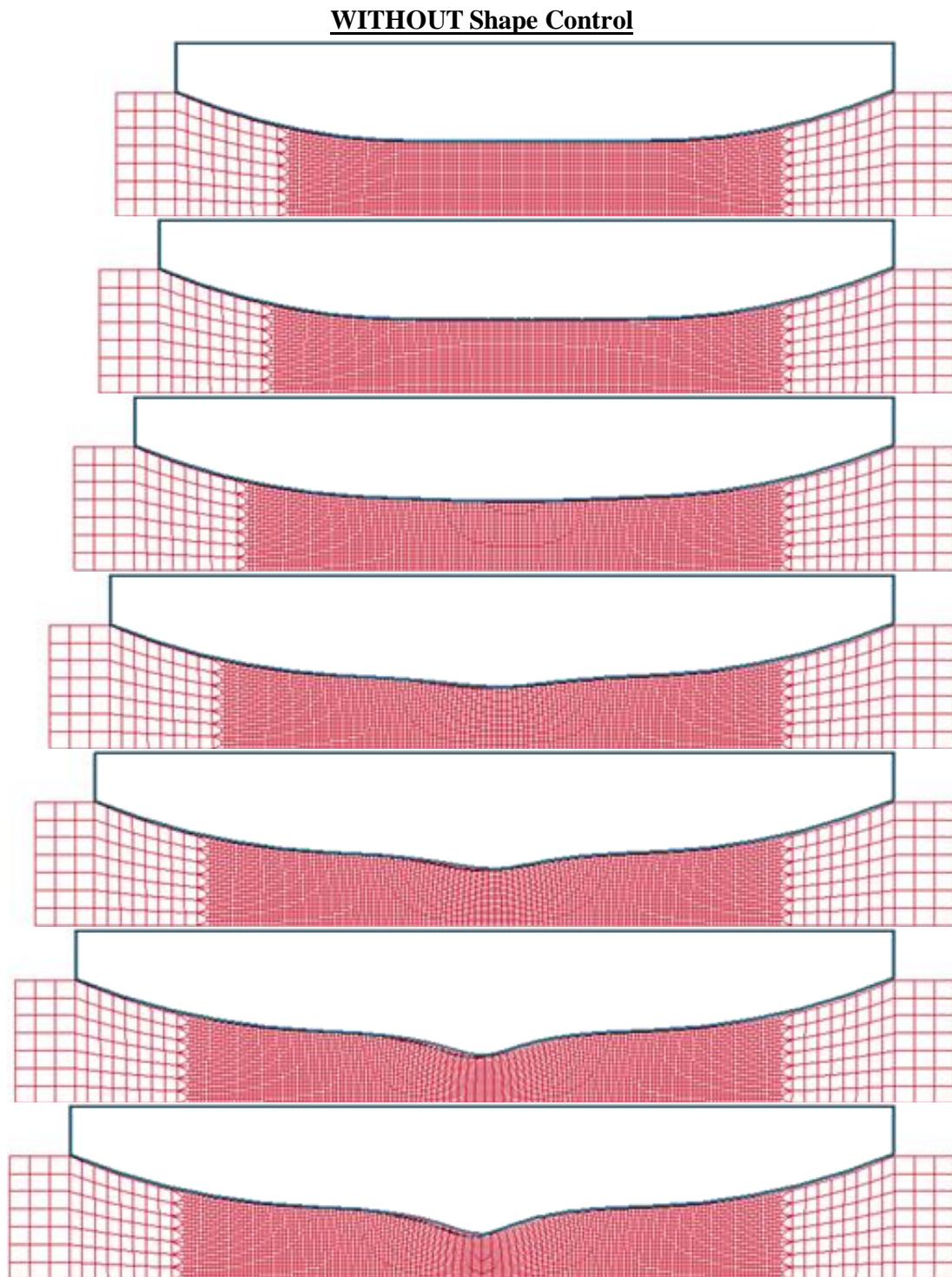


Fig. 5.23: a) Comparison between the computed (with or without shape control) and experimental force vs. displacement curves and b) comparison in terms of optimized J-C (hardening part) models for a standard specimen ( $D=3$  mm;  $L=5$  mm) of T91 steel tested at  $10^{-3} \text{ s}^{-1}$  and  $25$  °C.

Table 5.6: J-C parameters obtained performing numerical optimizations with and without the specimen shape control for T91 steel.

	<b>A</b>	<b>B</b>	<b>n</b>	<b>rRMSE</b>
	MPa	MPa	-	%
WITHOUT shape control	327	692	0.160	0.82
WITH shape control	384	636	0.172	1.33

The qualitative comparisons made in terms of sequences of the deformed specimen shapes are reported in Fig. 5.24 and 5.25. The Fig. 5.24 refers to the simulation performed by using the optimized parameters in which the control of the shape was not considered, while the sequence in Fig. 5.25 represents the result of the optimization with the control of the specimen shape. It is important to specify that the sequences of deformed shapes shown in Fig. 5.24 exclusively depend from the set of parameters used and no contact algorithm was applied; the mould is shown only to highlight if there are qualitative differences between the two simulations.



*Fig. 5.24: Sequence of the specimen deformation obtained from the optimization without the control of the shape for T91 steel.*

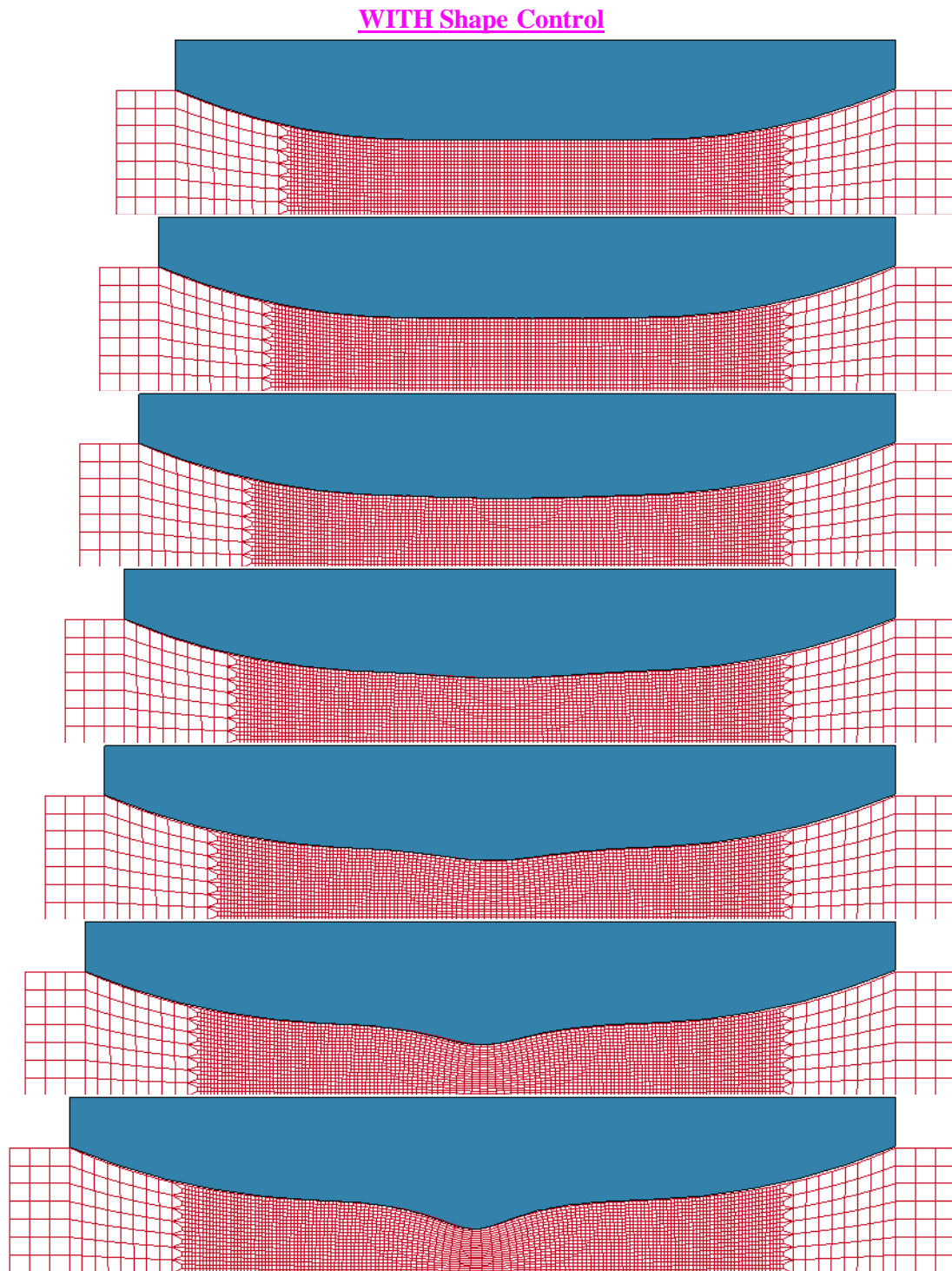


*Fig. 5.25: Sequence of the specimen deformation obtained from the optimization with the control of the shape for T91 steel.*

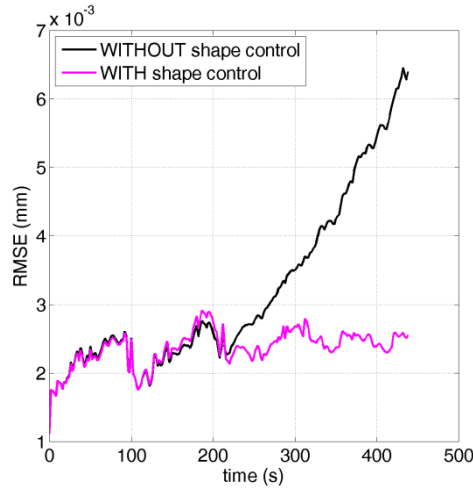


Fig. 5.26: Root Mean Squared Error evolution calculated between the simulated specimen shape and the experimental one by using two different numerical approaches for T91 steel.

Observing the Fig. 5.23a, 5.24 and 5.25, the optimization which takes into account the shape of the specimen allows to identify a set of parameters which permits to simultaneously describe with good accuracy the experimental response of the material (1.33% of relative Root Mean Squared Error) and the actual deformation of the specimen shape. Instead, the set of parameters extracted with the classical optimization approach, only based on the comparison of the experimental and computed force vs. displacement curves, allows a good prediction of the material response (0.82% of rRMSE), but the shape of the specimen obtained from the simulation is not very accurate. This last aspect was investigated by calculating, in the gage length area, the RMSE (Eq. 4.13) between the simulated specimen shape (obtained with both sets of parameters) and mould one during the deformation (see Fig. 5.26). At the beginning of the test, the specimen deforms in the same way by using both sets of parameters, instead, when the necking becomes significant, the error grows up by using the parameters obtained without to consider the experimental specimen shape. The set of parameters extracted from both the optimizations are practically equivalent in the prediction of the material response (see Fig. 5.23b), but it is not a general rule. Thus, for T91 steel, the advanced

optimization procedure proposed here leads to an optimum which fulfils both the objectives and allows to increase the reliability of the material model.

The same analysis was performed for the heavy sintered molybdenum. In Fig. 5.27a, the results in terms of force vs. displacement curves are compared, while in Fig. 5.28 and 5.29, the sequences of the deformed specimen shapes obtained from both optimization procedures are shown. The sets of parameters identified are reported in Table 5.7 and the corresponding flow stress curves are compared in Fig. 5.27b.

Table 5.7: J-C parameters obtained performing numerical optimizations with and without the specimen shape control for heavy sintered molybdenum.

	<i>A</i>	<i>B</i>	<i>n</i>	<i>rRMSE</i>
	MPa	MPa	-	%
WITHOUT shape control	621	554	0.900	4.93
WITH shape control	547	615	0.739	6.53

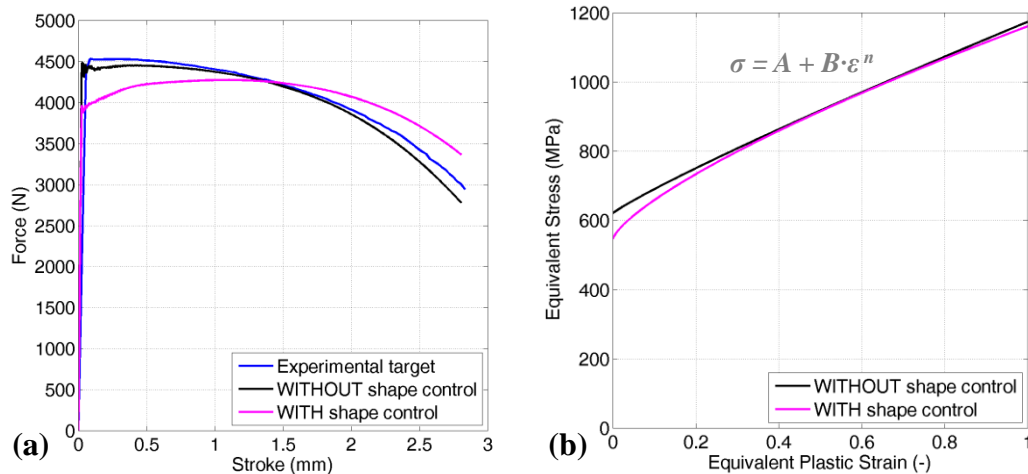
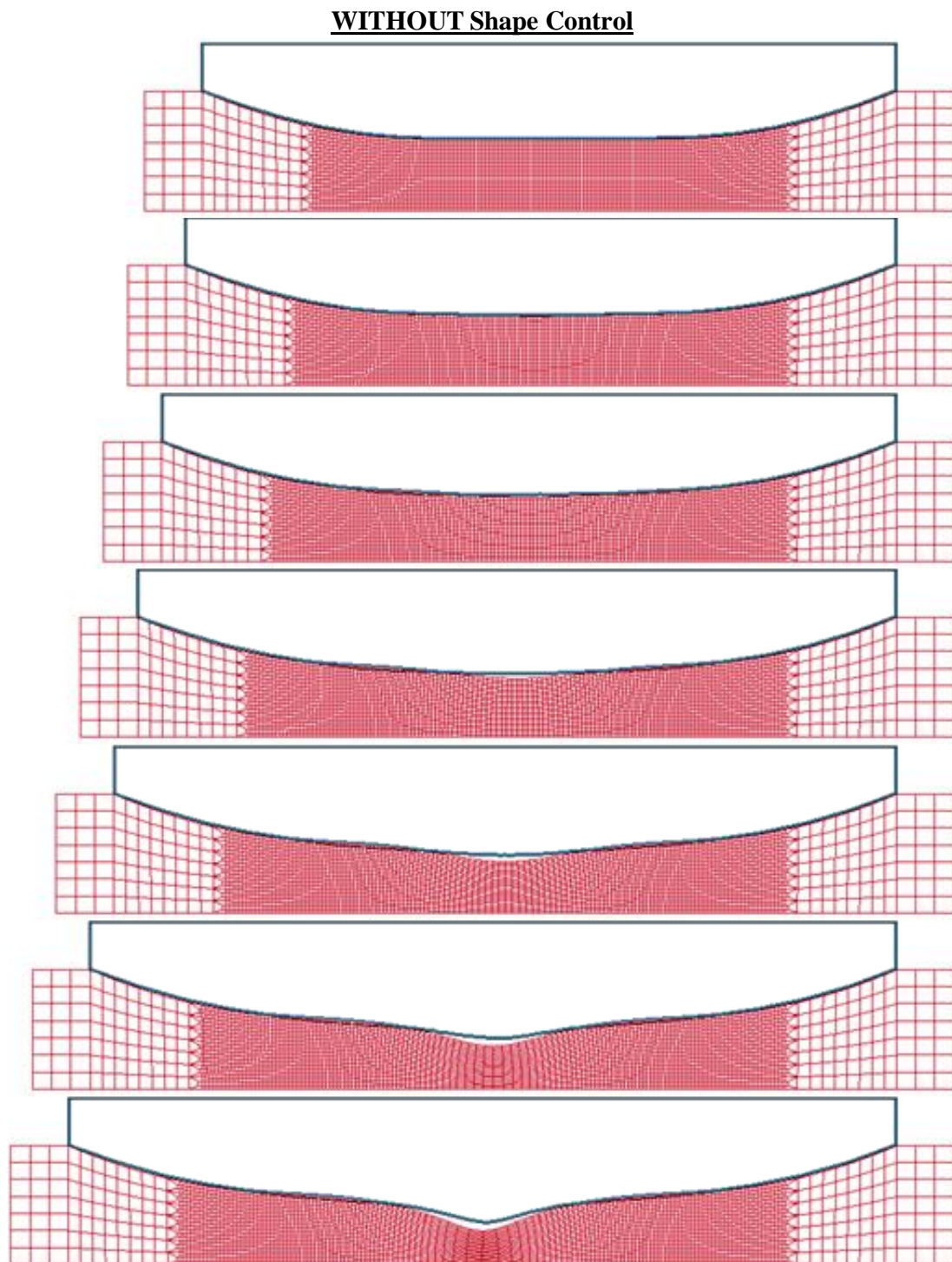
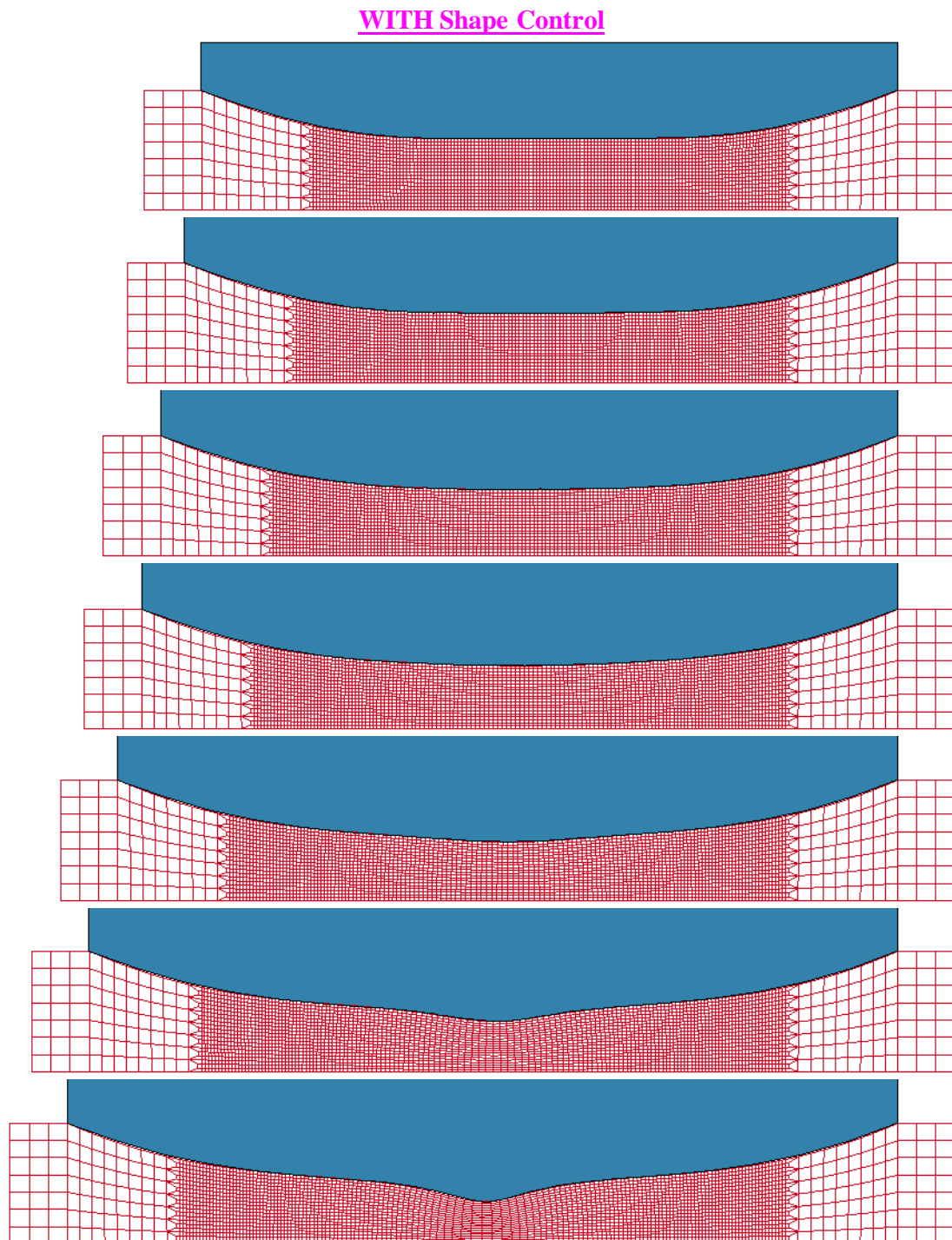


Fig. 5.27: a) Comparison between the computed (with or without shape control) and experimental force vs. displacement curves and b) comparison in terms of optimized J-C (hardening part) models for a standard specimen ( $D=3$  mm;  $L=5$  mm) of heavy sintered molybdenum tested at  $10^{-3} \text{ s}^{-1}$  and  $25$  °C.



*Fig. 5.28: Sequence of the specimen deformation obtained from the optimization without the control of the shape for heavy sintered molybdenum.*



*Fig. 5.29: Sequence of the specimen deformation obtained from the optimization with the control of the shape for heavy sintered molybdenum.*

In this case, the optimization which does not consider the control of the specimen shape leads to a set of parameters that reproduces with accuracy the material response (see Fig. 5.27a), but it does not allow to correctly predict the shape of the specimen (see Fig. 5.28). On the contrary, with the set of parameters obtained with the control of the specimen shape, the transversal deformation of the specimen is well reproduced (see Fig. 5.29), while the computed force vs. displacement relations is far from the experimental one. For this reason the flow stress curves reported in Fig. 5.27b are not in agreement. Also in this case, the accuracy of the simulations to reproduce the experimental specimen shape was evaluated by calculating the RMSE, in the gage length zone, between the simulated specimen shape (obtained with both sets of parameters) and mould one during the deformation (see Fig. 5.30). As observed for T91 steel, with the set of parameters obtained by controlling the specimen shape the RMSE remains almost constant from the start to the end of the test, while the parameters identified without the control of the specimen shape could conduct to a gradual increasing of the error, as happened in this case.

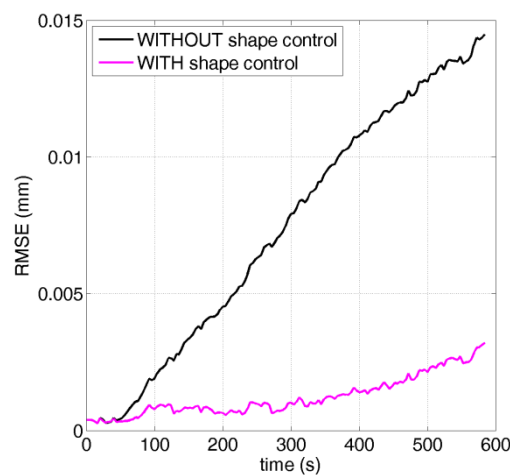


*Fig. 5.30: Root Mean Squared Error evolution calculated between the simulated specimen shape and the experimental one by using two different numerical approaches for heavy sintered molybdenum.*

Observing with attention the images recorded during the test, the specimen appears to show a uniform deformation for long time (until about mid of the total

elongation), which is in contrast with the force vs. displacement curve, where the instability condition occurs almost immediately (see Fig. 5.27a). Actually, this aspect was not completely understood; probably, being a sintered material the possible presence of voids inside the specimen could generate this unusual behaviour. In this sense, also changing the material model the final results should not change. These observations could justify the difficulties for both optimization methods to reach a satisfactory result.

Finally, it is important to point out that the methodology proposed here could be used both to verify the reliability of the material model and, eventually, to improve it. Obviously, this procedure requires a relevant amount of work with respect to the classical one, but it could give some advantages as in the case of T91 steel, in which the material model prediction was improved, or to put in evidence critical aspects as for the heavy sintered molybdenum.



## 6. Conclusions

The final goal of this thesis was to analyze and propose different methodologies for the calibration of strength models suited to describe the dynamic behaviour of metals. In dynamic conditions, the behaviour of metals is generally characterized by an increase of the strength due to the high strain-rate (strain-rate hardening) and, simultaneously, a decrease of the strength due to the increase of temperature (thermal softening), related to the conversion of plastic work into heat. Depending on the material, the strain-rate and temperature sensitivities could be coupled or uncoupled and change as function of the strain. For this reason, it is fundamental to deeply investigate the material response varying the loading condition. In particular, in this thesis, the attention was focused on some of the most common material models implemented in the commercial FE codes: the Johnson-Cook (J-C) and the Zerilli-Armstrong (Z-A) models were considered. In the J-C model the strain-rate and temperature sensitivities are considered independent, while in the Z-A model the coupled effect of temperature and strain-rate is taken into account. Moreover, also a modified version of the Z-A model was considered, in order to be able to take into account for the coupling between strain and temperature. The process for the identification of the model parameters is, in general, composed by two sequential phases: the individuation of the experimental data and the data analysis. Both them were deeply discussed in this work, focusing the attention on the critical aspects and proposing some possible solutions to solve them.

The investigation was performed for three different metals, allowing to point out advantages and disadvantages of the applied procedures, depending on the materials behaviour. The materials were the high chromium ferritic/martensitic T91 steel, which is a high strength steel, the copper-based composite Glidcop Al-15 in which the FCC matrix behaviour is reinforced by a dispersion of alumina and the heavy sintered molybdenum, which has a BCC structure. For each of them an experimental testing campaign, varying the strain-rate and the temperature, was performed. The experimental results were analyzed and the data were used for the calibration of the strength models.

In order to completely investigate the mechanical response of these metals in dynamic conditions, different experimental techniques were used. For all materials tensile tests were performed because this kind of test allows to investigate the material behaviour up to fracture. For the low strain-rates the classical electro-mechanical testing equipment was used reaching the nominal strain-rate of  $10^{-1} \text{ s}^{-1}$ . The behaviour at medium strain-rates was investigated up to  $10^1 \text{ s}^{-1}$  by using a servo-hydraulic testing machine. The investigation of high strain-rate behaviour, nominally at  $10^3 \text{ s}^{-1}$ , was performed by using the standard Tensile Hopkinson Bar apparatus. Analyzing the features of the Hopkinson Bar, it was observed that reducing the dimensions of this testing equipment, in accordance with the reduction of the specimen geometry, it was possible to perform tensile tests at strain-rates up to  $10^4 \text{ s}^{-1}$ . In this perspective, a miniaturized Tensile Hopkinson Bar was designed and realized to carry out tests at very high strain-rates. In order to perform more accurate analysis, two digital acquisition systems were used: this allowed to directly extract the deformation applied to the specimen, avoiding any effects due to clearance or machine deformability. For tests at low strain-rates a high resolution camera was adopted, while an high speed camera was used to record the images sequence in high strain-rate tests. The investigation of the materials response varying the temperature was performed by using an induction coil system in both low and high strain-rates. The choice of this heating system with respect to the other heating systems, was performed since it allows to achieve very quickly high temperatures (up to  $1000 \text{ }^\circ\text{C}$

for the investigated materials) and to limit the size of heating zone (reducing the influence of the temperature increase on the testing machine and the measurement systems, such as strain-gages, transducers, etc.). A specific solenoid was designed in order to guarantee the optical access (for high resolution and high speed video) also for tests at high temperature. To this aim, a solenoid with a fork shape was designed. The temperature was controlled by means of a PID controller on the basis of the temperature measurements coming from thermocouples directly welded on the specimen surface. A system based on trigger signals was used to synchronize the testing equipment with the high speed camera and the heating system. The mechanical behaviour of T91 steel was investigated at different strain-rates at room temperature and at different temperature in quasi-static loading condition. The same was performed also for Glidcop Al-15 and pure molybdenum, but in addition also the high dynamic behaviour at different temperatures was investigated.

The experimental results were compared in terms of true stress vs. true plastic strain and for each material the strain-rate and temperature sensitivities were analyzed. The main features can be summarized as follows. All the investigated materials resulted to be both strain-rate and temperature sensitive. In case of Glidcop Al-15, it was found a typical behaviour as expected for BCC material (yield stress as a function of temperature and strain-rate) despite it is a FCC matrix composite, probably due to alumina dispersion. A significantly different behaviour was found for the thermal softening by varying the strain-rate: this suggested to use a thermal strength model for the material behaviour prediction. For pure sintered molybdenum a sort of early instability appears, probably related to the sintered nature, which made the data analysis more difficult. Also for this material, a coupled strength model was expected to be used. By comparing the strain-rate sensitivity, it was found that the pure molybdenum (BCC lattice structure) had the highest sensitivity.

For the data analysis, and consequently for the materials model identification, different procedures were analyzed, increasing the complexity, but at the same time the goodness of the extracted models.

The first step was a purely analytical approach, in which the experimental data were fitted with a strength model, by the minimization of the distance between experimental and predicted quantities. Since beyond of the maximum load the localized necking phase starts in the specimen, the true stress vs. true strain relation is no longer representative of the effective behaviour of the material. For this reason, in this first phase, the mechanical response of the materials was considered within of a small range of true plastic strain (up to 15%), in which the effects of the localized necking were evaluated negligible. Moreover, the non-uniform distributions of stress, strain, strain-rate and temperature inside the specimen were neglected as well as the self-heating at high strain-rate. The J-C and Z-A models were analyzed in detail in order to evaluate their suitability to reproduce the experimental results. Since in the testing campaign performed on T91 steel the coupled effect of strain-rate and temperature on the material response was not investigated, the J-C model (which does not consider this dependency) was adopted to predict the experimental results. An analytical procedure based on the separated individuation of the parameters related to the strain hardening (on quasi-static experimental data), strain-rate hardening (on data obtained at different strain-rates) and thermal softening (on data obtained at different temperatures) terms of the model was applied and the resulting flow stress curves were compared with the experimental ones. Some limits of the model were put in evidence, but the model was able to reproduce the experimental data with a sufficient level of accuracy. Instead, the Z-A model was calibrated to reproduce the mechanical response of Glidcop Al-15 and heavy sintered molybdenum. For both materials a multi-objective optimization procedure was performed, in which all the experimental data were simultaneously taken into account. Also in this case the flow stress curves obtained with the optimized models were compared with the experimental ones. The results show that the Z-A model is more suited to describe the behaviour of the heavy sintered molybdenum instead of Glidcop Al-15. In order to try to improve the quality of the results, by taking into account also the coupling between strain and temperature, in addition to the coupling between strain-rate and temperature, the modified version of the Z-A model was

optimized for both the materials. Also in this case, the multi-objective procedure was applied and this allows to obtain a relevant improvement in the prediction of the material response.

Since the validity of the analytical optimization procedures was limited at low range of strains due to the difficulties in the evaluation of the effective material behaviour beyond the onset of the localized necking, the problem of the instability in tension was analyzed. In tensile tests, using round test specimens, the state of stress changes from uniaxial tension to a complex triaxial tension condition as the neck develops in local deformation. In order to deal with this issue, some analytical models can be found in the scientific literature, as for example the approximate model proposed by Bridgman to estimate the equivalent stress-strain relation during local deformation after necking. This equation is based on the actual dimensions of the specimen up to fracture, i.e. the minimum section of the specimen and the radius of the necking curvature. In order to extract these information, in this thesis, an image analysis procedure was developed and presented. This method was applied to the results obtained for T91 steel and its benefits shown to extend the range of applicability of the analytical optimization method also at high strain up to fracture. In accordance to the Bridgman equation, the equivalent stress vs. equivalent plastic strain curve up to fracture was obtained for T91 steel considering a test performed in quasi-static at room temperature. However, even if the Bridgman equation allows to consider the strain localization in the specimen, it does not consider the non-uniform distribution of the quantities inside the specimen.

In order further improve the quality of the identification process, by taking into account also this aspect, numerical inverse methods were considered. In more detail, the main objective was the determination of a selected set of unknown parameters (of the chosen strength model) in a numerical model. Starting from a trial point, the unknown parameters were estimated iteratively by comparing experimentally measured with numerically computed quantities for the same material test conditions. The great advantage of this procedure was that no hypothesis about the internal specimen or component stress-strain, temperature, or strain-rate fields had to be

made a priori. The goodness of the numerical simulation to predict the experimental results mainly depends on the used material model and its set of parameters. In this sense, different numerical inverse optimization procedures were analyzed in order to identify the most suitable. In this perspective, both Single-Objective Optimizations (SOO) and Multi-Objective Optimizations (MOO) were described. In the first case the optimization was oriented to identify the best set of model parameters for a specific test condition, while by performing MOO the final goal was to identify the best set of model parameters able to describe with accuracy the global behaviour of considered material (e.g. at different temperatures and strain-rate). In both the cases, the optimization was based on the minimization of the distance between experimental and computed quantities expressed in terms of global quantities, such as stroke vs. force curves. The numerical simulations were performed by using the FE code LS-DYNA<sup>®</sup>, and the optimizations of the parameters were performed with a dedicated algorithm included in the software LS-OPT<sup>®</sup>.

As first attempt, for all the investigated material a mixed numerical-analytical optimization procedure was performed. In practice, for each test a SOO was performed in order to obtain the correctly computed equivalent stress vs. equivalent plastic strain up to fracture, after that the previously described analytical approach was used. With this procedure the validity of the optimized model was extended up to fracture, and the quality of the models prediction was increased.

A further improvement was obtained by using a completely numerical approach, in which a MOO procedure was applied to the experimental data obtained from different loading conditions to simultaneously extract the material model parameters. This procedure was applied for T91 steel and different solutions were proposed, depending on the range of applicability of the optimized J-C models.

This last procedure allowed to obtain reliable results, in which non-uniform and localized fields inside the specimen as well as self-heating effects were considered. Nevertheless, the material model parameters were determined only on the basis of the comparison between global quantities, and this did not guarantee that the deformed specimen shape, obtained from the simulation, was able to correctly

---

reproduce the experimental one. In order to increase the reliability of the numerical model to describe the behaviour of the materials, the last step of this thesis, was the development of an advanced numerical optimization procedure based on the control of the specimen shape during the deformation process. The information about the correct specimen shape was introduced creating another component in the FE model which deforms exactly as observed during the test. This was achieved by imposing to the additional components (which is a sort of mould) the time history displacement corresponding to the specimen profile, as extracted from high resolution (in quasi-static loading condition) or high speed (in dynamic loading condition) cameras. By setting a contact algorithm between the components, it was possible to measure the contact force, which represents an appropriate quantity for the evaluation of the goodness of the deformation. As a matter of fact, when it is null, the specimen deforms exactly as the mould and it grows up when the two components penetrate. Thus for each numerical model, the optimization had two objectives: one was the minimization of the error between the experimental and computed force vs. displacement curves and the second one was the minimization of the contact force between the specimen and the mould. Obviously, due to the complexity of the problem, the setting of the procedure needed to be carefully handled. As a matter of fact, it was found that the magnitude of the contact force has to be kept as low as possible to limit its influence on the longitudinal force inside the specimen. Moreover, it was necessary to properly evaluate the relative weight to assign to each objective function, since changing it, it is possible to condition the results of the optimization process in order to increase the importance of one (or more) objective(s) with respect to the other(s).

For simplicity, this procedure was used to optimized only the strain-hardening terms of the J-C model for the quasi-static tests performed on T91 steel and heavy sintered molybdenum. The results obtained with this procedure were compared with those obtained with the classical one. In case of T91 the procedure allowed to improve the goodness of the results: the optimized model was able to correctly compute both the force-displacement response and the deformed profile history. On

the contrary, no satisfactory results were obtained for molybdenum, probably as a consequence of the not well understood behaviour of this sintered material.

As general conclusion, it was possible to assert that the developed procedure allowed for a significant improve in the material model parameters identification, representing a sufficiently complete data analysis procedure, in which the global material response, the self heating and the deformation history could be taken into account and no simplifying assumption had to be done. Obviously, this methodology required a big effort from both the experimental and the computational point of view.

## References

- [1] Meyers M.A., et al., “Constitutive description of dynamic deformation: physically-based mechanisms”, *Mat. Science and Eng. A*, vol. 322 (2002) 194-216.
- [2] Lennon A.M., Ramesh K.T., “The influence of crystal structure on the dynamic behavior of materials at high temperatures”, *Int. Journal. of Plasticity* (2004) 269-290.
- [3] Kanel G.I., et. al., “Shock-wave phenomena and the properties of condensed matter”, ISBN 978-1-4419-1916-8 (2004), 83-109.
- [4] Zamani J., Etemadi E., “Constitutive equations for metallic crystals under very high strain rates loadings”, *Int. Conf. on Advanced Materials Eng., IPCSIT vol.15* (2011).
- [5] Follansbee P.S., Kocks U.F., “A constitutive description of the deformation of copper based on the use of the mechanical threshold stress as an internal state variable”, *Acta metal.*, vol. 36, no. 1 (1988) 81-93.
- [6] Macdougall D., “Determination of the plastic work converted to heat using radiometry”, *Exp. Mech.*, vol. 40, I. 3 (2000) 298-306.
- [7] Ashuach Y., et al., “Multi-step Kolsky bar loading of materials which fail by adiabatic shear banding”, *J. of Physics: Conference Series*, vol. 500 (2014) 182002.
- [8] Kapoor R., Nemat-Nasser S., “Determination of temperature rise during high strain rate deformation”, *Mechanics of Materials*, vol. 27 (1998) 1-12.
- [9] Steinberg D., “Equation of state and strength properties of selected materials”, Lawrence Livermore National Laboratory, (1996).
- [10] Sierakowski R.L., “Strain rate behavior of metals and composites”, IGF Cassino (1997).

- 
- [11] Newby J.R., et. al., “Mechanical testing – Volume 8”, ASM Handbook (1985).
- [12] Peroni M., “Experimental methods for material characterization at high strain-rate: analytical and numerical improvements”, Ph. D. Thesis (2008).
- [13] Bantia N., et. al., “Impact testing of concrete using a drop-weight impact machine”, *Experimental Mechanics*, vol. 29 I. 1 (1989) 63-69.
- [14] Sevkat. E., et. al., “Drop-weight impact of plain-woven hybrid glass-graphite/toughened epoxy composites”, *Composites: Part A*, vol. 40 (2009) 1090-1110.
- [15] Xia K., Yao W., “Dynamic rock tests using split Hopkinson (Kolsky) bar system – A review”, *J. Rock Mech. Geotech. Eng* (2015) 1-33.
- [16] Delvare F., et. al., “A non-equilibrium approach to processing Hopkinson Bar bending test data: Application to quasi-brittle materials”, *Int. J. Impact Eng.*, vol. 37 (2010) 1170-1179.
- [17] Gilat A., Cheng C.S., “Modeling torsional split Hopkinson bar tests at strain rates above  $10000\text{ s}^{-1}$ ”, *Int. J. of Plasticity* (2002) 787-799.
- [18] Rodríguez J., et. al., “Splitting tests: an alternative to determine the dynamic tensile strength of ceramic materials”, *J. de Physique IV*, vol. 4 (1994) C8 101-106.
- [19] Cheng W., Song B., “Split Hopkinson (Kolsky) Bar: Design, testing and Applications”, *Mechanical Engineering Series Springer*, New York (2011) ISBN 978-1-4419-7981-0.
- [20] Cadoni E., et. al., “Strain-rate behavior in tension of the tempered martensitic reduced activation steel Eurofer97”, *J. of Nuclear Materials*, vol. 414 (2011) 360-366.
- [21] Peroni L., et. al., “Investigation of the mechanical behaviour of AISI 316L stainless steel syntactic foams at different strain-rates”, *Composites: Part B*, vol. 66 (2014) 430-442.
- [22] Taylor. G., “The use of flat-ended projectiles for determining dynamic yield stress. I. Theoretical considerations”, *Proc. R. Soc. Lond. A*, vol.194 (1948) 289-299.
- [23] Whiffin. A.C., “The use of flat-ended projectiles for determining dynamic yield stress. II. Tests on various metallic materials”, *Proc. R. Soc. Lond. A*, vol.194 (1948) 300-322.
- [24] Carrington W.E., Gayler M.L.V., “The use of flat-ended projectiles for determining dynamic yield stress. III. Changes in microstructure caused by

---

deformation under impact at high-striking velocities”, Proc. R. Soc. Lond. A, vol. 194 (1948) 323-331.

[25] Zhou F., et. al., “Analysis of the brittle fragmentation of an expanding ring”, Computational Mat. Science, vol. 37 (2006) 74-85.

[26] Janiszewski J., “Ductility of selected metals under electromagnetic ring test loading conditions”, Int. J. of Solids and Structures, vol. 49 (2012) 1001-1008.

[27] Gray III G.T., et. al., “Influence of shock prestraining and grain size on the dynamic tensile extrusion response of copper: experiments and modeling”, 14<sup>th</sup> American Phys. Soc. Topical Conf. of Cond. Mat. (2006) 725-728.

[28] Ramesh K.T., “High strain rate and impact experiments”, Springer Handbook of Experimental Solid Mechanics, Part D-33 (2008) ISBN: 978-0-387-26883-5.

[29] Kanel G.I., “Behavior of brittle materials under dynamic loading”, Institute for Advanced Technology (2000).

[30] Oscarson J.H., Graff K.F., “Spall fracture and dynamic response of materials”, Battelle Memorial Institute (1968).

[31] Allen D.J., et. al., “Optimizing material strength constants numerically extracted from Taylor impact data”, Experimental Mechanics, vol. 37, I. 3 (1997) 333-338.

[32] Cao F., et. al., “Dynamic tensile extrusion response of tantalum”, Acta Mat., vol. 56 (2008) 5804-5817.

[33] Burkett M.W., Clancy S.P., “Eulerian hydrocode modeling of a dynamic tensile extrusion experiment”, Proc. of the 11<sup>th</sup> Hypervel. Impact Symp., (2010).

[34] Furmanski J., et. al., “Large-strain time-temperature equivalence in high density polyethylene for prediction of extreme deformation and damage”, EPJ Web of Conf. 56 (2012).

[35] Furmanski J., et. al., “Dynamic-Tensile-Extrusion for investigating large strain and high strain rate behavior of polymers”, Polymer Testing, vol. 31 (2012) 1031-1037.

[36] Furmanski J., et. al., “Extreme tensile damage and failure in glassy polymers via Dynamic-Tensile-Extrusion”, Dynamic Behavior of Materials – Conf. Proc. of the Soc. For Exp. Mech. Series, vol. 1 (2014) 107-112.

[37] Park K.T., et. al., “Dynamic tensile extrusion behavior of coarse grained and ultrafine grained OFHC Cu”, Mat. Sci. & Eng. A, vol. 569 (2013) 61-70.

- 
- [38] Park K.T., et. al., “Analysis on dynamic tensile extrusion behavior of UFG OFHC Cu”, 6<sup>th</sup> Int. Conf. on Nanomat. By Severe Plastic Def – IOP Conf. Series: Mat. Sci. and Eng., vol. 63 (2014).
- [39] Arrieta H.V., Espinosa H.D., “The role of thermal activation on dynamic stress-induced inelasticity and damage in ti-6Al-4V”, *Mechanics of Materials.*, vol. 33 (2001) 573-591.
- [40] Field J.E., et. al., “Review of experimental techniques for high rate deformation and shock studies”, *Int. J. of Impact Eng.*, vol. 30 (2004) 725-775.
- [41] Marsh S.P., “LASL Shock Hugoniot Data”, University of California Press (1980).
- [42] Davoodi D., et. al., “An experimental and numerical analysis of the heat transfer problem in SHPB at elevated temperatures”, *Meas. Sci. Technol.*, vol. 16 (2005) 2101-2108.
- [43] Bariani P.F., et. al., “Enhancing performances of SHPB for determination of flow curves”, *CIRP Annals Manufacturing Technology*, vol. 50, I. 1 (2001) 153-156.
- [44] Lin Y.C., et. al., “A modified Johnson-Cook model for tensile behaviors of typical high-strength alloy steel”, *Mat. Sci. and Eng. A*, vol. 527 (2010) 6980-6986.
- [45] Jaspers S.P.F.C., Dautzenberg J.H., “Material behaviour in conditions similar to metal cutting: flow stress in the primary shear zone”, *J. of Mat. Process. Tech.*, vol. 122 (2002) 322-330.
- [46] Samataray D., et. al., “A comparative study on Johnson Cook, modified Zerilli-Armstrong and Arrhenius-type constitutive models to predict elevated temperature flow behaviour in modified 9Cr-1Mo steel”, *Comp. Mat. Science*, vol. 47 (2009) 568-576.
- [47] Albert D.E., Gray III G.T., “Mechanical and microstructural response of Ti-24Al-11Nb as a function of temperature and strain rate”, *Acta mater.*, vol. 45, no. 1 (1997) 343-356.
- [48] Li Y., et. al., “A critical assessment of high-temperature dynamic mechanical testing of metals”, *Int. J. of Impact Eng.*, vol. 36 (2009) 177-184.
- [49] Lee W.S., Lin C.F., “Plastic deformation and fracture behaviour of Ti-6Al-4V alloy loaded with high strain rate under various temperatures”, *Mat. Sci. and Eng. A*, vol. 241 (1998) 48-59.
- [50] Nemat-Nasser S., Isaacs J.B., “Direct measurement of isothermal flow stress of metals at elevated temperatures and high strain rates with application to Ta and Ta-W alloys”, *Acta mater.*, vol. 45 (1997) 907-919.

- 
- [51] Chiddister J.L., Malvern L.E., “Compression-impact testing of aluminium at elevated temperatures”, *Exp. Mech.*, vol. 3, I. 4 (1963) 81-90.
- [52] Cane C., Laloui L., “Experimental study of thermal effects on the mechanical behaviour of a clay”, *Int. J. Numer. Anal. Meth. Geomech.*, vol. 28 (2004) 209-228.
- [53] Lindholm U.S., Yeakley L.M., “High strain-rate testing: Tension and compression”, *Exp. Mech.*, vol. 8, I. 1 (1968) 1-9.
- [54] Rosenberg Z., et. al., “A new technique for heating specimens in split-Hopkinson-bar experiments using induction-coil heaters”, *Exp. Mech.*, vol. 26, I. 3 (1986) 275-278.
- [55] Vilamosa V., et. al., “Measurement of local strain and heat propagation during high-temperature testing in a split-Hopkinson tension bar system”, *EPJ Web of Conf.* 26, 01015 (2012).
- [56] Abotula S., et. al., “Dynamic constitutive behaviour of Hastelloy X under thermo-mechanical loads”, *J. Mater. Sci.*, vol. 46 (2011) 4971-4979.
- [57] “Understanding Infrared Heating”. Heraeus Noblelight. 2005-2011. <http://www.noblelight.net/>.
- [58] Zhang D.N., et. al., “A modified Johnson-Cook model of dynamic tensile behaviours for 7075-T6 aluminium alloy”, *J. of Alloys and Compounds*, vol. 619 (2015) 186-194.
- [59] Wang Y., et. al., “A constitutive description of tensile behaviour for brass over a wide range of strain rates”, *Mat. Sci. and Eng. A*, vol. 372 (2004) 186-190.
- [60] Wierzbicki T., et. al., “Calibration and evaluation of seven fracture models”, *Int. J. Mech. Sci.*, vol. 47 (2005) 719-743.
- [61] Johnson G.R., Cook W.A., “Fracture characteristic of three metals subjected to various strains, strain rates, temperature and pressure”, *Eng. Fract. Mech.*, vol. 21, I. 1 (1985) 31-48.
- [62] Holmquist T.J., et. al., “Constitutive modelling of aluminum nitride for large strain, high-strain rate, and high-pressure applications”, *Int. J. Impact Eng.*, vol. 25 (2001) 211-231.
- [63] Giglio M., et. al., “Investigation about the influence of the mechanical properties of lead core and brass jacket of a NATO 7.62mm ball bullet in numerical simulations of ballistic impacts”, *EPJ Web Conf.* 26, 04010 (2012).
- [64] Alia A., Souli M., “High explosive simulation using multi-material formulations”, *Applied Therm. Eng.*, vol. 26 (2006) 1032-1042.

- 
- [65] Scapin M., “Shock-wave and high strain-rate phenomena in matter: modeling and applications”, Ph. D. Thesis (2013).
- [66] Fichera C., et. al., “Numerical simulation of landmine explosions: comparison between different modelling approaches”, V Int. Conf. on Comp. Meth. Coupled Prob. in Sci. Eng. (2013) 708-719.
- [67] Kolsky H. “An investigation of the mechanical properties of materials at very high rates of loading”, Proc. Phys. Soc. Lond. B, vol. 62 (1949) 676-700.
- [68] Hopkinson B., “A method of measuring the pressure produced in the detonation of high explosives or by the impact of bullets”, Phil. Trans. of the Royal Society of London, vol. 213 (1914) 437-456.
- [69] Yang L.M., Shim V.P.M., “An analysis of stress uniformity in split Hopkinson bar test specimens”, Int. J. of Impact Eng., vol. 31 (2005) 129-150.
- [70] Wu X.J., Gorham D.A., “Stress equilibrium in the Split Hopkinson Pressure Bar Test”, J. Phys. IV, vol. 7 (1997) 91-96.
- [71] Fairbairn E.M.R, Ulm F.J., “A tribute to Fernando L.L.B. Carneiro (1913-2001) engineer and scientist who invented the Brazilian test”, Mat. and Struct., vol. 35 (2002) 195-196.
- [72] Iwamoto T., Yokoyama T., “Effects of radial inertia and end friction in specimen geometry in split Hopkinson pressure bar tests: a computational study”, Mech. of Mat., vol. 51 (2012) 97-109.
- [73] Lee. O.S., Kim M.S., “Dynamic material property characterization by using split Hopkinson pressure bar (SHPB) technique”, Nuc. Eng. and Design, vol. 226 (2003) 119-125.
- [74] Bragov A.M., Lomunov A.K., “Methodological aspects of studying dynamic material properties using the Kolsky method”, Int. J. Impact Eng., vol. 16, no. 2 (1995) 321-330.
- [75] Chen W., et. al., “Tension and compression tests of two polymers under quasi-static and dynamic loading”, J. of Polymer Testing, vol. 21 (2002) 113-121.
- [76] Børvik T., et. al., “Strength and ductility of Weldox 460 E steel at high strain rates, elevated temperatures and various stress triaxialities”, Eng. Fract. Mech., vol. 72 (2005) 1071-1087.
- [77] Clausen A.H., et. al., “Flow and fracture characteristics of aluminium alloy AA5083-H116 as function of strain rate, temperature and triaxiality”, Mat. Science and Eng. A, vol. 364 (2004) 260-272.

- 
- [78] Solomos G., et. al., "Strain rate effects in nuclear steels at room and higher temperatures", *Nuclear Eng. and Design*, vol. 229 (2004) 139-149.
- [79] Bortzusky M., et. al., "Recommendations for dynamic tensile testing of sheet steels", *Int. Iron and Steel Inst., High Strain Rate Experts Group* (2005).
- [80] Kariem M.A., et. al., "Misalignment effect in the split Hopkinson pressure bar technique", *Int. J. of Impact Eng.*, vol. 47 (2012) 60-70.
- [81] Frew D.J., et. al., "Pulse shaping techniques for testing brittle materials with a Split Hopkinson Pressure Bar", *Exp. Mech.*, vol. 42, I. 1 (2002) 93-106.
- [82] Naghdabadi R., et. al., "Experimental and numerical investigation of pulse-shaped split Hopkinson pressure bar test", *Mat. Sci. and Eng. A*, vol. 539 (2012) 285-293.
- [83] Gerlach R., et. al., "A novel method for pulse shaping of Split Hopkinson tensile bar signals", *Int. J. of Impact Eng.*, vol. 38 (2011) 976-980.
- [84] Jia D., Ramesh K.T., "A rigorous assessment of the miniaturization in the Kolsky bar system", *Exp. Mech.*, vol. 44, no. 5 (2004) 445-454.
- [85] Lindholm U.S., "Deformation maps in the region of high dislocation velocity", *High Vel. Def. of Solids, Int. Union of Theor. and App. Mech.* (1979) 26-35.
- [86] Follansbee P.S., et. al., "The transition to drag controlled deformation in copper at high strain rates", *Institute of Physics Conf. Series*, vol. 705 (1987) 71-80.
- [87] Siviour C.R., et. al., "A miniaturized Split Hopkinson Pressure Bar for very high strain rate testing", *Air Force Research Laboratory, Munitions Directorate, AFRL-MN-EG-TR-2005\_7014* (2004).
- [88] Dharan C.K.H., Hauser F.E., "Determination of stress-strain characteristics at very high strain rates", *Exp. Mech.*, vol. 10 (1970) 370-376.
- [89] Gorham D.A., et. al., "An improved method for compressive stress-strain measurements at very high strain rates", *Proc.: Math. and Phys. Sci.*, vol. 438, no. 1902 (1992) 153-170.
- [90] Malinowski J.Z., et. al., "Miniaturized compression test at very high strain rates by direct impact", *Exp. Mech.*, vol. 47 (2007) 451-463.
- [91] Lim J., et. al., "Effects of gage length, loading rates, and damage on the strength of PPTA fibers", *Int. J. of Impact Eng.*, vol. 38 (2011) 219-227.

- 
- [92] Luo H., et. al., "Tensile behavior of a polymer film at high strain rates", Proc. of the XI<sup>th</sup> Int. Cong. and Expos. (2008) 451-463.
- [93] Bolduc M., Arsenault R., "Development of a strain-gage installation method for high-speed impact of strikers on a Split Hopkinson bar apparatus", EPJ Web of Conf. 26, 01033 (2012).
- [94] Fellows N.A., Harding J., "Use of high-speed photography to study localisation during high-strain-rate torsion testing of soft iron", Mat. Sci. and Eng. A, vol. 298 (2001) 90-99.
- [95] Grytten F., et. al., "Use of digital image correlation to measure large-strain tensile properties of ductile thermoplastics", Polymer Testing, vol. 28 (2009) 653-660.
- [96] Sánchez-Arévalo F.M., Pulos G., "Use of digital image correlation to determine the mechanical behavior of materials", Mat. Charact., vol. 59 (2008) 1572-1579.
- [97] Majazooobi G.H. et. al., "Determination of materials parameters under loading – Part II: Optimization", Comp. Mat. Sci., vol. 49 (2010) 201-208.
- [98] Noble J.P., et. al., "The use of the Hopkinson bar to validate constitutive relations at high rates of strain", J. of the Mech. and Phys. of Solids, vol. 47 (1999) 1187-1206.
- [99] Jagannathan L., Jawahar C.V., "Prospective correction methods for camera-based document analysis", Proc. First Int. Workshop on Camera-based Document Analysis and Recognition (2005) 148-154.
- [100] Yin X.C., et. al., "Perspective rectification for mobile phone camera-based documents using a hybrid approach to vanishing point detection", Proc. Second Int. Workshop on Camera-based Document Analysis and Recognition (2007) 37-44.
- [101] Yin X.C., et. al., "Robust vanishing point detection for mobilecam-based documents", Int. Conf. on Document Analysis and Recognition (2011) 136-140.
- [102] Fazzini M., et. al., "Study of image characteristics on digital image correlation error assessment", Optics and Lasers in Eng., vol. 48 (2010) 335-339.
- [103] Haddadi H., Belhabib S., "Use of rigid-body motion for the investigation and estimation of the measurement errors related to digital image correlation technique", Optics and Lasers in Eng., vol. 46 (2008) 185-196.
- [104] Lecompte D., et. al., "Quality assessment of speckle patterns for digital image correlation", Optics and Lasers in Eng., vol. 44 (2006) 1132-1145.

- [105] PixeLINK<sup>®</sup> PL-B777 camera datasheet – <http://www.pixelink.com/>.
- [106] LeCroy WaveStation 2012 datasheet – <http://teledynelecroy.com/>.
- [107] SA5 ultra high-speed video system datasheet – <http://www.photron.com/>.
- [108] Bobbili R., et. al., “Prediction of flow stress of 7017 aluminium alloy under high strain rate compression at elevated temperatures”, Def. Tech., In Press (2014) 1-6.
- [109] Kajberg J., Sundin K.G., “Material characterization using high-temperature Split Hopkinson pressure bar”, J. of Mat. Process. Tech., vol. 213 (2013) 522-531.
- [110] Kapoor R., Nemat-Nasser S., “Comparison between high and low strain-deformation of Tantalum”, Metal. and Mat. Trans. A, vol. 31 (2000) 815-823.
- [111] Lee W.S., et. al., “High temperature deformation and fracture behaviour of 316L stainless steel under high strain rate loading”, J. of Nuclear Mat., vol. 420 (2012) 226-234.
- [112] Lennon A.M., Ramesh K.T., “A technique for measuring the dynamic behaviour of materials at high temperatures”, Int. J. of Plasticity, vol. 14, no. 12 (1998) 1279-1292.
- [113] Scapin M., et. al., “Mechanical behavior of Glidcop Al-15 at high temperature and strain rate”, J. of Mat. Eng. and Perf., vol. 23, I. 5 (2014) 1641-1650.
- [114] Sumantra M., et. al., “Constitutive equations to predict high temperature flow stress in a Ti-modified austenitic stainless steel”, Mat. Sci. and Eng. A, vol. 500 (2009) 114-121.
- [115] Seo S., et. al., “Constitutive equation for Ti-6Al-4V at high temperatures measured using the SHPB technique”, Int. J. of Impact Eng., vol. 31 (2005) 735-754.
- [116] Lee W.S., Chen C.W., “High temperature impact properties and dislocation substructure of Ti-6Al-7Nb biomedical alloy”, Mat. Sci. & Eng. A, vol. 576 (2013) 91-100.
- [117] Kuokkala V.T., et. al., “High and low temperature techniques in Hopkinson split bar testing”, Proc. of the IMPLAST 2010 Conf. (2010).
- [118] Macdougall D.A.S., Harding J., “The measurement of specimen surface temperature in high-speed tension and torsion tests”, Int. J. Impact Eng., vol. 21, no. 6 (1998) 473-488.

- 
- [119] Xuan C., et. al., “An SHTB-based experimental technique for elevated temperature”, 2<sup>nd</sup> Int. Conf. on Elect. & Mech. Eng. and Inf. Tech. (2012) 321-325.
- [120] Kassner M.E., Geantil P., “Yield stress of 21-6-9 stainless steel over very wide ranges of strain rates and temperatures”, J. of Mat. Eng. and Perf., vol. 21, I. 1 (2012) 69-73.
- [121] Johnson G.R., Cook W.A., “A constitutive model and data for metals subjected to large strains, high strain rates and high temperatures”, 7<sup>th</sup> Int. Symp. on Ballistic (1983) 541-547.
- [122] Armstrong R.W., Zerilli F.J., “Dislocation mechanics based analysis of material dynamics behavior”, J. de Physique, vol. 49, no. 9 (1988) 529-534.
- [123] Tracker 4.8 Help Manual – <http://www.cabrillo.edu/>.
- [124] Klueh R.L., Nelson A.T., “Ferritic/martensitic steels for next-generation reactors”, J. of Nuc. Mat., vol. 371 (2007) 37-52.
- [125] Scapin M., et. al., “Tensile behavior of T91 steel over a wide range of temperatures and strain-rate up to  $10^4 \text{ s}^{-1}$ ”, J. of Mat. Eng. and Perform., vol. 23, I. 8 (2014) 3007-3017.
- [126] Zhang Y., et. al., “Application of high velocity impact welding at varied different length scales”, J. of Mat. Process. Tech., vol. 211 (2011) 944-952.
- [127] Psyk V., et. al., “Electromagnetic forming-A review”, J. of Mat. Process. Tech., vol. 211 (2011) 787-829.
- [128] de Groh III H.C., et. al., “Comparison of GRCo-84 to other Cu alloys with high thermal conductivities”, J. of Mat. Eng. Perform., vol. 17, I. 4 (2007) 594-606.
- [129] Valdiviez R., et. al., “The use of dispersion strengthened copper in accelerator designs”, XX Int. Linac Conf. (2000) 956-958.
- [130] Scapin M., et. al., “Effects induced by LHC high energy beam in copper structures”, J. of Nuclear Mat., vol. 420 (2012) 463-472.
- [131] Shields J.A., “Applications of molybdenum metal and its alloys”, Int. Molybdenum Ass. (2013) ISBN 978-1-907470-30-1.
- [132] Zerilli F.J., Armstrong R.W., “Dislocation-mechanics-based constitutive relations for material dynamics calculations”, J. Appl. Phys., vol. 61, no. 5 (1987) 1816-1825.

- [133] Malygin G.A., “Analysis of the strain-rate sensitivity of flow stresses in nanocrystalline FCC and BCC metals”, *Physics of the Solid State*, vol. 49, n. 12 (2007) 2266-2273.
- [134] Wei Q., et. al., “Effect of nanocrystalline and ultrafine grain sizes on the strain rate sensitivity and activation volume: fcc versus bcc metals”, *Mat. Sci. & Eng. A*, vol. 381 (2004) 71-79.
- [135] Roylance D., “The dislocation basis of yield and creep”, Department of Mat. Sci. and Eng. Massachusetts Inst. of Technology (2001).
- [136] Yang F., Li J.C.M., “Deformation behavior of tin and some tin alloys”, *Lead-Free Electronic Solders* (2006) 191-210.
- [137] Gambirasio L., Rizzi E., “On the calibration strategies of the Johnson-Cook strength model: Discussion and applications to experimental data”, *Mat. Sci. & Eng. A*, vol. 610 (2014) 370-413.
- [138] Özel T, Karpuz Y., “Identification of constitutive material model parameters for high-strain rate metal cutting conditions using evolutionary computational algorithms”, vol. 22 (2007) 659-667.
- [139] Gladman D., et. al., “LS-DYNA<sup>®</sup> keyword user’s manual – Volume II – Material Models”, LSTC (2013).
- [140] Chen S.R., et. al., “Constitutive modeling of a 5182 Aluminum as a function of strain rate and temperature”, *Hot Def. of Aluminum Alloys II Symp.* (1998).
- [141] Chen S.R., et. al., “Constitutive relations for Molybdenum under high-strain-rate deformation”, *Molybdenum and Molybdenum alloys Symp.* (1998).
- [142] Chen S.R., et. al., “Mechanical properties and constitutive relations for Tantalum and Tantalum alloys under high-rate deformation”, *Tantalum Annual Meeting* (1996).
- [143] Tanner A.B., et. al., “Modeling temperature and strain rate history effects in OFHC Cu”, *Int. J. of Plasticity*, vol. 15 (1999) 575-603.
- [144] Armstrong R.W., Walley S.M., “High strain rate properties of metals and alloys”, *Int. Mat. Reviews*, vol. 53, no. 3 (2008) 105-128.
- [145] Lin Y.C., Chen X.M., “A combined Johnson-Cook and Zerilli-Armstrong model for hot compressed typical high-strength alloy steel”, *Comp. Mat. Sci.*, vol. 49 (2010) 628-633.

- 
- [146] Scapin M., et. al., "Parameters identification in strain-rate and thermal sensitive visco-plastic material model fo an alumina dispersion strengthened copper", *Int. J. of Impact Eng.*, vol. 40-41 (2012) 58-57.
- [147] Langrand B., et al., "Identification technique of constitutive model parameters for crashworthiness modelling", *Aerospace Sci. and Tech.*, no. 4 (1999) 215-227.
- [148] Notta-Cuvier D., et. al., "Identification of Johnson-Cook's viscoplastic model parameters using the virtual fields method: Application to Titanium alloy Ti6Al4V", *Strain*, vol. 49 (2013) 22-45.
- [149] Short A., Bäker M., "Determination of Johnson-Cook parameters from machining simulations", *Comp. Mat. Sci.*, vol. 52 (2012) 298-304.
- [150] Milani A.S., et. al., "An improved multi-objective identification of Johnson-Cook material parameters", *Int. J. of Impact Eng.*, vol. 36 (2009) 294-302.
- [151] Bridgman P.W., "Studies in large plastic flow and fracture", McGraw-Hill (1952) 9-37.
- [152] Bridgman P.W., "The stress distribution in the neck of a specimen", *Trans. ASM*, vol. 32 (1944) 553-574.
- [153] Tsuchida N., et. al., "Estimation of the true stress and true strain until just before fracture by the stepwise tensile test and Bridgman equation for various metals and alloys", *Mat. Trans.*, vol. 53, no. 1 (2012) 133-139.
- [154] Li H.Y., et. al., "A modified Johnson Cook model for elevated temperature flow behavior of T24 steel", *Mat. Sci. & Eng. A*, vol. 577 (2013) 138-146.
- [155] Singh N.K., et. al., "Dynamic tensile behavior of multi phase yield strength steel", *Mat. & Design*, vol. 32 (2011) 5091-5098.
- [156] Zhang H., et. al., "A modified Zerilli-Armstrong model for alloy IC10 over a wide range of temperatures and strain rates", *Mat. Sci. and Eng. A*, vol. 527 (2009) 328-333.
- [157] Li H.Y., et. al., "A comparative study on modified Johnson Cook, modified Zerilli-Armstrong and Arrhenius-type constitutive models to predict the hot deformation behavior in 28CrMnMoV steel", *Mat. And Design*, vol. 49 (2013) 493-501.
- [158] Samantaray D., et. al., "A thermo-viscoplastic constitutive model to predict elevated-temperature flow behaviour in a titanium-modified austenitic stainless steel", *Mat. Sci. and Eng. A*, vol. 526 (2009) 1-6.

- 
- [159] Marshall E.R., Shaw M.C., *Trans. ASM*, vol. 44 (1952) 705-725.
- [160] Hopperstad O.S., et. al., “On the influence of stress triaxiality and strain rate on the behaviour of a structural steel. Part I. Experiments”, *Europ. J. of Mech. A/Solids*, vol. 22 (2003) 1-13.
- [161] Alves M., Jones N., “Influence of hydrostatic stress on the failure of axisymmetric notched specimen”, *J. of the Mech. and Phys. of Solids*, vol. 47 (1999) 643-667.
- [162] La Rosa G., et. al., “Postnecking elastoplastic characterization: degree of approximation in the Bridgman method and properties of the flow-stress/true-stress ratio”, *Metal. and Mat. Trans. A*, vol. 34 (2003) 615-624.
- [163] Mirone G., “The dynamic effect of necking in Hopkinson bar tension tests”, *Mech. of Mat.*, vol. 58 (2013) 84-96.
- [164] Mirone G., “A new model for the elastoplastic characterization and the stress-strain determination on the necking section of a tensile specimen”, *Int. J. of Solids and Struct.*, vol. 41 (2004) 3545-3564.
- [165] Sasso M., et. al., “Material characterization at high strain rate by Hopkinson bar tests and finite element optimization”, *Mat. Sci. and Eng. A*, vol. 487 (2008) 289-300.
- [166] Sato K., et. al., “A method to investigate strain rate effects on necking and fracture behaviors of advanced high-strength steels using digital imaging strain analysis”, *Int. J. of Impact Eng.*, vol. 75 (2015) 11-26.
- [167] Børvik T., et. al., “On the influence of stress triaxiality and strain rate on the behaviour of a structural steel. Part II. Numerical study”, *Europ. J. of Mech. A/Solids*, vol. 22 (2003) 15-32.
- [168] Osovski S., et. al., “Dynamic tensile necking: influence of specimen geometry and boundary conditions”, *Mech. of Mat.*, vol. 62 (2013) 1-13.
- [169] Børvik T., et. al., “A computational model of viscoplasticity and ductile damage for impact and penetration”, *Europ. J. of Mech. A/Solids*, vol. 20 (2001) 685-712.
- [170] Stander N., et. al., “LS-OPT<sup>®</sup> User’s Manual: A design optimization and probabilistic analysis tool for the engineering analyst – Version 5.1”, Livermore Software Technology Corporation, June 2014.
- [171] Henchi I., et. al., “Material constitutive parameter identification using an electromagnetic ring expansion experiment coupled with LS-DYNA<sup>®</sup> and LS-OPT<sup>®</sup>”, 10<sup>th</sup> Int. LS-DYNA<sup>®</sup> Users Conference - Optimization, (2008).

[172] Cooreman S., et. al., “Elasto-plastic material parameter identification by inverse methods: calculation of the sensitivity matrix”, *Int. J. of Solids and Struct.*, vol. 44 (2007) 4329-4341.

[173] Manes A., et. al., “Analysis of strain rate behaviour of an Al 6061 T6 alloy”, *Proc. Eng.*, vol. 10 (2011) 3477-3482.

[174] Kajberg J., Wikman B., “Viscoplastic parameter estimation by high strain-rate experiments and inverse modelling – Speckle measurements and high-speed photography”, *Int. J. of Solids and Structures*, vol. 44 (2007) 145-164.

[175] Koc P., Štock B., “Computer-aided identification of the yield curve of a sheet metal after onset of necking”, *Comp. Mat. Sci.*, vol. 31 (2004) 155-168.

[176] Sedighi M., et. al., “An approach in parametric identification of high strain rate constitutive model using Hopkinson pressure bar test results”, *Mat. Sci. and Eng. A.*, vol. 527 (2010) 3521-3528.

[177] Zhou J.M., et. al., “New inverse method for identification of constitutive parameters”, *Trans. Nonferrous Met. Soc. China*, vol. 16 (2006) 148-152.

[178] Grazka M., Janiszewski J., “Identification of Johnson-Cook equation constants using Finite Element Method”, *Eng. Trans.*, vol. 60 (2012) 215-223.

[179] Klocke F., et. al., “Inverse identification of the constitutive equation of Inconel 718 and AISI 1045 from FE machining simulations”, *Proc. CIRP*, vol. 8 (2013) 212-217.

[180] Pujana J., et. al., “Analysis of the inverse identification of constitutive equations applied in orthogonal cutting process”, *Int. J. of Machine Tools & Manuf.*, vol. 47 (2007) 2153-2161.

[181] Goel T., Stander N., “Multi-Objective Optimization using LS-OPT”, *LS-DYNA Conference* (2007).

[182] Bandyopadhyay S., Saha S., “Unsupervised classification”, (2013) doi: 10.1007/978-3-642-32451-2\_2.

